2011

Galaxy cluster mass measurements based on joint x-ray and Sunyaev Zel'dovich effect data

Nicole L. Hasler

GALAXY CLUSTER MASS MEASUREMENTS BASED ON JOINT X-RAY AND SUNYAEV ZEL'DOVICH EFFECT DATA

by

NICOLE L. HASLER

A DISSERTATION

Submitted in partial fulfillment of the requirements
for the degree of Doctor of Philosophy
in
The Department of Physics
to
The School of Graduate Studies
of
The University of Alabama in Huntsville

HUNTSVILLE, ALABAMA
2011

In presenting this dissertation in partial fulfillment of the requirements for a doctoral degree from The University of Alabama in Huntsville, I agree that the Library of this University shall make it freely available for inspection. I further agree that permission for extensive copying for scholarly purposes may be granted by my advisor, or in his absence, by the Chair of the Department, or the Dean of the School of Graduate Studies. It is also understood that due recognition shall be given to me and to the University of Alabama in Huntsville in any such scholarly use which may be made of any material in this dissertation.

Nicole L. Hasler — 6/24/11

(student signature) (date)

DISSERTATION APPROVAL FORM

Submitted by Nicole L. Hasler in partial fulfillment of the requirements for the degree of Doctor of Philosophy in Physics and accepted on behalf of the Faculty of the School of Graduate Studies by the disseratation committee.

We, the undersigned members of the Graduate Faculty of The University of Alabama in Huntsville, certify that we have advised and/or supervised the candidate on the work described in this dissertation. We further certify that we have reviewed the dissertation manuscript and approve it in partial fulfillment of the requirements for the degree of Doctor of Philosophy in Physics.

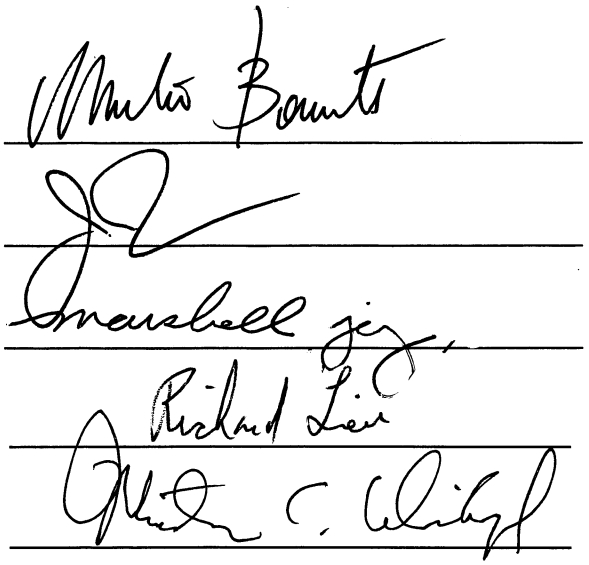

Committee Chair

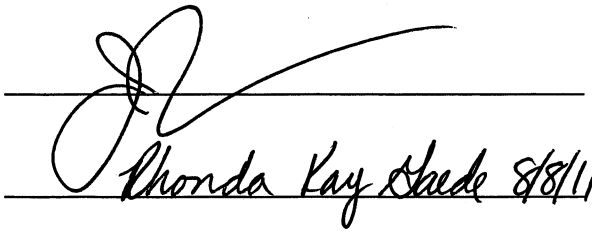

Department Chair

College Dean

Graduate Dean

ABSTRACT

School of Graduate Studies
The University of Alabama in Huntsville

Degree Doctor of Philosophy College/Dept. Science/Phsyics

Name of Candidate Nicole L. Hasler

Title Galaxy Cluster Mass Measurements Based on Joint X-ray and Sunyaev Zel'dovich Effect Data

Galaxy clusters trace the growth of structure of the universe and their abundance and evolution reflect the underlying cosmological parameters, such as Ω_M, σ_8, and the dark energy equation of state parameter. A new analytic model was developed which describes the physical properties of the intra-cluster medium (ICM) (Bulbul et al., 2010). The model has the advantage of simultaneously fitting X-ray and Sunyaev Zel'dovich Effect (SZE) data. A method of the joint analysis of X-ray and SZE data using the self-consistent model allows for the measurement of the gas mass fraction without the need to impose external priors on the cosmological parameters.

Massive clusters are expected to trace the matter content of the universe. The cluster gas mass fraction radial profile was measured out to r_{500} for 25 relaxed clusters using Chandra data. When combined with the stellar mass fraction, the cluster baryon fraction at r_{500} is 0.177 ± 0.024 agrees with the cosmic baryon fraction measured by WMAP ($\Omega_B/\Omega_M = 0.167 \pm 0.006$;Komatsu et al., 2011). This verifies that massive relaxed clusters accurately trace the primordial content of the universe provided that the measurement of the gas mass fraction is determined at large radii.

The gas mass fraction is an essential astrophysical quantity for probing cosmological questions. The behavior of the gas mass fraction as it evolves with redshift has never been determined observationally. Using the joint X-ray and SZE analy-

sis method, the redshift evolution is measured with minimal assumptions about the cosmology for 25 clusters spanning a redshift range $0.09 - 1.06$.

The joint analysis method can also be used to investigate discrepancies between the ICM pressure inferred from X-ray and SZE observations. Agreement between the SZE and X-ray pressure are within a few percent. The average of the ratio of the two pressures is 1.02 ± 0.04. Therefore no evidence is found for the presence of significant sources of systematic uncertainty in the measurement of the ICM pressure from X-ray and SZE observations. Improvements to this dissertation may be made by expanding the sample and using better quality data.

Abstract Approval:

Committee Chair 

Department Chair 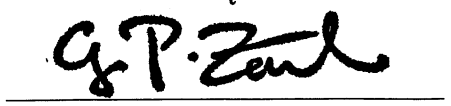

Graduate Dean 

ACKNOWLEDGMENTS

The last five years have been extremely challenging and exhausting. It has definitely been a very long road in which I have grown stronger and more confident thanks to the help and support of many people who I would like to acknowledge.

I was very lucky to have Max as my advisor and honestly could not have asked for a better person to guide me through my dissertation. He is passionate about science and this shows in his research and teaching. He was extremely patient with me as I stumbled through practice questions preparing for my quals and defense. I will truly miss working with Max.

None of the analysis would be finished if it wasn't for Marshall. He ran countless Markov chains so I could finally finish my dissertation. He is an amazing advisor who always stands by his students and pushes them to their full potential. For this I can't thank him enough.

I would also like to acknowledge my committee, Dr. Martin Weisskopf, Dr. Jack Fix, and Dr. Richard Lieu, for their help and time. I want to also thank Esra Bulbul and David Landry for their help with the X-ray analysis.

My family has given me nothing but love and support, especially my grandparents, Ma and Poppy. My parents have stood by my side every step of the way and never stopped believing I would make it through the PhD program. They dropped everything to help me whenever I needed it. I will never forget this. I would also like to thank my sisters for always keeping me humble and making me laugh when times got tough.

Although my family is 600 miles away, I have found a family here in Huntsville among some of the most amazing people I am proud to call my friends. I always looked forward to my Thursday night dinner and drinks with Jessica and greatly value her advice. Laci kept me grounded and I could always count on her to make me laugh. I think I would've gone crazy if I didn't have her in my life. Finally, I want to thank Mark, the love of my life. He always was there with a shoulder to cry when the stress became too much. Finally, I would like to thank God for being by my side every step of this journey. Thank you to all.

TABLE OF CONTENTS

LIST OF FIGURES

LIST OF TABLES

LIST OF SYMBOLS

Symbol	**Meaning**
$M_{\odot}$	Solar Mass
K	Kelvin
ICM	Intra-cluster medium
f_{gas}	Gas mass fraction
M_{gas}	Gas mass
M_{tot}	Total mass
Ω_b	Baryon density
Ω_M	Matter density
Ω_Λ	Dark energy density
ΛCDM	Λ cold dark matter model
$SCDM$	Standard dark matter model
H_o	Hubble constant
km	kilometers
s	seconds
Mpc	Mega parsec
r_{2500}	Radius within which the average density of the cluster is 2500 times the critical density of the universe at the redshift
r_{500}	Radius within which the average density of the cluster is 500 times the critical density of the universe at the redshift
SZE	Sunyaev Zel'dovich effect

GHz	Giga-hertz
CMB	Cosmic microwave background
mm	milimeters
MJy	Mega Jansky
sr	Steradians
$OVRO$	Owens Valley Radio Observatory
$BIMA$	Berkley Illinois Maryland Association
$ROSAT$	Roentgen Satellite is an orbiting X-ray observatory
$XMM - Newton$	X-ray Multi-Mirror Mission - Newton is an orbiting X-ray observatory
$H(z)$	Hubble expansion rate
Y	Integrate pressure
$WMAP$	Wilkinson microwave anistropy probe
ρ	Total mass density
ρ_i	Normalization factor in the total mass density profile
r	Radius
r_s	Scale radius
β	Slope in total mass density profile
ϕ	Gravitational potential
$T(r)$	Electron temperature profile
n	Polytropic index
ρ_{gas}	Density of gas
k_b	Boltzmann constant

m_p	Proton mass
μ	Total mean molecular weight
T_o	Temperature normalization constant
$n_e(r)$	Electron number density profile
G	Gravitational constant
n_{eo}	Electron density normalization constant
$P_e(r)$	Electron pressure profile
P_{eo}	Electron pressure normalization constant
$\tau_{cool}(r)$	Taper function
r_{cool}	Cooling scale radius
α	The amount of cooling in the core
γ	Index of taper function
SZA	Sunyaev Zel'dovich Array
$CIAO$	Chandra Interactive Analysis of Observations
$CALDB$	Calibration database
keV	Kilo electron-volts
$FWHM$	Full width at half maximum
m	Meters
S_X	Surface brightness
z	Redshift
Λ_{ee}	Emissivity- X-ray cooling function in units of counts $cm^3\ s^{-1}$
A	Abundance
l	Line of sight

cm	Centimeters
Δ_{SZ}	SZE decrement
T_{CMB}	Temperature of cosmic microwave background
σ_T	Thomson cross section
$f(x, T_e)$	Frequency dependence of the SZE temperature signature using the relativistic corrections
m_e	Electron mass
c	Speed of light
D_A	Angular diameter distance
y	Compton y parameter
$Y(u, v)$	Integrated compton-y parameter
$g(x)$	Frequency dependence of the SZE flux
I_0	Primary cosmic microwave background intensity
r_Δ	Radius within which the average density of the cluster is Δ times the critical density of the universe at the redshift
$E(z)$	Evolution of the universe
Ω_k	Curvature parameter
FRW	Friedman-Robertson-Walker cosmological model
n_H	Neutral column density
RA	Right Ascension
Dec	Declination
src	Source

$ObsID$	Observation Identification number
$EXPO$	Exposure time
$P.A.$	Position Angle
rms	Root mean square
$\Delta\alpha$	Offset from the pointing center in right ascension
$\Delta\delta$	Offset from the pointing center in declination
λ	Wavelength
deg	Degree
hrs	Hours
$ACIS$	Advanced CCD Imaging Spectrometer on Chandra
P	Total pressure
ρ_c	Critical density of universe
Δ	Overdensity constrast
$\overline{x}$	Weighted mean
$\sigma^2_{weighted}$	Weighted sample variance
f_{baryon}	Cluster baryon fraction
f_{star}	Stellar mass fraction
dp	Datapoints
dof	Degrees of freedom
$\propto$	Proportionality
E	CMB photon energy
γ	Lorentz factor
p	Radiative pressure

u_{NRel}	Energy density for non-relativistic electron
N	Number of electrons
u_{Rel}	Energy density for relativistic electrons
Y_{sph}	Spherical integrated pressure
$NVSS$	The National Radio Astronomy Observatory Very Large Array Sky Survey
$FIRST$	Faint Images of the Radio Sky at Twenty-Centimeters
t	time

For Ma

CHAPTER 1

INTRODUCTION TO GALAXY CLUSTERS

Galaxy clusters are used to study cosmology since they are tracers of the matter content in the universe. By mass, galaxy clusters are composed of approximately 3 % galaxies (Lin et al., 2003; Gonzalez et al., 2007), 15% hot ionized gas (Vikhlinin et al., 2006), and the remainder is dark matter (Allen et al., 2008). Galaxy clusters contain 30-300 galaxies, have a typical radius of a few mega-parsecs and a mass of $10^{14} - 10^{15}$ $M_{\odot}$.The ionized hot gas in galaxy clusters has a temperature of $10^{7} - 10^{8}$ K which emits X-rays primarily through bremsstrahlung radiation. X-ray observations are used to measure the mass of the hot ionized plasma also known as the intra-cluster medium (ICM).

The ratio of the hot gas mass to the total mass (baryonic + dark matter) is defined as the gas mass fraction:

$$f_{gas} = \frac{M_{gas}}{M_{tot}}, \tag{1.1}$$

where M_{gas} is the gas mass and M_{tot} is the total mass. This quantity is of cosmological importance because at large radii it is expected to closely match cosmic baryon fraction which is the ratio of the baryonic matter to the total matter density of the universe, Ω_b/Ω_M. Previous studies have used measurements of the gas mass fraction (Allen et al., 2008; Ettori et al., 2009) to constrain cosmological parameters, such as Ω_M, Ω_Λ, and the equation of state of dark energy.

For measuring cluster masses using X-ray measurements, prior knowledge about the cosmology is required. Figure 1.1, shows the gas mass fraction measured from the same dataset (taken from Allen et al., 2008) for two different sets of cosmological parameters:

- Λ Cold Dark Matter Model (ΛCDM): $H_o = 70\ km/s/Mpc, \Omega_M = 0.30, \Omega_\Lambda = 0.70$
- Standard Cold Dark Matter Model (SCDM): $H_o = 50\ km/s/Mpc, \Omega_M = 1.0, \Omega_\Lambda = 0.0$

As seen in Figure 1.1, there is a significant difference when the gas mass fraction is determined using the SCDM model and the ΛCDM model: this difference is a result of the the gas mass fraction being dependent on cosmology when measured by X-ray observations. This cosmology dependence will be explained in Chapter 4. Some of the previous studies found $f_{gas}(r_{2500}) = 0.119 \pm 0.003 \pm^{0.007}_{0.014}$ (LaRoque et al., 2006) and $f_{gas}(r_{500}) = 0.12 \pm 0.004$ (Zhang et al., 2008) for X-ray only measurements assuming a ΛCDM cosmology with $H_o = 72\ km/s/Mpc, \Omega_M = 0.27, \Omega_\Lambda = 0.73$. A more comprehensive summary of measurements of the gas mass fraction is provided in Section 4.1.

Another approach for measuring cluster masses uses Sunyaev Zel'dovich effect (SZE) observations (Grego et al., 2001; LaRoque et al., 2006; Menanteau et al., 2010; Vanderlinde et al., 2010). The Sunyaev Zel'dovich effect occurs when the Cosmic Microwave Background (CMB) photons scatter off the energetic electrons in the ICM. A slight shift in the CMB spectrum is observed. For frequencies below 218 GHz a

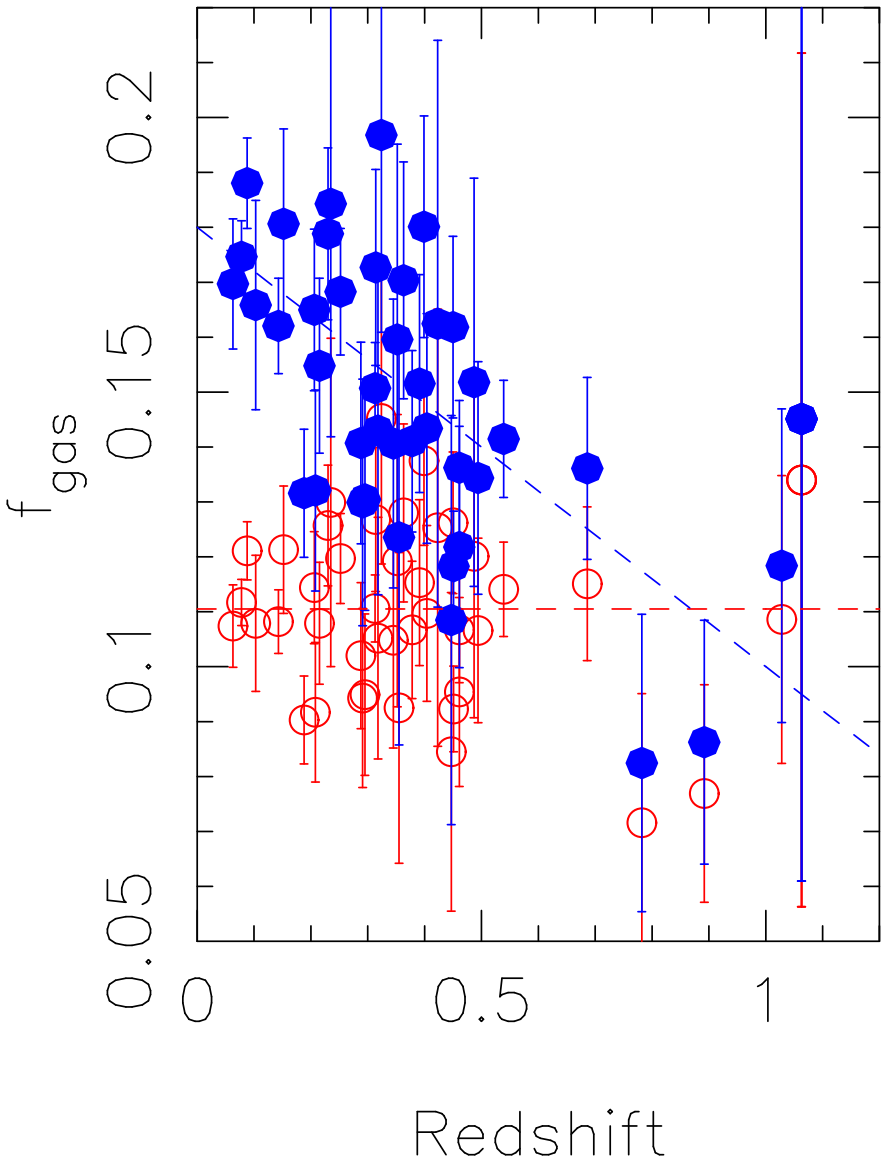

Figure 1.1: Plot of the gas mass fraction as a function of redshift from Allen et al. (2008). The open symbols (red) use a ΛCDM model to calculate the angular diameter distance and the filled symbols (blue) use a SCDM model.

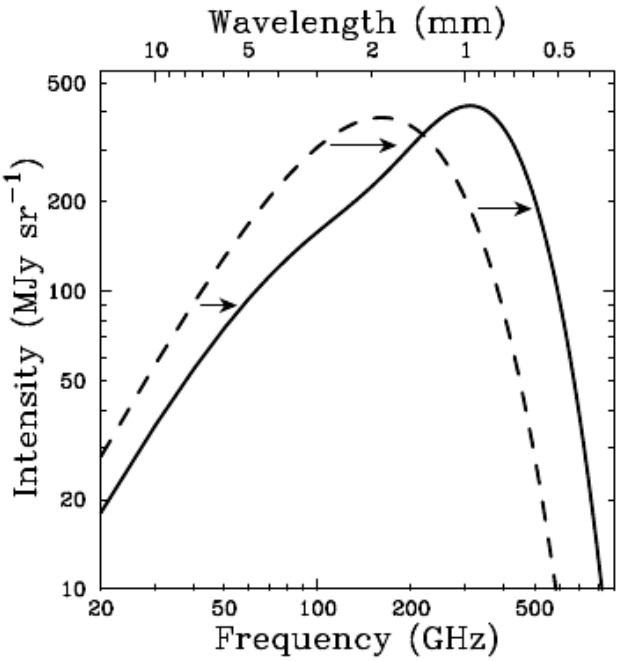

Figure 1.2: Adapted from Carlstrom et al. (2002): Cosmic Microwave Background spectrum distorted by the Sunyaev Zel'dovich effect (solid line). This distortion is exaggerated to show the SZE.

decrement in the intensity is observed, above 218 GHz an increment is seen (Sunyaev & Zel'dovich, 1972), and at 218 GHz a null, see Figure 1.2.

LaRoque et al. (2006) measured $f_{gas}(r_{2500}) = 0.121 \pm 0.005 \pm^{0.009}_{0.016}$ for 39 clusters using SZE observations which were taken with the Owens Valley Radio Observatory (OVRO) and the Berkley Illinois Maryland Association (BIMA) at 30 GHz.

Chapter 5 discusses a joint X-ray and SZE analysis method to measure the gas mass fraction without assumptions about the underlying cosmology.

1.1 Model for the Analysis of X-ray and Sunyaev Zel'dovich effect Observations

For this project, a self-consistent model was developed which is able to fit joint X-ray and Sunyaev Zel'dovich (SZ) effect observations. The new physically motivated

model describes the physical properties of clusters: density, temperature, and pressure of the intra-cluster medium. This model is based on an analytic distribution by Navarro et al. (1997) for the cluster mass density, generalized according to Suto et al. (1998) and following a procedure described by Ascasibar et al. (2003) and Ascasibar & Diego (2008) in which the mass density is combined with a polytropic equation of state to model the gas at large radii. This analytic model has a limited number of parameters which describe the global properties of the cluster. For clusters without a cool core, five parameters are sufficient to describe the density, temperature, and pressure. Over time clusters settle into hydrostatic equilibrium and the gas at the core becomes dense and cools. Clusters with a cooler temperature in the core are referred to as cool core clusters. For cool core clusters, three additional parameters are introduced in a taper function by Vikhlinin et al. (2006) to describe the temperature and density at small radii. By taking advantage of the ideal gas law the pressure profile can be derived from the density and temperature profiles. This provides us with a self-consistent model for the density, temperature, and pressure profiles for a hot plasma in hydrostatic equilibrium which can be used for joint X-ray and SZE analysis.

A number of models suitable for SZE observations are available in the literature, for example Nagai et al. (2007) and Mroczkowski et al. (2009). The model has the advantage of simultaneous applicability to both X-ray and SZE observations, which will be used extensively in this research (see Section 1.4). The derivation of the new models is presented in Chapter 2.

1.2 The Distribution of Baryons in Clusters from X-ray Observations

X-ray observations are a useful tool for measuring the cluster masses and gas mass fraction in clusters. The measurements of the gas mass fraction out to a significant fraction of the virial radius (e.g., r_{500}) for a large sample of clusters can be used to test whether the baryon fraction in clusters is consistent with the currently favored cosmological parameter set. However, recent studies using ROSAT, XMM-Newton, and Chandra observations have found the gas mass fraction (Allen et al., 2002, 2004; Vikhlinin et al., 2006; Arnaud et al., 2007; Allen et al., 2008; Zhang et al., 2008; Ettori et al., 2009) to fall short of the cosmic baryon fraction measured, $\Omega_B/\Omega_M = 0.1675 \pm 0.006$ by the Wilkinson Microwave Anisotropy Probe (WMAP) 7 year data (Komatsu et al., 2011).

The distribution of baryons in relaxed clusters is investigated by measuring the gas mass fraction out to r_{500} using Chandra observations. The results are described in Chapter 4.

1.3 Redshift Evolution of the Gas Mass Fraction in Galaxy Clusters

A combined analysis of X-ray and SZE observations of galaxy clusters can be used for a variety of astrophysical applications (Birkinshaw & Hughes, 1994; Hughes & Birkinshaw, 1998; Reese et al., 2002; LaRoque et al., 2006; Bonamente et al., 2006). The joint analysis allows for the direct measurement of the cluster gas mass fraction without the need to impose external priors on cosmological parameters (e.g., the Hubble expansion rate $H(z)$). Such an analysis can directly probe the evo-

lution of cluster gas mass fractions with redshift, providing an important complement to X-ray only cosmological studies that rely on simulations to supply this function (Allen et al., 2008). In this project, a method for the joint analysis of X-ray and SZE data using a self-consistent set of analytic models is presented to describe the physical properties of clusters. This method is demonstrated by appling it to two intermediate redshift clusters, Abell 1835 and Abell 2631, with high signal to noise data from Chandra and the Sunyaev Zel'dovich Array (SZA) observations (Hasler et al., 2011). In Chapter 3, the models accurately describe the surface brightness and temperature profiles in the X-ray data and fit the 30 GHz SZE data using a minimal number of parameters.

After verifying that the joint analysis method works on X-ray and SZE observations for two clusters, this method is applied to 25 relaxed galaxy clusters spanning a redshift range of 0.09-1.06. This joint measurement of the gas mass fraction from a sample of clusters spanning a large redshift range can be used to test the assumption that the gas mass fraction is constant with redshift (Sasaki, 1996; Pen, 1997). Knowledge of the evolution of the gas mass fraction as a function of redshift is required to obtain accurate constraints on cosmological parameters (for example, Allen et al., 2004, 2008; Ettori et al., 2009). In Chapter 5 a linear fit is applied to the gas mass fraction measurements at r_{500} to determine the redshift evolution of the gas mass fraction.

1.4 Comparison of X-ray and Sunyaev Zel'dovich Effect Measurements of the Electron Pressure

The joint analysis method may also be used to provide accurate measurements of the integrated electron pressure in X-ray and SZE observations in galaxy clusters. The X-ray observables are the electron temperature and surface brightness, the latter dependent on the square of the electron density according to the surface brightness equation; the SZE observable, on the other hand, is directly proportional to the electron pressure integrated along the line of sight. The integrated pressure, referred to as the Y parameter, is a fundamental mass proxy in cosmological studies, since the volume integral of pressure is the cluster thermal energy, which closely tracks the total gravitating mass (Kravtsov et al., 2006).

Each observational technique is subject to unique systematics that may bias their measurements. For example, certain measurements of the electron pressure with WMAP are in disagreement with X-ray predictions (Lieu et al., 2006; Bielby & Shanks, 2007), and the power spectrum measured by the South Pole Telescope (Lueker et al., 2010) and the Atacama Cosmology Telescope (Fowler et al., 2010) may be explained with the possibility that current X-ray models of the gas pressure overestimate the thermal pressure of electrons, particularly in the cluster outskirts (Battaglia et al., 2010; Shaw et al., 2010; Trac et al., 2010). Therefore a joint measurement from both X-ray and SZE data is useful for investigating their systematics. For these measurements, the model provides a unique parametrization that consistently describes the X-ray and SZE observables, and therefore mitigates the effect of using different models for X-ray and SZE observables. In order to use the integrated pressure as a cosmological tool it is necessary to check the agreement between

independent methods of measurement, in particular with a model that has a consistent parametrization for all observables. The X-ray and SZE integrated pressure are compared in 25 clusters, in Chapter 6.

The material presented in Chapter 2 was published in Bulbul, Hasler, Bonamente, and Joy (2010). The material presented in Chapter 3 has been submitted for publication in the Astrophysical Journal (Hasler et al., 2011), and additional papers based on the results of Chapters 4, 5, and 6 are in preparation for publication.

1.5 Structure of Dissertation

The analytic models used to fit X-ray and SZE observations are described in Chapter 2. In Chapter 3, the joint X-ray and SZE analysis method used for obtaining cluster masses and demonstrate this approach on two clusters, Abell 1835 and Abell 2631. Chapter 4 investigates the distribution of baryons in clusters from X-ray observations. In Chapter 5, the joint analysis method described in Chapter 3 is applied to a sample of 25 relaxed clusters and measure the evolution of the gas mass fraction in galaxy clusters. Chapter 6 discusses the comparison of the X-ray and SZE integrated pressure of the relaxed cluster sample. Finally, the conclusions of this dissertation are discussed in Chapter 7.

CHAPTER 2

MODEL FOR THE ANALYSIS OF X-RAY AND SUNYAEV ZEL'DOVICH EFFECT OBSERVATIONS

A new analytic model describing the intra-cluster medium of galaxy clusters is investigated in this chapter. This model is based on an analytic distribution of the cluster mass density described by the Navarro et al. (1997) distribution, which is generalized by following Suto et al. (1998), Ascasibar et al. (2003), and Ascasibar & Diego (2008). The mass density is combined with a polytropic equation of state for the gas to provide self-consistent density, temperature, and pressure profiles for a plasma in hydrostatic equilibrium. In this chapter the analytic radial profiles for the physical quantities are derived which is relevant to X-ray and SZE observations.

2.1 Mass Density Distribution

A total mass density profile is assumed which is based on the Navarro et al. (1997) distribution and has been generalized using a simplified version of the Suto et al. (1998) profiles:

$$\rho = \frac{\rho_i}{\frac{r}{r_s}(1+\frac{r}{r_s})^{\beta}}, \tag{2.1}$$

where ρ_i is the normalization factor, r_s is the scale radius, and $\beta + 1$ is the slope at large radii. The total mass can be obtained by taking the volume integral of the

density:

$$M_{tot} = \int \rho dV = \int_0^r dr \int_0^\pi d\theta \int_0^{2\pi} d\phi \rho r^2 sin(\theta) = 4\pi \int_0^r \frac{r^2 \rho_i dr}{(\frac{r}{r_s})(1+\frac{r}{r_s})^\beta}. \tag{2.2}$$

This integral can be simplified by letting $x = r/r_s$ and $dx = dr/r_s$.

$$M_{tot} = 4\pi\rho_i \int \frac{x r_s^3 dx}{(1+x)^\beta} \tag{2.3}$$

Now, use integration by parts:

$$\int_b^a u dv = uv|_b^a + \int_b^a v du. \tag{2.4}$$

In the case, $u = r_s^3 x$, $du = r_s^3 dx$, $dv = \frac{dx}{(1+x)^\beta}$, and $v = \frac{1}{(1-\beta)} \frac{1}{(1+x)^{\beta-1}}$

$$M_{tot} = 4\pi\rho_i r_s^3 \int_0^{r/r_s} \frac{x dx}{(1+x)^\beta} = \frac{x}{(1-\beta)} \frac{1}{(1+x)^{\beta-1}}|_0^{r/r_s} - \int_0^{r/r_s} \frac{1}{(1-\beta)} \frac{dx}{(1+x)^{\beta-1}}, \tag{2.5}$$

which reduces to

$$M_{tot} = \frac{4\pi\rho_i r_s^3}{(\beta-2)(\beta-1)} \left[1 + \frac{1 - r/r_s(\beta-1)}{(1+r/r_s)^{\beta-1}} \right]. \tag{2.6}$$

The total mass can be evaluated at $\beta = 2$ using L'Hospital's Rule:

$$\lim_{x \to a} \frac{f'(x)}{g'(x)}. \tag{2.7}$$

In the case $\beta \to 2$, $f(x) = 4\pi\rho_i r_s^3((1+r/r_s)^{\beta-1} + 1 - r/r_s(\beta-1))$, and $g(x) = (\beta-2)(\beta-1)((1+r/r_s)^{\beta-1})$. Therefore,

$$M_{tot}(\beta = 2) = 4\pi\rho_i r_s^3 \left[ln(1+r/r_s) - \frac{r/r_s}{1+r/r_s} \right]. \tag{2.8}$$

The total mass is therefore continuous at $\beta = 2$.

2.2 Gravitational Potential of Galaxy Clusters

The gravitational potential is defined as

$$d\phi(r) = \frac{GM(r)}{r^2}dr \tag{2.9}$$

$$\phi(r) = \int_0^r \frac{GM(r)}{r^2}dr. \tag{2.10}$$

Equation 2.6 is substituted into Equation 2.10 and simplify this equation by letting $x = r/r_s$ and $dx = dr/r_s$,

$$\phi(x) = \frac{4\pi\rho_i r_s^2}{(\beta-2)}\left[\int_0^{r/r_s}\frac{dx}{(\beta-1)x^2r_s^2} + \int_0^{r/r_s}\frac{dx}{(1-\beta)(1+x)^{\beta-1}x^2r_s^2}\right.$$
$$\left. - \int_0^{r/r_s}\frac{dx}{(1+x)^{\beta-1}xr_s^2} = \frac{4\pi\rho_i r_s^2}{(\beta-2)}\Big[\phi_A(x) + \phi_B(x) + \phi_C(x)\Big]\right.$$

First evaluate the first integral (A) of the equation,

$$\phi_A(x) = \int_0^{r/r_s}\frac{dx}{(\beta-1)x^2r_s^2} = -\frac{1}{(\beta-1)rr_s} \tag{2.11}$$

$$\phi_B(x) = \int_0^{r/r_s}\frac{dx}{(1-\beta)(1+x)^{\beta-1}x^2r_s^2} = \frac{1}{(1-\beta)r_s^2}\int_0^{r/r_s}\frac{dx}{(1+x)^{\beta-1}x^2}. \tag{2.12}$$

This integral can be determined using Gradshteyn and Ryzhik (1996) Equation 2.118;

$$\int\frac{dx}{x^n z_1 m} = -\frac{1}{(n-1)ax^{n-1}z_1^{m-1}} + \frac{b(2-n-m)}{a(n-1)}\int\frac{dx}{x^{n-1}z_1^m}, \tag{2.13}$$

where $z_k = a + bx^k$. In the case of $\phi_B(r)$, $n = 2$, $z_1 = 1 + x$, $m = (\beta - 1)$, $a = 1$, and $b = 1$, this results in

$$\phi_B(x) = \frac{1}{(1-\beta)r_s^2}\Bigg[- \frac{1}{x(1+x)^{\beta-2}} - (\beta-1)\int_0^{r/r_s} \frac{dx}{x(1+x)^{\beta-1}}. \tag{2.14}$$

For the last integral use the following equation from Gradshteyn and Ryzhik (1996):

$$\int_0^{r/r_s} \frac{dx}{xz_1^m} = \frac{1}{z_1^{m-1}a(m-1)} + 1/a\int_0^{r/r_s} \frac{dx}{z_1^{m-1}}, \tag{2.15}$$

where $a = 1$ and $m = \beta - 1$.

$$\phi_C(x) = \frac{1}{r_s^2}\int \frac{dx}{x(1+x)^{\beta-1}} = \frac{1}{(1+x)^{\beta-2}(\beta-2)} + \int \frac{dx}{x(1+x)^{\beta-2}}. \tag{2.16}$$

When the three integrals are added together,

$$\phi(x) = \frac{4\pi\rho_i r_s^2}{(\beta-2)}\Bigg[- \frac{1}{(\beta-2)r/r_s r_s^2} + \frac{1}{(1-\beta)r_s^2}\Bigg[- \frac{1}{r/r_s(1+r/r_s)^{\beta-2}} \tag{2.17}$$

$$-(\beta-1)\int_0^{r/r_s} \frac{dx}{r/r_s(1+r/r_s)^{\beta-2}}\Bigg] - \frac{1}{r_s^2}\Bigg(\frac{1}{(1+r/r_s)^{\beta-2}(\beta-2)} - \frac{1}{(\beta-2)} \tag{2.18}$$

$$+\int_0^{r/r_s} \frac{dx}{r/r_s(1+r/r_s)^{\beta-2}}\Bigg)\Bigg]. \tag{2.19}$$

Which is reduced by simplifying and appling the boundary condition $\phi(\infty) = 0$,

$$\phi(r) = -\frac{4\pi\rho_i r_s^2}{(\beta-1)(\beta-2)}\Bigg(\frac{(1+r/r_s)^{\beta-2}-1}{r/r_s(1+r/r_s)^{\beta-2}}\Bigg). \tag{2.20}$$

To find the central potential $\phi(0) = \phi_0$ use L'Hospital's rule. In this case

$$f'(x) = 4\pi\rho_i r_s^2(\beta-2)(1+r/r_s)^{\beta-3} \tag{2.21}$$

$$g'(x) = (\beta-2)(\beta-1)[r/r_s(1+r/r_s)^{\beta-2}(\beta-2) + (1+r/r_s)^{\beta-2}]. \tag{2.22}$$

Therefore at $x = 0$,

$$\frac{f'}{g'} = (\beta - 2) \tag{2.23}$$

and

$$\phi_0 = \frac{4\pi\rho_i r_s^2}{(\beta - 1)}. \tag{2.24}$$

Therefore,

$$\phi(r) = \phi_0 \left(\frac{1}{(\beta - 2)} \frac{(1 + r/r_s)^{\beta-2} - 1}{r/r_s (1 + r/r_s)^{\beta-2}} \right), \tag{2.25}$$

where $\phi_0 = -\frac{4\pi G\rho_i r_s^2}{(\beta-1)}$. The gravitational potential can also be evaluated at $\beta = 2$ by using L'Hospital's Rule,

$$\phi(r) = \phi_0 \left[\frac{ln(1 + r/r_s)}{r/r_s} \right]. \tag{2.26}$$

The gravitational potential is a continuous function for $\beta > 1$, which is shown in Figure 2.1.

2.3 Gas Density and Temperature Profile

The assumption of a polytropic gas for the intra-cluster medium in galaxy clusters at large radii is applied to the model. The polytropic density and temperature relationship are defined as

$$\frac{\rho_g(r)}{\rho_o} = \left[\frac{T(r)}{T_o} \right]^n, \tag{2.27}$$

where ρ_g is the gas density, ρ_o is the density normalization factor, $T(r)$ is the temperature of the cluster, T_o is the temperature normalization factor, and n is the polytropic index. The polytropic index $n > 0$ is a free parameter in the model which describes an isothermal profile of the gas when $n \to \infty$.

Spherical symmetry and hydrostatic equilibrium are assumed when modeling relaxed galaxy clusters. Hydrostatic equilibrium is defined as

$$\frac{1}{\rho_{gas}}\frac{dP}{dr} = -\frac{d\phi}{dr}. \tag{2.28}$$

Equation 2.28 is expanded using the ideal gas law $P = n_e k_b T(r) = \frac{\rho_g(r)}{\mu m_p} k_b T(r)$,

$$\frac{dP}{dr} = \frac{1}{\mu m_p}\left[k_b T(r)\frac{d\rho_g(r)}{dr} + k_b \rho_g(r)\frac{dT(r)}{dr}\right] = \rho_g \frac{d\phi}{dr}. \tag{2.29}$$

$$\frac{1}{\mu m_p}\left[k_b T(r)\frac{dCT(r)^n}{dr} + k_b CT(r)^n\frac{dT(r)}{dr}\right] = CT(r)^n\frac{d\phi}{dr}, \tag{2.30}$$

where $C = \rho_o/T_0^n$ from the polytropic relationship (Equation 26) and gets canceled in each term.

$$k_b T(r) n T(r)^{n-1}\frac{dT(r)}{dr} + k_b T(r)^n\frac{dT(r)}{dr} = T(r)^n\frac{d\phi}{dr}\mu m_p \tag{2.31}$$

$$k_b n\frac{dT(r)}{dr} + k_b\frac{dT(r)}{dr} = \frac{d\phi}{dr}\mu m_p \tag{2.32}$$

$$k_b(n+1)\int_0^T dT(r) = \int_0^\phi d\phi \tag{2.33}$$

The temperature is a function of the potential:

$$T(r) = \frac{\phi(r)\mu m_p}{k_b(n+1)}. \tag{2.34}$$

Equation 2.25 is substituted into Equation 2.34 and to find the temperature profile,

$$T(r) = T_o\left(\frac{1}{(\beta-2)}\frac{(1+r/r_s)^{\beta-2}-1}{r/r_s(1+r/r_s)^{\beta-2}}\right), \tag{2.35}$$

where $T_o = \frac{4\pi G \mu m_p r_s^2 \rho_i}{k_b (n+1)(\beta-1)}$. Using the polytropic relationship yields the density profile,

$$n_e(r) = n_{eo}\left(\frac{1}{(\beta-2)}\frac{(1+r/r_s)^{\beta-2}-1}{r/r_s(1+r/r_s)^{\beta-2}}\right)^n, \tag{2.36}$$

where n_{eo} is the electron density normalization factor. The density and temperature profiles are used to model the X-ray observables, surface brightness and spectroscopic temperature, see Chapter 3 for details on the fits.

The ideal gas law is used to derive the pressure profile,

$$P_e(r) = P_{eo}\left(\frac{1}{(\beta-2)}\frac{(1+r/r_s)^{\beta-2}-1}{r/r_s(1+r/r_s)^{\beta-2}}\right)^{n+1}, \tag{2.37}$$

where P_{eo} is the pressure normalization factor.

In the limit $\beta \to 2$, the pressure is a continuous function,

$$P_e(r) = P_{eo}\left(\frac{ln(1+r/r_s)}{r/r_s}\right)^{n+1}. \tag{2.38}$$

The pressure profile is used for modeling the Sunyaev Zel'dovich effect, see Chapter 3.

2.4 Modeling Cool Core Clusters

Many clusters have cool cores and a simple polytropic density model is unable to accurately describe the cluster at small radii. Therefore a Vikhlinin et al. (2006) cool core taper function is introduced to model the temperature at small radii,

$$\tau_{cool}(r) = \frac{\alpha + (r/r_{cool})^\gamma}{1+(r/r_{cool})^\gamma}, \tag{2.39}$$

where $\alpha = [0,1]$ measures the amount of cooling in the core, and r_{cool} is the cooling scale radius. A taper function is added to the temperature profile,

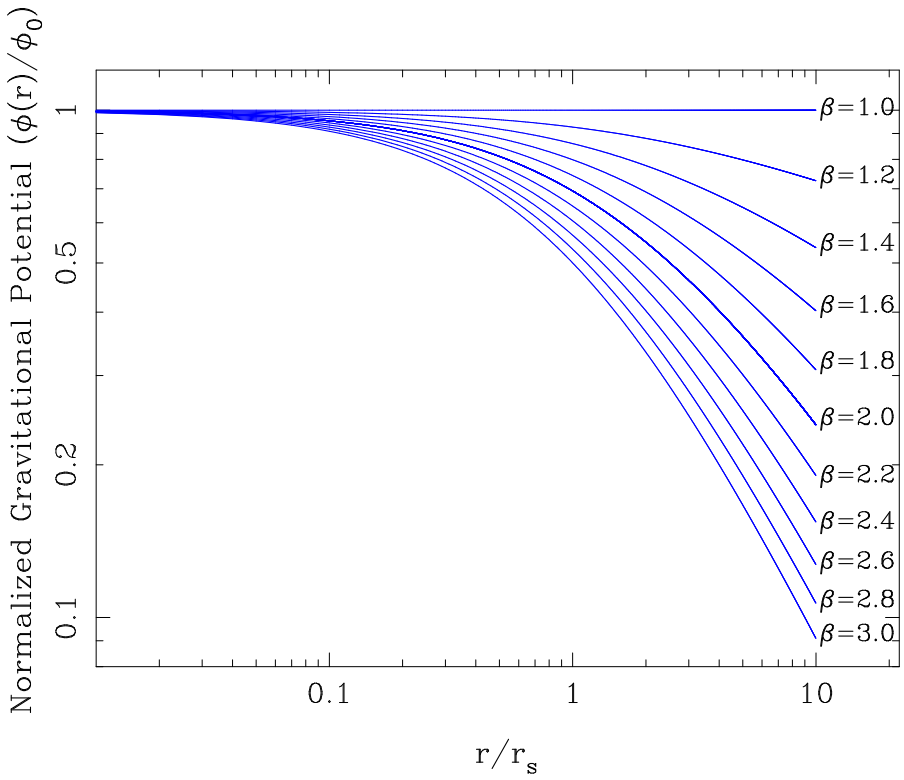

Figure 2.1: Normalized gravitational potential for different values of β.

$$T(r) = T_{poly}(r)\tau_{cool}(r) = T_o\left(\frac{1}{(\beta-2)}\frac{(1+r/r_s)^{\beta-2}-1}{r/r_s(1+r/r_s)^{\beta-2}}\right)\tau_{cool}(r). \tag{2.40}$$

To find the density profile for cool cores, it is assumed that the pressure distribution is the same as the polytropic case. Therefore the electron number density,

$$n_e(r) = \frac{P_e(r)}{k_b T(r)} = n_{eo}\left(\frac{1}{(\beta-2)}\frac{(1+r/r_s)^{\beta-2}-1}{r/r_s(1+r/r_s)^{\beta-2}}\right)^n \tau_{cool}^{-1}(r). \tag{2.41}$$

Figure 2.2 shows the normalized density and temperature profiles for a taper function with various values of β.

The hydrostatic equilibrium equation is combined with Equations 2.40 and 2.41 to find the total mass,

$$M(r) = \frac{4\pi\rho_i r_s^3}{(\beta-2)}\left(\frac{1}{(\beta-1)} + \frac{1/(1-\beta) - r/r_s}{(1+r/r_s)^{\beta-1}}\right)\tau_{cool}(r). \tag{2.42}$$

The only difference between the cool core total mass profile and the polytropic total mass profiles is the taper function, which is significant only at small radii. At large radii, the effect of the taper function vanishes, and the thermodynamics of the gas is described by the polytropic equation of state. Fits to this model are demonstrated in Chapter 3.

2.5 Summary

This model has a number of features that make it suitable for the analysis of X-ray and SZE observations of clusters. The model is analytic, and has a limited number of parameters which describe the global properties of clusters. For clusters which do not have a cool core, 5 parameters are sufficient to describe the distribution of the density, temperature, and pressure. The gas density and temperature are linked by the polytropic equation of state, and the total matter density is related to the plasma properties by the hydrostatic equilibrium. The model has the advantage of simultaneously fitting X-ray and SZE data and therefore it is suitable for this project. The model presented in this chapter is published in Bulbul et al. 2010.

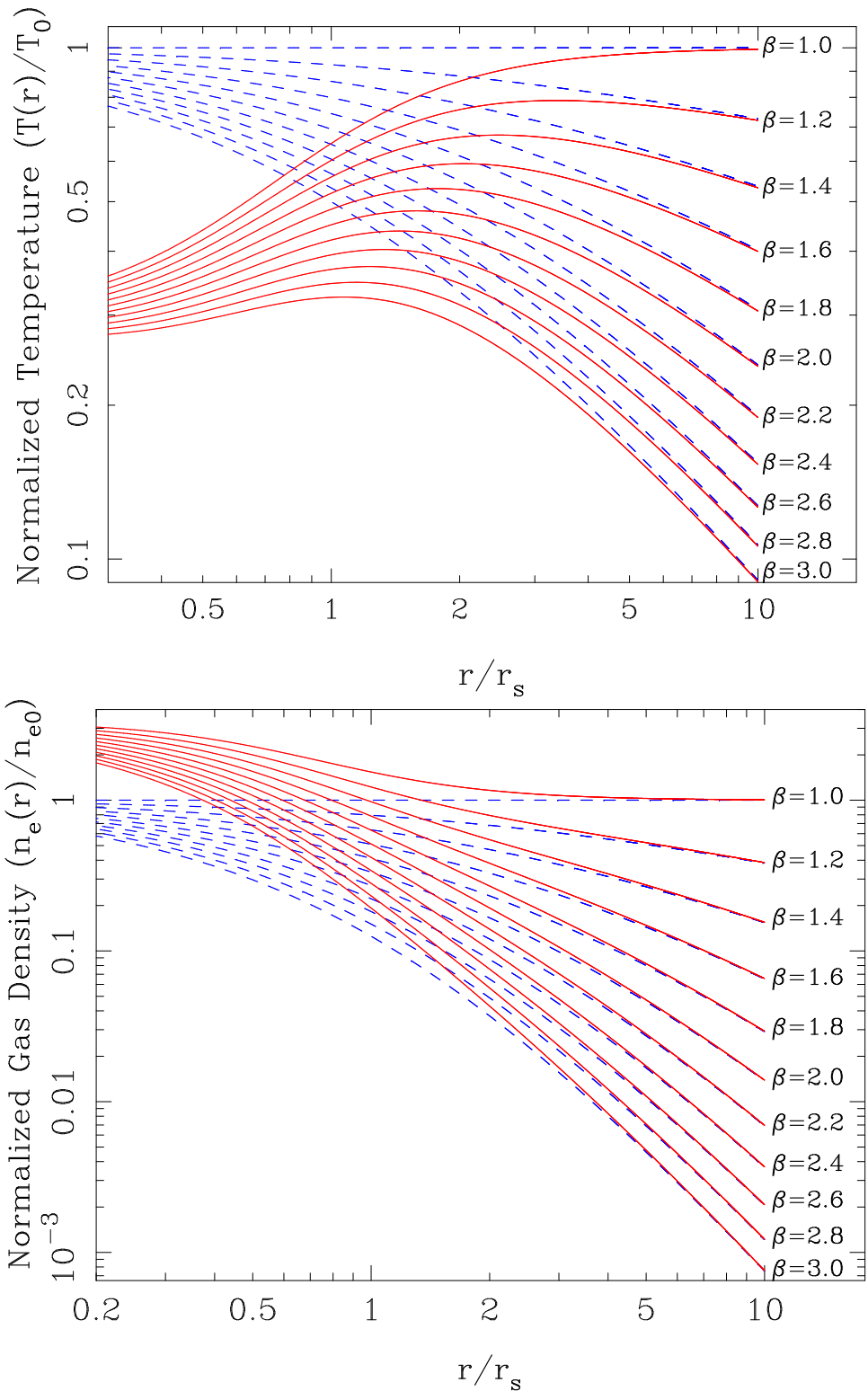

Figure 2.2: Solid red lines are the normalized temperature and density profiles for a taper function with parameters $\alpha = 0.3$, $r_{cool} = r_s$, and $\gamma = 2.0$, and variable values for β; blue dashed lines are the models without the cool core taper function.

CHAPTER 3

METHOD OF ANALYSIS FOR X-RAY AND SUNYAEV ZEL'DOVICH EFFECT DATA

3.1 Introduction

Galaxy clusters trace the growth of structure in the universe. Their abundance and evolution is critically sensitive to underlying cosmological parameters such as Ω_M, σ_8, and the dark energy equation of state parameter w. Recent work has focused on using galaxy clusters to constrain cosmology, including dark energy constraints from X-ray measurements of the gas mass fraction (Allen et al., 2008; Ettori et al., 2009), cosmological parameter constraints from the growth of structure via X-ray (Mantz et al., 2008, 2010; Vikhlinin et al., 2009) SZE cluster surveys (Vanderlinde et al., 2010; Marriage et al., 2010; Sehgal et al., 2010; Muchovej et al., 2010a; Williamson et al., 2011), and gas mass fraction constraints using a combination of SZE and X-ray observations (LaRoque et al., 2006).

In this chapter, a method for the joint analysis of X-ray and SZE cluster observations using a self-consistent analytic model for the physical properties of the intra-cluster medium (Bulbul et al., 2010) is presented. The model provides analytic expressions for the radial density, temperature, and pressure profiles, and is therefore simultaneously applicable to both X-ray and SZE observables. The joint analysis allows measurement of the cluster gas mass fraction without the need to impose ex-

ternal priors on cosmological parameters such as the Hubble expansion rate $H(z)$. Such an analysis applied to a sample of clusters can directly probe the evolution of cluster gas mass fractions with redshift. The method is demonstrated using high signal-to-noise data from *Chandra* and Sunyaev-Zel'dovich Array (SZA) observations of two intermediate-redshift clusters, Abell 1835 and Abell 2631.

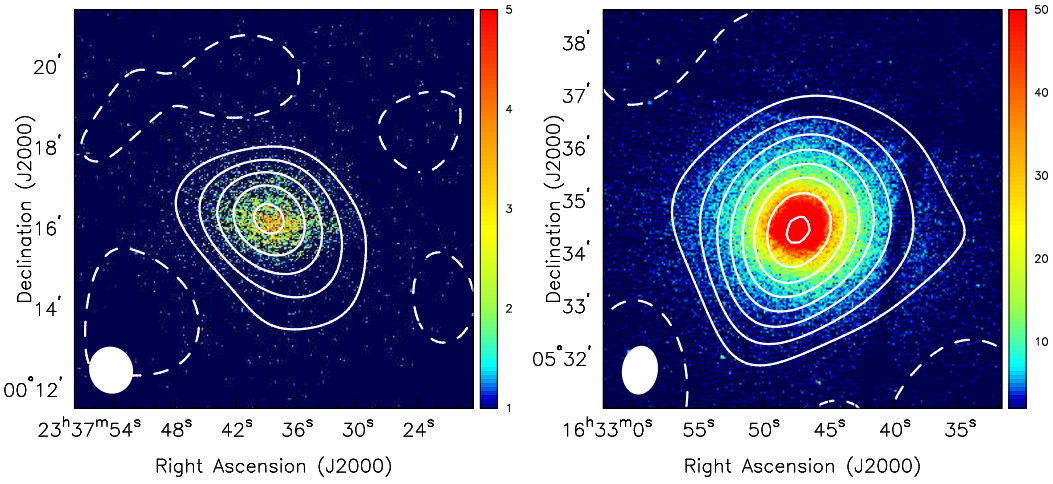

Figure 3.1: SZE contours overlaid on X-ray false color images of Abell 2631 (*left*) and Abell 2204 (*right*). The *Chandra* X-ray surface brightness data are from the energy range 0.7–7.0 keV. The color bars reflect the number of counts detected by Chandra in the 0.7-7 keV band. The SZE data are from the SZA, and the contour levels are (+2,-2,-4,-6,-8,...) times the rms noise (see Table 3.1). The synthesized beams of the SZ observations are shown in the lower left corner of each image. (From Hasler et al. 2011)

3.2 Data Reduction

3.2.1 *Chandra* Imaging and Spectroscopy

The *Chandra* X-ray data are in the form of event files, which are used to generate both images and spectra. Additional blank-sky composite event files are used

for background subtraction. The event files are reduced using CIAO 4.3.1 and CALDB 4.3, following the reduction procedure described in Bulbul et al. (2010). Details of each cluster observation can be found in Table 3.1.

The X-ray images in the 0.7-7 keV band are used to measure the X-ray surface brightness profile of the cluster. In order to subtract the background from the surface brightness, the blank-sky image are rescaled to match the cluster surface brightness in a peripheral region that is free of cluster signal. The peripheral regions chosen are at a distance $\geq$ 500 arcsec from the cluster center for Abell 2631 (corresponding to 2.7 Mpc in the standard flat ΛCDM cosmology), and $\geq$ 550 arcsec (1.7 Mpc) for Abell 2204.

Spectra are extracted in annular regions centered at the peak of the X-ray emission. These regions cover an area out to the radius where the surface brightness profile reaches the background, which is near r_{500} (the radius within which the average density is 500 times the critical density at the cluster redshift) for these observations. From the blank-sky data, background spectra are also extracted and processed. The blank-sky spectra are rescaled to match the count rate of the cluster spectra in the 9.5-12 keV band. In this band, *Chandra* has no effective area for the detection of photons, and the detected counts originate from a particle background that is time variable. Hickox & Markevitch (2006) showed that the flux within the 2–7 keV and 9.5–12 keV energy bands can vary with time, but the ratio of the two bands remains constant. Subtracting the blank-sky data rescaled by the higher-energy band therefore accurately removes the background from the lower-energy band. The spectra are fit with an optically thin plasma emission model (APEC) where the abundance, temperature, and normalizations are the free parameters.

After rescaling the blank-sky spectra and removing the background from the cluster data, residuals may still be present in the soft 0.7–2 keV energy band. These soft X-ray residuals may be due to Galactic and extragalactic emission, and may vary as function of position (e.g., Snowden et al., 1997) and time (e.g., Takei et al., 2008). For each cluster observation, a peripheral region that is free of cluster emission—the same region used to rescale the background images—is used to determine whether soft residuals are present after the blank-sky background has been subtracted. The presence of soft residuals are detected in both Abell 2163 and Abell 2204. The residual spectra are fit using a phenomenological model that includes a power law and a plasma emission model, and this model is rescaled by area and included in the spectral fit for each annulus (e.g., Snowden, 1998; Nevalainen et al., 2005; Maughan et al., 2008).

3.2.2 Interferometric Observations with the SZA

Abell 2631 and Abell 2204 were also observed with the Sunyaev-Zel'dovich Array (SZA), an eight-element interferometer designed for the detection and imaging of the SZE. Each antenna in the array is 3.5 m in diameter and has a primary beam FWHM of $10.7'$ at the center frequency of the observing band (31 GHz). For these observations, six of the SZA antennas were closely packed together to provide sensitivity to arcminute-scale SZ signals, and the remaining two antennas were placed further out to constrain the flux contributions from unresolved radio sources, as described in Muchovej et al. (2007). The unflagged on-source time for Abell 2631 was 16.1 hours and 19.6 hours for Abell 2204. The details of the observations are given in Table 3.1,

and the point sources detected in each field are listed in Table 3.2. In the analysis of the cluster SZE described below, the parameters of the SZE decrement and the radio sources are fitted simultaneously.

The SZA data are reduced using a set of routines written in MATLAB* that constitute a complete pipeline for flagging, calibrating, and reducing visibility data. The reduction pipeline, described in (Muchovej et al., 2007), converts the data to physical units and corrects for instrumental phase and amplitude variations. Data are flagged for corruption due to bad weather, sources of radio interference, and other instrumental effects that could impact their quality. The pipeline outputs calibrated unflagged visibilities, i.e., components of the Fourier transform of the sky brightness multiplied by the primary beam response, along with their corresponding statistical weights and positions in the Fourier $(u-v)$ plane.

3.3 Modeling the X-ray and SZE data

The observable from X-ray data is the surface brightness,

$$S_{\rm x} = \frac{1}{4\pi(1+z)^3}\int n_e^2 \Lambda_{ee}(T_e, A) d\ell, \tag{3.1}$$

where ℓ is the line of sight through the cluster, n_e is the electron density, T_e is the electron temperature, A is the metallicity, and $\Lambda_{ee}(T_e, A)$ is the X-ray cooling function (in units of counts cm^3 s^{-1}) as a function of electron temperature and metallicity. Note that the density, temperature, and metallicity can vary along the line of sight. The temperature and metallicity are measured using the X-ray spectroscopic data.

*http://www.mathworks.com/products/matlab

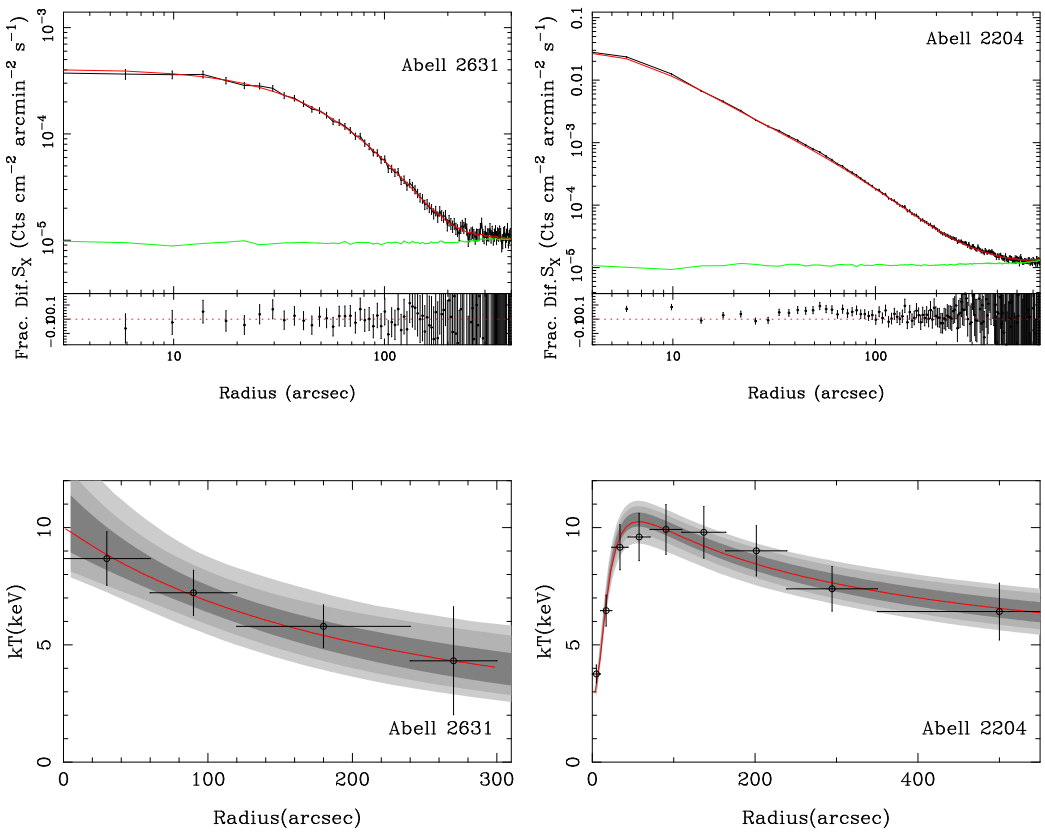

Figure 3.2: X-ray surface brightness and temperature profiles for Abell 2631 (*left column*) and Abell 2204 (*right column*). *Top panels:* Surface brightness profiles where the black points are derived from the X-ray images, the red line shows the best fit model, and the green line is the background level determined from the blank sky observations. The residuals show the fractional difference between the model and the data. A 1% systematic uncertainty has been added in quadrature to the datapoints. The surface brightness profiles are plotted beyond the fitted region to show the agreement between the cluster emission and background. *Bottom panels:* Temperature profiles where the red line shows the best fit model and the dark, medium, and light grey regions show the 68%, 95.4%, and 99.7% confidence levels obtained from the model fits. A 10% systematic uncertainty has been added in quadrature to the temperature bins (see Section 3.4.5.1 for details about the systematic uncertainities). For Abell 2631, the combined $\chi^2 = 30.2$ for 75 d.o.f. and Abell 2204, $\chi^2 = 123.7$ for 139 d.o.f.

The observable from the SZE data is the amplitude of the spectral distortion of the Cosmic Microwave Background (CMB) in the direction of the cluster. This distortion is due to inverse Compton scattering of CMB photons off ICM electrons, and results

in a decrement in the CMB brightness temperature at frequencies $\lesssim$ 218 GHz. The magnitude of the decrement is proportional to the electron pressure integrated along the line of sight (Sunyaev & Zel'dovich, 1972):

$$\Delta T_{\rm SZ} = T_{\rm CMB} \int \sigma_{\rm T} f(x, T_e) n_e \frac{kT_e}{m_e c^2} d\ell, \tag{3.2}$$

where $T_{\rm CMB}$ is the temperature of the CMB, $f(x, T_e)$ contains the frequency dependence of the SZE temperature signature using the relativistic corrections provided by Itoh et al. (1998) and Nozawa et al. (2006), $\sigma_{\rm T}$ is the Thomson cross section, m_e is the electron mass, and c is the speed of light. Assuming spherical symmetry, the line of sight integration element $d\ell$ relates to the angular element (in radians) as $d\ell = D_{\rm A} d\theta$, where $D_{\rm A}$ is the angular diameter distance.

From Equations 4.1 and 3.2,

$$S_x \propto \int D_A n_e^2 \Lambda_{ee}(T_e, A) d\theta \tag{3.3}$$

$$\Delta T_{\rm SZ} \propto \int D_A n_e T_e d\theta. \tag{3.4}$$

The combination of X-ray imaging spectroscopy and SZE observations therefore can be used to measure simultaneously the distribution of the electron density, the electron temperature, and the angular diameter distance (e.g., Hughes & Birkinshaw, 1998; Grego et al., 2000; Reese et al., 2002; Grainge et al., 2002; Saunders et al., 2003; Bonamente et al., 2006). For further discussion on the SZE and its use for cosmology, see reviews by Birkinshaw (1999) and Carlstrom et al. (2002).

The density and temperature profiles of the hot plasma in galaxy clusters are described using the model proposed by Bulbul et al. (2010):

$$n_e(r) = n_{e0} \phi(r, r_s, \beta)^n \tau_{cool}^{-1} \tag{3.5}$$

$$T(r) = T_0 \phi(r, r_s, \beta) \tau_{cool}, \tag{3.6}$$

where $\phi(r, r_s, \beta) = \frac{1}{(\beta-2)} \frac{(1+r/r_s)^{\beta-2}-1}{r/r_s(1+r/r_s)^{\beta-2}}$, $\tau_{cool} = (\alpha + (r/r_{\rm cool})^{\gamma})/(1 + (r/r_{\rm cool})^{\gamma})$ and T_0 is a normalization factor for the scaling of the temperature profile. One attractive feature of these models is that they provide a simple analytic form for the electron pressure:

$$P_e(r) = P_{e0} \phi(r, r_s, \beta)^{n+1}, \tag{3.7}$$

where $P_{e0} = n_{e0} k T_0$ is the pressure normalization. The free parameters of the model, which are used to jointly fit the X-ray and SZE data, are $n_{e0}, T_0, r_s, r_{\rm cool}, \alpha, \beta, \gamma, n$ and the distance D_A.

3.3.1 X-ray Data Analysis

The ICM models are fit to the X-ray surface brightness and temperature using a Monte Carlo Markov chain (MCMC) technique with a Metropolis-Hastings algorithm, as described in Bonamente et al. (2004). The annular bins in the temperature profile (Figure 3.2) were chosen by starting with an initial $10''$ bin and then increasing each bin by 50% of the width of the previous bin to give roughly the same counts per bin. Following the analysis of the systematic uncertainties for the X-ray data described in Bulbul et al. (2010), a 1% systematic uncertainty is adopted on the count rate of each bin of the surface brightness profile and a 10% systematic uncertainty on the temperature of each spectral region as discussed in Section 3.4.5.1. Figure 3.2 shows the temperature and surface brightness profiles, along with the best-fit models, for Abell 2631 and Abell 2204. Since the model has the same parameters for both density and temperature, the surface brightness profile carries a larger weight in the fit. The

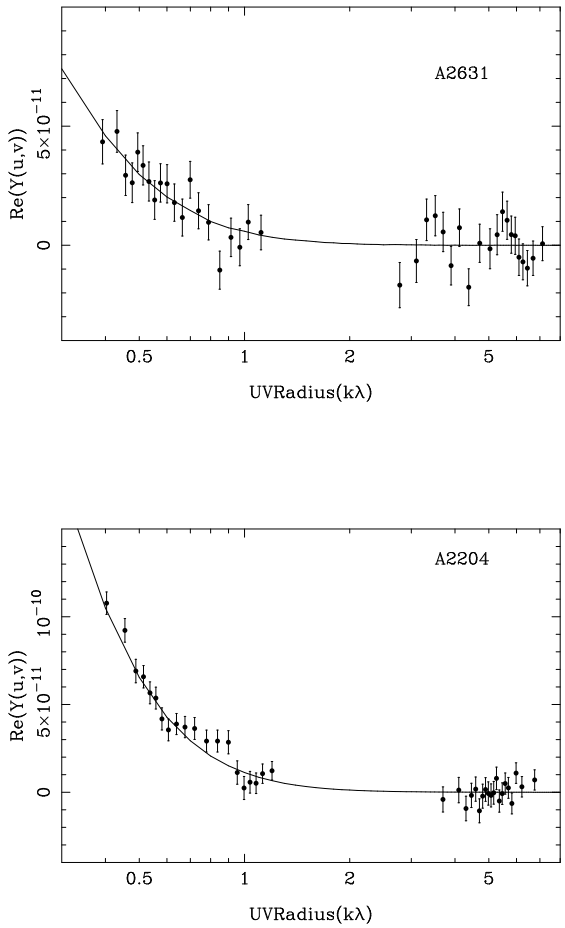

Figure 3.3: SZE visibility profiles for Abell 1835 (*top*) and Abell 2631 (*bottom*) plotted as a function of $u - v$ radius ($\sqrt{u^2 + v^2}$). The plots show the real components of the measured visibilities along with the best fit model. For Abell 2631, $\chi^2 = 39.4$ for 38 d.o.f. and for Abell 2204, $\chi^2 = 34.4$ for 38 d.o.f.

model fits are acceptable for both clusters to within the plotted errors, which include the systematic uncertainties associated with the surface brightness and temperature discussed in Section 3.4.5.

3.3.2 SZE Data Analysis

The visibilities $V_\nu(u,v)$ measured by the SZA can be related to the integrated Compton-y parameter $Y(u,v)$ by

$$Y(u,v) \equiv \frac{V_\nu(u,v)}{g(x)\, I_0}, \tag{3.8}$$

where $g(x)$ corrects for the frequency dependence of the SZE flux, I_0 is the primary CMB intensity, $I_0 = 2(k_B T_{\rm CMB})^3/(hc)^2$. Figure 3.3 shows $Y(u,v)$ along with the best-fit model for each of the clusters.

3.4 Joint Analysis of X-ray and SZE Data

First, a consistency check of the determination of the pressure profiles is performed from the X-ray and SZE data. Next, determinations of the angular diameter distance and the radial profile of the gas mass fraction are determined using the consistent parametrization of density, temperature and pressure provided by the ICM model for the joint analysis of the X-ray and SZE observables.

3.4.1 Consistency of X-ray and SZE Measurements of the Electron Pressure Profiles

Both X-ray and SZE observations provide measurements of the radial distribution of the electron pressure. The X-ray observables are the electron temperature and surface brightness, the latter dependent on the square of the electron density according to Equation 4.1; the SZE observable, on the other hand, is directly proportional to the electron pressure integrated along the line of sight (Equation 3.2).

The two observables can be affected by different sources of systematic uncertainties. For example, the presence of non-thermal X-ray emission (e.g., Million & Allen, 2009; Bonamente et al., 2005; Sarazin & Lieu, 1998) could result in the increase of the X-ray emission above the level of the thermal gas, and radio emission from cluster halos (e.g., Brunetti et al., 2007) may partially fill the SZE decrement, resulting in a lower measured SZE signal. Another source of systematic uncertainty when using X-ray and SZE data is the lack of spherical symmetry (e.g., Sulkanen, 1999), resulting in a different measurement of the pressure from X-ray and SZE observations, and an uncertainty in the measurement of $f_{\rm gas}$ by as much as 20% (see Section 3.4.5.4). A joint measurement of the pressure profile is therefore useful to determine the presence of sources of emission that can cause differences between the X-ray and SZE radial pressure profile.

A joint fit to the X-ray and SZE data is performed within the framework of the Bulbul et al. (2010) model (Equation 3.7), with the normalization of the SZE pressure model independent of the X-ray density and temperature normalizations, and the common parameters in the models (r_s, β, and n) linked between the two datasets. This requires the X-ray and SZE pressure to have the same shape, and the angular scales on the sky are related through the angular diameter distance to the cluster. In this analysis, the angular diameter distance appropriate for a ΛCDM model with $h = 0.73$, $\Omega_M = 0.27$ and $\Omega_\Lambda = 0.73$ is adopted.

The pressure normalization parameters for Abell 2631 and Abell 2204 are provided in Table 3.3. For both clusters, the pressure inferred from the X-ray and SZE measurements are within 20% of one another, consistent with the known systematic effects; results for a larger sample of clusters will be presented in Hasler et al. (2011).

It is important to notice that the measurement of the ratio of X-ray pressure to the SZE pressure depends on the choice of the Hubble parameter, since the pressure normalizations are degenerate with the value of D_A assumed in the analysis.

3.4.2 Direct Measurement of the Angular Diameter Distance

A joint X-ray and SZE analysis is performed which enables us to place direct constraints on the angular diameter distance without using priors on the cosmological parameters (e.g., Hughes & Birkinshaw, 1998; Birkinshaw, 1999; Reese et al., 2002; Bonamente et al., 2006). For this analysis, the shape parameters are linked and the pressure normalizations between the X-ray and SZE data, and allow D_A to vary. For Abell 2631 and Abell 2204 the measured angular diameter distances are $D_A = 639 \pm^{103}_{92}$ Mpc and $D_A = 590 \pm^{52}_{47}$ Mpc. The measurement of D_A for Abell 2204 is in agreement with that of Bonamente et al. (2006), and both are within 2σ of the values for a standard ΛCDM cosmology. Table 3.4 lists all best-fit parameters for the joint fit to the two clusters.

3.4.3 Radial Profiles of the Gas Mass Fraction Independent of Cosmological Parameters

By using direct measurement of D_A as described in Section 3.4.2, radial profiles of the gas mass, total mass, and the gas mass fraction are obtained without the need to use priors on the cosmological parameters. The gas mass $M_{\rm gas}$ is computed by integrating the gas density profile within the volume,

$$M_{\rm gas} = 4\pi\mu_e m_p \int n_e(r) r^2 dr = 4\pi\mu_e m_p {D_{\rm A}}^3 \int n_e(\theta)\theta^2 d\theta, \qquad (3.9)$$

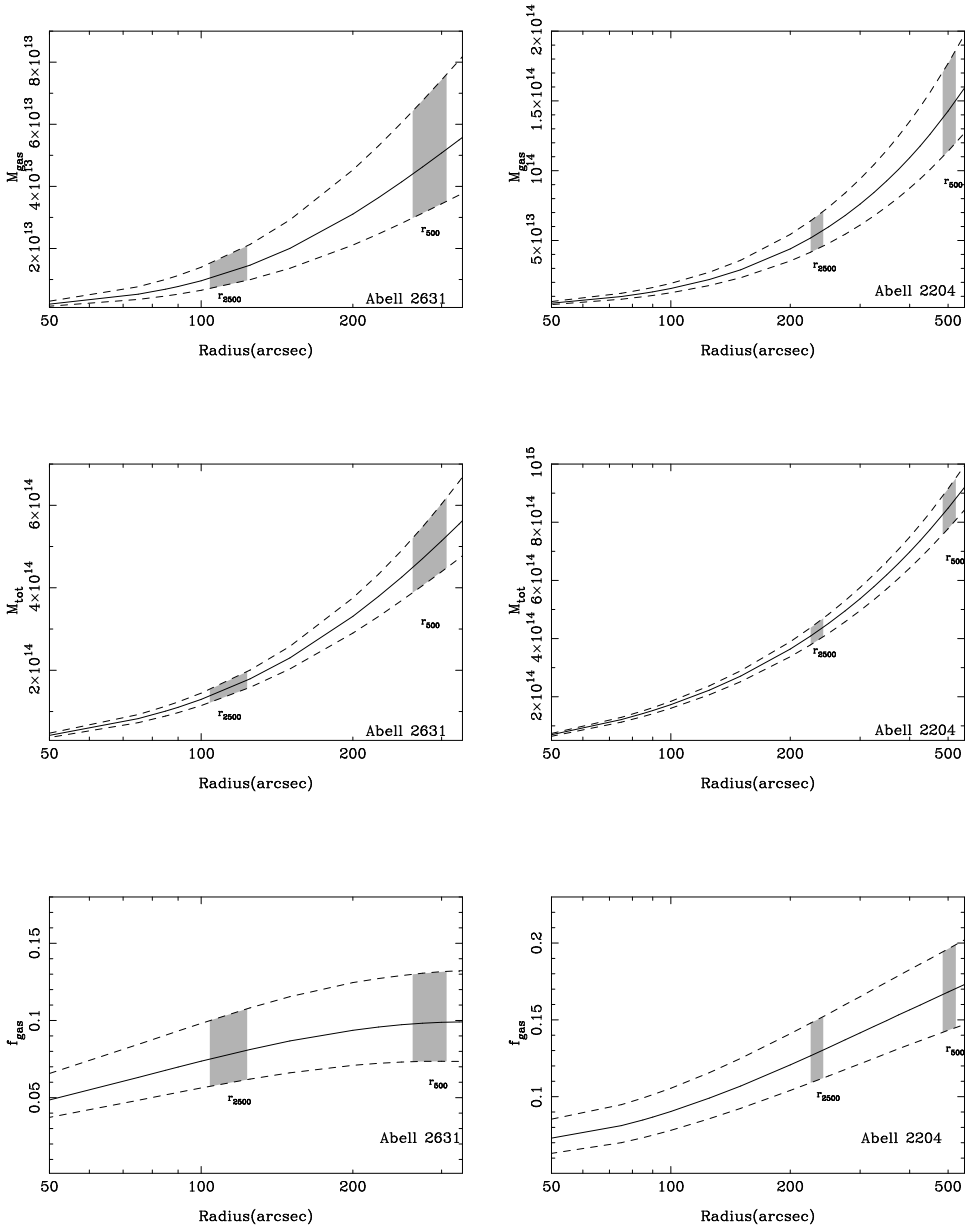

Figure 3.4: Top Panel: Gas mass profiles determined from the joint analysis of *Chandra*/SZA observations for Abell 2631 and Abell 2204. Middle Panel: Total mass profiles. Bottom Panel: Gas mass fraction profiles. The dashed lines are the 68% confidence level at each radius. Grey areas show the measurements at radii r_{2500} and r_{500}, obtained by marginalization over the cosmological parameters.

where μ is the mean molecular weight, m_p is the proton mass, and $dr = D_{\rm A} d\theta$. The total mass $M_{\rm tot}$ is computed assuming hydrostatic equilibrium between the gravita-

tional mass and the thermal pressure of the gas:

$$M_{\rm tot}(r) = \frac{4\pi\rho_i r_s^3}{(\beta-2)}\left(\frac{1}{\beta-1} + \frac{1/(1-\beta) - r/r_s}{(1+r/r_s)^{\beta-1}}\right)\tau_{cool}(r), \tag{3.10}$$

where $\rho_i = (T_0 k(n+1)(\beta-1))/(4\pi G\mu m_p r_s^2)$.

Figure 3.4 shows the radial profiles of the gas mass, total mass, and gas mass fraction for Abell 1835 and Abell 2631. The uncertainties reflect the fact that D_A is also measured directly from the data, and that no assumption about the value of the cosmological parameters H_0, Ω_M or Ω_Λ was used.

3.4.4 Measurement of the Gas Mass Fraction at an Overdensity Radius

The use of $f_{\rm gas}$ measurements for cosmological applications (e.g., via the distribution of $f_{\rm gas}$ with redshift, Allen et al., 2008) requires that $f_{\rm gas}$ be measured within an overdensity radius. The radius r_Δ is defined as the radius within which the average matter density of the cluster is Δ times the critical density of the universe at the cluster's redshift:

$$r_\Delta^3 \equiv \frac{M_{\rm tot}(r_\Delta)}{\frac{4\pi}{3}\Delta\rho_c(z)}, \tag{3.11}$$

where $\rho_c(z) = (3H_0^2E^2(z))/(8\pi G)$ is the critical density of the universe, H_0 is the Hubble constant, and $E^2(z)= \Omega_{\rm M}(1+z)^3 + \Omega_\Lambda + \Omega_{\rm k}(1+z)^2$.

Although the joint X-ray and SZE analysis provides cosmology-independent constraints on D_A and on the radial profile of $f_{\rm gas}(r)$ (Sections 3.4.2 and 3.4.3), the radius r_Δ and therefore all quantities calculated out to this radius retain a cosmological dependence through the factor $\rho_c(z)$ appearing in Equation 3.11. In the following the method to marginalize the measurement of $f_{\rm gas}(r_\Delta)$ over the cosmological parame-

ters is described, which results only in a weak cosmology dependence of the joint measurements of $f_{\rm gas}(r_\Delta)$.

In what follows, the standard flat Friedman-Robertson-Walker (FRW) cosmological model is adopted, parametrized by H_0 and $\Omega_{\rm M}$, with $\Omega_\Lambda = 1 - \Omega_{\rm M}$, known to provide a good fit to other cosmic distance data (Allen et al., 2008; Freedman et al., 2009; Percival et al., 2010).

For each cluster and at each step in the Markov chain, the D_A value measured from the data corresponds to a curve in the (H_0, $\Omega_{\rm M}$) plane described by

$$\begin{aligned} H_0 &= \frac{c \sinh |\Omega_k|^{1/2}}{D_A(1+z)|\Omega_k|^{1/2}} \int_0^z \frac{d\zeta}{E(\zeta)} \\ &= \frac{c}{D_A(1+z)} \int_0^z \frac{d\zeta}{[\Omega_M((1+\zeta)^3 - 1) - 1]^{1/2}}, \end{aligned} \tag{3.12}$$

where the second line follows from the assumption of spatial flatness. A random value of $\Omega_{\rm M}$ is drawn from a uniform distribution on [0,1], calculate the corresponding H_0 from Equation 3.13, and then use this pair of values H_0 and $\Omega_{\rm M}$ to calculate r_Δ according to Equation 3.11. Finally, the corresponding $f_{\rm gas}(r_\Delta)$ is calculated from the other fit parameters of the chain. This approach has the advantage of using minimal prior information on the cosmological parameters, with $\Omega_{\rm M}$ free to range between 0 and 1, and D_A measured directly from the data. This method properly accounts for the covariance between r_Δ, $f_{\rm gas}(r_\Delta)$, D_A and the other parameters of the fit. For the flat FRW model and the low redshifts in question, this procedure corresponds, to very good approximation, to the use of uniform priors on H_0 and $\Omega_{\rm M}$. However that this correspondence does not necessarily hold for higher redshifts (z$\sim$1) nor for other cosmological models.

The measurements of $f_{\rm gas}$ at r_{2500} and r_{500} are indicated as grey areas in Figure 3.4 and are listed in Table 3.4. The gas mass fraction measured at r_{2500} and r_{500} for each cluster is weakly dependent on cosmology due to the broad cosmological priors applied in the calculation of r_{Δ}.

For comparison, the measurements of masses and $f_{\rm gas}$ using the X-ray data with a fixed D_A calculated from the standard flat ΛCDM cosmology are provided, and priors on Ω_M from the WMAP measurements of Komatsu et al. (2011). The results are reported in Table 3.5.

3.4.5 Sources of Systematic Uncertainty

The sources of systematic uncertainty on the gas mass fraction and the integrated X-ray and SZE pressure are listed in Table 3.6. The individual errors are added in quadrature to determine the total systematic uncertainty on f_{gas} and the integrated pressure. Systematics from *Chandra* instrument calibration and the X-ray background are included in the fitting of the data, and the value of masses and f_{gas} in Tables 3.4 and 3.5 account for these systematics. Since this joint analysis method can be applied to larger samples of clusters, we also indicate whether the impact of each source of systematic uncertainty is reduced with sample size.

3.4.5.1 Instrument Calibration

Chandra's ACIS effective area has a spatially dependent non-uniformity at the level of ±1%, and therefore a ±1% uncertainty is applied to the surface brightness. A ±10% uncertainty is adopted on the temperature measurements to account for uncertainty in the low-energy calibration of the effective area. (see e.g., Bulbul et al.,

2010). These uncertainty estimates for the *Chandra* calibration are folded into the mass measurements reported in Tables 3.3, 3.4, and 3.5.

Frequent observations of Mars are used to calibrate the SZA absolute flux scale; the Rudy (1987) flux model is used which has an estimated absolute calibration uncertainty of ±5%. The stability of the instrumental gain is ±3%, as determined from repeated calibrator measurements in SZA survey fields (Muchovej et al., 2010a). The absolute calibration and instrumental gain yield a global ±6% uncertainty on the SZA calibration. Therefore a ±6% systematic error is applied to the pressure profile and, as discussed in LaRoque et al. (2006), this leads to a ±12% systematic uncertainty to the gas mass fraction measurements at r_{2500} and r_{500}. The uncertainty associated with instrument calibration does not average down.

3.4.5.2 Kinetic SZE

Reese et al. (2002) reports that for a cluster with a temperature of 8.0 keV and with a typical velocity along the line of sight of 300 km/s (Watkins, 1997; Colberg et al., 2000), the kinetic SZE would be ±4% of the thermal SZE for 30 GHz observations. Accordingly a ±4% uncertainty due to the kinetic SZE is applied on the gas mass fraction and the SZEpressure profiles for measurements at r_{2500} and r_{500}. This source of uncertainty averages down by a factor of the square root of the size of the sample.

3.4.5.3 Radio Source Contamination

Undetected radio sources not accounted for in modeling could lead to a biased measurement of the SZE decrement. the Faint Images of the Radio Sky at Twenty-Centimeters (FIRST) database is used as a reference for locating compact radio

sources within $10'$ of the cluster center. Most radio sources that will affect the 30 GHz data (rms noise= $\sim$ 0.25 mJy) will have counterparts in the FIRST survey (rms noise= 0.15 mJy at 1.4 GHz); inverted spectrum sources may not have counterparts at 1.4 GHz and will affect the measurement of the SZE decrement, but they comprise a small fraction of the source population (Muchovej et al., 2010b, Fig. 3.3).

The effect of undetected point sources is determined by placing a radio source model at each FIRST source, fixing the position and marginalizing over the flux. In the pressure model (Equation 3.7), the parameters r_s, n, β, and D_A are fixed and let P_{eo} be free. The pressure profiles are compared with the original analysis (see Table 3.3) and find a $\leq 1\%$ difference in the pressure of each cluster. Therefore a 1% uncertainty is applied on the pressure and 2% uncertainity on the gas mass fraction at r_{2500} and r_{500}.

3.4.5.4 Asphericity

Although a spherical model is assumed in the analysis, most clusters do not appear to be be circular in shape in X-ray or radio observations. LaRoque et al. (2006) reports a $10-20\%$ uncertainty in the measurement of the gas mass fraction due to asphericity; therefore a $\pm 20\%$ is used as a conservative estimate for measurements at r_{2500} and r_{500}. This uncertainty also averages down by a factor of the square root of the sample size, as shown in Sulkanen (1999).

3.4.5.5 Hydrostatic Equilibrium Assumption

The assumption of hydrostatic equilibrium at large radii results in an underestimate of the total mass. This is due to the presence of non-thermal pressure which can bias hydrostatic equilibrium measurements of the total mass (Evrard et al. 1990). According to Lau et al. (2009), the total mass of a relaxed cluster, such as Abell 2204 will be biased 6% at r_{2500} and 8% at r_{500}, and by 9% at r_{2500}. 11% at r_{500} for unrelaxed systems such as Abell 2631. Therefore a systematic uncertainty of -9% and -11% is adopted in the error analysis for measurements at r_{2500} and r_{500}.

3.4.5.6 X-ray Background

The X-ray background is determined from the ACIS blank sky composite event file. The blank sky background level is normalized for each observation using an emission-free region on the ACIS detector. The background normalization factor is adjusted by a factor of $\pm 2\sigma$ and propagated this through the analysis, and found that this produces a $\pm 2\%$ uncertainty on the background count rate. This uncertainty affects the surface brightness and temperature measurements resulting in an $\pm 2\%$ and $\pm 9\%$ uncertainty on the gas mass fraction measurements at r_{2500} and r_{500} and a $\pm 2\%$ uncertainty on the X-ray pressure profiles at both radii. This uncertainty averages down by a factor of the square root of the sample size.

3.4.5.7 Model Assumptions

To estimate systematic uncertainties associated with the use of the Bulbul et al. (2010) model, we compare the X-ray masses with those calculated using the Vikhlinin et al. (2006) model, which provides an independent parameterization of the thermo-

dynamic quantities. From this comparison, the gas mass fraction measurements at r_{500} differ by $\pm 2\%$ at r_{2500} and $\pm 6\%$ at r_{500}. The systematic uncertainty on the pressure profiles is estimated by comparing the integrated pressure, which results in an uncertainty of $\pm 3\%$ at r_{2500} and $\pm 5\%$ at r_{500}. Further details on systematic uncertainties associated with the use of the Bulbul et al. (2010) model will be addressed with the analysis of a larger sample in Landry et al. (2011).

3.5 Conclusions

The Bulbul et al. (2010) cluster model demonstrated the ability for simultaneous fitting of X-ray data and Sunyaev-Zel'dovich effect data. The model employs a compact parameterization that relates the three primary thermodynamic quantities by the ideal gas law at all radii. We consider X-ray data from *Chandra* and 30-GHz SZE data from the SZA for two clusters, Abell 1835 and Abell 2631, and find that the model adequately captures the radial variation in both the X-ray surface brightness and SZE Compton-y profiles. For both clusters, separate determination of the electron pressure from the X-ray and SZE data yield profiles that are statistically consistent.

Joint analysis of the X-ray and SZE data provides a direct measure of D_A, the angular diameter distance to the cluster, that is independent of cosmology. For both clusters, this analysis yields a measure of D_A that is consistent with the standard ΛCDM calculation. Using the measured angular diameter distance as a constraint between H_0 and $\Omega_{\rm M}$, and marginalize over the implicit cosmology dependence of the overdensity radius r to obtain estimates of $f_{\rm gas}$ at r_{2500} and r_{500} that are only weakly dependent on $\Omega_{\rm M}$.

Possible sources of systematic errors are discussed in the $f_{\rm gas}$ determination, and find that most will be mitigated if $f_{\rm gas}$ is averaged over a large sample of clusters. A sample spanning a large redshift range can be used to constrain the evolution of $f_{\rm gas}$ with redshift, required for accurate determination of cosmological parameters from clusters (for example, Sasaki, 1996; Pen, 1997; Allen et al., 2004, 2008; Ettori et al., 2009); results from such an analysis will be presented in Hasler et al. (2011). Moreover, measurements of $f_{\rm gas}$ out to a significant fraction of the virial radius, e.g., r_{500}, for a large sample of clusters can be used to test whether the cluster baryon fraction is consistent with currently favored cosmological parameters.

Table 3.1: Cluster information

Cluster	z	n_H (10^{20}cm^{-2})	*RA* (J2000)	*Dec* (J2000)	*Chandra* Observations		SZA Observations			
					ObsID	EXPO (ks)	On-src Time (hrs)	FWHM (arcsec)	P.A. (deg)	rms Noise* (mJy)
Abell 2631	0.27	3.55	23:37:40.1	+00:16:33	3248/11728	25.0	16.1	152×117	17.2	0.4
Abell 2204	0.15	5.67	16:32:47.2	+05:34:32	7940	72.9	19.6	157×115	-7.7	0.4

*FWHM (full-width at half maximum of the synthesized beam), P.A.(position angle of the synthesized beam), and rms noise are for short baselines ($\leq 2k\lambda$).

Table 3.2: Radio Sources in Cluster Field

Cluster	Pointing Center		30 GHz Source						
	RA (J2000)	*Dec* (J2000)	src	$\Delta\alpha$ (arcsec)	$\Delta\delta^*$ (arcsec)	Flux (mJy)	FWHM (arcsec)	P.A. (deg)	rms Noise** (mJy)
Abell 2631	23:37:38.8	+00:16:06.499	1	21.3	36.5	3.7	26.5×16.6	42.7	0.25
			2	205.0	-130.0	0.5			
Abell 2204	16:32:46.88	+05:34:32.401	1	0.4	1.2	7.0	21.1×18.4	-82.1	0.22
			2	-417.8	-360.1	21.6			
			3	195.0	-130.1	0.7			

*$\Delta\alpha$ and $\Delta\delta$ are the offsets from the pointing center.

**FWHM, P.A. and rms noise are for long baselines ($> 2k\lambda$).

Table 3.3: Pressure Normalization Values

Cluster	$P_{eo}(SZ)(10^{-10}ergscm^{-3})$	$P_{eo}(X)(10^{-10}ergscm^{-3})$	$P_{eo}(SZ)/P_{eo}(X)$
Abell 2631	$1.00\pm^{0.11}_{0.11}$	$1.21\pm^{0.15}_{0.14}$	$0.820\pm^{0.094}_{0.091}$
Abell 2204	$9.90\pm^{0.60}_{0.60}$	$9.71\pm^{0.47}_{0.47}$	$1.019\pm^{0.049}_{0.048}$

Table 3.4: Results from Joint X-ray/SZE Analysis

Cluster	Model Parameters										
	n_{e0} (10^{-2}cm^{-3})	r_s (arcsec)	n	β	T_0^a (keV)	$r_{\rm cool}$ (arcsec)	α	γ^b	$D_{\rm A}{}^b$ (Mpc)	χ^2	d.o.f.
Abell 2631	$0.87\pm^{0.07}_{0.06}$	$340.2\pm^{76.2}_{79.3}$	$5.42\pm^{1.68}_{0.87}$	$3.23\pm^{0.82}_{0.64}$	$9.4\pm^{0.8}_{0.9}$	-	-	-	$639.4\pm^{103.3}_{92.2}$	80	114
Abell 2204	$4.08\pm^{0.23}_{0.25}$	$20.9\pm^{1.3}_{1.2}$	$7.82\pm^{1.50}_{0.91}$	$1.32\pm^{0.05}_{0.06}$	$14.3\pm^{0.7}_{0.9}$	$19.6\pm^{0.5}_{0.6}$	$0.17\pm^{0.08}_{0.07}$	2.0	$590.1\pm^{51.9}_{46.6}$	155	176

Cluster	Cluster Masses							
	Masses Evaluated For Δ= 2500				Masses Evaluated For Δ=500			
	r_Δ (")	Mgas ($10^{13}M_\odot$)	$M_{\rm tot}$ ($10^{14}M_\odot$)	$f$gas	r_Δ (")	Mgas ($10^{13}M_\odot$)	$M_{\rm tot}$ ($10^{14}M_\odot$)	$f$gas
Abell 2631	$112.9\pm^{10.7}_{8.8}$	$1.13\pm^{0.49}_{0.35}$	$1.55\pm^{0.27}_{0.24}$	$0.078\pm^{0.024}_{0.018}$	$283.0\pm^{23.6}_{20.1}$	$4.75\pm^{2.11}_{1.44}$	$4.87\pm^{1.07}_{0.84}$	$0.098\pm^{0.032}_{0.025}$
Abell 2204	$233.0\pm^{9.1}_{8.0}$	$5.45\pm^{1.22}_{1.07}$	$4.24\pm^{0.32}_{0.33}$	$0.129\pm^{0.021}_{0.018}$	$502.8\pm^{19.4}_{18.3}$	$14.37\pm^{3.44}_{2.80}$	$8.50\pm^{0.81}_{0.77}$	$0.168\pm^{0.028}_{0.024}$

[a]The reader is cautioned that T_0 is not a global temperature, but rather a model parameter in Equation 4.3.

[b]The parameters γ and $D_{\rm A}$ are fixed in the model.

Table 3.5: Results from X-ray Analysis

Cluster	Model Parameters n_{e0} (10^{-2}cm^{-3})	r_s (arcsec)	n	β	T_0^a (keV)	$r_{\rm cool}$ (arcsec)	α	γ^b	$D_{\rm A}$ (Mpc)	χ^2	d.o.f.
Abell 2631	$0.76\pm^{0.03}_{0.02}$	$523.8\pm^{40.2}_{22.3}$	$3.93\pm^{1.62}_{0.76}$	$5.79\pm^{5.20}_{2.61}$	$10.4\pm^{1.3}_{1.3}$	-	-	-	840.0	28	75
Abell 2204	$4.11\pm^{0.19}_{0.18}$	$22.6\pm^{1.2}_{1.2}$	$6.64\pm^{0.90}_{0.68}$	$1.38\pm^{0.05}_{0.05}$	$15.1\pm^{0.7}_{0.7}$	$19.9\pm^{0.6}_{0.5}$	$0.17\pm^{0.07}_{0.07}$	2.0	526.0	123	139

	Cluster Masses							
	Masses Evaluated For Δ= 2500				Masses Evaluated For Δ=500			
Cluster	r_Δ (")	Mgas ($10^{13}M_\odot$)	$M_{\rm tot}$ ($10^{14}M_\odot$)	$f$gas	r_Δ (")	Mgas ($10^{13}M_\odot$)	$M_{\rm tot}$ ($10^{14}M_\odot$)	$f$gas
Abell 2631	$119.3\pm^{6.1}_{6.4}$	$2.67\pm^{0.25}_{0.24}$	$2.28\pm^{0.37}_{0.35}$	$0.117\pm^{0.008}_{0.007}$	$275.6\pm^{21.0}_{18.0}$	$9.31\pm^{0.64}_{0.59}$	$5.63\pm^{1.39}_{1.04}$	$0.165\pm^{0.024}_{0.024}$
Abell 2204	$234.0\pm^{4.1}_{3.9}$	$4.11\pm^{0.09}_{0.09}$	$3.73\pm^{0.20}_{0.18}$	$0.110\pm^{0.003}_{0.003}$	$496.4\pm^{12.9}_{10.5}$	$10.57\pm^{0.34}_{0.24}$	$7.16\pm^{0.57}_{0.44}$	$0.148\pm^{0.006}_{0.007}$

[a]The reader is cautioned that T_0 is not a global temperature, but rather a model parameter in Equation 4.3.

[b]The parameter γ is fixed in the model.

Table 3.6: Sources of Uncertainty

	r_{2500}			r_{500}		
	Effect on $f_{\rm gas}$	Effect on Pressure		Effect on $f_{\rm gas}$	Effect on Pressure	
Source	(%)	SZE(%)	X-ray (%)	(%)	SZE(%)	X-ray (%)
Kinetic SZE	±4	±4	...	±4	±4	...
Radio Point Sources	±2	±1	...	±2	±1	...
Asphericity	±20	±10	±10	±20	±10	±10
X-ray background	±5	...	±1	±9	...	±2
SZA calibration	±12	±6	...	±12	±6	...
Hydrostatic Equilibrium[a]	-9	...	...	-11	...	...
Model Assumptions	±2	±3	±3	±6	±5	±5
Total Systematic	$\pm^{24}_{26}$	±13	±11	$\pm^{26}_{28}$	±14	±12
Chandra calibration uncertainties*						
Surface Brightness[b]	±10					
Temperature[c]	±1					

*These systematic uncertainites are added to the data prior to the fit, and their effect is included in the derived masses and pressure at all radii.

[a]Uncertainty is theoretically motivated by Lau et al. (2009) as discussed in Section 4.3.4.

[b]Determined from the spatial variations of the effective area. Reference: http://cxc.harvard.edu/cal/

[c]Determined from the energy variation of the effective area and calibration software. Reference:http://cxc.harvard.edu/ciao4.1/why/caldb4.1.1 hrma.html

CHAPTER 4

THE DISTRIBUTION OF BARYONS IN CLUSTERS FROM X-RAY OBSERVATIONS

4.1 Introduction and Sample Selection

According to cosmological simulations, slight fluctuations in the matter density distribution of the universe at early epoch decoupled from the Hubble flow, started to collapse due to gravity and merge together to form larger structures. Galaxy clusters are the largest structures that have undergone gravitational collapse and reached equilibrium (Kravtsov et al., 2005; Borgani & Kravtsov, 2009). For this reason, massive relaxed galaxy clusters are expected to trace the matter content of the universe. The cluster gas mass fraction, which is the ratio of the gas to total mass is expected to agree with the cosmic baryon fraction. The cosmic baryon fraction, $\Omega_b/\Omega_M = 0.167 \pm 0.006$ (Komatsu et al., 2011) has been measured by the Wilkinson Microwave Anisotropy Probe (WMAP) using the 7 year data.

WMAP data provides testing on the cosmological models. A basic cosmological model is considered, starting with a flat universe with radiation, baryons, cold dark matter, the cosmological constant, and a power-law power spectrum of adiabatic primordial fluctuations. This model is compared to the power spectrum of the fluctuation of matter and the best fit model is the ΛCDM model. Although, the ΛCDM model is determined to be the best fit for the WMAP data, Ω_M and Ω_Λ are

ani-correlated as seen in Figure 4.1. Priors on the Hubble constant are required to place constraints Ω_M and Ω_Λ because WMAP measure the total density of the universe. Komatsu et al. (2011) measured $\Omega_b h^2$ and $\Omega_M h^2$ using WMAP 7 year data by assuming priors on the Hubble constant determined from (Riess et al., 2009).

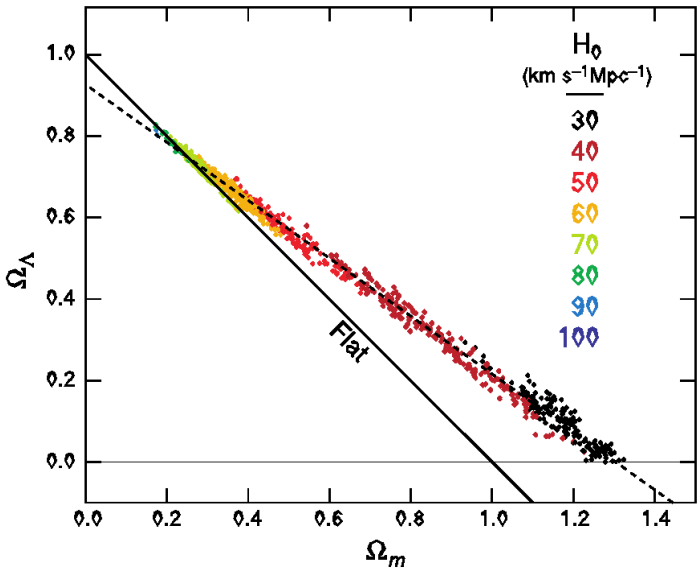

Figure 4.1: Range of nonflat cosmological models consistent with the WMAP data only. The models in the figure are all power-law CDM models with dark energy and dark matter, but without the constraint $\Omega_M + \Omega_\Lambda = 1$. The different colors correspond to values of the Hubble constant as indicated in the figure. While models with $\Omega_\Lambda = 0$ are not disfavored by the WMAP data only, the combination of WMAP data plus measurements of the Hubble constant strongly constrain the geometry and composition of the universe within the framework of these models. The dashed line shows an approximation to the degeneracy track: $\Omega_K = -0.3040 + 0.4067\Omega_\Lambda$. Note that for these open universe models, a flat prior is assumed on Ω_Λ (Spergel et al., 2006).

Previous studies of the gas mass fraction (Allen et al., 2002; Sanderson et al., 2003; Allen et al., 2004; LaRoque et al., 2006; Vikhlinin et al., 2006; Arnaud et al., 2007; Allen et al., 2008; Zhang et al., 2008; Ettori et al., 2009) have fallen short of the cosmic baryon fraction, see Figure 4.2. For example, $f_{gas}(r_{2500}) = 0.119 \pm 0.003 \pm^{0.007}_{0.014}$ (LaRoque et al., 2006) and $f_{gas}(r_{500}) = 0.12 \pm 0.004$ (Zhang et al., 2008).

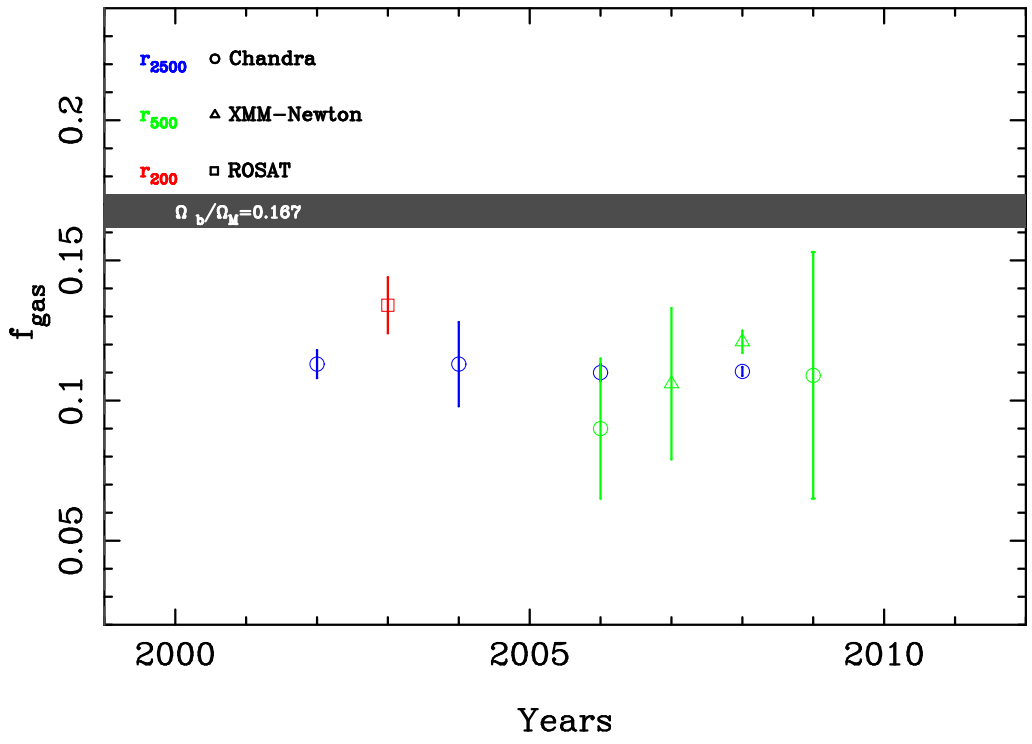

Figure 4.2: Summary of previous studies that have measured the gas mass fraction using ROSAT, XMM-Newton, and Chandra X-ray observations (Allen et al., 2002; Sanderson et al., 2003; Allen et al., 2004; LaRoque et al., 2006; Vikhlinin et al., 2006; Arnaud et al., 2007; Allen et al., 2008; Zhang et al., 2008; Ettori et al., 2009).

In this chapter , the radial distribution of the baryons in clusters is determined by measuring the gas mass fraction radial profile for a sample of 25 massive relaxed clusters. This sample is a subset from Allen et al. (2008) which consists of massive and relaxed clusters. Only the clusters with a declination above -15^o were used in this project since the SZE observatory discussed in Chapter 2 is located in the northern hemisphere. Table 4.1 contains the cluster details about the Chandra observations. The goal is to test whether the cluster baryon fraction (gas mass fraction plus stellar fraction) at r_{500} is consistent with Ω_b/Ω_M, and if the most massive and relaxed clusters accurately trace the primordial content.

4.2 Chandra Data Reduction

The Chandra data are reduced using the software packages, CIAO 4.3.1 and CALDB 4.3. The Advanced CCD Imaging Spectrometer (ACIS) was used to obtain the data. After the data are downloaded from the archive, the following corrections:

- Afterglow correction

  The afterglow is the residual charge left over from a cosmic ray that has interacted with the Chandra CCD. If this excess charge is not removed it can lead to a false detection of faint sources.

- Bad pixel and Hot pixel filtering: Bad pixel correction detects the defected pixels and excludes them from the event file. Furthermore hot pixels need to be filtered from the event file. This process searches for pixels that are associated with cosmic ray afterglows, hot pixels or astronomical sources.

- Charge transfer inefficiency (CTI) correction: As charge is transferred in the CCD, some charge may become trapped which leads to a reduction in the charge read out of the detector (see the CTI-correction web pages for more details, $http://cxc.harvard.edu/ciao/why/cti.html$).

- Time-dependent gain (TGAIN) correction: The time-dependent gain adjustment is necessary because the spectral response of the CCDs change slowly with time. This effect is due to the increasing changes in the CTI.
($http://cxc.harvard.edu/cal/Acis/Cal_prods/tgain/index.html$)

After the raw data has been filtered and calibrated, the X-ray images were binned by pixels of $1.968'' \times 1.968''$ in the energy range 0.7 - 7.0 keV. This energy range was selected because Chandra's effective area is the most sensitive in the 0.7-7.0 keV energy band, see Figure 4.3.

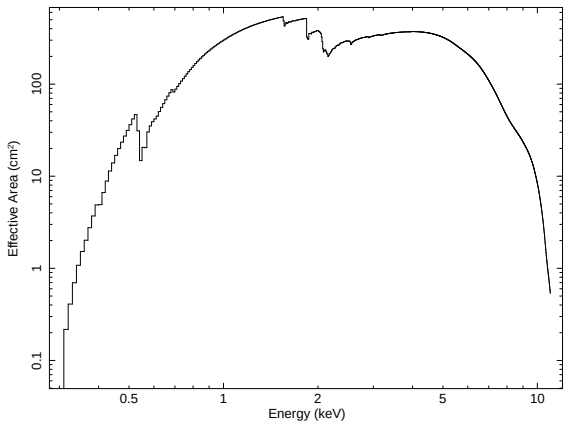

Figure 4.3: The on-axis effective area curve of Chandra ACIS-I instrument.

The blank sky composite event files are used for the background subtraction. The surface brightness profile is determined using the images in the 0.7–7.0 keV energy band. In order to obtain the correct background subtraction, the blank sky

background image is rescaled to match the cluster surface brightness in an emission free region (Figure 4.4).

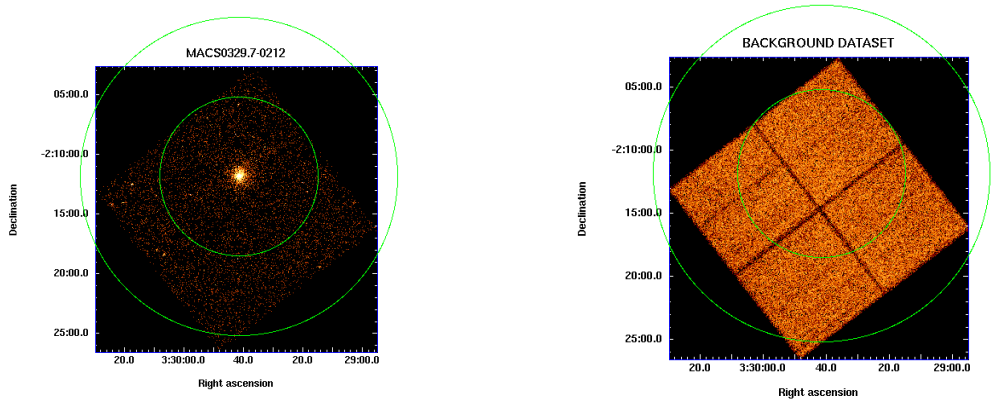

Figure 4.4: Green circle shows the emission free region (point sources and regions around the chip are excluded) for (a) image of MACS0329 and (b) blank sky image of MACS0329.

The spectra are extracted in annular bins from the clusters center and extend out to where the cluster emission reaches the background, which is determined from the surface brightness profile. Spectra are also extracted from the blank sky observation. All point sources and the regions around the chips are excluded in the spectra. The blank-sky spectra is rescaled to match the count rate of the cluster spectra in the 9.5-12 keV energy band. Chandra has no effective area for the photons detected in this energy band (see Figure 4.3).

The high-energy particles that induce x-ray background vary with time due to changes in solar activity. The last panel of Figure 4.5 shows the change in the 9.5-12.0 keV energy band with time. The top and middle panel of Figure 4.5 shows the 2-7/9.5-12.0 keV bands for VFAINT and FAINT Chandra processing modes. Although the 2-7 keV band flux changes with time, the spectral shape is invariant (Hickox & Markevitch, 2006). Therefore constancy of the 2-7/9.5-12.0 keV band flux

enables a simple procedure for an accurate background subtraction. Subtracting the blank sky data rescaled by the higher energy band therefore accurately removes the background from the lower energy band.

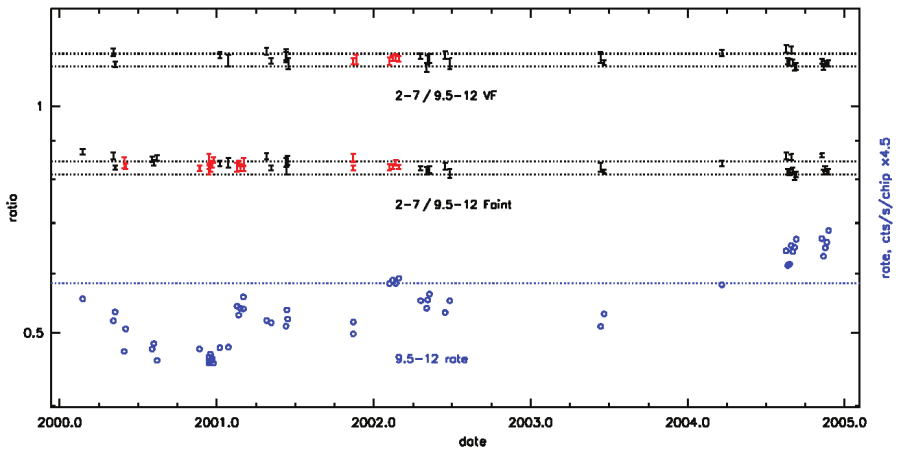

Figure 4.5: Top panel: Ratio of the 2-7 keV to 9.5-12.0 keV bands processed in VFAINT mode for Chandra ACIS-I blank sky observations. Middle panel:Ratio of the 2-7 keV to 9.5-12.0 keV bands processed in FAINT mode for Chandra ACIS-I blank sky observations. Bottom panel: The 9.5-12.0 keV count rate. (Reproduced from Hickox & Markevitch 2006)

After rescaling the blank sky spectra, residual emission may still be present in the 0.7-2 keV band. This emission is due to Galatic and extra-galactic emission which vary as a function of position (e.g, Snowden et al., 1997) and time (e.g, Takei et al., 2008). In this case, an emission free region is used (same region used to rescale the background) to determine if the residuals are present after the blank sky background has been subtracted. These residuals are fit with a power law and plasma emission model, which is added to each cluster spectrum to account for these soft residuals.

4.3 Modeling and Analysis

In X-ray observations, the observable is the surface brightness,

$$S_{\rm x} = \frac{1}{4\pi(1+z)^3} \int n_e^2 \Lambda_{ee}(T_e, A) d\ell, \tag{4.1}$$

where z is the redshift, n_e is the electron number density, T_e is the electron temperature, A is the metallicity (all three of which can vary along the line of sight), $\Lambda_{ee}(T_e, A)$ is the X-ray cooling function (counts cm^3 s^{-1}) as a function of electron temperature and metallicity, and ℓ is the line of sight through the cluster. The ICM temperature and abundance of metals are measured from the X-ray spectroscopic data.

The model used is discussed in detail in Chapter 2 to model the density and temperature profiles of the hot plasma in galaxy clusters,

$$n_e(r) = n_{e0} \left[\frac{1}{(\beta-2)} \frac{(1+r/r_s)^{\beta-2} - 1}{r/r_s (1+r/r_s)^{\beta-2}} \right]^n \tau_{cool}^{-1} \tag{4.2}$$

$$T(r) = T_0 \left[\frac{1}{(\beta-2)} \frac{(1+r/r_s)^{\beta-2} - 1}{r/r_s (1+r/r_s)^{\beta-2}} \right] \tau_{cool}, \tag{4.3}$$

where $\tau_{cool} = \frac{\alpha + (r/r_{\rm cool})^\gamma}{1+(r/r_{\rm cool})^\gamma}$ is the cool core taper, β is the slope, r_s is the scale radius, n is the polytropic index, n_{e0} and T_0 are the normalization factors for the density and temperature profiles.

A Monte Carlo Markov chain (MCMC) technique is used with a Metropolis-Hastings algorithm described in Bonamente et al. (2004) to fit the model to the X-ray data. Monte Carlo Markov Chain (MCMC) is a statistical technique used for determining the probability distribution of the model parameters using the likelihood information.

The sources of uncertainty described in Chapter 3 are applied, and therefore use a 1% systematic uncertainty on each bin of the surface brightness profile and a 10% systematic uncertainty on each bin of the temperature profile. The fits to the X-ray observables (surface brightness and temperature profiles) for each cluster are shown in Section 4.5.

4.4 Constraints on Baryon Contents in Clusters from Radial Distribution of the Gas Mass Fraction

Chandra observations of 25 relaxed massive galaxy clusters are used to measure the cluster gas mass fraction. This sample is a subset from Allen et al. (2008) which consists of massive and relaxed clusters. Only the clusters with a declination above -15^o were used in this project since the SZE observatory discussed in Chapter 2 is located in the northern hemisphere. Table 4.1 contains the cluster details about the Chandra observations.

4.4.1 Gas Mass Fraction Measurements

The gas mass, $M_{\rm gas}$ is computed by integrating the gas density profile over the volume,

$$M_{\rm gas} = 4\pi\mu m_p \int n_e(r) r^2 dr = 4\pi\mu m_p {D_{\rm A}}^3 \int n_e(\theta)\theta^2 d\theta, \tag{4.4}$$

where μ is the mean molecular weight, m_p is the proton mass, and $dr = D_{\rm A} d\theta$, with D_A the angular diameter distance to the cluster. The total mass $M_{\rm tot}$ is computed by assuming hydrostatic equilibrium:

$$\frac{dP}{dr} = -\frac{GM_{tot}(r)\rho}{r^2}, \tag{4.5}$$

where $P = (\mu_e/\mu)P_e$ is the total pressure, P_e is the electron pressure, ρ is the hot gas density, k is the Boltzmann constant, and G is the Gravitational constant.

Since clusters vary in size, a fiducial radius cannot be used to make the measurements. Therefore measurements are made using an overdensity radius, r_Δ, defined as the radius within which the average matter density of the cluster is Δ times the critical density of the universe at the cluster's redshift:

$$r_\Delta^3 = \frac{M_{\rm tot}(r_\Delta)}{\frac{4\pi}{3}\Delta\rho_c(z)}, \tag{4.6}$$

where $\rho_c(z) = \frac{3H_0^2E^2(z)}{8\pi G}$ is the critical density of the universe, H_0 is the Hubble constant, and $E^2(z)= \Omega_{\rm M}(1+z)^3 + \Omega_\Lambda + \Omega_{\rm k}(1+z)^2$.

4.4.2 Results

For X-ray mass measurements, a ΛCDM cosmology ($H_o = 73km/s/Mpc$, $\Omega_M = 0.27$, and $\Omega_\Lambda = 0.73$) is assumed to determine the angular diameter distance in the gas mass and total mass equations (Equations 5.2 and 5.3). An increasing gas mass fraction as a function of radius is found for all clusters (profiles can be found at the end of Chapter 4); The gas mass fraction profiles are rescaled to r/r_{500} for all clusters and the weighted average profile can be seen in Figure 4.6. With the exception of Allen et al. (2008), many studies observe an increasing gas mass fraction with a decreasing overdensity (Vikhlinin et al., 2006; McCarthy et al., 2007; Rasheed et al., 2010). Tables 4.2 and 4.3 show the parameter distributions and the mass measurements at r_{2500} and r_{500}.

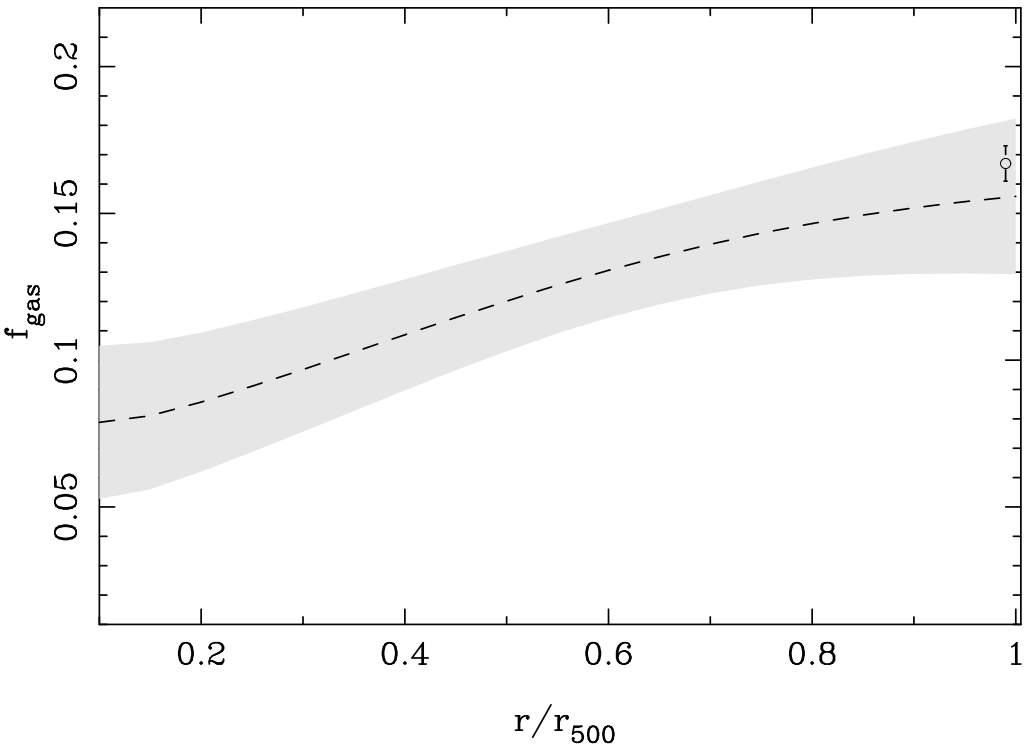

Figure 4.6: The weighted average of the gas mass fraction from X-ray analysis where $f_{gas}(r_{500}) = 0.156 \pm 0.026$. The dotted line is the weighted average and the shaded area is the 1 σ of the weighted sample. The data point is the cosmic baryon fraction measured by WMAP (Komatsu et al., 2011).

Since the measurements of f_{gas} have varying error bars, the weighted mean is used which is defined as

$$\overline{x} = \frac{\sum_{i=1}^{N}(x_i/\sigma_i^2)}{\sum_{i=1}^{N}(1/\sigma_i^2)}, \tag{4.7}$$

where x_i represents each datapoint in the sample and σ_i^2 is the variance of each

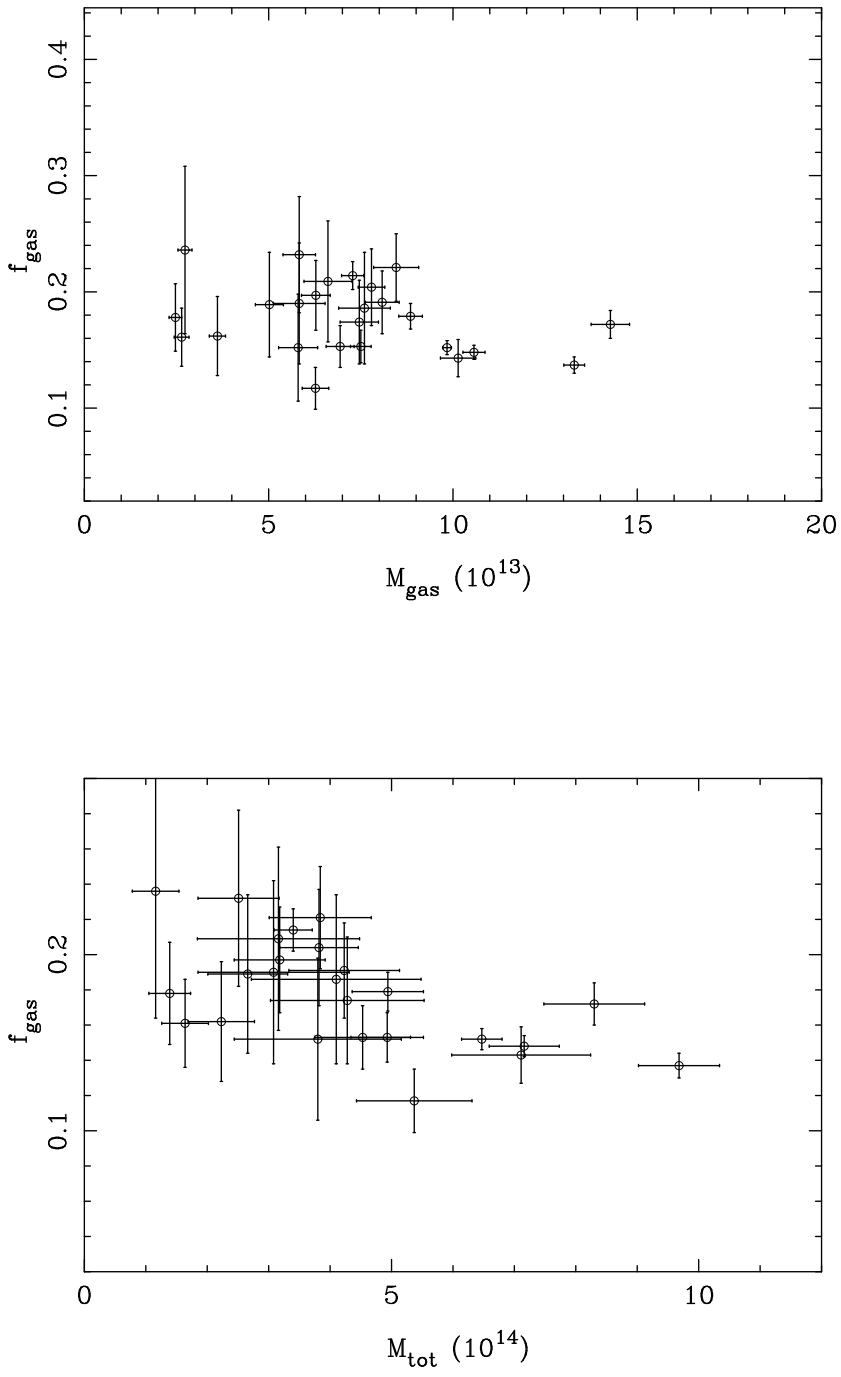

Figure 4.7: Top Panel: Gas mass fraction vs gas mass. Bottom Panel: Gas mass fraction versus total mass. The gas mass fraction shows no clear dependence on the gas mass or total mass.

datapoint. The weighted sample variance is given by

$$\sigma^2_{weighted} = \frac{\sum_{i=1}^{N} 1/\sigma_i^2 (x_i - \overline{x})^2}{\sum_{i=1}^{N} (1/\sigma_i^2)}. \quad (4.8)$$

The weighted average is

$$< f_{gas}(r_{500}) >= 0.156 \pm 0.026 \quad (4.9)$$

from the X-ray analysis.

Figure 4.7 shows the gas mass fraction plotted against the gas mass and total mass. In both cases the gas mass fraction show no dependence on either mass. This is expected since the sample consists of massive clusters.

4.5 Discussion of Results

In this dissertation, Chandra X-ray observations for 25 clusters are used to measure the gas mass, total mass, and gas mass fraction. Since the angular diameter distance cannot be measured from X-ray data alone, a ΛCDM cosmology ($H_o = 73 km/s/Mpc$, $\Omega_M = 0.27$, and $\Omega_\Lambda = 0.73$) is assumed in the calculation, which is required for mass measurements.

In order to compare the measurement with the cosmic baryon fraction accurately the baryons present in galaxies needs to be taken into account. Therefore the cluster baryon fraction is used which is defined as

$$f_{baryon} = f_{gas} + f_{star}, \quad (4.10)$$

where $f_{star} = M_{star}/M_{tot}$, which is defined as the ratio of the mass of the stars associated with galaxies and gas to total mass. Giodini et al. (2009) used a sample

of 118 galaxies and low mass galaxy clusters to measure the gas mass fraction and concluded that the stellar mass fraction decreases with total mass. The sample has an average total mass of 3.0×10^{14} solar masses at r_{500} and therefore has a stellar mass fraction of 0.021 ± 0.002. The stellar mass fraction and gas mass fraction are added together; therefore,

$$f_{baryon}(r_{500}) = 0.177 \pm 0.024, \tag{4.11}$$

which agrees with the cosmic baryon fraction

$$\Omega_b/\Omega_M = 0.167 \pm 0.006 \tag{4.12}$$

measured by WMAP (Komatsu et al., 2011). This shows that massive relaxed galaxy clusters accurately trace the primordial content of the universe provided that the measurement of f_{gas} is done at large radii, such as r_{500}.

The measurement at r_{2500} agrees with previous studies of the gas mass fraction (LaRoque et al., 2006; Allen et al., 2008). However, the results found at r_{500} are higher compared to Zhang et al. (2008) and Ettori et al. (2009). One possible explanation for a higher value of $f_{gas}(r_{500})$ than previous measurements is that the sample used for this project consists of massive galaxy clusters. Massive galaxy clusters have a deep potential well which keeps the gas bound despite energy input from supernovae and AGN (Voit, 2005). On the other hand, low mass galaxy clusters and groups have lower gas mass fractions (f_{gas}=0.03-0.07, Sanderson et al. (2003); Vikhlinin et al. (2006); Gastaldello et al. (2007)) because they have shallow potential wells and AGN heating can drive the gas outside the potential well (Sun et al., 2009). Previous studies included low mass systems which will result in a lower measurement of the average gas mass fraction.

Another possible explanation for finding a measurement that agrees with the cosmic baryon fraction is that the sample used for this project consists of relaxed galaxy clusters. These clusters appear spherical in X-ray images and are the mostly likely candidates for being in hydrostatic equilibrium. Therefore masses calculated using hydrostatic equilibrium and a spherically symmetrical model are expected to be accurate at r_{500} (Lau et al., 2009). Some previous studies included unrelaxed systems in their samples which introduce systematics in the measurement of the gas mass fraction.

Table 4.1. Cluster Sample.

Cluster	z	R.A. (J2000)	Dec. (J2000)	nH (10^{+20})	ACIS S/I	*Chandra* ObsID	Exp. Time (ks)
MACSJ0159.8-0849	0.40	01 59 49.4	-08 49 58	2.06	I	3265	16.4
					I	6106	34.3
					I	9376	19.5
Abell 383	0.19	02 48 03.5	-03 31 45	3.40	I	524	9.9
					I	2320	18.5
MACSJ0329.7-0212	0.45	03 29 41.7	-02 11 48	3.43	I	6108	32.7
					I	3257	9.6
					I	3582	19.3
Abell 478	0.09	04 13 25.2	+10 27 5	34.29	I	6102	10.0
MACSJ0429.6-0253	0.40	04 29 36.1	-02 53 08	3.23	I	3271	23.2
3C186	1.06	07 44 17.5	+37 53 17	5.11	S	9407	66.3
					S	9408	39.6
					S	9774	75.1
					S	9775	15.9
MACSJ0744.9+3927	0.69	07 44 52.9	+39 27 27	5.66	I	6111	49.5
					I	3197	20.2
					I	3585	19.7
MACSJ0947.2+7623	0.34	09 47 13.1	+76 23 14	2.28	I	2202	11.7
Zwicky 3146	0.29	10 23 39.4	+04 11 14	2.46	I	909	45.2
					I	9371	36.3
MACSJ1115.8+0129	0.35	11 15 52.1	+01 29 53	4.34	I	9375	39.6
MS1137.5+6625	0.78	11 40 22.4	+66 08 15	0.95	I	536	109.6
Abell 1413	0.14	11 55 18.1	+23 24 17	3.60	I	5003	66.6
					I	1661	9.1
					I	5002	34.4
ClJ1226.9+3332	0.89	12 26 58.1	+33 32 47	1.83	I	5014	31.6
					I	3180	29.9
MACSJ1311.0-0311	0.49	13 11 01.6	-03 10 40	1.82	I	6110	63.0
					I	3258	13.1
					I	9381	29.0
RXJ1347.5-1145	0.45	13 47 30.6	-11 45 10	4.60	I	3592	54.8
Abell 1835	0.25	14 01 01.9	+02 52 43	2.04	I	6880	117.9
					I	6881	36.8
					I	7370	40.0
MACSJ1423.8+2404	0.54	14 23 47.9	+24 04 43	2.20	I	1657	18.2
MACS1427.3+4408	0.49	14 27 16.2	+44 07 31	1.19	I	6112	8.8
					I	9380	25.8
					I	9808	14.9
RXJ1504.1-0248	0.21	15 04 07.9	-02 48 16	5.97	I	5793	39.2
					I	4935	11.9
MACSJ1532.9+3021	0.36	15 32 53.9	+30 20 59	2.30	I	1665	8.2
MACSJ1621.6+3810	0.46	16 21 24.8	+38 10 09	1.13	I	6172	29.2
					I	3254	9.6
					I	6109	36.7
					I	9379	29.7
					I	10785	29.7
Abell 2204	0.15	16 32 47.2	+05 34 32	5.67	I	7940	76.9
MACSJ1720.3+3536	0.39	17 20 16.8	+35 36 27	3.46	I	6107	29.1
					I	3280	20.6
					I	7718	7.0
RXJ2129.6+0005	0.23	21 29 39.9	+00 05 20	3.63	I	552	10.0
Abell 2537	0.29	23 08 22.1	-02 11 29	4.62	I	9372	38.5

Table 4.2: Model parameter distribution from Chandra X-ray data.

Cluster	$n_{eo}(10^{-2})$ (cm^{-3})	r_s (arcsec)	n	β	T_o (keV)	r_{cool} (arcsec)	α	γ	D_A	χ^2_{tx}(dp) (Mpc)	χ^2_{sb}(dp)	χ^2_{tot}(dof)	p-value
MACSJ0159.8-0849	$2.40\pm^{0.28}_{0.24}$	$26.6\pm^{4.9}_{4.2}$	$5.32\pm^{1.72}_{1.04}$	$1.66\pm^{0.21}_{0.19}$	$15.5\pm^{1.6}_{1.6}$	$13.4\pm^{0.9}_{0.9}$	$0.23\pm^{0.02}_{0.02}$	2.0	1079	2.1 (6)	54.9 (60)	57.0 (58)	0.51
Abell 383	$3.32\pm^{0.49}_{0.50}$	$20.4\pm^{5.8}_{3.3}$	$5.56\pm^{2.28}_{1.60}$	$1.53\pm^{0.28}_{0.17}$	$7.2\pm^{1.1}_{0.8}$	$14.3\pm^{1.3}_{1.3}$	$0.29\pm^{0.04}_{0.04}$	2.0	620	3.5 (8)	62.8 (76)	66.3 (77)	0.80
MACS0329.7-0212	$3.05\pm^{0.79}_{0.46}$	$19.8\pm^{9.9}_{6.4}$	$3.28\pm^{1.22}_{0.81}$	$2.08\pm^{0.74}_{0.40}$	$12.4\pm^{2.1}_{1.9}$	$11.7\pm^{0.5}_{0.6}$	$0.32\pm^{0.07}_{0.05}$	$4.1\pm^{0.9}_{0.6}$	1150	1.0 (5)	34.0 (45)	35.0 (42)	0.77
Abell 478	$4.73\pm^{0.28}_{0.24}$	$45.5\pm^{3.8}_{3.9}$	$7.61\pm^{2.61}_{1.87}$	$1.39\pm^{0.13}_{0.10}$	$8.3pm^{0.8}_{0.6}$	$15.0\pm^{1.4}_{1.2}$	$0.28\pm^{0.04}_{0.02}$	2.0	326	3.1 (9)	81.7 (121)	84.8 (123)	0.99
MACSJ0429.6-0253	$2.81\pm^{0.52}_{0.41}$	$19.9\pm^{4.3}_{4.5}$	$4.03\pm^{1.36}_{1.02}$	$1.87\pm^{0.37}_{0.28}$	$13.9\pm^{2.0}_{1.8}$	$11.8\pm^{1.3}_{1.2}$	$0.19\pm^{0.04}_{0.03}$	2.0	1071	1.9 (5)	33.8 (45)	35.8 (43)	0.77
3C186	$4.62\pm^{1.13}_{0.72}$	$9.4\pm^{3.7}_{2.9}$	$5.24\pm^{3.36}_{2.02}$	$1.61\pm^{0.42}_{0.25}$	$9.0\pm^{2.6}_{1.6}$	-	-	-	1639	0.3 (2)	12.8 (15)	13.1 (12)	0.36
RXJ0439.0+0521	$2.68\pm^{0.42}_{0.39}$	$23.3\pm^{7.4}_{4.5}$	$3.53\pm^{0.90}_{0.58}$	$1.99\pm^{0.34}_{0.26}$	$9.8\pm^{1.0}_{1.0}$	$14.6\pm^{1.1}_{1.3}$	$0.22\pm^{0.03}_{0.03}$	2.0	681	2.6 (7)	26.2 (60)	28.8 (60)	0.99
MACSJ0744.9+3927	$2.55\pm^{0.87}_{0.40}$	$18.0\pm^{5.9}_{6.2}$	$3.28\pm^{1.15}_{0.54}$	$1.98\pm^{0.32}_{0.33}$	$16.8\pm^{2.3}_{2.6}$	$11.1\pm^{1.4}_{1.5}$	$0.32\pm^{0.10}_{0.06}$	2.0	1433	1.3(5)	23.9(44)	25.2(42)	0.98
MACSJ0947.2+7623	$5.31\pm^{0.82}_{1.05}$	$11.2\pm^{2.8}_{2.3}$	$3.88\pm^{1.13}_{0.98}$	$1.72\pm^{0.33}_{0.18}$	$18.1\pm^{2.7}_{2.0}$	$22.0\pm^{2.2}_{1.9}$	$0.30\pm^{0.04}_{0.05}$	2.0	993	0.4(5)	41.6(60)	42.0(58)	0.94
Zwicky 3146	$3.53\pm^{0.97}_{0.92}$	$19.5\pm^{3.2}_{3.4}$	$6.38\pm^{2.41}_{1.77}$	$1.47\pm^{0.22}_{0.23}$	$14.0\pm^{4.6}_{2.9}$	$17.2\pm^{8.8}_{5.4}$	$0.83\pm^{0.68}_{0.46}$	$0.9\pm^{0.2}_{0.1}$	870	7.1 (9)	36.9 (76)	44.0 (77)	0.99
MACSJ1115.8+0129	$2.48\pm^{0.34}_{0.34}$	$29.0\pm^{6.3}_{4.4}$	$3.73\pm^{0.29}_{0.22}$	2.0	$14.5\pm^{1.1}_{1.1}$	$16.9\pm^{1.6}_{1.3}$	$0.28\pm^{0.04}_{0.04}$	2.0	991	1.7(5)	30.2(60)	31.9(59)	0.99
MS1137.5+6625	$2.63\pm^{0.15}_{0.13}$	$30.3\pm^{5.7}_{4.8}$	$2.70\pm^{1.05}_{0.45}$	$3.31\pm^{0.97}_{0.97}$	$10.3\pm^{2.6}_{2.6}$	-	-	-	1497	2.1(4)	32.3(30)	34.4(29)	0.22
Abell 1413	$1.72\pm^{0.13}_{0.12}$	$60.2\pm^{8.7}_{6.4}$	$5.97\pm^{1.30}_{1.26}$	$1.58\pm^{0.20}_{0.12}$	$10.2\pm^{0.9}_{0.7}$	$26.8\pm^{2.5}_{2.6}$	$0.52\pm^{0.03}_{0.03}$	2.0	501	6.2(9)	102.6(106)	108.8(108)	0.46
CLJ1226.9+3332	$3.57\pm^{0.20}_{0.17}$	$29.5\pm^{6.3}_{5.9}$	$3.42\pm^{1.80}_{0.59}$	$2.64\pm^{0.59}_{0.72}$	$16.6\pm^{4.2}_{3.2}$	-	-	-	1603	0.9(4)	11.1(30)	12.0(29)	0.99
MACSJ1311.0-0311	$1.68\pm^{0.32}_{0.28}$	$35.9\pm^{13.1}_{9.0}$	$4.17\pm^{0.89}_{0.63}$	$2.21\pm^{0.35}_{0.27}$	$12.4\pm^{1.5}_{1.1}$	$23.4\pm^{2.6}_{2.5}$	$0.34\pm^{0.06}_{0.05}$	2.0	1214	0.9(6)	19.3(30)	20.2(29)	0.89
RXJ1347.5-1145	$3.89\pm^{0.42}_{0.39}$	$31.2\pm^{10.1}_{8.0}$	$2.28\pm^{0.16}_{0.18}$	$3.10\pm^{0.74}_{0.41}$	$60.6\pm^{6.8}_{5.7}$	$16.5\pm^{1.5}_{1.3}$	$0.11\pm^{0.02}_{0.02}$	$1.3\pm^{0.1}_{0.2}$	1154	2.6(6)	29.4(60)	32.0(58)	0.99
Abell 1835	$5.25\pm^{0.31}_{0.29}$	$17.4\pm^{1.1}_{1.1}$	$2.71\pm^{6.05}_{3.72}$	$1.09\pm^{0.02}_{0.02}$	$10.9\pm^{0.5}_{0.4}$	$17.3\pm^{0.4}_{0.3}$	$0.47\pm^{0.02}_{0.02}$	$4.3\pm^{0.4}_{0.3}$	788	2.9(9)	68.1(91)	70.4(92)	0.95
CL1415.2+3612	$3.78\pm^{0.41}_{0.43}$	$9.5\pm^{4.0}_{2.2}$	$2.47\pm^{1.17}_{0.52}$	$2.42\pm^{0.63}_{0.54}$	$11.3\pm^{4.0}_{3.1}$	-	-	-	1626	0.8(3)	22.5(30)	23.3(28)	0.72
MACSJ1423.8+2404	$1.96\pm^{0.54}_{0.34}$	$32.2\pm^{11.3}_{11.9}$	$2.04\pm^{0.45}_{0.27}$	$3.54\pm^{0.95}_{0.90}$	$26.5\pm^{4.0}_{4.1}$	$14.4\pm^{1.4}_{1.3}$	$0.11\pm^{0.03}_{0.03}$	2.0	1276	0.5(4)	37.8(45)	38.3(42)	0.63
MACSJ1427.3+4408	$2.52\pm^{0.46}_{0.48}$	$5.28\pm^{1.8}_{1.1}$	$3.60\pm^{0.73}_{0.67}$	$1.47\pm^{0.13}_{0.09}$	$18.2\pm^{3.0}_{2.1}$	$19.8\pm^{1.6}_{1.4}$	$0.24\pm^{0.04}_{0.04}$	2.0	1204	1.7(5)	58.0(45)	59.7(43)	0.05
RXJ1504.1-0248	$3.41\pm^{0.22}_{0.24}$	$31.3\pm^{3.9}_{3.5}$	$3.15\pm^{0.38}_{0.27}$	$2.12\pm^{0.19}_{0.17}$	$21.8\pm^{1.3}_{1.5}$	$35.1\pm^{0.9}_{0.9}$	$0.20\pm^{0.01}_{0.01}$	2.0	694	7.4(9)	89.4(106)	96.8(108)	0.75
MACSJ1532.9+3021	$3.54\pm^{0.06}_{0.07}$	$17.8\pm^{6.5}_{5.4}$	$3.61\pm^{1.45}_{0.97}$	$1.90\pm^{0.46}_{0.30}$	$14.4\pm^{2.8}_{2.3}$	$25.5\pm^{3.6}_{3.1}$	$0.28\pm^{0.06}_{0.05}$	2.0	977	0.8(5)	31.4(60)	32.2(58)	0.99
MACSJ1621.6+3810	$2.25\pm^{0.49}_{0.45}$	$18.0\pm^{16.7}_{4.8}$	$2.76\pm^{0.67}_{0.69}$	$2.19\pm^{1.29}_{0.29}$	$16.0\pm^{3.0}_{2.1}$	$10.3\pm^{1.1}_{1.0}$	$0.23\pm^{0.05}_{0.04}$	2.0	1173	6.1(6)	32.7(45)	38.8(44)	0.69
Abell 2204	$4.12\pm^{0.19}_{0.18}$	$22.6\pm^{1.2}_{1.2}$	$6.64\pm^{0.89}_{0.68}$	$1.38\pm^{0.05}_{0.05}$	$15.1\pm^{0.7}_{0.7}$	$19.9\pm^{0.6}_{0.5}$	$0.17\pm^{0.01}_{0.01}$	2.0	526	1.9(9)	121.1(137)	123.0(139)	0.83
MACSJ1720.3+3536	$1.72\pm^{0.22}_{0.15}$	$61.5\pm^{14.3}_{16.2}$	$2.70\pm^{0.43}_{0.26}$	$3.39\pm^{0.50}_{0.69}$	$15.0\pm^{1.3}_{1.3}$	$12.4\pm^{0.9}_{1.0}$	$0.13\pm^{0.01}_{0.01}$	2.0	1058	4.6(6)	35.3(60)	39.9(59)	0.97
RXJ2129.6+0005	$3.04\pm^{0.61}_{0.56}$	$18.8\pm^{5.5}_{3.8}$	$7.44\pm^{4.2}_{2.1}$	$1.36\pm^{0.18}_{0.15}$	$10.0\pm^{1.5}_{1.4}$	$17.2\pm^{1.9}_{2.1}$	$0.41\pm^{0.07}_{0.07}$	2.0	743	2.8(7)	43.5(76)	46.3(76)	0.99
Abell 2537	$1.76\pm^{0.31}_{0.39}$	$26.7\pm^{12.2}_{6.1}$	$6.37\pm^{2.51}_{2.31}$	$1.50\pm^{0.41}_{0.16}$	$11.6\pm^{1.9}_{1.4}$	$25.0\pm^{9.2}_{6.3}$	$0.74\pm^{0.12}_{0.13}$	2.0	875	0.7(5)	52.8(76)	53.5(74)	0.96

Table 4.3: Cluster Masses from Chandra X-ray data.

Cluster	$r_{2500}(arcsec)$	$M_{gas}(r_{2500})10^{13}M_{\odot}$	$M_{tot}(_{2500})10^{14}M_{\odot}$	$f_{gas}(r_{2500})$	$r_{500}(arcsec)$	$M_{gas}(r_{500})10^{13}M_{\odot}$	$M_{tot}(_{500})10^{14}M_{\odot}$	$f_{gas}(r_{500})$
MACSJ0159.8-0849	$104.1\pm^{3.1}_{3.4}$	$3.94\pm^{0.15}_{0.17}$	$3.63\pm^{0.33}_{0.35}$	$0.108\pm^{0.007}_{0.006}$	$221.9\pm^{11.1}_{10.8}$	$10.14\pm^{0.48}_{0.47}$	$7.11\pm^{1.13}_{0.98}$	$0.143\pm^{0.016}_{0.014}$
Abell 383	$133.9\pm^{7.0}_{7.2}$	$1.43\pm^{0.09}_{0.09}$	$1.18\pm^{0.20}_{0.18}$	$0.121\pm^{0.013}_{0.011}$	$282.1\pm^{23.6}_{21.0}$	$3.61\pm^{0.22}_{0.26}$	$2.23\pm^{0.54}_{0.51}$	$0.162\pm^{0.034}_{0.024}$
MACS0329.7-0212	$72.5\pm^{3.9}_{2.6}$	$2.25\pm^{0.16}_{0.20}$	$1.59\pm^{0.27}_{0.30}$	$0.142\pm^{0.018}_{0.012}$	$144.4\pm^{11.6}_{13.2}$	$5.83\pm^{0.44}_{0.50}$	$2.51\pm^{0.66}_{0.63}$	$0.232\pm^{0.050}_{0.035}$
Abell 478	$292.3\pm^{10.4}_{13.4}$	$2.97\pm^{0.13}_{0.17}$	$1.85\pm^{0.20}_{0.24}$	$0.161\pm^{0.014}_{0.010}$	$636.4\pm^{33.5}_{42.8}$	$7.79\pm^{0.36}_{0.44}$	$3.82\pm^{0.64}_{0.72}$	$0.204\pm^{0.033}_{0.022}$
MACSJ0429.6-0253	$89.6\pm^{7.0}_{7.7}$	$2.41\pm^{0.23}_{0.25}$	$2.26\pm^{0.57}_{0.53}$	$0.107\pm^{0.019}_{0.014}$	$181.6\pm^{19.4}_{21.3}$	$5.80\pm^{0.53}_{0.60}$	$3.80\pm^{1.36}_{1.19}$	$0.152\pm^{0.046}_{0.030}$
3C186	$26.4\pm^{1.4}_{1.4}$	$0.76\pm^{0.06}_{0.06}$	$0.77\pm^{0.13}_{0.12}$	$0.099\pm^{0.009}_{0.008}$	$57.9\pm^{4.2}_{4.1}$	$2.64\pm^{0.20}_{0.20}$	$1.64\pm^{0.38}_{0.33}$	$0.161\pm^{0.025}_{0.021}$
RXJ0439.0+0521	$122.9\pm^{6.5}_{6.3}$	$1.28\pm^{0.08}_{0.07}$	$1.24\pm^{0.21}_{0.18}$	$0.104\pm^{0.011}_{0.010}$	$243.3\pm^{17.3}_{17.0}$	$2.98\pm^{0.17}_{0.17}$	$1.93\pm^{0.44}_{0.38}$	$0.154\pm^{0.026}_{0.022}$
MACSJ0744.9+3927	$60.0\pm^{3.2}_{3.0}$	$2.93\pm^{0.27}_{0.21}$	$2.19\pm^{0.32}_{0.37}$	$0.134\pm^{0.011}_{0.016}$	$122.9\pm^{8.3}_{7.6}$	$8.46\pm^{0.61}_{0.56}$	$3.84\pm^{0.83}_{0.67}$	$0.221\pm^{0.029}_{0.026}$
MACSJ0947.2+7623	$102.9\pm^{8.1}_{7.9}$	$3.37\pm^{0.24}_{0.28}$	$2.56\pm^{0.56}_{0.56}$	$0.132\pm^{0.023}_{0.016}$	$204.3\pm^{20.7}_{20.8}$	$7.60\pm^{0.70}_{0.68}$	$4.10\pm^{1.38}_{1.13}$	$0.186\pm^{0.048}_{0.034}$
Zwicky 3146	$133.4\pm^{8.1}_{7.2}$	$4.40\pm^{0.32}_{0.28}$	$3.11\pm^{0.36}_{0.35}$	$0.142\pm^{0.009}_{0.008}$	$282.3\pm^{13.4}_{13.6}$	$10.17\pm^{0.44}_{0.44}$	$6.28\pm^{0.88}_{0.82}$	$0.162\pm^{0.017}_{0.015}$
MACSJ1115.8+0129	$102.0\pm^{5.7}_{5.5}$	$6.26\pm^{0.23}_{0.22}$	$2.49\pm^{0.44}_{0.38}$	$0.131\pm^{0.013}_{0.012}$	$207.1\pm^{13.7}_{12.1}$	$8.08\pm^{0.46}_{0.45}$	$4.23\pm^{0.90}_{0.73}$	$0.191\pm^{0.027}_{0.025}$
MS1137.5+6625	$33.4\pm^{2.5}_{2.9}$	$0.81\pm^{0.09}_{0.10}$	$0.84\pm^{0.21}_{0.21}$	$0.097\pm^{0.015}_{0.011}$	$67.4\pm^{5.1}_{4.7}$	$2.47\pm^{0.17}_{0.16}$	$1.39\pm^{0.34}_{0.27}$	$0.178\pm^{0.029}_{0.026}$
Abell 1413	$211.6\pm^{4.9}_{5.4}$	$2.69\pm^{0.10}_{0.10}$	$2.36\pm^{0.17}_{0.18}$	$0.114\pm^{0.005}_{0.004}$	$461.2\pm^{17.7}_{20.0}$	$7.50\pm^{0.28}_{0.32}$	$4.93\pm^{0.59}_{0.61}$	$0.153\pm^{0.014}_{0.011}$
CLJ1226.9+3332	$51.9\pm^{3.5}_{3.8}$	$2.98\pm^{0.27}_{0.29}$	$2.58\pm^{0.56}_{0.53}$	$0.116\pm^{0.016}_{0.012}$	$104.9\pm^{9.3}_{8.4}$	$7.46\pm^{0.52}_{0.47}$	$4.28\pm^{1.25}_{0.95}$	$0.174\pm^{0.036}_{0.030}$
MACSJ1311.0-0311	$77.3\pm^{5.5}_{4.7}$	$2.14\pm^{0.18}_{0.15}$	$2.25\pm^{0.52}_{0.39}$	$0.095\pm^{0.012}_{0.012}$	$159.6\pm^{15.3}_{12.5}$	$4.72\pm^{0.32}_{0.26}$	$4.14\pm^{1.31}_{0.91}$	$0.114\pm^{0.025}_{0.022}$
RXJ1347.5-1145	$103.5\pm^{2.7}_{2.8}$	$6.81\pm^{0.23}_{0.25}$	$6.54\pm^{0.52}_{0.52}$	$0.104\pm^{0.005}_{0.005}$	$188.8\pm^{6.2}_{6.4}$	$14.27\pm^{0.52}_{0.52}$	$8.30\pm^{0.82}_{0.82}$	$0.172\pm^{0.012}_{0.010}$
Abell 1835	$154.7\pm^{2.8}_{3.4}$	$5.00\pm^{0.11}_{0.13}$	$4.03\pm^{0.23}_{0.26}$	$0.124\pm^{0.005}_{0.004}$	$354.2\pm^{7.8}_{7.9}$	$13.29\pm^{0.28}_{0.26}$	$9.68\pm^{0.66}_{0.63}$	$0.137\pm^{0.007}_{0.006}$
CL1415.2+3612	$37.9\pm^{2.8}_{2.9}$	$1.10\pm^{0.09}_{0.10}$	$0.83\pm^{0.22}_{0.19}$	$0.133\pm^{0.020}_{0.026}$	$68.9\pm^{6.4}_{6.8}$	$2.73\pm^{0.19}_{0.19}$	$1.16\pm^{0.38}_{0.33}$	$0.236\pm^{0.072}_{0.048}$
MACSJ1423.8+2404	$73.4\pm^{7.2}_{7.1}$	$2.52\pm^{0.32}_{0.31}$	$2.41\pm^{0.80}_{0.64}$	$0.105\pm^{0.021}_{0.016}$	$135.0\pm^{15.9}_{15.6}$	$5.83\pm^{0.70}_{0.70}$	$3.08\pm^{1.23}_{0.95}$	$0.190\pm^{0.052}_{0.039}$
MACSJ1427.3+4408	$73.5\pm^{2.1}_{2.2}$	$2.29\pm^{0.09}_{0.10}$	$1.89\pm^{0.17}_{0.17}$	$0.121\pm^{0.006}_{0.006}$	$150.7\pm^{4.4}_{4.7}$	$7.28\pm^{0.30}_{0.31}$	$3.40\pm^{0.31}_{0.31}$	$0.214\pm^{0.012}_{0.010}$
RXJ1504.1-0248	$167.4\pm^{4.7}_{4.2}$	$4.53\pm^{0.15}_{0.13}$	$3.27\pm^{0.29}_{0.24}$	$0.139\pm^{0.007}_{0.007}$	$324.2\pm^{12.6}_{11.9}$	$9.68\pm^{0.35}_{0.32}$	$4.87\pm^{0.59}_{0.52}$	$0.199\pm^{0.017}_{0.016}$
MACSJ1532.9+3021	$96.3\pm^{8.6}_{6.8}$	$2.93\pm^{0.28}_{0.21}$	$1.94\pm^{0.58}_{0.39}$	$0.151\pm^{0.024}_{0.024}$	$191.4\pm^{23.4}_{18.3}$	$6.61\pm^{0.65}_{0.54}$	$3.16\pm^{1.32}_{0.83}$	$0.209\pm^{0.052}_{0.048}$
MACSJ1621.6+3810	$74.6\pm^{3.7}_{6.7}$	$1.97\pm^{0.13}_{0.23}$	$1.83\pm^{0.29}_{0.45}$	$0.108\pm^{0.018}_{0.009}$	$143.9\pm^{10.9}_{14.4}$	$5.02\pm^{0.38}_{0.50}$	$2.66\pm^{0.65}_{0.72}$	$0.189\pm^{0.045}_{0.026}$
Abell 2204	$234.0\pm^{4.1}_{3.9}$	$4.11\pm^{0.09}_{0.09}$	$3.73\pm^{0.20}_{0.18}$	$0.110\pm^{0.003}_{0.003}$	$496.4\pm^{12.9}_{10.5}$	$10.57\pm^{0.30}_{0.24}$	$7.16\pm^{0.57}_{0.45}$	$0.148\pm^{0.008}_{0.007}$
MACSJ1720.3+3536	$90.0\pm^{5.1}_{4.9}$	$2.61\pm^{0.20}_{0.19}$	$2.16\pm^{0.39}_{0.33}$	$0.121\pm^{0.012}_{0.011}$	$174.3\pm^{12.5}_{11.3}$	$6.28\pm^{0.39}_{0.37}$	$3.18\pm^{0.74}_{0.58}$	$0.197\pm^{0.030}_{0.027}$
RXJ2129.6+0005	$135.6\pm^{6.4}_{6.5}$	$2.52\pm^{0.16}_{0.16}$	$2.18\pm^{0.32}_{0.30}$	$0.116\pm^{0.010}_{0.009}$	$295.4\pm^{16.1}_{16.1}$	$6.94\pm^{0.38}_{0.39}$	$4.53\pm^{0.78}_{0.70}$	$0.153\pm^{0.018}_{0.016}$
Abell 2537	$119.2\pm^{5.0}_{4.7}$	$2.25\pm^{0.14}_{0.13}$	$2.59\pm^{0.34}_{0.30}$	$0.087\pm^{0.006}_{0.005}$	$259.0\pm^{14.3}_{17.0}$	$6.27\pm^{0.36}_{0.40}$	$5.37\pm^{0.94}_{0.99}$	$0.117\pm^{0.018}_{0.013}$

4.6 Surface Brightness and Temperature Profiles

In this section, the fits to the surface brightness and temperature profiles for each cluster are shown.

4.6.1 MACSJ0159.8-0849

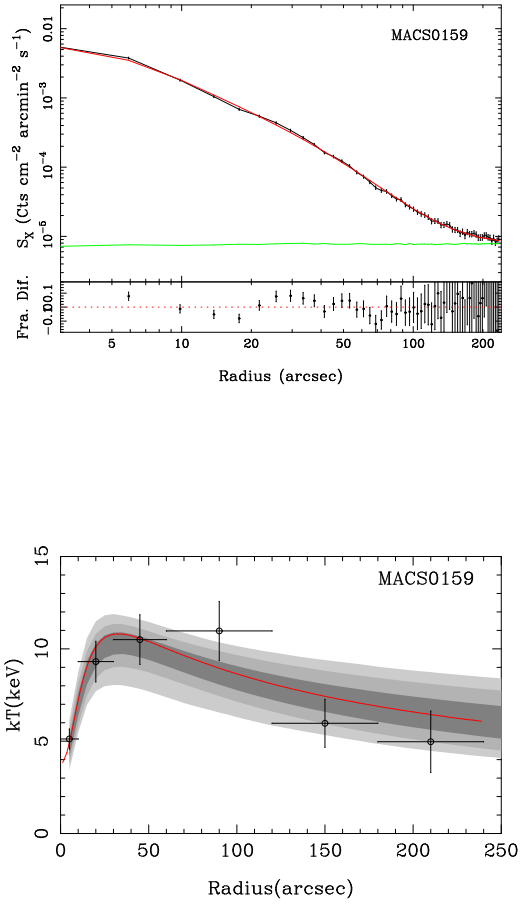

Figure 4.8: MACSJ0159.8-0849: *Top panel:* Surface brightness profiles where the black points are derived from the X-ray images, the red line shows the best fit model, and the green line is the background level determined from the blank sky observations. The residuals show the fractional difference between the model and the data. A 1% systematic uncertainty has been added in quadrature to the datapoints. The surface brightness profiles are plotted beyond the fitted region to show the agreement between the cluster emission and background. *Bottom panel:* Temperature profiles where the red line shows the best fit model and the dark, medium, and light grey regions show the 68%, 95.4%, and 99.7% confidence levels obtained from the model fits.

4.6.2 Abell 383

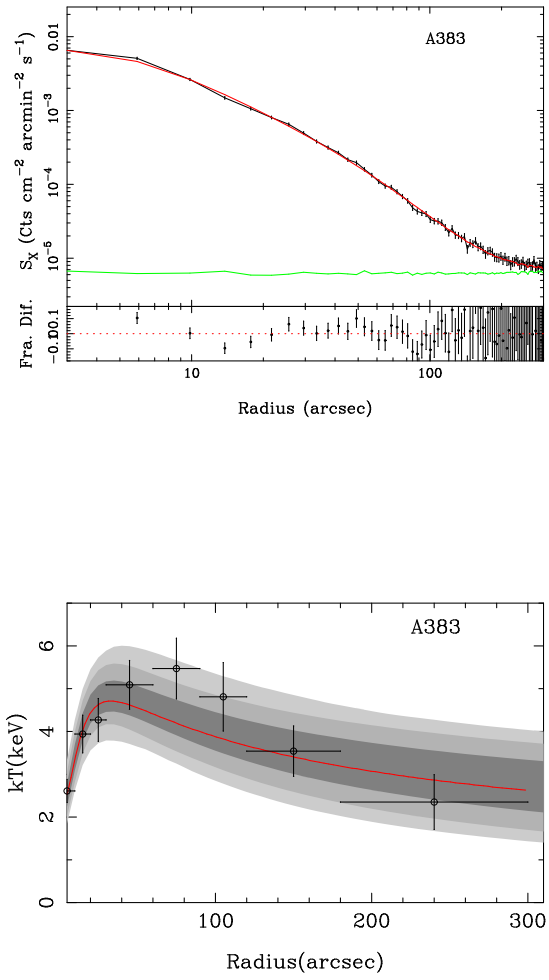

Figure 4.9: Abell 383: *Top panel:* Surface brightness profiles where the black points are derived from the X-ray images, the red line shows the best fit model, and the green line is the background level determined from the blank sky observations. The residuals show the fractional difference between the model and the data. A 1% systematic uncertainty has been added in quadrature to the datapoints. The surface brightness profiles are plotted beyond the fitted region to show the agreement between the cluster emission and background. *Bottom panel:* Temperature profiles where the red line shows the best fit model and the dark, medium, and light grey regions show the 68%, 95.4%, and 99.7% confidence levels obtained from the model fits.

4.6.3 MACSJ0329.7-0212

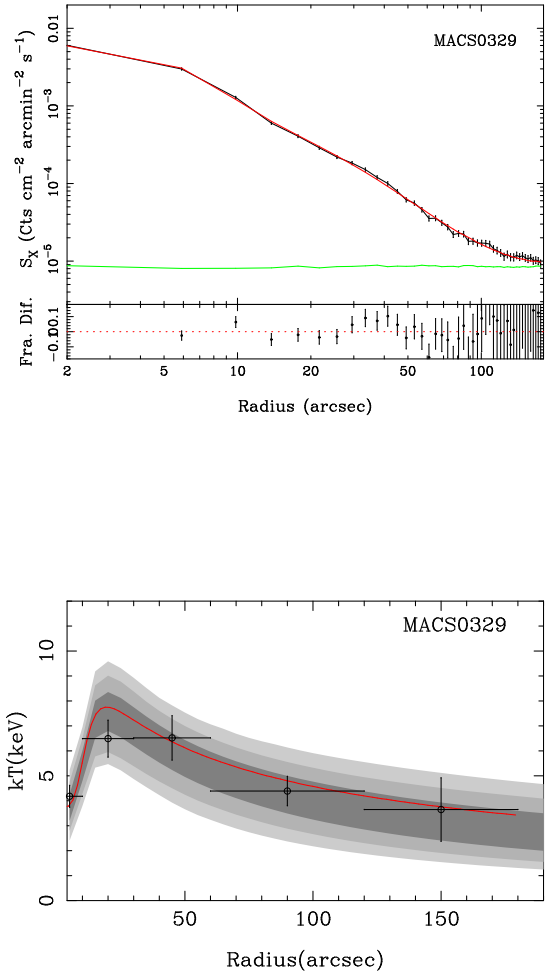

Figure 4.10: MACSJ0329.7-0212: *Top panel:* Surface brightness profiles where the black points are derived from the X-ray images, the red line shows the best fit model, and the green line is the background level determined from the blank sky observations. The residuals show the fractional difference between the model and the data. A 1% systematic uncertainty has been added in quadrature to the datapoints. The surface brightness profiles are plotted beyond the fitted region to show the agreement between the cluster emission and background. *Bottom panel:* Temperature profiles where the red line shows the best fit model and the dark, medium, and light grey regions show the 68%, 95.4%, and 99.7% confidence levels obtained from the model fits.

4.6.4 Abell 478

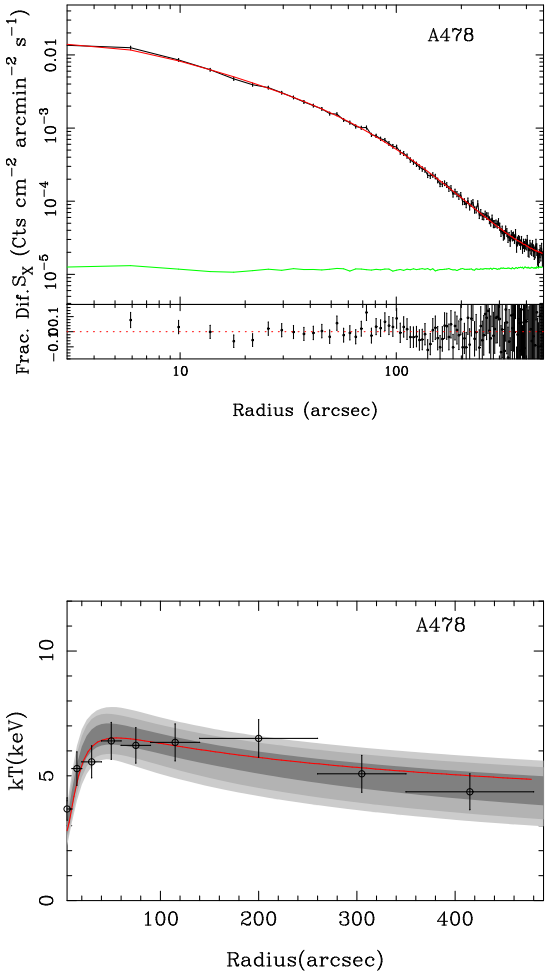

Figure 4.11: Abell 478: *Top panel:* Surface brightness profiles where the black points are derived from the X-ray images, the red line shows the best fit model, and the green line is the background level determined from the blank sky observations. The residuals show the fractional difference between the model and the data. A 1% systematic uncertainty has been added in quadrature to the datapoints. The surface brightness profiles are plotted beyond the fitted region to show the agreement between the cluster emission and background. *Bottom panel:* Temperature profiles where the red line shows the best fit model and the dark, medium, and light grey regions show the 68%, 95.4%, and 99.7% confidence levels obtained from the model fits.

4.6.5 MACSJ0429.6-0253

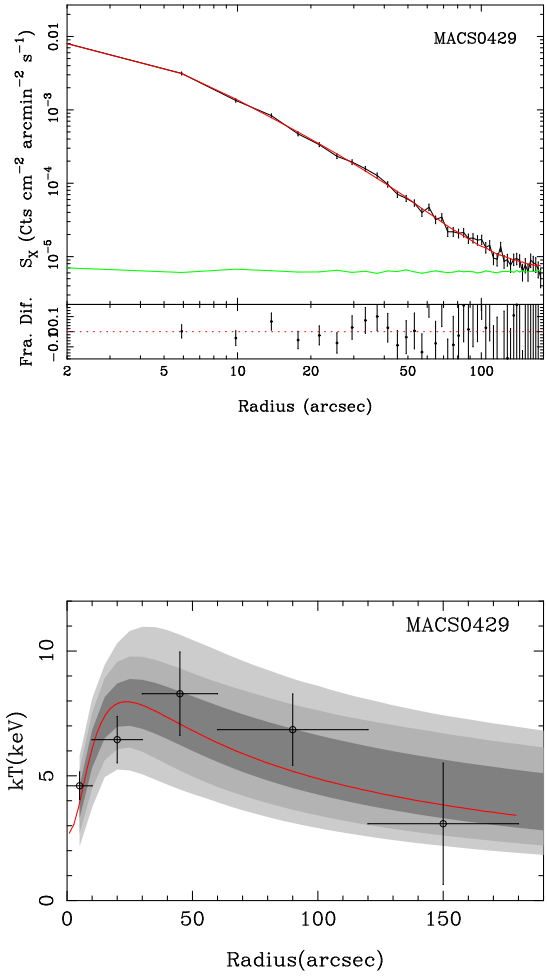

Figure 4.12: MACSJ0429.6-0253: *Top panel:* Surface brightness profiles where the black points are derived from the X-ray images, the red line shows the best fit model, and the green line is the background level determined from the blank sky observations. The residuals show the fractional difference between the model and the data. A 1% systematic uncertainty has been added in quadrature to the datapoints. The surface brightness profiles are plotted beyond the fitted region to show the agreement between the cluster emission and background. *Bottom panel:* Temperature profiles where the red line shows the best fit model and the dark, medium, and light grey regions show the 68%, 95.4%, and 99.7% confidence levels obtained from the model fits.

4.6.6 3C186

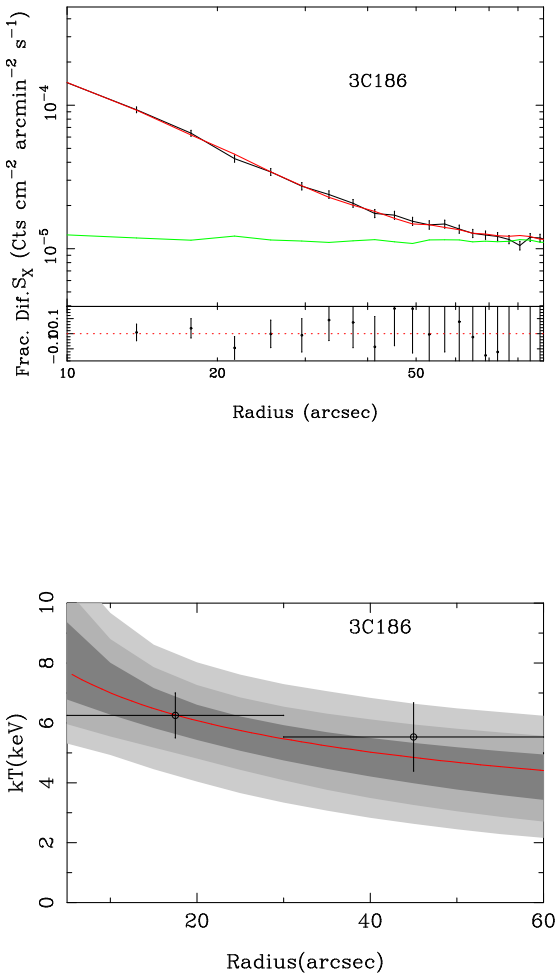

Figure 4.13: 3C186: *Top panel:* Surface brightness profiles where the black points are derived from the X-ray images, the red line shows the best fit model, and the green line is the background level determined from the blank sky observations. The residuals show the fractional difference between the model and the data. A 1% systematic uncertainty has been added in quadrature to the datapoints. The surface brightness profiles are plotted beyond the fitted region to show the agreement between the cluster emission and background. *Bottom panel:* Temperature profiles where the red line shows the best fit model and the dark, medium, and light grey regions show the 68%, 95.4%, and 99.7% confidence levels obtained from the model fits.

4.6.7 MACSJ0744.9+3927

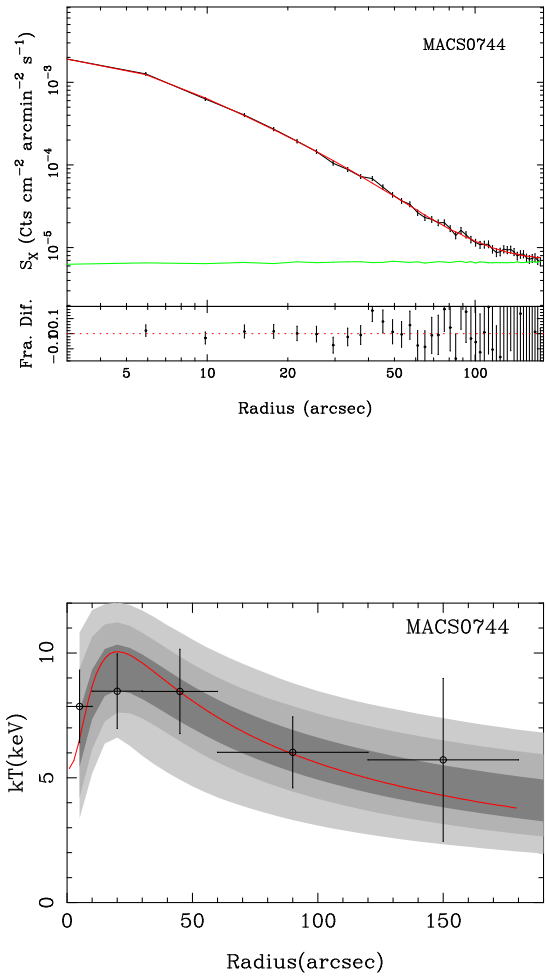

Figure 4.14: MACSJ0744.9+3927: *Top panel:* Surface brightness profiles where the black points are derived from the X-ray images, the red line shows the best fit model, and the green line is the background level determined from the blank sky observations. The residuals show the fractional difference between the model and the data. A 1% systematic uncertainty has been added in quadrature to the datapoints. The surface brightness profiles are plotted beyond the fitted region to show the agreement between the cluster emission and background. *Bottom panel:* Temperature profiles where the red line shows the best fit model and the dark, medium, and light grey regions show the 68%, 95.4%, and 99.7% confidence levels obtained from the model fits.

4.6.8 MACSJ0947.2+7623

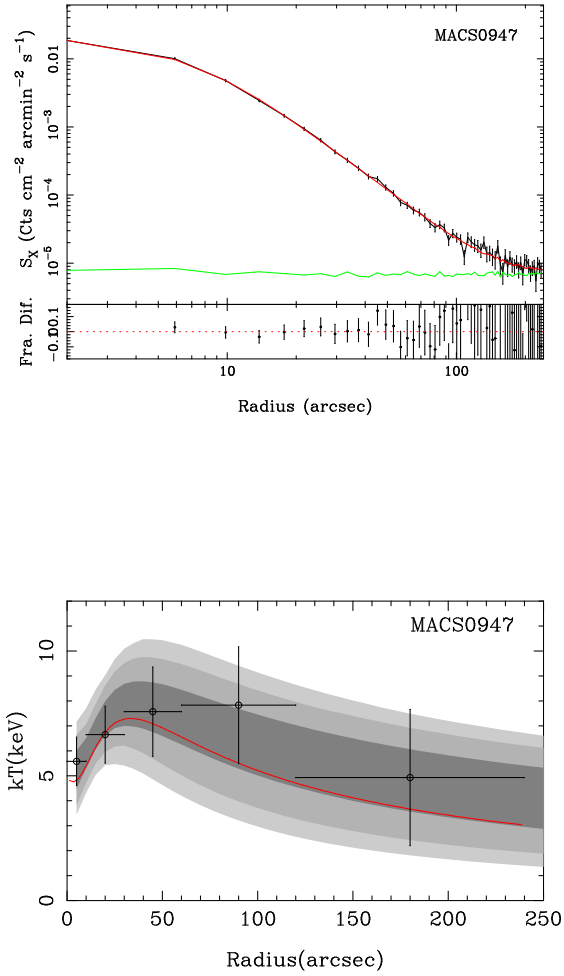

Figure 4.15: MACSJ0947.2+7623: *Top panel:* Surface brightness profiles where the black points are derived from the X-ray images, the red line shows the best fit model, and the green line is the background level determined from the blank sky observations. The residuals show the fractional difference between the model and the data. A 1% systematic uncertainty has been added in quadrature to the datapoints. The surface brightness profiles are plotted beyond the fitted region to show the agreement between the cluster emission and background. *Bottom panel:* Temperature profiles where the red line shows the best fit model and the dark, medium, and light grey regions show the 68%, 95.4%, and 99.7% confidence levels obtained from the model fits.

4.6.9 Zwicky 3146

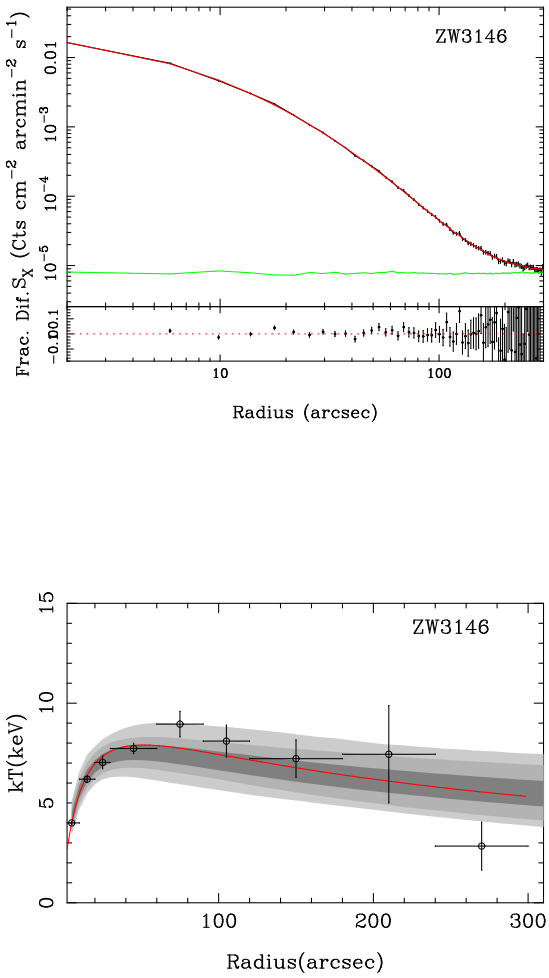

Figure 4.16: Zwicky 3146: *Top panel:* Surface brightness profiles where the black points are derived from the X-ray images, the red line shows the best fit model, and the green line is the background level determined from the blank sky observations. The residuals show the fractional difference between the model and the data. A 1% systematic uncertainty has been added in quadrature to the datapoints. The surface brightness profiles are plotted beyond the fitted region to show the agreement between the cluster emission and background. *Bottom panel:* Temperature profiles where the red line shows the best fit model and the dark, medium, and light grey regions show the 68%, 95.4%, and 99.7% confidence levels obtained from the model fits.

4.6.10 MACSJ1115.8+0129

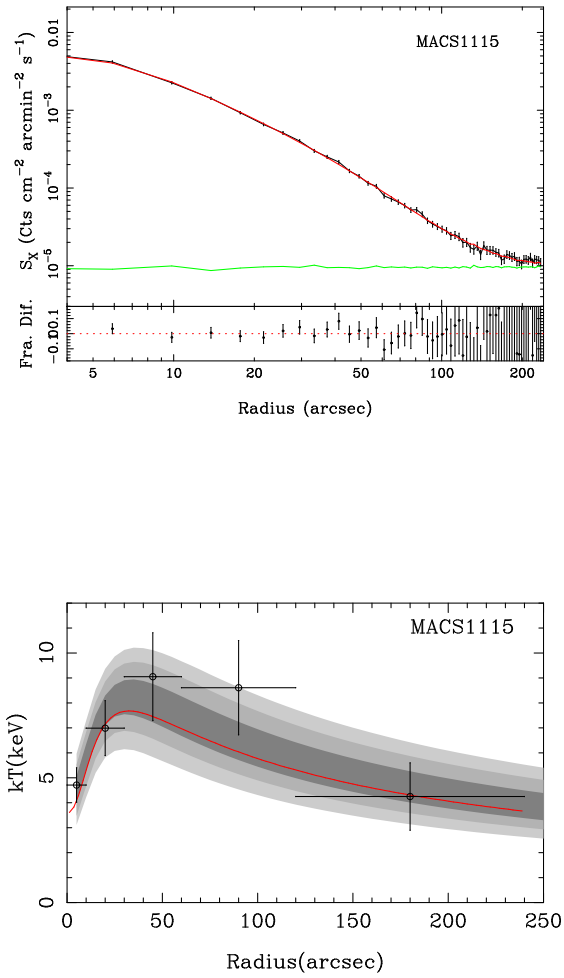

Figure 4.17: MACSJ1115.8+0129: *Top panel:* Surface brightness profiles where the black points are derived from the X-ray images, the red line shows the best fit model, and the green line is the background level determined from the blank sky observations. The residuals show the fractional difference between the model and the data. A 1% systematic uncertainty has been added in quadrature to the datapoints. The surface brightness profiles are plotted beyond the fitted region to show the agreement between the cluster emission and background. *Bottom panel:* Temperature profiles where the red line shows the best fit model and the dark, medium, and light grey regions show the 68%, 95.4%, and 99.7% confidence levels obtained from the model fits.

4.6.11 MS1137.5+6625

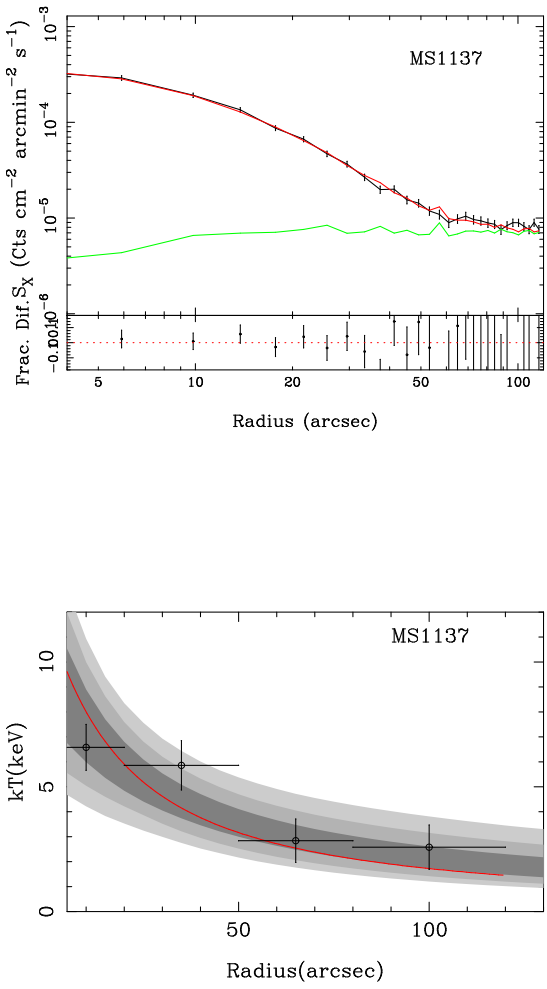

Figure 4.18: MS1137.5+6625: *Top panel:* Surface brightness profiles where the black points are derived from the X-ray images, the red line shows the best fit model, and the green line is the background level determined from the blank sky observations. The residuals show the fractional difference between the model and the data. A 1% systematic uncertainty has been added in quadrature to the datapoints. The surface brightness profiles are plotted beyond the fitted region to show the agreement between the cluster emission and background. *Bottom panel:* Temperature profiles where the red line shows the best fit model and the dark, medium, and light grey regions show the 68%, 95.4%, and 99.7% confidence levels obtained from the model fits.

4.6.12 Abell 1413

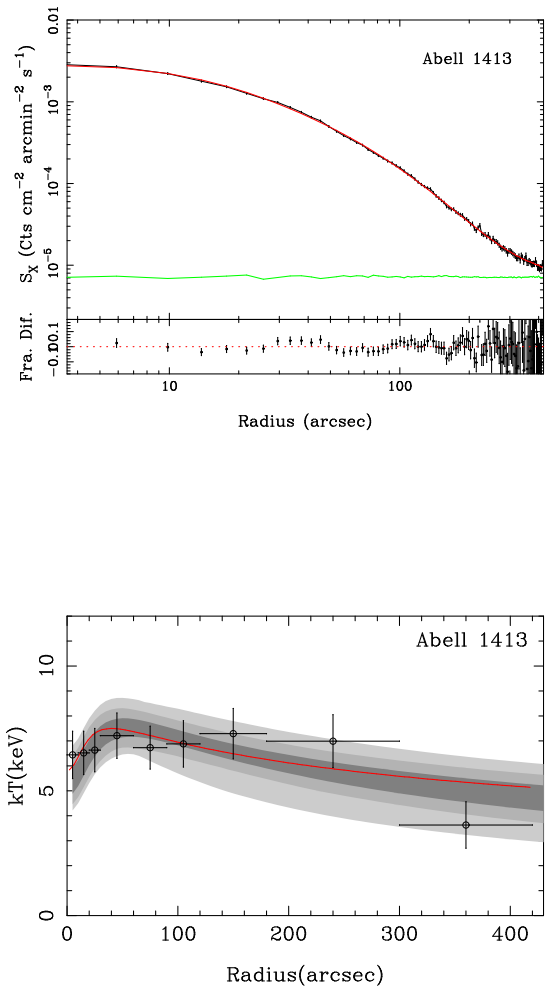

Figure 4.19: Abell 1413: *Top panel:* Surface brightness profiles where the black points are derived from the X-ray images, the red line shows the best fit model, and the green line is the background level determined from the blank sky observations. The residuals show the fractional difference between the model and the data. A 1% systematic uncertainty has been added in quadrature to the datapoints. The surface brightness profiles are plotted beyond the fitted region to show the agreement between the cluster emission and background. *Bottom panel:* Temperature profiles where the red line shows the best fit model and the dark, medium, and light grey regions show the 68%, 95.4%, and 99.7% confidence levels obtained from the model fits.

4.6.13 CLJ1226.9+3332

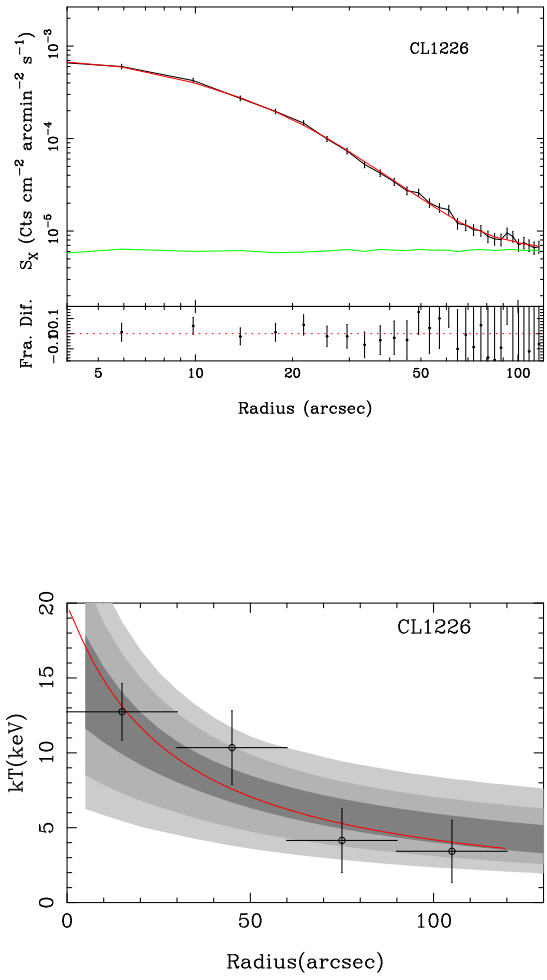

Figure 4.20: CLJ1226.9+3332: *Top panel:* Surface brightness profiles where the black points are derived from the X-ray images, the red line shows the best fit model, and the green line is the background level determined from the blank sky observations. The residuals show the fractional difference between the model and the data. A 1% systematic uncertainty has been added in quadrature to the datapoints. The surface brightness profiles are plotted beyond the fitted region to show the agreement between the cluster emission and background. *Bottom panel:* Temperature profiles where the red line shows the best fit model and the dark, medium, and light grey regions show the 68%, 95.4%, and 99.7% confidence levels obtained from the model fits.

4.6.14 MACSJ1311.0-0311

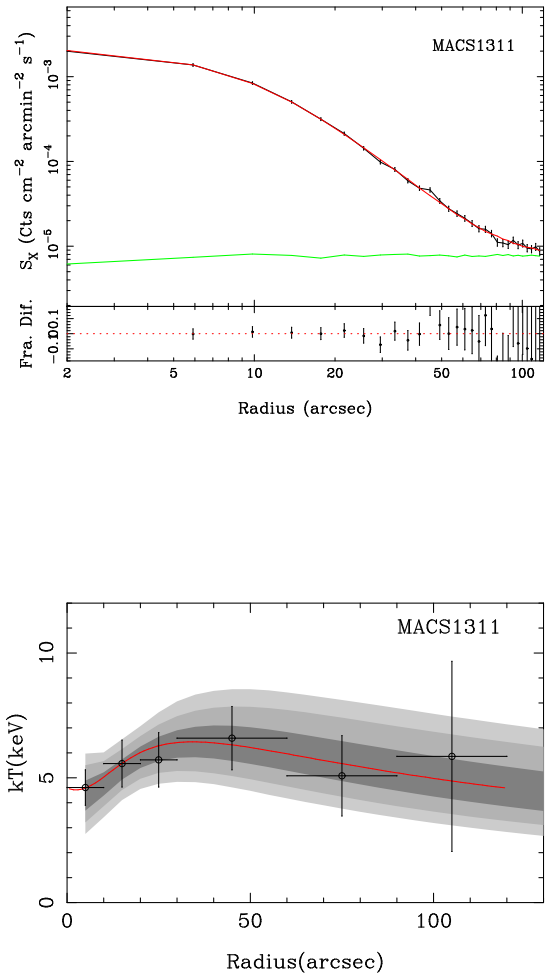

Figure 4.21: MACSJ1311.0-0311: *Top panel:* Surface brightness profiles where the black points are derived from the X-ray images, the red line shows the best fit model, and the green line is the background level determined from the blank sky observations. The residuals show the fractional difference between the model and the data. A 1% systematic uncertainty has been added in quadrature to the datapoints. The surface brightness profiles are plotted beyond the fitted region to show the agreement between the cluster emission and background. *Bottom panel:* Temperature profiles where the red line shows the best fit model and the dark, medium, and light grey regions show the 68%, 95.4%, and 99.7% confidence levels obtained from the model fits.

4.6.15 RXJ1347.5-1145

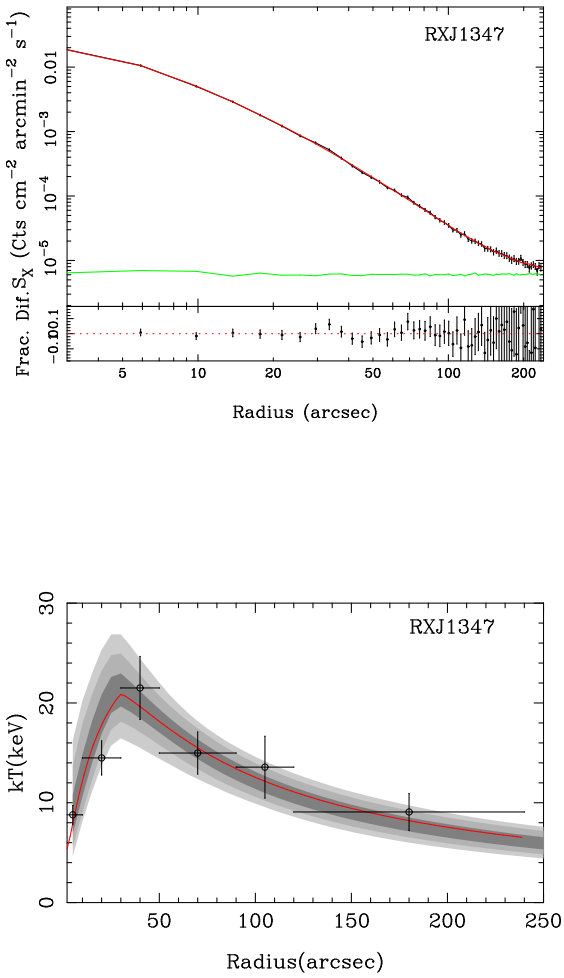

Figure 4.22: RXJ1347.5-1145: *Top panel:* Surface brightness profiles where the black points are derived from the X-ray images, the red line shows the best fit model, and the green line is the background level determined from the blank sky observations. The residuals show the fractional difference between the model and the data. A 1% systematic uncertainty has been added in quadrature to the datapoints. The surface brightness profiles are plotted beyond the fitted region to show the agreement between the cluster emission and background. *Bottom panel:* Temperature profiles where the red line shows the best fit model and the dark, medium, and light grey regions show the 68%, 95.4%, and 99.7% confidence levels obtained from the model fits.

4.6.16 Abell 1835

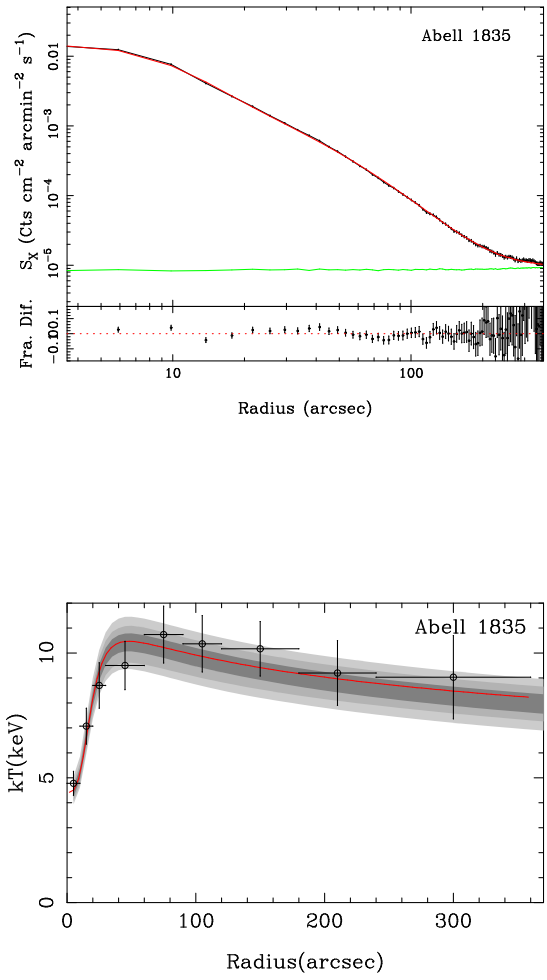

Figure 4.23: Abell 1835: *Top panel:* Surface brightness profiles where the black points are derived from the X-ray images, the red line shows the best fit model, and the green line is the background level determined from the blank sky observations. The residuals show the fractional difference between the model and the data. A 1% systematic uncertainty has been added in quadrature to the datapoints. The surface brightness profiles are plotted beyond the fitted region to show the agreement between the cluster emission and background. *Bottom panel:* Temperature profiles where the red line shows the best fit model and the dark, medium, and light grey regions show the 68%, 95.4%, and 99.7% confidence levels obtained from the model fits.

4.6.17 MACSJ1423.8+2404

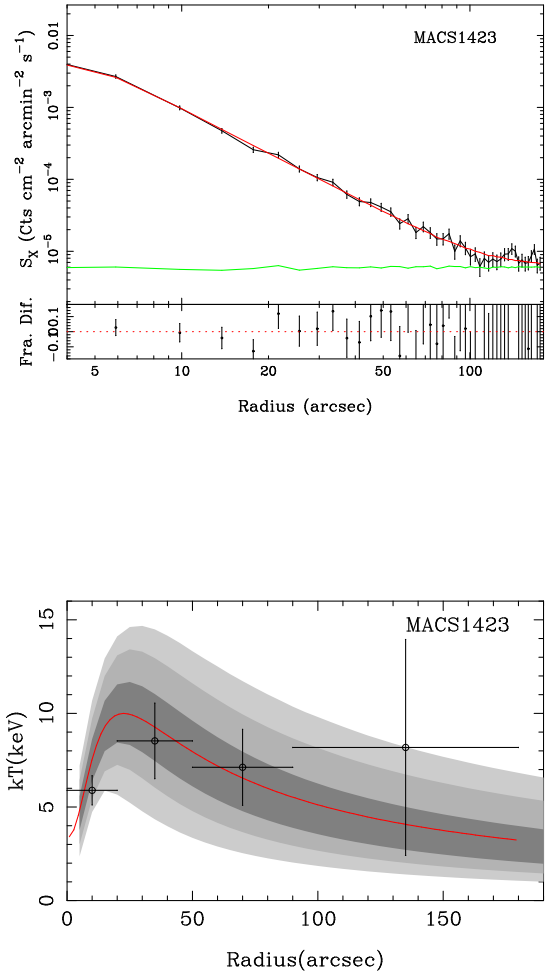

Figure 4.24: MACSJ1423.8+2404: *Top panel:* Surface brightness profiles where the black points are derived from the X-ray images, the red line shows the best fit model, and the green line is the background level determined from the blank sky observations. The residuals show the fractional difference between the model and the data. A 1% systematic uncertainty has been added in quadrature to the datapoints. The surface brightness profiles are plotted beyond the fitted region to show the agreement between the cluster emission and background. *Bottom panel:* Temperature profiles where the red line shows the best fit model and the dark, medium, and light grey regions show the 68%, 95.4%, and 99.7% confidence levels obtained from the model fits.

4.6.18 MACSJ1427.3+4408

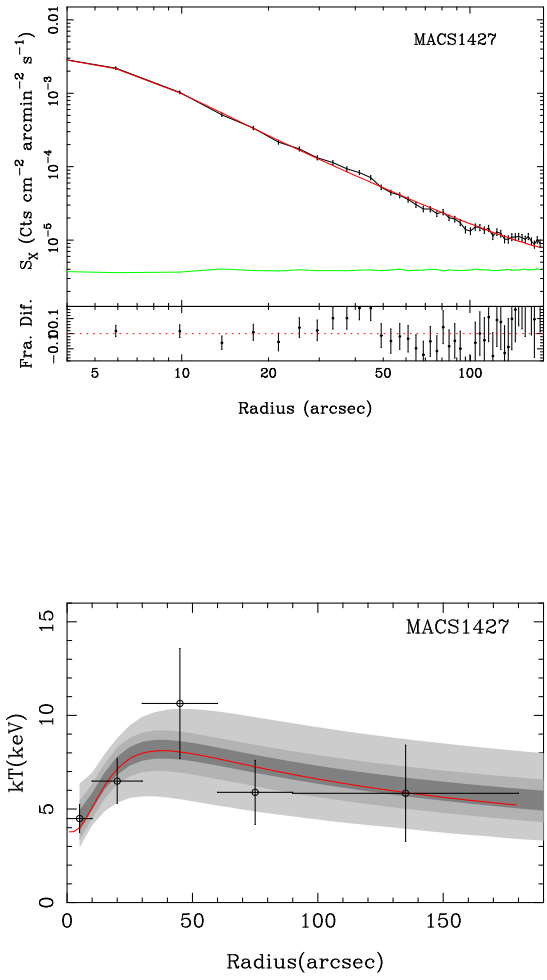

Figure 4.25: MACSJ1427.3+4408: *Top panel:* Surface brightness profiles where the black points are derived from the X-ray images, the red line shows the best fit model, and the green line is the background level determined from the blank sky observations. The residuals show the fractional difference between the model and the data. A 1% systematic uncertainty has been added in quadrature to the datapoints. The surface brightness profiles are plotted beyond the fitted region to show the agreement between the cluster emission and background. *Bottom panel:* Temperature profiles where the red line shows the best fit model and the dark, medium, and light grey regions show the 68%, 95.4%, and 99.7% confidence levels obtained from the model fits.

4.6.19 RXJ1504.1-0248

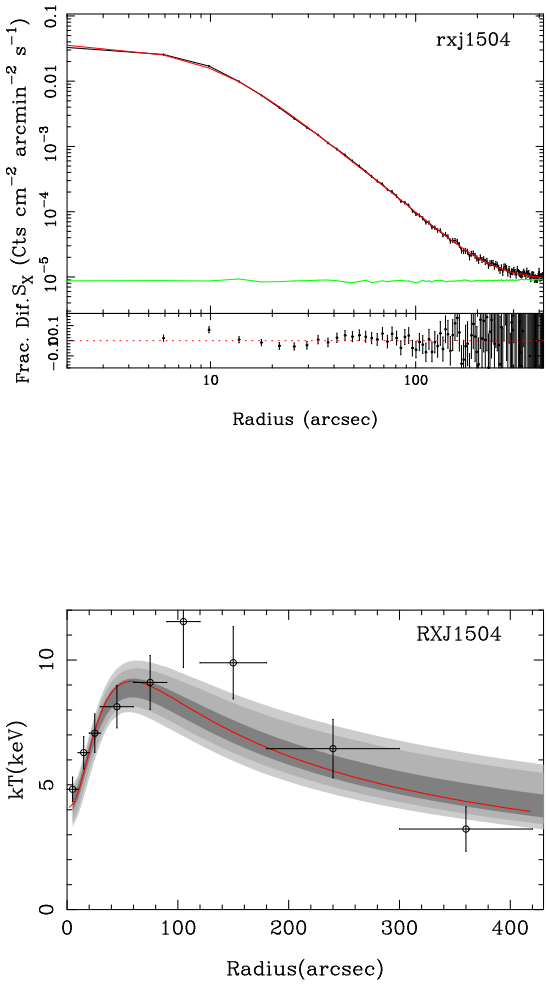

Figure 4.26: RXJ1504.1-0248: *Top panel:* Surface brightness profiles where the black points are derived from the X-ray images, the red line shows the best fit model, and the green line is the background level determined from the blank sky observations. The residuals show the fractional difference between the model and the data. A 1% systematic uncertainty has been added in quadrature to the datapoints. The surface brightness profiles are plotted beyond the fitted region to show the agreement between the cluster emission and background. *Bottom panel:* Temperature profiles where the red line shows the best fit model and the dark, medium, and light grey regions show the 68%, 95.4%, and 99.7% confidence levels obtained from the model fits.

4.6.20 MACSJ1532.9+3021

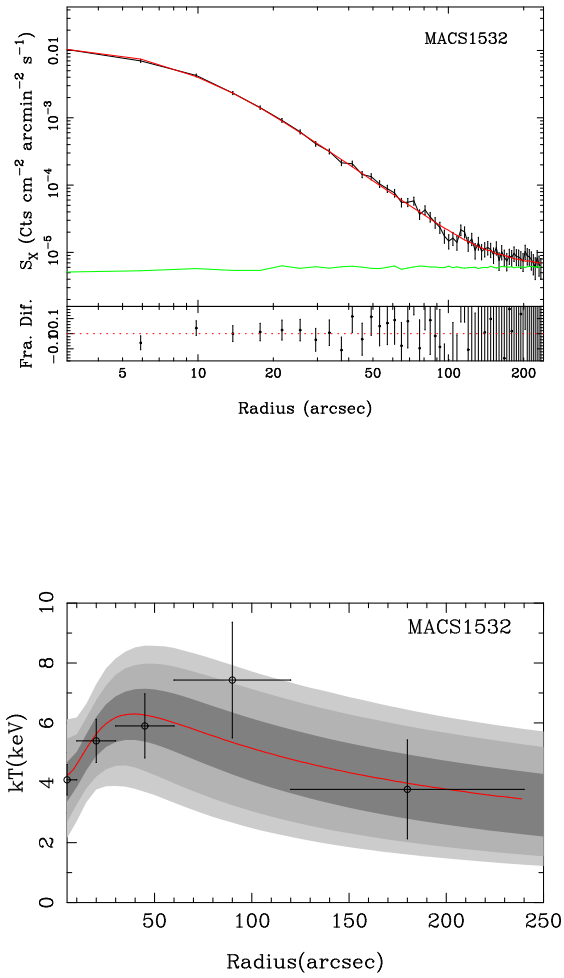

Figure 4.27: MACSJ1532.9+3021: *Top panel:* Surface brightness profiles where the black points are derived from the X-ray images, the red line shows the best fit model, and the green line is the background level determined from the blank sky observations. The residuals show the fractional difference between the model and the data. A 1% systematic uncertainty has been added in quadrature to the datapoints. The surface brightness profiles are plotted beyond the fitted region to show the agreement between the cluster emission and background. *Bottom panel:* Temperature profiles where the red line shows the best fit model and the dark, medium, and light grey regions show the 68%, 95.4%, and 99.7% confidence levels obtained from the model fits.

4.6.21 MACSJ1621.6+3810

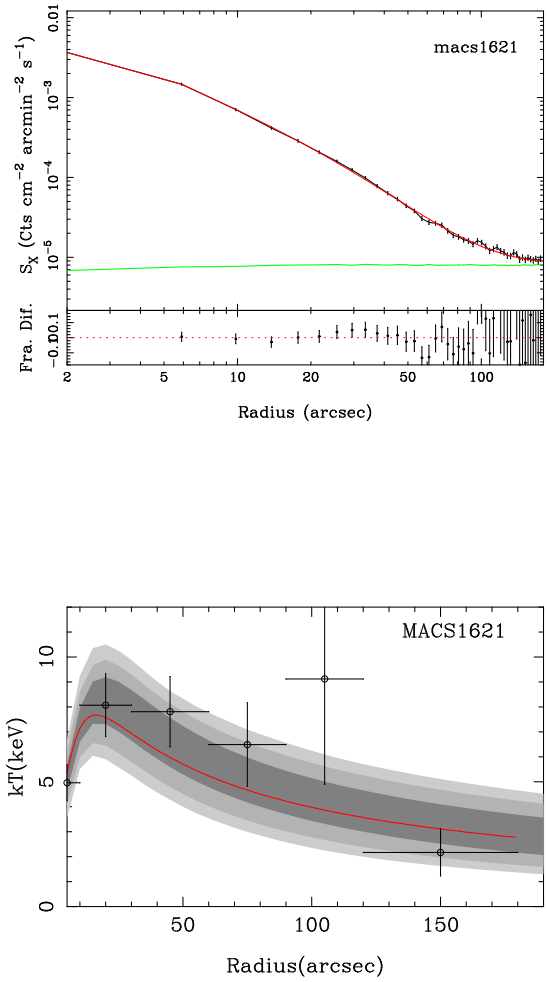

Figure 4.28: MACSJ1621.6+3810: *Top panel:* Surface brightness profiles where the black points are derived from the X-ray images, the red line shows the best fit model, and the green line is the background level determined from the blank sky observations. The residuals show the fractional difference between the model and the data. A 1% systematic uncertainty has been added in quadrature to the datapoints. The surface brightness profiles are plotted beyond the fitted region to show the agreement between the cluster emission and background. *Bottom panel:* Temperature profiles where the red line shows the best fit model and the dark, medium, and light grey regions show the 68%, 95.4%, and 99.7% confidence levels obtained from the model fits.

4.6.22 Abell 2204

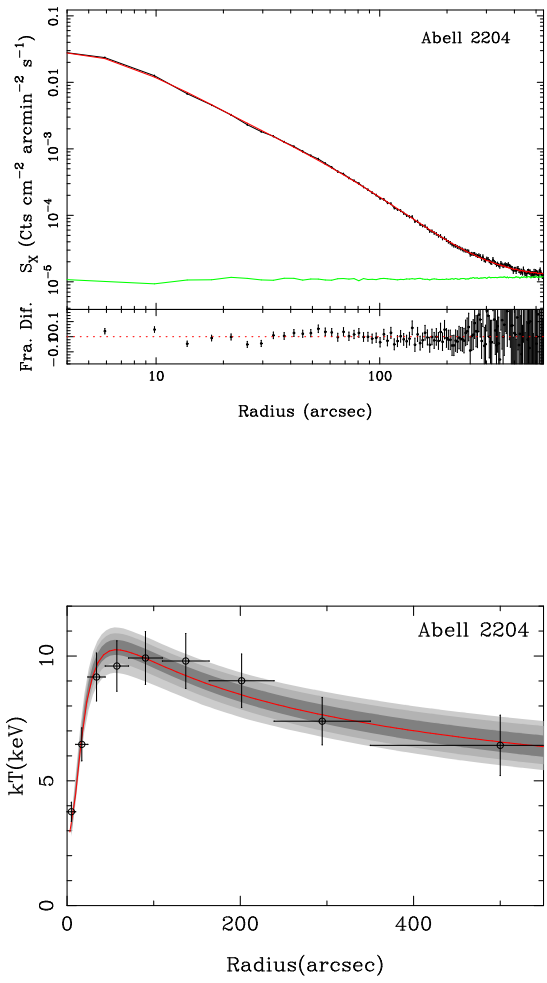

Figure 4.29: Abell 2204: *Top panel:* Surface brightness profiles where the black points are derived from the X-ray images, the red line shows the best fit model, and the green line is the background level determined from the blank sky observations. The residuals show the fractional difference between the model and the data. A 1% systematic uncertainty has been added in quadrature to the datapoints. The surface brightness profiles are plotted beyond the fitted region to show the agreement between the cluster emission and background. *Bottom panel:* Temperature profiles where the red line shows the best fit model and the dark, medium, and light grey regions show the 68%, 95.4%, and 99.7% confidence levels obtained from the model fits.

4.6.23 MACSJ1720.3+3536

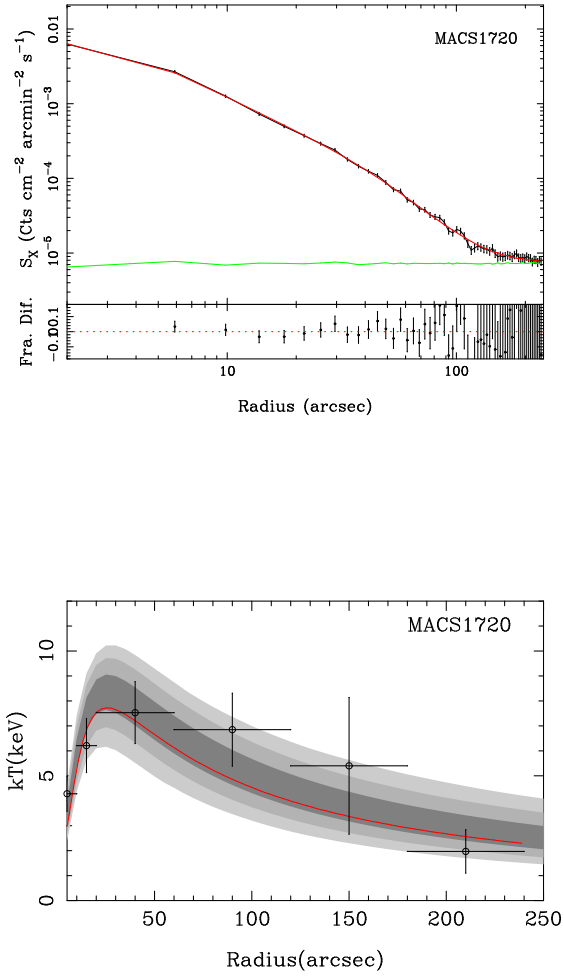

Figure 4.30: MACSJ1720.3+3536: *Top panel:* Surface brightness profiles where the black points are derived from the X-ray images, the red line shows the best fit model, and the green line is the background level determined from the blank sky observations. The residuals show the fractional difference between the model and the data. A 1% systematic uncertainty has been added in quadrature to the datapoints. The surface brightness profiles are plotted beyond the fitted region to show the agreement between the cluster emission and background. *Bottom panel:* Temperature profiles where the red line shows the best fit model and the dark, medium, and light grey regions show the 68%, 95.4%, and 99.7% confidence levels obtained from the model fits.

4.6.24 RXJ2129.6+0005

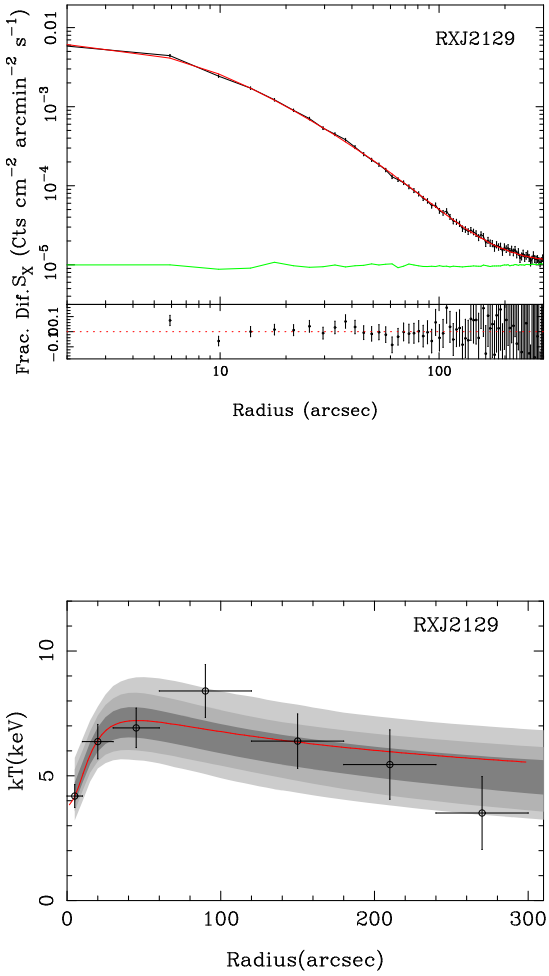

Figure 4.31: RXJ2129.6+0005: *Top panel:* Surface brightness profiles where the black points are derived from the X-ray images, the red line shows the best fit model, and the green line is the background level determined from the blank sky observations. The residuals show the fractional difference between the model and the data. A 1% systematic uncertainty has been added in quadrature to the datapoints. The surface brightness profiles are plotted beyond the fitted region to show the agreement between the cluster emission and background. *Bottom panel:* Temperature profiles where the red line shows the best fit model and the dark, medium, and light grey regions show the 68%, 95.4%, and 99.7% confidence levels obtained from the model fits.

4.6.25 Abell 2537

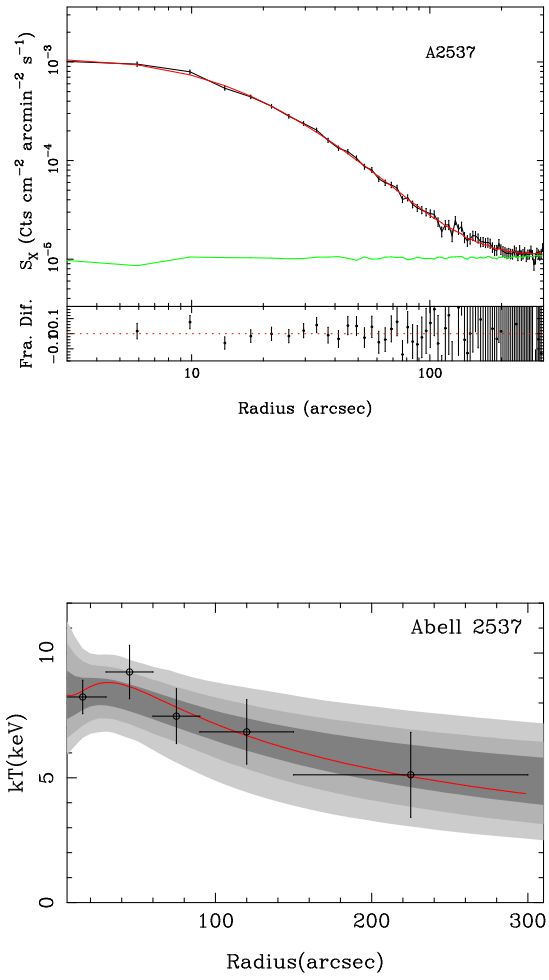

Figure 4.32: Abell 2537: *Top panel:* Surface brightness profiles where the black points are derived from the X-ray images, the red line shows the best fit model, and the green line is the background level determined from the blank sky observations. The residuals show the fractional difference between the model and the data. A 1% systematic uncertainty has been added in quadrature to the datapoints. The surface brightness profiles are plotted beyond the fitted region to show the agreement between the cluster emission and background. *Bottom panel:* Temperature profiles where the red line shows the best fit model and the dark, medium, and light grey regions show the 68%, 95.4%, and 99.7% confidence levels obtained from the model fits.

4.7 Radial Gas Mass Fraction

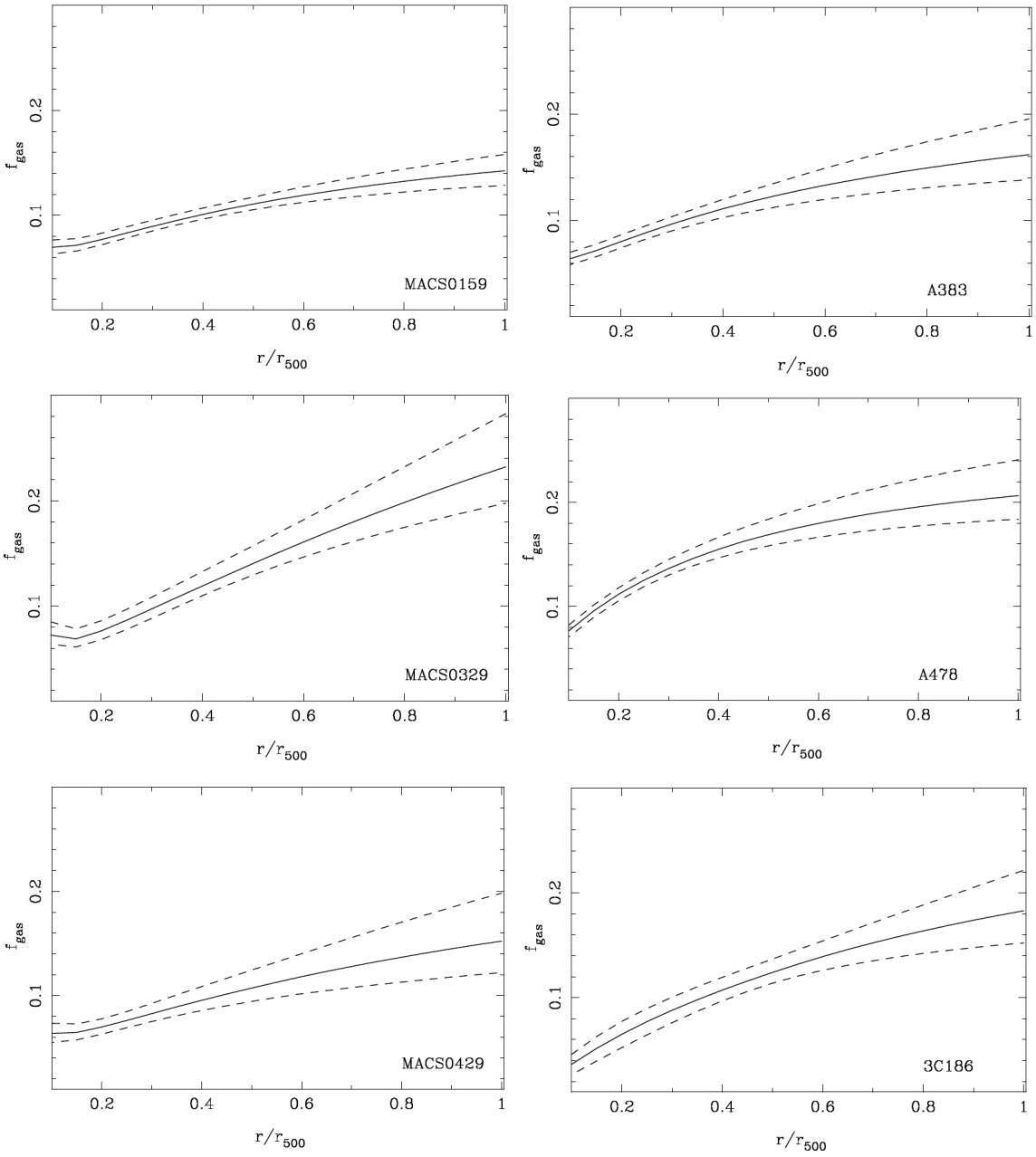

Figure 4.32: Radial gas mass fraction measured out to r_{500}.

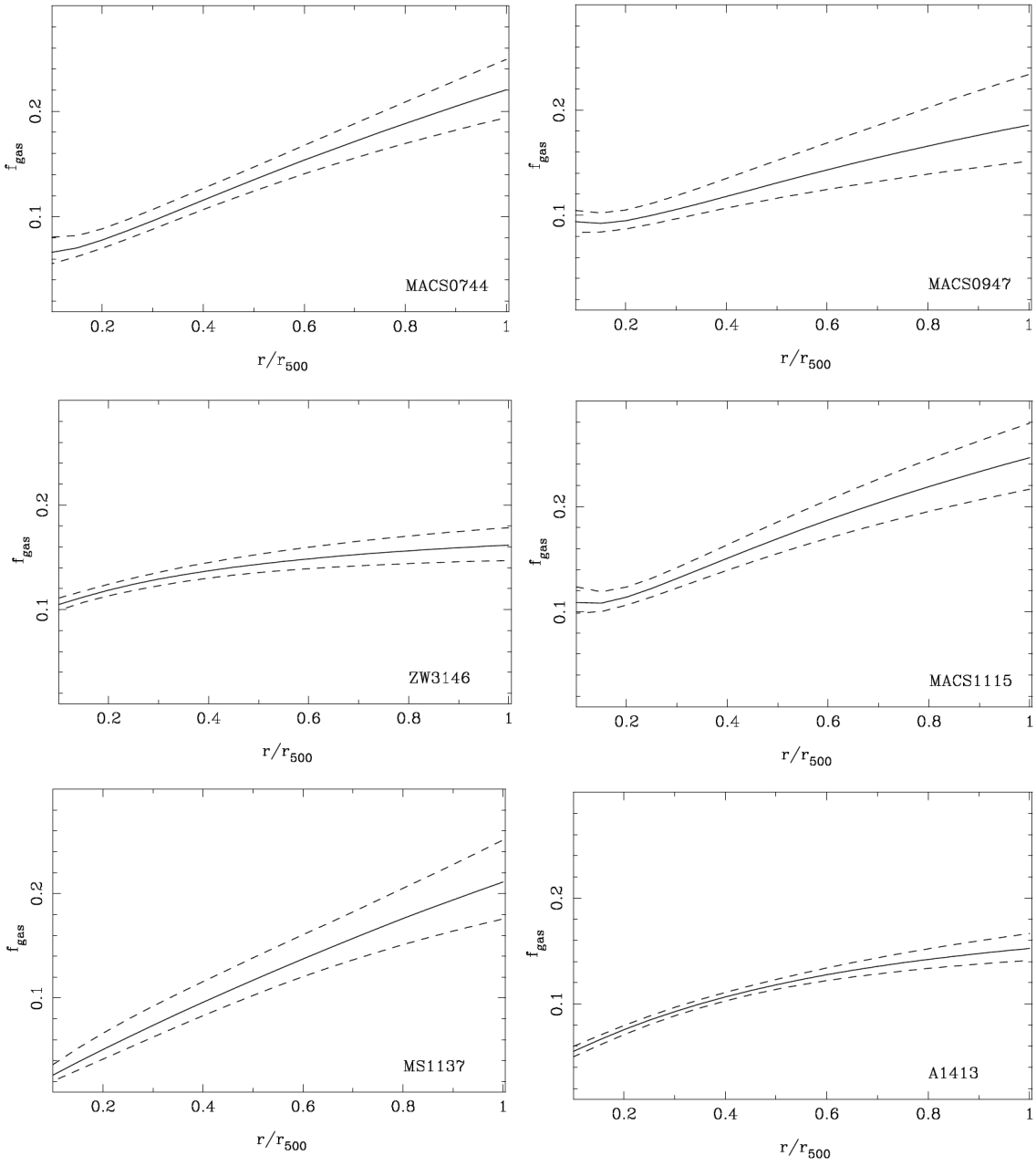

Figure 4.32: Continued.

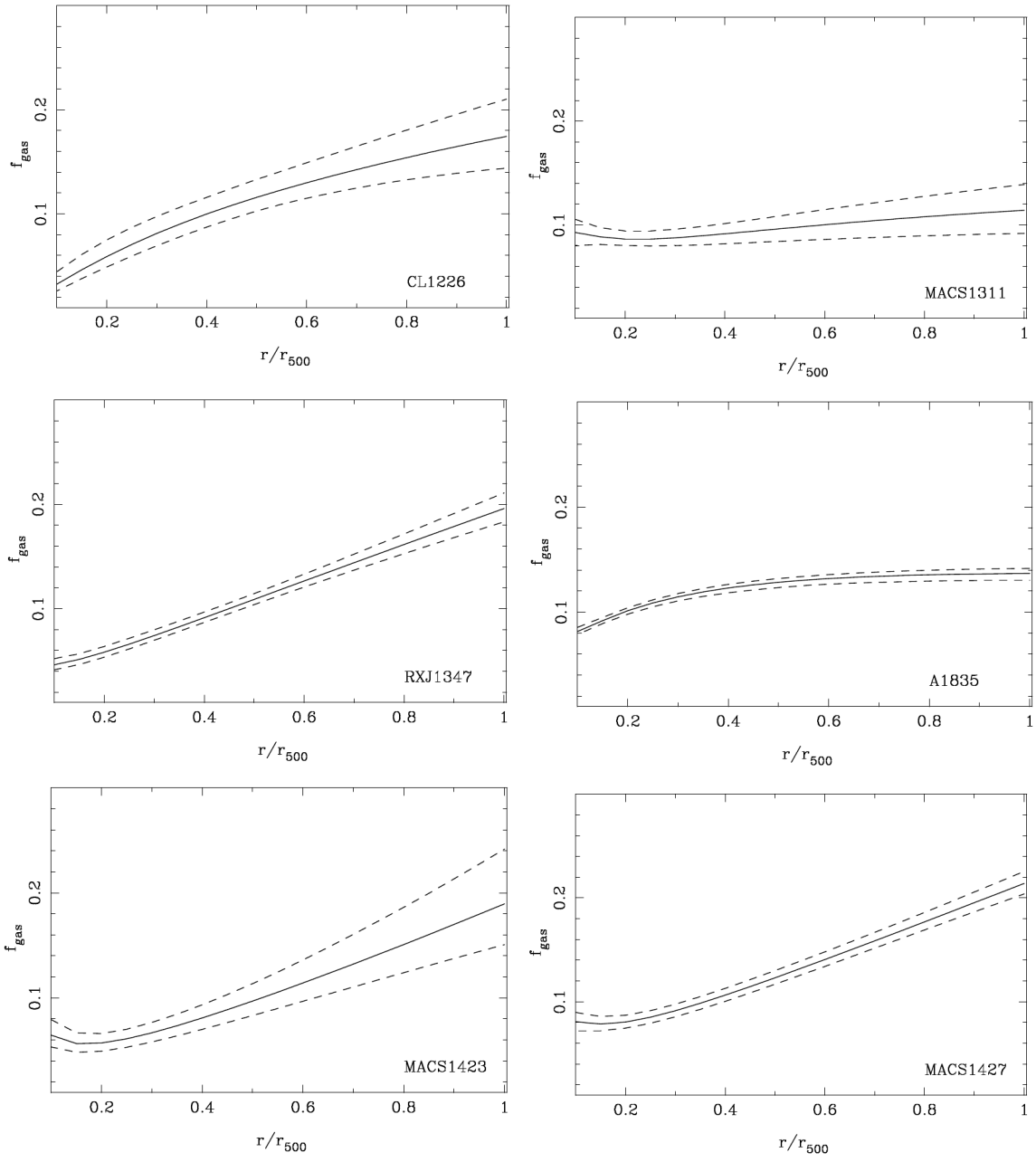

Figure 4.32: Continued.

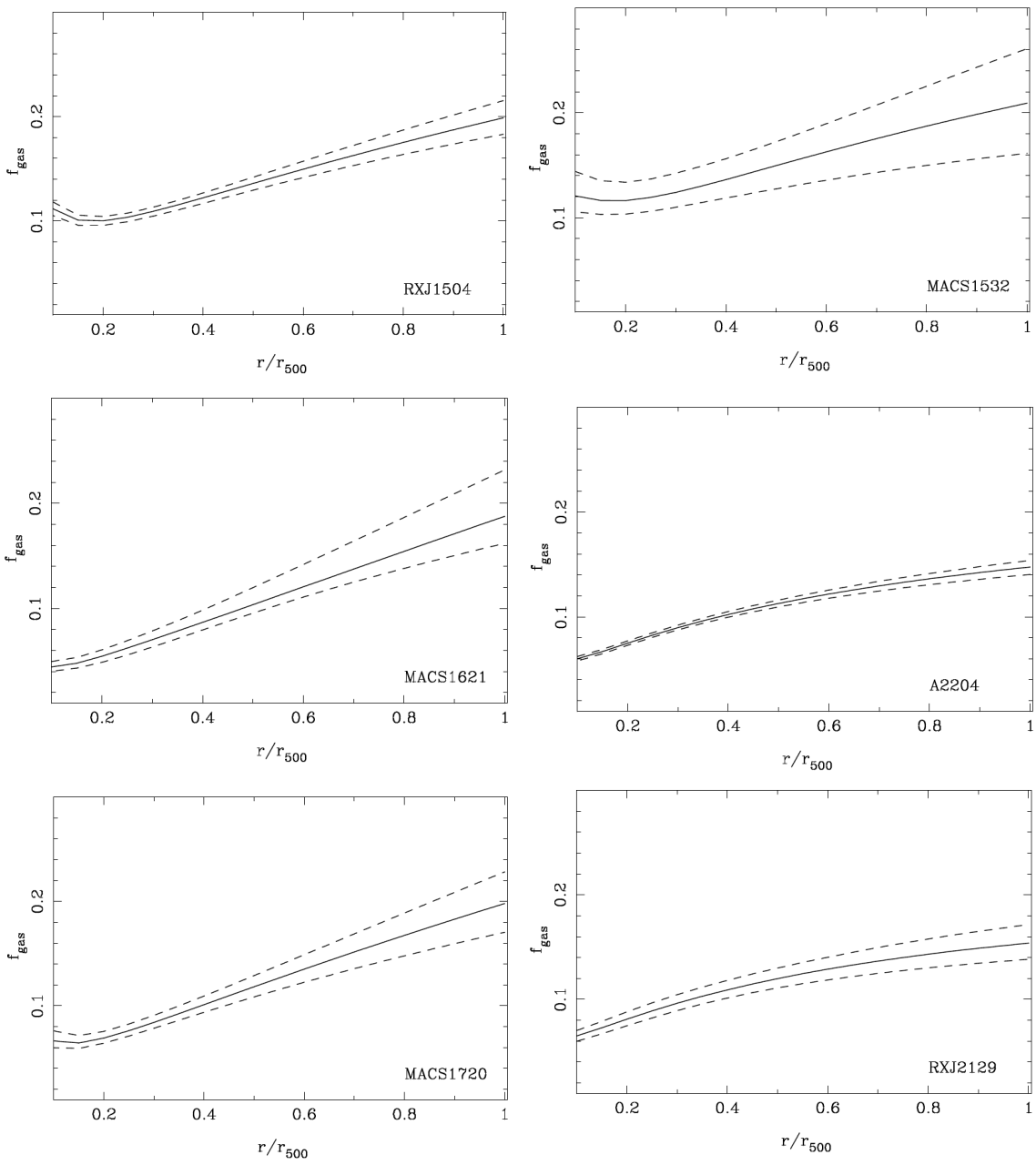

Figure 4.32: Continued.

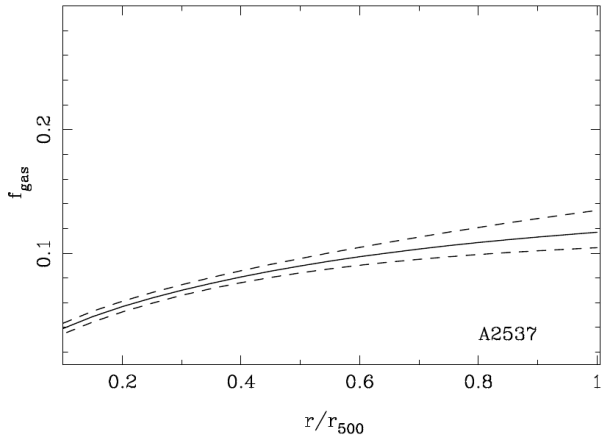

Figure 4.32: Continued.

CHAPTER 5

REDSHIFT EVOLUTION OF THE GAS MASS FRACTION IN GALAXY CLUSTERS

5.1 Redshift Evolution of the Gas Mass Fraction in Galaxy Clusters

Galaxy clusters can be used to constrain cosmological parameters since they trace the matter content of the universe. The hot ionized gas in galaxy clusters emits X-rays primarily through bremmstrahlung radiation. Therefore X-ray observations can be used to measure cluster masses. Some recent examples specifically relevant to the work presented here have used X-ray data alone (Allen et al., 2008; Mantz et al., 2008; Ettori et al., 2009; Vikhlinin et al., 2009; Mantz et al., 2010; Menanteau et al., 2010; Vanderlinde et al., 2010) or the combination of X-ray observations and SZE measurements (e.g., (LaRoque et al., 2006) to exploit the evolution of the gas fractions in clusters.

The gas mass fraction (the ratio of the gas to total mass in a cluster) is an important astrophysical quantity for probing cosmological questions. At large radii the gas mass fraction is expected to agree with the cosmic baryon fraction (Ω_b/Ω_M), as discussed and confirmed in Chapter 4.

The gas mass fraction as a function of redshift has never been determined observationally. The known behavior of $f_{gas}(z)$ is required for constraining cosmological

parameters, Ω_M and Ω_Λ using the Allen et al. (2008) method. Allen et al. (2008) assumes that $f_{gas}(z)$ is constant with redshift which has been suggested by non-radiative simulations of massive galaxy clusters (Eke et al., 1998; Crain et al., 2007). The Allen et al. (2008) procedure for constraining Ω_M and Ω_Λ is

- A dataset of 42 massive relaxed clusters ($T \geq 5$keV) are used to calculate $f_{gas}(z)$ with a ΛCDM cosmology for the assumed angular diameter distance.

- From Equation 3.9, $M_{gas} \propto D_A^3 n_e$. The X-ray observable (the surface brightness) can be used to find a relationship between the electron density and the angular diameter distance, $n_e \propto D_A^{-1/2}$. This relationship can be substituted into the gas mass proportionality, $M_{gas} \propto D_A^{5/2}$. The total mass is directly proportional to D_A. Therefore $f_{gas} \propto D_A^{3/2}$. This relationship can be used to rescale the dataset for a different cosmology by,

$$f_{gas} = C\left(\frac{\Omega_b}{\Omega_M}\right)\left[\frac{D_A^{\Lambda CDM}}{D_A}\right]^{3/2}, \tag{5.1}$$

  where C is a constant (see Allen et al. (2008) for details), D_A and $D_A^{\Lambda CDM}$ are the angular diameter distance for the test dataset and the original dataset (ΛCDM cosmology).

- A Markov Chain Monte Carlo technique is used to randomly draw a set of cosmological parameters, (Ω_M, Ω_Λ) and then rescale the original dataset according to Equation 5.1.

- Finally, the new dataset is determined if it is an acceptable fit to the assumed $f_{gas}(z)$ ($f_{gas}(z)$=constant for this case).

- For a non-flat universe with weak priors on $\Omega_b h^2$ and h, Allen et al. (2008) found $\Omega_M = 0.27 \pm 0.06$ and $\Omega_\Lambda = 0.86 \pm 0.19$.

A direct measurement of $f_{gas}(z)$ can be determined using a joint X-ray/SZE analysis which uses a self-consistent set of analytic models to describe the physical properties of galaxy clusters, as discussed in detail in Chapter 2. The joint analysis allows for the measurement of the gas mass fraction with the need to impose external priors (e.g., the Hubble expansion rate $H(z)$) on cosmological parameters. Such an analysis can directly probe the evolution of the cluster gas mass fraction with redshift, providing an important complement to X-ray only cosmological studies that rely on simulations for information about the gas mass fraction as a function of redshift. The evolution of the gas mass fraction with redshift may indicate the evolution in the formation of galaxy clusters, specifically the way in which the baryons evolve as function of time (Voit, 2005; Borgani & Kravtsov, 2009).

5.2 Constraints on the Evolution of the Gas Mass Fraction

Chandra observations of 25 relaxed massive galaxy clusters are used to measure the cluster gas mass fraction. The data were reduced using the procedure discussed in Chapter 4 Section 4.3 and fit with the Bulbul et al. (2010) density and temperature models using a Monte Carlo Markov chain technique. The model fits to the X-ray observables (surface brightness and temperature) can be found at the end of the Chapter 4.

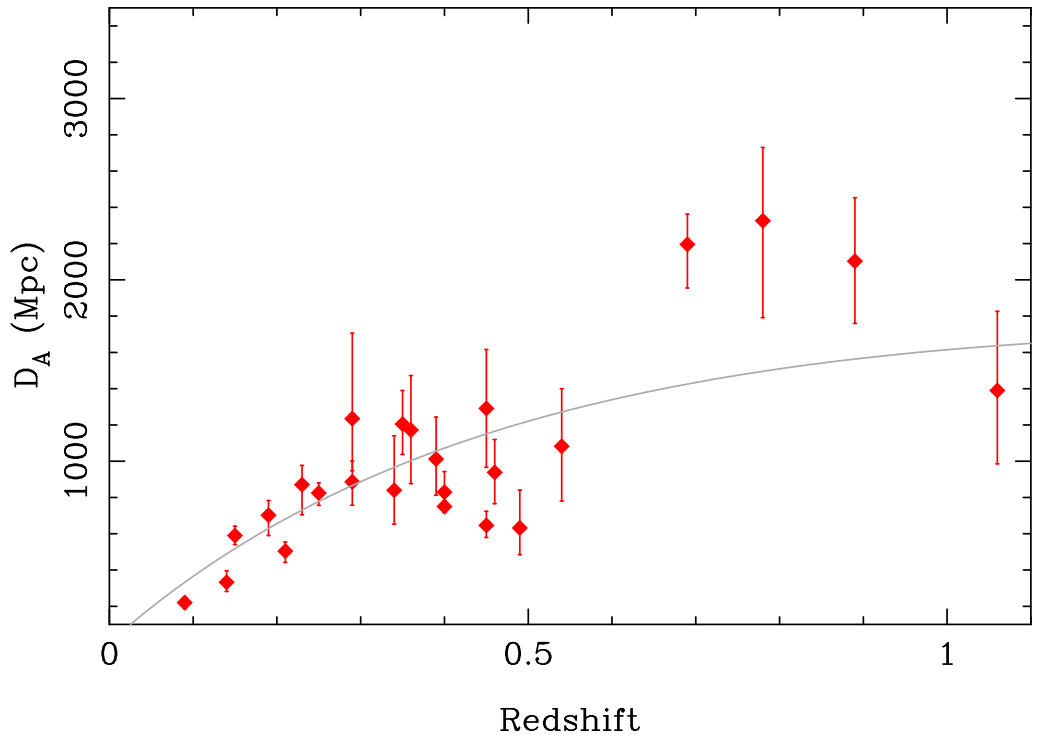

Figure 5.1: Angular diameter distance measured from joint X-ray/SZE analysis. The grey solid line show the angular diameter distance as a function of redshift assuming a ΛCDM cosmology.

5.2.1 Measurement of the Angular Diameter Distance

From a joint X-ray and SZE analysis, the angular diameter distance can be measured without making assumptions about the underlying cosmology (Hughes & Birkinshaw, 1998; Birkinshaw, 1999; Reese et al., 2002; Bonamente et al., 2006). In this analysis the parameters between the X-ray and SZE datasets are linked allowing D_A to vary. Figure 5.1 shows the measurements obtained for the sample. Table 5.2 contains the parameter fits to the joint analysis.

5.2.2 Cluster Masses

The angular diameter distance is required to measure the cluster masses without prior knowledge about the cosmology. The gas mass, $M_{\rm gas}$ is computed by integrating the gas density profile over the volume,

$$M_{\rm gas} = 4\pi\mu_e m_p \int n_e(r) r^2 dr = 4\pi\mu_e m_p {D_{\rm A}}^3 \int n_e(\theta)\theta^2 d\theta, \tag{5.2}$$

where μ is the mean molecular weight, m_p is the proton mass, and $dr = D_{\rm A} d\theta$. The total mass $M_{\rm tot}$ is computed, assuming hydrostatic equilibrium dominated by thermal pressure support:

$$M_{\rm tot}(r) = \frac{4\pi\rho_i r_s^3}{(\beta-2)} \left(\frac{1}{\beta-1} + \frac{1/(1-\beta) - r/r_s}{(1+r/r_s)^{\beta-1}} \right) \tau_{cool}(r), \tag{5.3}$$

where $\rho_i = \frac{T_0 k (n+1)(\beta-1)}{4\pi G \mu m_p r_s^2}$. Figure 5.2 shows the radial profiles of the gas mass, total mass, and gas mass fraction which are measured without assumptions about the cosmology for two selected clusters from Hasler et al. (2011). The radial plots for the entire sample can be found in Section 5.4.

5.2.3 Mass Measurements at r_Δ

Typically $f_{\rm gas}$ is measured out to a radius r_Δ, defined as the radius within which the average matter density of the cluster is Δ times the critical density of the universe at the cluster's redshift:

$$r_\Delta^3 = \frac{M_{\rm tot}(r_\Delta)}{\frac{4\pi}{3}\Delta\rho_c(z)}, \tag{5.4}$$

where $\rho_c(z) = \frac{3H_0^2 E^2(z)}{8\pi G}$ is the critical density of the universe, H_0 is the Hubble constant, and $E^2(z) = \Omega_{\rm M}(1+z)^3 + \Omega_\Lambda + \Omega_{\rm k}(1+z)^2$.

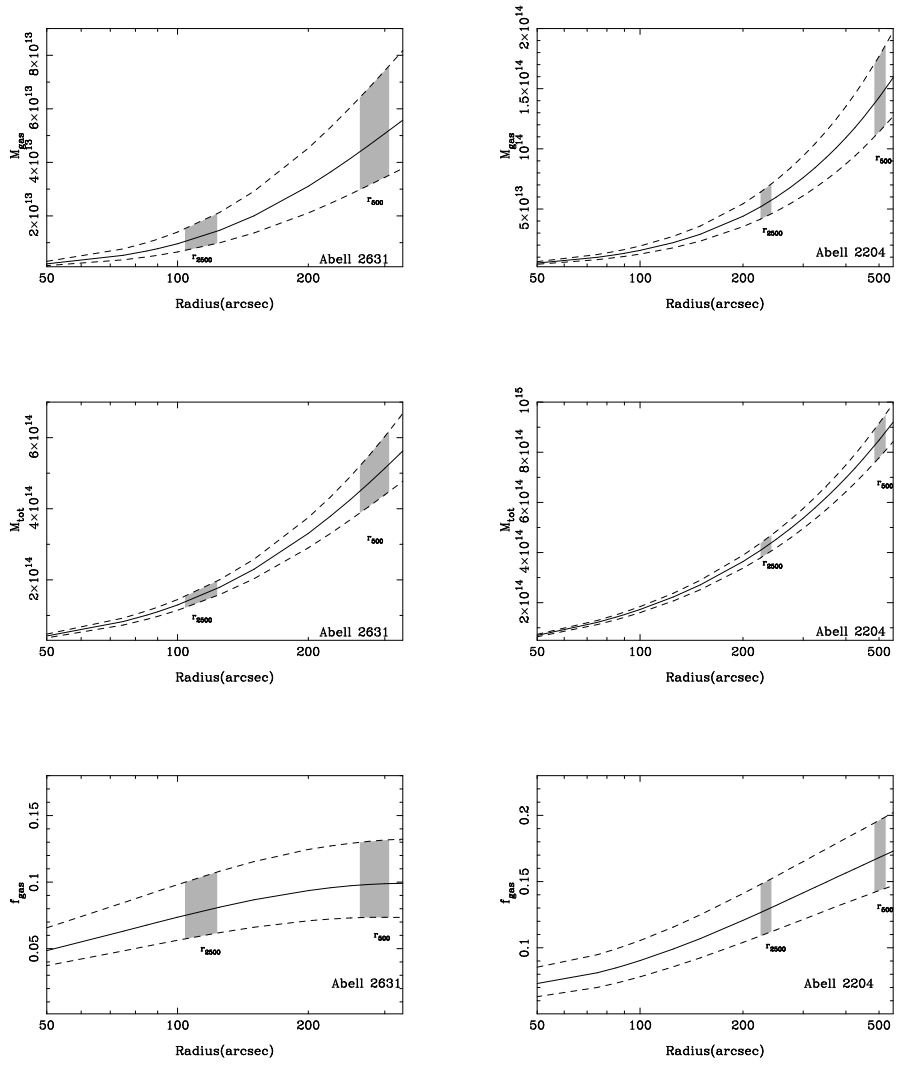

Figure 5.2: Top Panel: Gas mass profiles determined from the joint analysis of *Chandra*/SZA observations for Abell 2631 and Abell 2204. Middle Panel: Total mass profiles. Bottom Panel: Gas mass fraction profiles. The dashed lines are the 68% confidence level at each radius. Grey areas show the measurements at radii r_{2500} and r_{500}, obtained by marginalization over the cosmological parameters (from Hasler et al. 2011).

Although the joint X-ray and SZE analysis provides cosmology-independent constraints on D_A, and thus on the $f_{\rm gas}(r)$ profile, the radii r_Δ and associated gas mass fractions $f_{\rm gas}(r_\Delta)$ retains a cosmological dependence through the factor of $\rho_c(z)$ appearing in Equation 5.4. While this is an unavoidable consequence of using a cosmology-dependent radius, the impact on the results of the assumptions regarding the background cosmology, can be minimized by adopting a model for the cosmic expansion history and marginalizing over the corresponding space of cosmological parameters. This method of analysis was explained in Section 3.4.4 and is repeated here for completeness.

For each cluster and at each step in the Markov chain produced from the joint X-ray and SZE fit, the D_A value from the chain corresponds to a curve in the (H_0,$\Omega_{\rm M}$) plane described by

$$\begin{aligned} H_0 &= \frac{c \sinh |\Omega_k|^{1/2}}{D_A(1+z)|\Omega_k|^{1/2}} \int_0^z \frac{d\zeta}{E(\zeta)} \\ &= \frac{c}{D_A(1+z)} \int_0^z \frac{d\zeta}{[\Omega_M((1+\zeta)^3-1)-1]^{1/2}}, \end{aligned} \tag{5.5}$$

where the second line follows from the assumption of spatial flatness. A value of r_Δ is calculated by drawing a random value of $\Omega_{\rm M}$ from a uniform distribution on [0,1], calculating the corresponding H_0 from Equation 5.5, and then using the pair of values H_0 and $\Omega_{\rm M}$ to calculate r_Δ according to Equation 5.4. Finally, the corresponding $f_{\rm gas}(r_\Delta)$ is calculated from the other fit parameters of the chain. This approach has the advantage of using minimal prior information on the cosmological parameters. Table 5.3 shows the mass measurements for the entire sample.

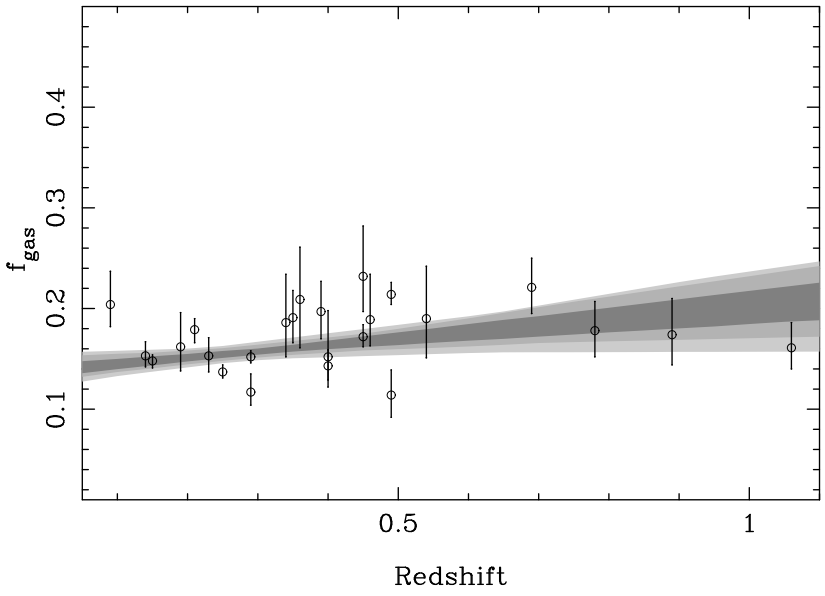

Figure 5.3: Evolution of the gas mass fraction determined from X-ray analysis of relaxed clusters at r_{500}.

5.3 Results

The gas mass fraction measured from the X-ray analysis was fit with a linear model to determine the evolution with redshift. Figure 5.3 shows a slight increase in the gas mass fraction with redshift although statistically consistent with flat at the 3σ level. The linear fit (y=a+bx) parameters are $a = 0.139 \pm 0.007$ and $b = 0.062 \pm 0.022$.

The gas mass fraction measurements from the joint analysis with a linear model to determine the evolution of the gas with redshift. The dark, medium, and light gray bands represent the 68%, 95%, and 99% confidence bands. Although no significant trend in the evolution of the gas mass fraction is observed and more data points are

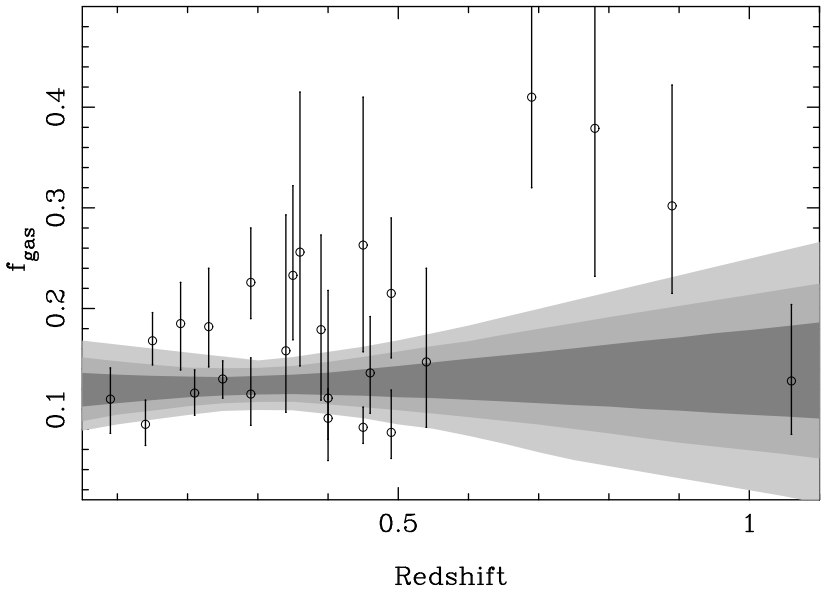

Figure 5.4: Evolution of the gas mass fraction determined from X-ray/SZE analysis of relaxed clusters at r_{500}.

needed at high redshift before any firm conclusions can be made. Measurements at r_{500} as a function of redshift can be found in Figure 5.4.

Given the limited statistical power of each data point in Figure 5.4, another approach to determine whether there is a difference in the measurement of f_{gas} as a function of redshift, is to divide the sample into 2 each bins, low redshift ($z < 0.39$) and high redshift clusters ($z \geq 0.39$). At r_{500} the low redshift clusters $< f_{gas} >= 0.136 \pm 0.010$ and for the high redshift clusters $< f_{gas} >= 0.119 \pm 0.016$. The gas mass fraction at low and high redshift agree within 1σ of each other. The median value of the low redshift clusters is 0.163 and the for the high redshift clusters 0.160. The difference between the weighted averages and the median are due to the scatter in the data.

5.4 Discussion

In this chapter, an analytic model discussed in Chapter 2 to describe the ICM density, temperature, and pressure is used to model Chandra and SZA observations for a sample of 25 relaxed clusters. Using the joint analysis method described in Chapter 3 the angular diameter distance can be directly measured which is an essential component to measuring the gas mass fraction without assumptions about the cosmology.

Figure 5.4 show no significant evidence of a gas mass fraction evolving with redshift. Although, this is consistent with the assumption made by Allen et al. (2008) more clusters at high redshift are required to confirm this.

This chapter has shown that measuring the gas mass fraction with minimal assumptions about the cosmology is possible. Better observations are needed to obtain tighter constraints on the measurements. Also more clusters at high redshift are required to determine the evolution of the gas mass fraction with redshift. Currently both are happening with other surveys.

Table 5.1: Cluster information about the SZA observations

Cluster Name	Pointing Center		On-src Time	Short Baslines			Long Baslines		
	RA (J2000)	*Dec* (J2000)	(hrs)	FWHM (arcsec)	P.A. (deg)	rms Noise (mJy)	FWHM (arcsec)	P.A. (deg)	rms Noise (mJy)
MACSJ0159.8-0849	01:59:49.4	-08:49:58.0	21.2	219×103	-41.9	0.65	23.5×20.4	-30.6	0.18
Abell 383	02:48:03.5	-03:31:45.0	25.0	159×128	-24.6	0.24	23×19.2	43.8	0.20
MACS0329.7-0212	03:29:41.7	-02:11:48.0	8.1	165×113	-40.9	0.37	22.6×18.5	48.8	0.28
Abell 478	04:13:25.2	+10:27:55.0	37.1	111×144	-25.9	0.22	21.2×17.7	84.9	0.13
MACSJ0429.6-0253	04:29:36.1	-02:53:08.0	22.1	169×116	-55.3	0.29	22.9×18.6	43.0	0.16
3C186	07:44:17.5	+37:53:17.2	13.7	137×118	-38.9	0.25	23.4×16	-72.1	0.22
MACSJ0744.9+3927	07:44:52.8	+39:27:36.7	12.7	113×105	-62.3	0.30	21.3×16.3	77.9	0.22
MACSJ0947.2+7623	09:47:13.1	+76:23:14.0	11.5	166×123	83.5	0.28	25.2×19.0	-87.0	0.23
Zwicky 3146	10:23:39.3	+04:11:13.4	6.8	163×111	-14.2	0.43	24.4×17.4	-50.9	0.36
MACSJ1115.8+0129	11:15:52.1	+01:29:52.0	26.2	152×116	-21.9	0.25	21.2×19.4	74.7	0.15
MS1137.5+6625	11:40:22.3	+66:08:16.1	19.6	114×96	-77.9	0.19	20×16.3	84.9	0.16
Abell 1413	11:55:18.0	+23:24:18.9	43.2	108×88	76.3	0.13	19.6×15.3	63.9	0.11
CLJ1226.9+3332	12:26:58.0	+33:32:45.0	16.0	119×108	32.9	0.21	21.3×16	86.3	0.17
MACSJ1311.0-0311	13:11:01.6	-03:10:40.0	4.6	102×86	56.9	0.31	23×16	44.7	0.42
RXJ1347.5-1145	13:47:30.7	-11:45:08.6	25.7	133×99	35.0	0.21	23.7×17.0	29.4	0.22
Abell 1835	14:01:02.0	+02:52:41.7	9.0	152×117	0.2	0.29	23.5×17.4	60.6	0.29
MACSJ1423.8+2404	14:23:47.9	+24:04:43.0	6.5	113×80	82.2	0.32	19.5×14.3	53.0	0.27
MACSJ1427.3+4408	14:27:16.2	+44:07:31.0	17.4	128×109	-57.0	0.20	21.7×16.1	77.7	0.17
RXJ1504.1-0248	15:04:07.9	-01:48:16.0	9.2	161×134	-57.2	0.38	26.8×16.9	45.2	0.23
MACSJ1532.9+3021	15:32:53.9	+30:20:59.0	14.6	134×80	61.4	0.20	22.5×15.1	53.0	0.18
MACSJ1621.6+3810	16:21:24.8	+38:10:09.0	44.0	114×85	76.9	0.13	20.1×15.1	67.8	0.12
Abell 2204	16:32:46.88	+05:34:32.401	19.6	21.1×18.4	-82.1	0.22	21.2×18.4	-82.1	0.22
MACSJ1720.3+3536	17:20:16.8	+35:36:27.0	36.2	122×108	-54.1	0.22	21.6×16.2	88.4	0.10
RXJ2129.6+0005	21:29:39.9	+00:05:19.8	24.5	167×113	-28.7	0.21	21.5×19.4	-71.2	0.18
Abell 2537	23:08:22.1	-02:11:29.0	24.8	172×114	-34.4	0.18	21.3×20.2	-24.9	0.19

Table 5.2: Parameter Fits from Joint Chandra and SZA Data.

Cluster Name	$n_{eo}(10^{-2})$ (cm^{-3})	r_s $(arcsec)$	n	β	T_o (keV)	r_{cool} $(arcsec)$	α_{cool}	p_{cool}	D_A (Mpc)
MACSJ0159.8-0849	$2.87\pm^{0.30}_{0.23}$	$24.8\pm^{2.5}_{3.3}$	$5.86\pm^{2.04}_{1.00}$	$1.57\pm^{0.13}_{0.17}$	$15.1\pm^{1.2}_{1.4}$	$13.1\pm^{0.8}_{0.8}$	$0.23\pm^{0.03}_{0.02}$	2.0	$829.4\pm^{113.6}_{111.6}$
Abell 383	$3.22\pm^{0.43}_{0.39}$	$19.7\pm^{4.7}_{3.1}$	$6.02\pm^{1.94}_{1.45}$	$1.49\pm^{0.18}_{0.14}$	$7.2\pm^{0.9}_{0.8}$	$14.1\pm^{1.4}_{1.3}$	$0.30\pm^{0.03}_{0.04}$	2.0	$702.1\pm^{81.0}_{112.0}$
MACS0329.7-0212	$3.39\pm^{0.92}_{0.74}$	$16.1\pm^{8.4}_{6.5}$	$3.78\pm^{1.00}_{0.86}$	$1.83\pm^{0.51}_{0.26}$	$11.7\pm^{2.1}_{2.1}$	$11.5\pm^{0.6}_{0.5}$	$0.34\pm^{0.01}_{0.01}$	$4.4\pm^{1.8}_{8.1}$	$1291.0\pm^{324.8}_{324.9}$
Abell 478	$5.53\pm^{0.55}_{0.38}$	$47.8\pm^{4.1}_{3.0}$	$8.24\pm^{1.20}_{1.16}$	$1.36\pm^{0.06}_{0.05}$	$8.5\pm^{0.4}_{0.6}$	$16.5\pm^{1.2}_{1.2}$	$0.27\pm^{0.02}_{0.03}$	2.0	$220.5\pm^{30.9}_{34.4}$
MACSJ0429.6-0253	$2.41\pm^{0.59}_{0.36}$	$57.7\pm^{17.9}_{20.4}$	$2.28\pm^{0.47}_{0.24}$	$4.20\pm^{0.94}_{1.22}$	$18.8\pm^{2.0}_{1.9}$	$13.4\pm^{1.3}_{1.1}$	$0.13\pm^{0.03}_{0.02}$	2.0	$750.0\pm^{31.5}_{26.9}$
3C186	$5.01\pm^{0.16}_{0.10}$	$9.7\pm^{3.4}_{2.8}$	$6.11\pm^{2.16}_{1.88}$	$1.53\pm^{0.26}_{0.14}$	$8.6\pm^{1.6}_{1.1}$	-	-	-	$1390.0\pm^{436.5}_{505.6}$
MACSJ0744.9+3927	$2.36\pm^{0.47}_{0.51}$	$13.8\pm^{7.2}_{3.7}$	$3.37\pm^{1.26}_{0.69}$	$1.86\pm^{0.39}_{0.28}$	$17.2\pm^{2.6}_{2.5}$	$11.4\pm^{1.4}_{1.4}$	$0.37\pm^{0.07}_{0.08}$	2.0	$2196.0\pm^{167.0}_{240.6}$
MACSJ0947.2+7623	$4.57\pm^{1.22}_{0.90}$	$14.7\pm^{5.4}_{4.4}$	$2.96\pm^{0.60}_{0.59}$	$2.06\pm^{0.46}_{0.27}$	$21.7\pm^{3.6}_{3.1}$	$23.2\pm^{2.0}_{1.9}$	$0.25\pm^{0.05}_{0.05}$	2.0	$840.2\pm^{299.7}_{187.1}$
Zwicky 3146	$2.89\pm^{0.25}_{0.31}$	$21.5\pm^{1.5}_{1.6}$	$5.60\pm^{0.71}_{0.74}$	$1.56\pm^{0.85}_{0.71}$	$15.2\pm^{0.7}_{0.9}$	$19.7\pm^{3.0}_{2.1}$	$0.10\pm^{0.02}_{0.02}$	$0.98\pm^{0.04}_{0.04}$	$1087.0\pm^{105.9}_{110.3}$
MACSJ1115.8+0129	$2.10\pm^{0.33}_{0.25}$	$32.4\pm^{7.4}_{6.8}$	$3.67\pm^{0.78}_{0.44}$	$2.06\pm^{0.26}_{0.25}$	$15.8\pm^{1.2}_{1.4}$	$17.5\pm^{1.3}_{1.4}$	$0.27\pm^{0.01}_{0.01}$	2.0	$1205.0\pm^{184.8}_{167.7}$
MS1137.5+6625	$2.05\pm^{0.31}_{0.22}$	$38.8\pm^{17.3}_{11.7}$	$2.42\pm^{0.67}_{0.33}$	$4.23\pm^{1.38}_{1.35}$	$11.8\pm^{2.3}_{1.7}$	-	-	-	$2326.0\pm^{404.0}_{534.6}$
Abell 1413	$1.94\pm^{0.20}_{0.17}$	$70.4\pm^{8.1}_{6.6}$	$5.20\pm^{1.31}_{0.82}$	$1.72\pm^{0.18}_{0.18}$	$10.5\pm^{0.8}_{0.8}$	$29.1\pm^{2.4}_{2.5}$	$0.48\pm^{0.03}_{0.02}$	2.0	$332.7\pm^{62.4}_{51.0}$
CLJ1226.9+3332	$3.17\pm^{0.36}_{0.30}$	$37.4\pm^{5.9}_{8.0}$	$2.66\pm^{0.55}_{0.71}$	$3.61\pm^{0.69}_{0.71}$	$20.2\pm^{3.0}_{3.6}$	-	-	-	$2103.0\pm^{350.3}_{343.0}$
MACSJ1311.0-0311	$1.35\pm^{0.26}_{0.24}$	$36.1\pm^{14.6}_{12.0}$	$4.46\pm^{1.82}_{1.31}$	$2.12\pm^{0.84}_{0.45}$	$12.5\pm^{1.9}_{1.9}$	$23.8\pm^{1.9}_{1.9}$	$0.34\pm^{0.07}_{0.05}$	2.0	$1910.0\pm^{332.6}_{347.1}$
RXJ1347.5-1145	$5.67\pm^{0.79}_{0.84}$	$32.6\pm^{8.0}_{6.3}$	$2.21\pm^{0.12}_{0.11}$	$3.32\pm^{0.56}_{0.32}$	$63.0\pm^{6.3}_{6.7}$	$15.3\pm^{1.2}_{1.2}$	$0.12\pm^{0.02}_{0.02}$	$1.38\pm^{0.88}_{0.95}$	$646.3\pm^{77.9}_{66.5}$
Abell 1835	$5.29\pm^{0.23}_{0.21}$	$16.7\pm^{0.9}_{0.8}$	$63.4\pm^{7.7}_{10.4}$	$1.04\pm^{0.08}_{0.04}$	$10.7\pm^{0.4}_{0.4}$	$17.2\pm^{0.4}_{0.3}$	$0.48\pm^{0.02}_{0.02}$	$4.48\pm^{0.41}_{0.28}$	$825.2\pm^{55.5}_{68.9}$
MACSJ1423.8+2404	$1.81\pm^{0.30}_{0.29}$	$67.6\pm^{19.1}_{28.1}$	$1.88\pm^{0.26}_{0.18}$	$5.80\pm^{1.39}_{1.97}$	$29.4\pm^{4.6}_{4.2}$	$15.4\pm^{11.8}_{11.5}$	$0.09\pm^{0.02}_{0.02}$	2.0	$1082.0\pm^{318}_{301}$
MACSJ1427.3+4408	$3.55\pm^{0.52}_{0.61}$	$5.7\pm^{1.5}_{1.0}$	$3.79\pm^{0.73}_{0.49}$	$1.47\pm^{0.08}_{0.10}$	$17.4\pm^{1.8}_{2.1}$	$18.8\pm^{1.4}_{1.4}$	$0.23\pm^{0.04}_{0.03}$	2.0	$632.2\pm^{208.4}_{147.5}$
RXJ1504.1-0248	$4.39\pm^{0.47}_{0.38}$	$28.0\pm^{2.1}_{2.7}$	$3.35\pm^{0.37}_{0.24}$	$2.02\pm^{0.10}_{0.14}$	$21.3\pm^{1.0}_{1.5}$	$34.4\pm^{1.0}_{0.9}$	$0.21\pm^{0.02}_{0.02}$	2.0	$504.4\pm^{50.1}_{62.5}$
MACSJ1532.9+3021	$3.57\pm^{1.08}_{0.86}$	$15.6\pm^{7.1}_{5.1}$	$3.99\pm^{1.44}_{1.03}$	$1.77\pm^{0.38}_{0.26}$	$14.1\pm^{2.8}_{2.6}$	$25.3\pm^{3.7}_{3.1}$	$0.30\pm^{0.09}_{0.06}$	2.0	$1172.0\pm^{299.9}_{295.0}$
MACSJ1621.6+3810	$1.86\pm^{0.31}_{0.28}$	$47.3\pm^{29.7}_{16.3}$	$2.05\pm^{0.34}_{0.23}$	$4.05\pm^{2.11}_{1.13}$	$19.8\pm^{1.4}_{1.9}$	$11.7\pm^{0.8}_{0.8}$	$0.17\pm^{0.02}_{0.02}$	2.0	$938.1\pm^{181.5}_{172.2}$
Abell 2204	$4.08\pm^{0.23}_{0.17}$	$20.9\pm^{1.3}_{1.2}$	$7.82\pm^{1.52}_{0.89}$	$1.32\pm^{0.06}_{0.05}$	$14.3\pm^{0.7}_{0.9}$	$19.6\pm^{0.5}_{0.6}$	$0.17\pm^{0.01}_{0.01}$	2.0	$590.1\pm^{51.9}_{49.6}$
MACSJ1720.3+3536	$1.49\pm^{0.19}_{0.16}$	$128.1\pm^{26.4}_{40.2}$	$2.48\pm^{0.24}_{0.23}$	$5.41\pm^{1.09}_{0.83}$	$16.1\pm^{1.3}_{1.2}$	$13.7\pm^{1.1}_{1.1}$	$0.11\pm^{0.01}_{0.01}$	2.0	$1012.0\pm^{231.7}_{199.6}$
RXJ2129.6+0005	$2.28\pm^{0.27}_{0.34}$	$24.5\pm^{7.4}_{4.1}$	$5.76\pm^{1.8}_{1.5}$	$1.51\pm^{0.25}_{0.14}$	$11.2\pm^{2.1}_{1.3}$	$19.4\pm^{1.8}_{1.8}$	$0.33\pm^{0.05}_{0.05}$	2.0	$870.7\pm^{106.0}_{166.1}$
Abell 2537	$1.55\pm^{0.38}_{0.26}$	$29.0\pm^{12.5}_{6.3}$	$5.57\pm^{3.00}_{1.36}$	$1.59\pm^{0.27}_{0.25}$	$12.1\pm^{1.6}_{1.2}$	$28.7\pm^{7.5}_{6.4}$	$0.69\pm^{0.11}_{0.11}$	2.0	$886.0\pm^{114.5}_{128.6}$

Table 5.3: Cluster Masses from Joint Chandra and SZA Data.

Cluster	$r_{2500}(arcsec)$	$M_{gas}(r_{2500})10^{13}M_{\odot}$	$M_{tot}(2500)10^{14}M_{\odot}$	$f_{gas}(r_{2500})$	$r_{500}(arcsec)$	$M_{gas}(r_{500})M_{\odot}$	$M_{tot}(500)M_{\odot}$	$f_{gas}(r_{500})$
MACSJ0159.8-0849	$98.3\pm^{10.2}_{6.8}$	$1.89\pm^{0.70}_{0.54}$	$2.65\pm^{0.37}_{0.32}$	$0.071\pm^{0.019}_{0.016}$	$213.8\pm^{20.1}_{15.8}$	$5.07\pm^{1.78}_{1.52}$	$5.46\pm^{0.83}_{0.74}$	$0.091\pm^{0.029}_{0.021}$
Abell 383	$131.7\pm^{7.7}_{7.1}$	$1.89\pm^{0.60}_{0.65}$	$1.33\pm^{0.23}_{0.22}$	$0.140\pm^{0.027}_{0.034}$	$279.6\pm^{19.7}_{18.7}$	$4.81\pm^{1.60}_{1.70}$	$2.56\pm^{0.61}_{0.54}$	$0.185\pm^{0.041}_{0.046}$
MACS0329.7-0212	$68.2\pm^{7.4}_{6.0}$	$2.75\pm^{1.83}_{1.37}$	$1.63\pm^{0.39}_{0.34}$	$0.163\pm^{0.088}_{0.063}$	$138.9\pm^{14.2}_{12.5}$	$7.43\pm^{5.25}_{3.73}$	$2.76\pm^{0.65}_{0.64}$	$0.263\pm^{0.147}_{0.106}$
Abell 478	$311.5\pm^{14.3}_{12.5}$	$1.21\pm^{0.43}_{0.38}$	$1.38\pm^{0.14}_{0.13}$	$0.089\pm^{0.024}_{0.025}$	$680.7\pm^{36.6}_{30.4}$	$3.10\pm^{1.15}_{0.98}$	$2.90\pm^{0.30}_{0.30}$	$0.110\pm^{0.031}_{0.034}$
MACSJ0429.6-0253	$83.6\pm^{9.0}_{7.4}$	$0.91\pm^{1.15}_{0.59}$	$1.42\pm^{0.36}_{0.35}$	$0.064\pm^{0.057}_{0.035}$	$155.4\pm^{18.5}_{15.9}$	$2.05\pm^{2.62}_{1.33}$	$1.84\pm^{0.48}_{0.47}$	$0.111\pm^{0.107}_{0.062}$
3C186	$32.4\pm^{6.6}_{3.2}$	$0.74\pm^{0.76}_{0.42}$	$0.84\pm^{0.32}_{0.24}$	$0.088\pm^{0.049}_{0.037}$	$71.6\pm^{13.6}_{7.5}$	$2.35\pm^{2.35}_{1.35}$	$1.80\pm^{0.71}_{0.57}$	$0.128\pm^{0.076}_{0.053}$
MACSJ0744.9+3927	$55.7\pm^{8.0}_{4.7}$	$7.62\pm^{2.15}_{1.81}$	$3.14\pm^{0.51}_{0.41}$	$0.244\pm^{0.047}_{0.049}$	$114.8\pm^{15.7}_{10.2}$	$2.29\pm^{0.58}_{0.54}$	$5.57\pm^{0.95}_{0.84}$	$0.410\pm^{0.097}_{0.090}$
MACSJ0947.2+7623	$97.3\pm^{8.7}_{7.8}$	$2.09\pm^{2.14}_{0.94}$	$2.00\pm^{0.42}_{0.35}$	$0.104\pm^{0.081}_{0.039}$	$187.0\pm^{17.9}_{17.1}$	$4.65\pm^{4.73}_{2.10}$	$2.93\pm^{0.62}_{0.56}$	$0.158\pm^{0.135}_{0.061}$
Zwicky 3146	$128.2\pm^{9.6}_{7.8}$	$7.38\pm^{1.86}_{1.81}$	$3.71\pm^{0.53}_{0.48}$	$0.196\pm^{0.038}_{0.030}$	$270.0\pm^{20.5}_{19.0}$	$17.07\pm^{4.47}_{4.14}$	$7.41\pm^{1.28}_{1.16}$	$0.226\pm^{0.054}_{0.036}$
MACSJ1115.8+0129	$101.9\pm^{8.8}_{6.7}$	$5.30\pm^{1.95}_{1.57}$	$3.27\pm^{0.37}_{0.32}$	$0.161\pm^{0.051}_{0.041}$	$207.6\pm^{18.0}_{14.9}$	$13.06\pm^{5.11}_{3.83}$	$5.58\pm^{0.72}_{0.61}$	$0.233\pm^{0.089}_{0.064}$
MS1137.5+6625	$41.2\pm^{6.2}_{3.7}$	$3.49\pm^{1.78}_{1.63}$	$1.65\pm^{0.40}_{0.36}$	$0.207\pm^{0.073}_{0.074}$	$79.6\pm^{10.9}_{7.8}$	$9.19\pm^{4.58}_{4.33}$	$2.35\pm^{0.68}_{0.53}$	$0.379\pm^{0.153}_{0.147}$
Abell 1413	$208.2\pm^{8.8}_{8.0}$	$0.95\pm^{0.50}_{0.31}$	$1.54\pm^{0.26}_{0.21}$	$0.062\pm^{0.019}_{0.014}$	$450.0\pm^{22.3}_{21.5}$	$2.59\pm^{1.45}_{0.84}$	$3.08\pm^{0.76}_{0.47}$	$0.085\pm^{0.024}_{0.021}$
CLJ1226.9+3332	$51.7\pm^{7.5}_{4.1}$	$6.02\pm^{2.87}_{2.05}$	$3.28\pm^{0.50}_{0.46}$	$0.183\pm^{0.067}_{0.052}$	$96.7\pm^{13.3}_{8.1}$	$13.98\pm^{9.61}_{4.97}$	$4.53\pm^{0.87}_{0.71}$	$0.302\pm^{0.120}_{0.087}$
MACSJ1311.0-0311	$73.4\pm^{8.5}_{5.7}$	$6.24\pm^{3.11}_{2.38}$	$3.40\pm^{0.75}_{0.65}$	$0.183\pm^{0.061}_{0.053}$	$154.6\pm^{17.4}_{14.4}$	$14.20\pm^{7.18}_{5.52}$	$6.66\pm^{1.79}_{1.68}$	$0.215\pm^{0.075}_{0.064}$
RXJ1347.5-1145	$114.5\pm^{9.5}_{6.3}$	$1.84\pm^{0.56}_{0.42}$	$3.80\pm^{0.28}_{0.26}$	$0.049\pm^{0.011}_{0.009}$	$206.1\pm^{16.5}_{11.5}$	$3.73\pm^{1.16}_{0.84}$	$4.55\pm^{0.41}_{0.39}$	$0.082\pm^{0.020}_{0.016}$
Abell 1835	$153.2\pm^{10.8}_{8.1}$	$5.52\pm^{1.06}_{1.06}$	$4.41\pm^{0.44}_{0.41}$	$0.124\pm^{0.017}_{0.018}$	$361.6\pm^{24.9}_{18.5}$	$15.14\pm^{2.84}_{2.88}$	$11.58\pm^{1.09}_{1.00}$	$0.130\pm^{0.018}_{0.019}$
MACSJ1423.8+2404	$77.7\pm^{8.4}_{6.8}$	$1.79\pm^{1.48}_{0.96}$	$2.24\pm^{0.57}_{0.50}$	$0.079\pm^{0.046}_{0.034}$	$139.7\pm^{15.6}_{12.8}$	$3.98\pm^{3.40}_{2.16}$	$2.66\pm^{0.72}_{0.63}$	$0.147\pm^{0.093}_{0.065}$
MACSJ1427.3+4408	$69.0\pm^{7.5}_{4.5}$	$0.43\pm^{0.42}_{0.21}$	$9.63\pm^{2.62}_{2.15}$	$0.045\pm^{0.025}_{0.015}$	$143.0\pm^{14.9}_{9.5}$	$1.36\pm^{1.36}_{0.66}$	$1.78\pm^{0.52}_{0.44}$	$0.077\pm^{0.042}_{0.026}$
RXJ1504.1-0248	$161.0\pm^{8.3}_{7.0}$	$1.93\pm^{0.53}_{0.53}$	$2.31\pm^{0.28}_{0.26}$	$0.083\pm^{0.014}_{0.016}$	$315.4\pm^{16.8}_{15.2}$	$4.19\pm^{1.16}_{1.14}$	$3.53\pm^{0.51}_{0.42}$	$0.116\pm^{0.023}_{0.022}$
MACSJ1532.9+3021	$93.8\pm^{8.9}_{7.7}$	$4.39\pm^{3.04}_{2.09}$	$2.30\pm^{0.37}_{0.36}$	$0.190\pm^{0.108}_{0.080}$	$188.9\pm^{20.4}_{17.0}$	$10.13\pm^{0.72}_{0.49}$	$3.90\pm^{0.77}_{0.68}$	$0.256\pm^{0.159}_{0.113}$
MACSJ1621.6+3810	$72.4\pm^{6.5}_{4.7}$	$1.09\pm^{0.61}_{0.43}$	$1.50\pm^{0.28}_{0.27}$	$0.073\pm^{0.026}_{0.021}$	$134.4\pm^{12.2}_{10.0}$	$2.66\pm^{1.48}_{1.06}$	$1.90\pm^{0.48}_{0.36}$	$0.136\pm^{0.056}_{0.040}$
Abell 2204	$233.0\pm^{9.1}_{8.0}$	$5.45\pm^{1.22}_{1.07}$	$4.24\pm^{0.32}_{0.32}$	$0.129\pm^{0.021}_{0.018}$	$502.8\pm^{19.4}_{18.3}$	$14.37\pm^{3.44}_{2.80}$	$8.50\pm^{0.81}_{0.77}$	$0.168\pm^{0.028}_{0.024}$
MACSJ1720.3+3536	$88.4\pm^{7.9}_{6.6}$	$2.29\pm^{1.34}_{0.87}$	$2.17\pm^{0.26}_{0.38}$	$0.107\pm^{0.050}_{0.038}$	$168.6\pm^{16.1}_{13.3}$	$5.38\pm^{3.40}_{2.06}$	$3.06\pm^{0.41}_{0.38}$	$0.179\pm^{0.094}_{0.070}$
RXJ2129.6+0005	$136.3\pm^{8.6}_{7.6}$	$3.50\pm^{1.33}_{1.23}$	$2.55\pm^{0.36}_{0.29}$	$0.134\pm^{0.040}_{0.035}$	$289.5\pm^{19.0}_{15.8}$	$9.51\pm^{3.52}_{3.52}$	$4.95\pm^{0.98}_{0.76}$	$0.182\pm^{0.058}_{0.040}$
Abell 2537	$115.7\pm^{9.2}_{7.0}$	$2.24\pm^{0.70}_{0.70}$	$2.60\pm^{0.33}_{0.33}$	$0.084\pm^{0.022}_{0.019}$	$251.4\pm^{20.8}_{18.0}$	$6.29\pm^{1.95}_{1.94}$	$5.36\pm^{0.80}_{0.74}$	$0.115\pm^{0.036}_{0.031}$

Table 5.4: Chi^2 values from Joint Chandra and SZA Data.

Cluster Name	χ^2_{tx}	χ^2_{sb}	χ^2_{sze}	χ^2_{tot}
MACSJ0159.8-0849	2.0(6)	54.4(60)	55.8(40)	112.2(98)
Abell 383	2.9(8)	66.1(76)	62.6(40)	131.6(116)
MACS0329.7-0212	1.8(5)	33.8 (45)	47.4(40)	83(81)
Abell 478	2.9 (9)	82.5 (121)	34.2(40)	119.6(162)
MACSJ0429.6-0253	2.4 (5)	34.4(45)	46.0(40)	82.8(82)
3C186	0.8(3)	12.9(28)	28.7(40)	71.1(116)
MACSJ0744.9+3927	0.7(5)	23.5 (45)	38.1(40)	62.3(82)
MACSJ0947.2+7623	0.6(5)	42(60)	33.5 (40)	76.1(97)
Zwicky 3146	5.1(9)	37.3(76)	28.7(40)	71.1(116)
MACSJ1115.8+0129	2.4(5)	31.5 (60)	49.4(40)	83.8(97)
MS1137.5+6625	1.5(4)	34.3(30)	56.6(40)	92.4 (68)
Abell 1413	7.2(9)	103.6 (106)	57.7(40)	168.6 (147)
CLJ1226.9+3332	0.7(4)	10.7 (30)	37.7(40)	48.9(68)
MACSJ1311.0-0311	0.9(6)	19.4(30)	46.4(40)	66.7(68)
RXJ1347.5-1145	4.2(6)	29.9(60)	47.6(40)	81.7 (97)
Abell 1835	2.6 (9)	70.2 (91)	36.2(40)	109(131)
MACSJ1423.8+2404	0.8(4)	37.8 (45)	27.0(40)	65.6(81)
MACSJ1427.3+4408	1.6(5)	54.2(45)	42.8(40)	98.6(82)
RXJ1504.1-0248	6.9(9)	89.5(106)	48 (40)	144.4(147)
MACSJ1532.9+3021	1.2(5)	32.2(60)	43.2(40)	76.6(97)
MACSJ1621.6+3810	6.3(6)	36.8(45)	40.5(40)	83.6 (83)
Abell 2204	1.8(9)	122.1(137)	44.3(40)	168.2(178)
MACSJ1720.3+3536	5.3(6)	34.8(60)	67.4(40)	107.5(98)
RXJ2129.6+0005	2.7(7)	44.6(76)	46.9(40)	94.2(85)
Abell 2537	1.4(5)	53(76)	66.5(40)	120.9(113)

5.5 Fits to the X-ray and SZE Observables

5.5.1 MACSJ0159.8-0849

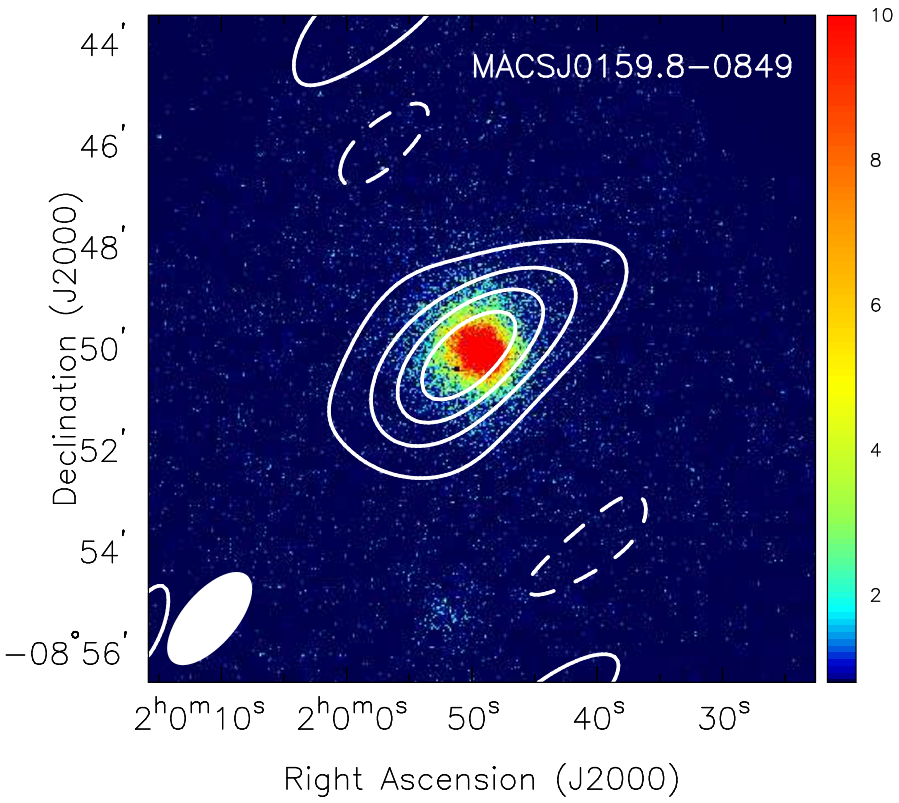

Figure 5.5: MACSJ0159.8-0849: SZE contours overlaid on X-ray false color images. The *Chandra* X-ray surface brightness data are from the energy range 0.7–7.0 keV. The color bars reflect the number of counts detected by Chandra in the 0.7-7 keV band. The SZE data are from the SZA, and the contour levels are (+2,-2,-4,...) times the rms noise (see Table 3.1). The synthesized beams of the SZE observations are shown in the lower left corner of each image.

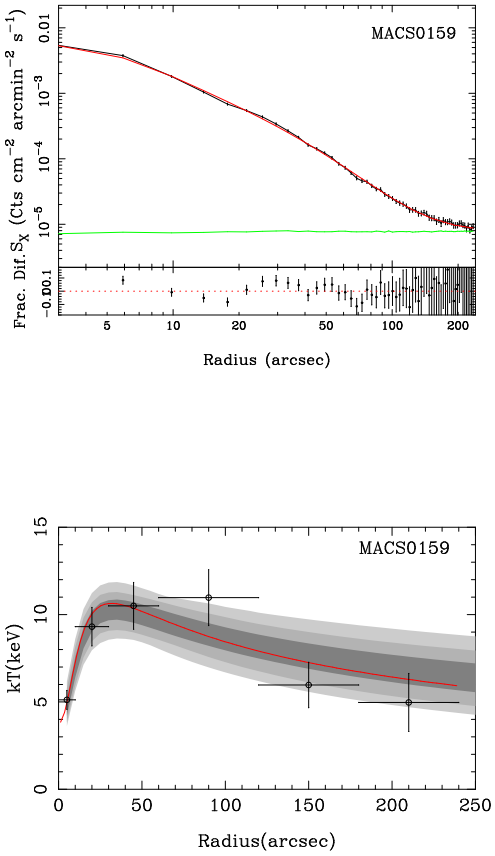

Figure 5.6: MACSJ0159.8-0849: Surface brightness and temperature profile from joint X-ray/SZE analysis.

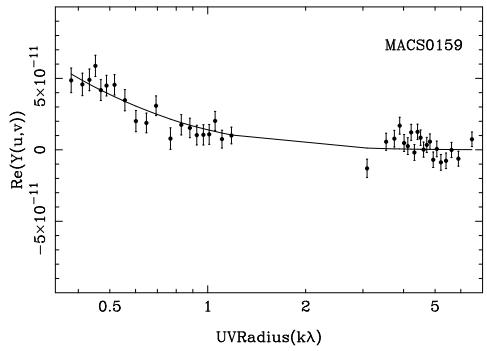

Figure 5.7: MACSJ0159.8-0849: SZE visibility profile plotted as a function of $u - v$ radius ($\sqrt{u^2 + v^2}$). The plots show the real components of the measured visibilities along with the best fit model.

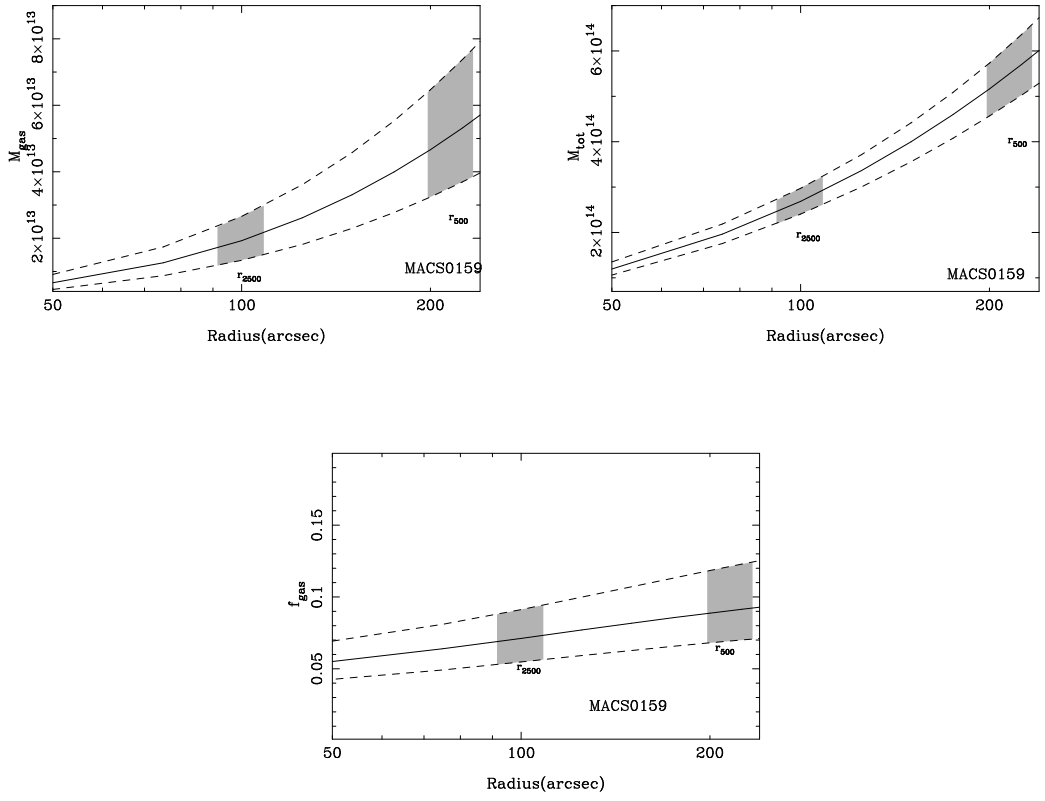

Figure 5.8: MACSJ0159.8-0849: Radial gas mass, total mass, and gas mass fraction profiles from joint X-ray/SZE analysis.

5.5.2 Abell 383

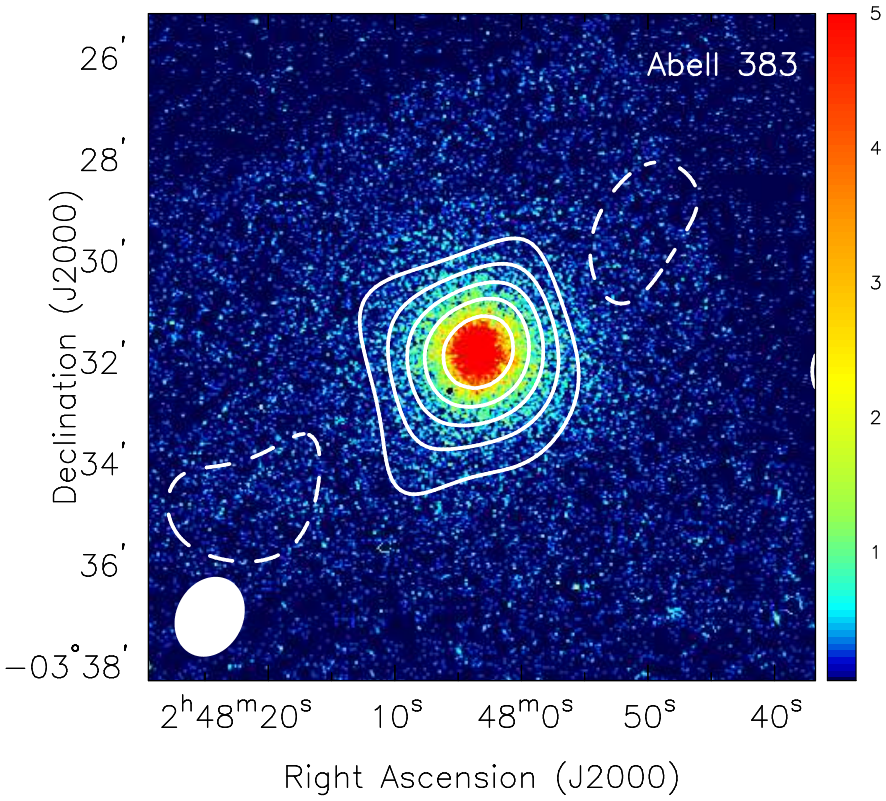

Figure 5.9: Abell 383:SZE contours overlaid on X-ray false color images. The *Chandra* X-ray surface brightness data are from the energy range 0.7–7.0 keV. The color bars reflect the number of counts detected by Chandra in the 0.7-7 keV band. The SZE data are from the SZA, and the contour levels are (+2,-2,-4,...) times the rms noise (see Table 3.1). The synthesized beams of the SZE observations are shown in the lower left corner of each image.

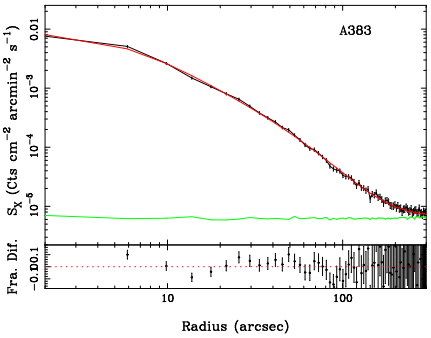

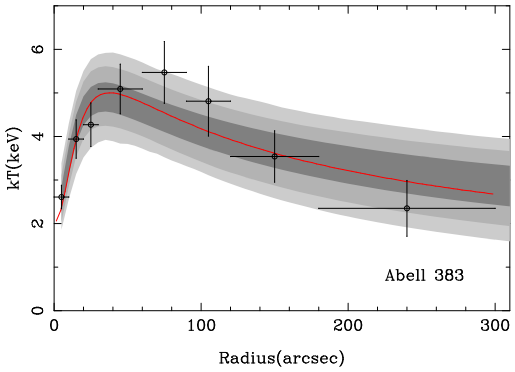

Figure 5.10: Abell 383: Surface brightness and temperature profile from joint X-ray/SZE analysis.

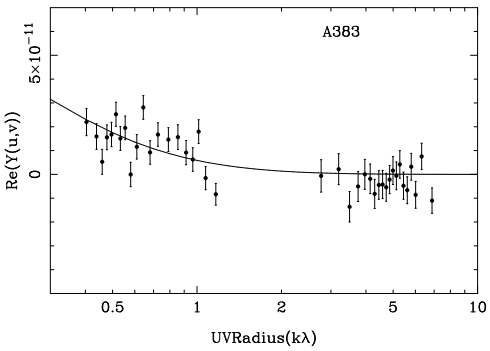

Figure 5.11: Abell 383: SZE visibility profile plotted as a function of $u - v$ radius ($\sqrt{u^2 + v^2}$). The plots show the real components of the measured visibilities along with the best fit model.

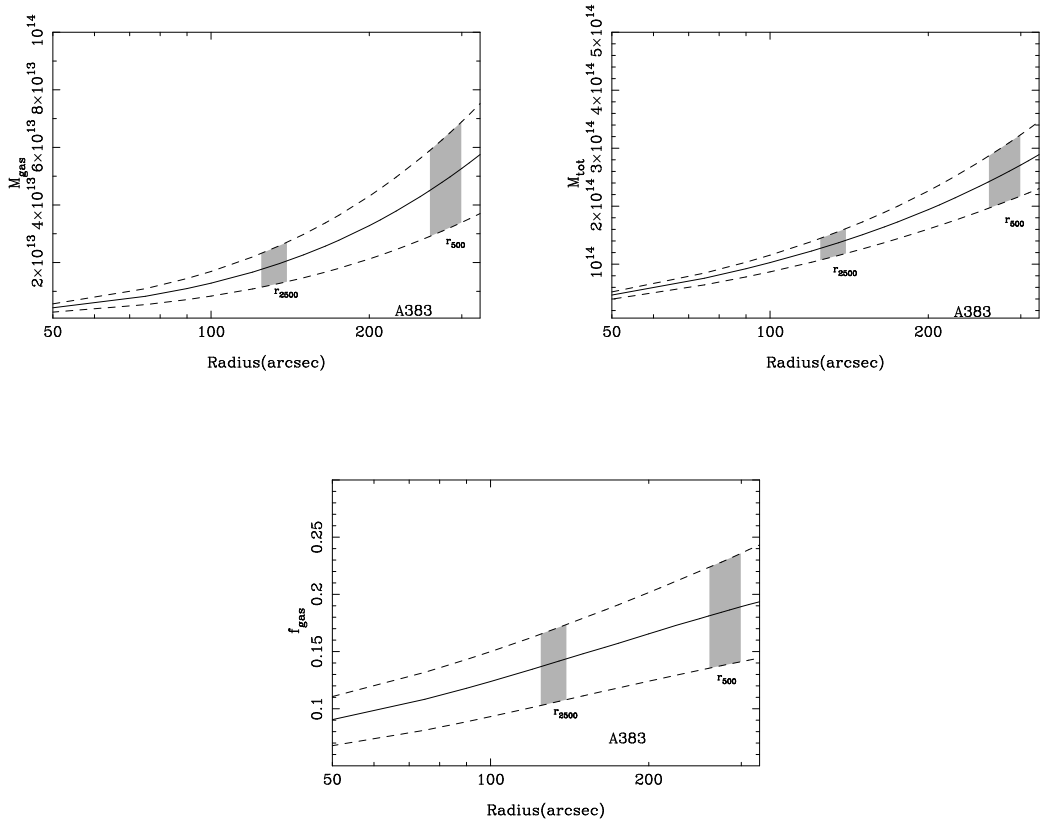

Figure 5.12: Abell 383: Radial gas mass, total mass, and gas mass fraction profiles from joint X-ray/SZE analysis.

5.5.3 MACSJ0329.7-0212

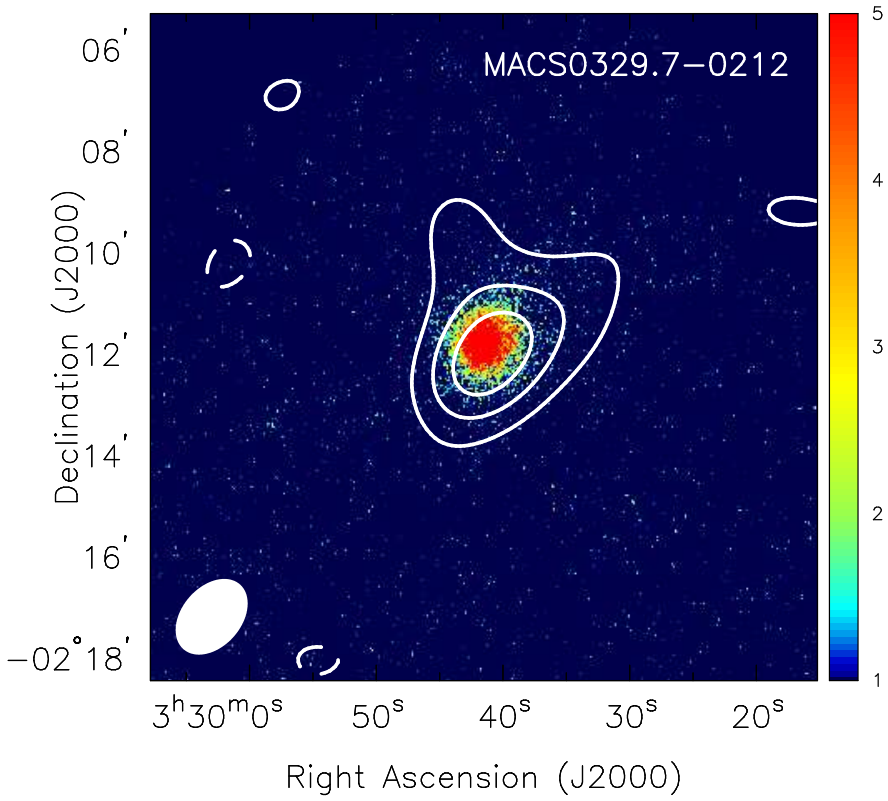

Figure 5.13: MACSJ0329.7-0212: SZE contours overlaid on X-ray false color images. The *Chandra* X-ray surface brightness data are from the energy range 0.7–7.0 keV. The color bars reflect the number of counts detected by Chandra in the 0.7-7 keV band. The SZE data are from the SZA, and the contour levels are (+2,-2,-4,...) times the rms noise (see Table 3.1). The synthesized beams of the SZE observations are shown in the lower left corner of each image.

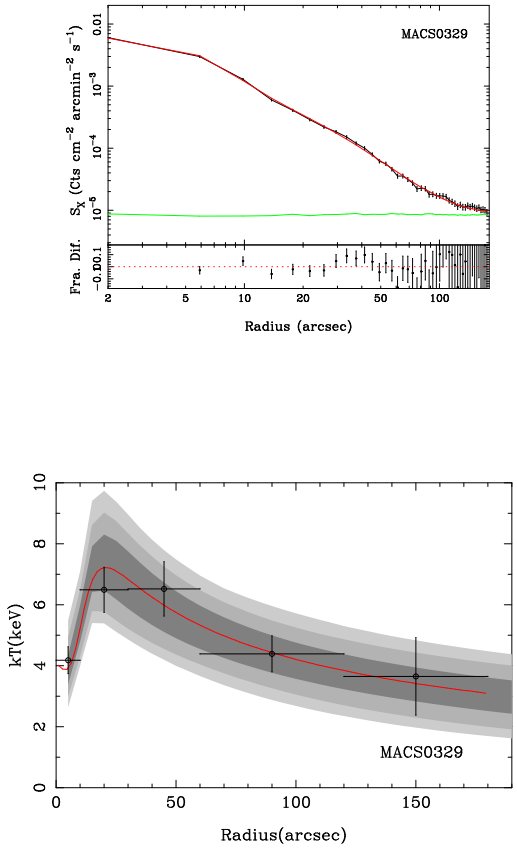

Figure 5.14: MACSJ0329.7-0212: Surface brightness and temperature profile from joint X-ray/SZE analysis.

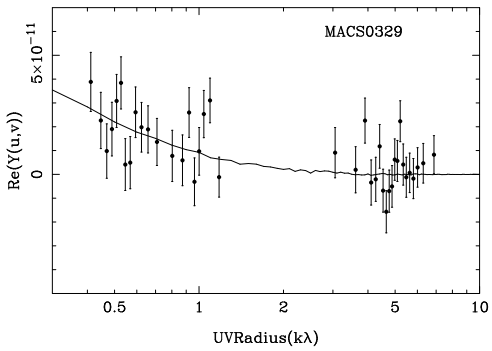

Figure 5.15: MACSJ0329.7-0212: SZE visibility profile plotted as a function of $u-v$ radius ($\sqrt{u^2+v^2}$). The plots show the real components of the measured visibilities along with the best fit model.

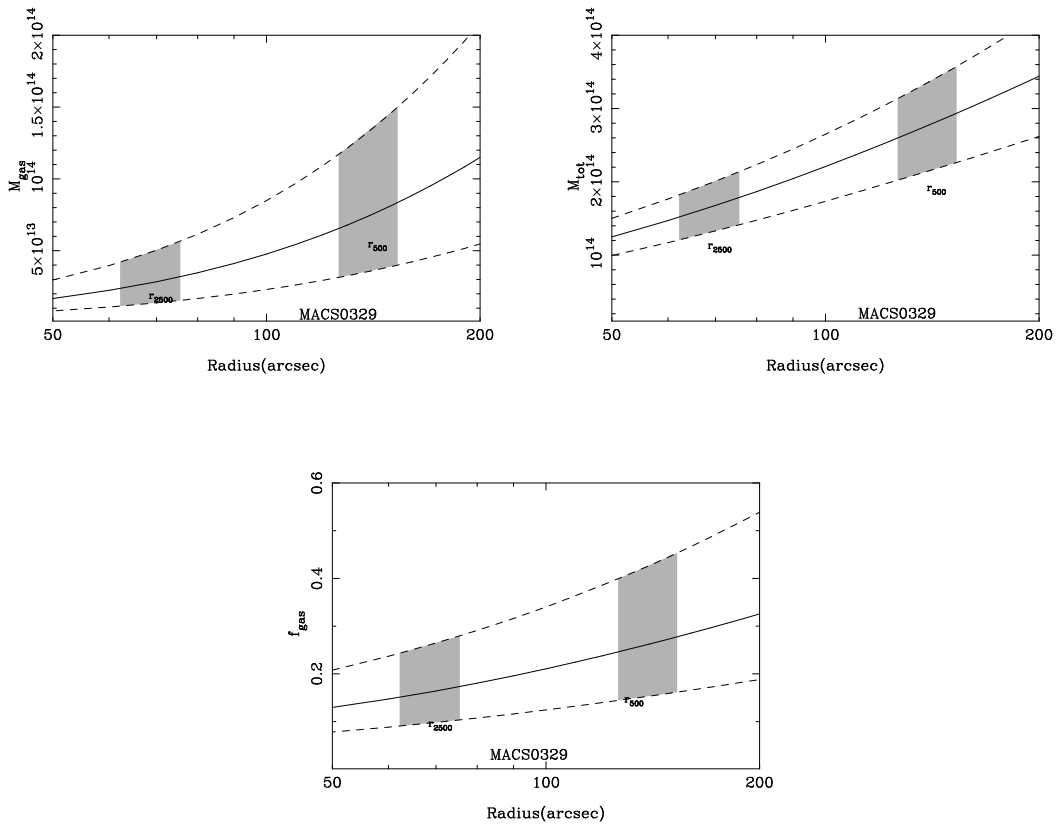

Figure 5.16: MACSJ0329.7-0212: Radial gas mass, total mass, and gas mass fraction profiles from joint X-ray/SZE analysis.

5.5.4 Abell 478

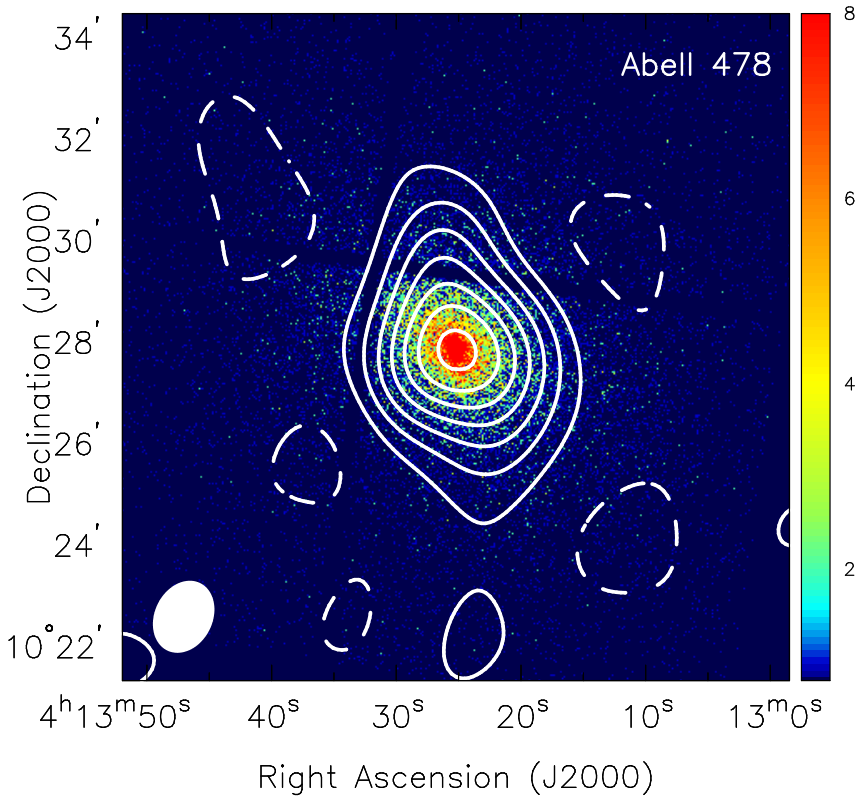

Figure 5.17: Abell 478: SZE contours overlaid on X-ray false color images. The *Chandra* X-ray surface brightness data are from the energy range 0.7–7.0 keV. The color bars reflect the number of counts detected by Chandra in the 0.7-7 keV band. The SZE data are from the SZA, and the contour levels are (+2,-2,-4,...) times the rms noise (see Table 3.1). The synthesized beams of the SZE observations are shown in the lower left corner of each image.

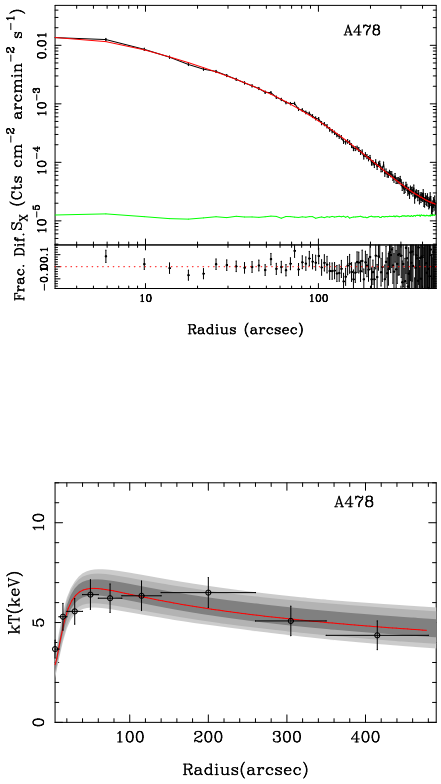

Figure 5.18: Abell 478: Surface brightness and temperature profile from joint X-ray/SZE analysis.

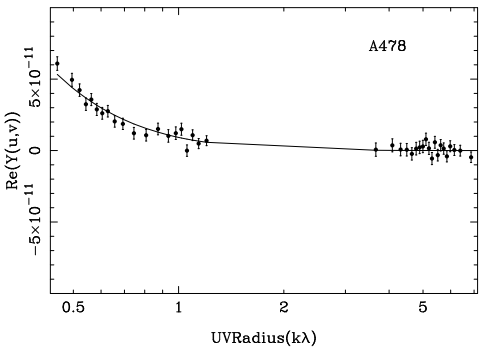

Figure 5.19: Abell 478: SZE visibility profile plotted as a function of $u - v$ radius ($\sqrt{u^2 + v^2}$). The plots show the real components of the measured visibilities along with the best fit model.

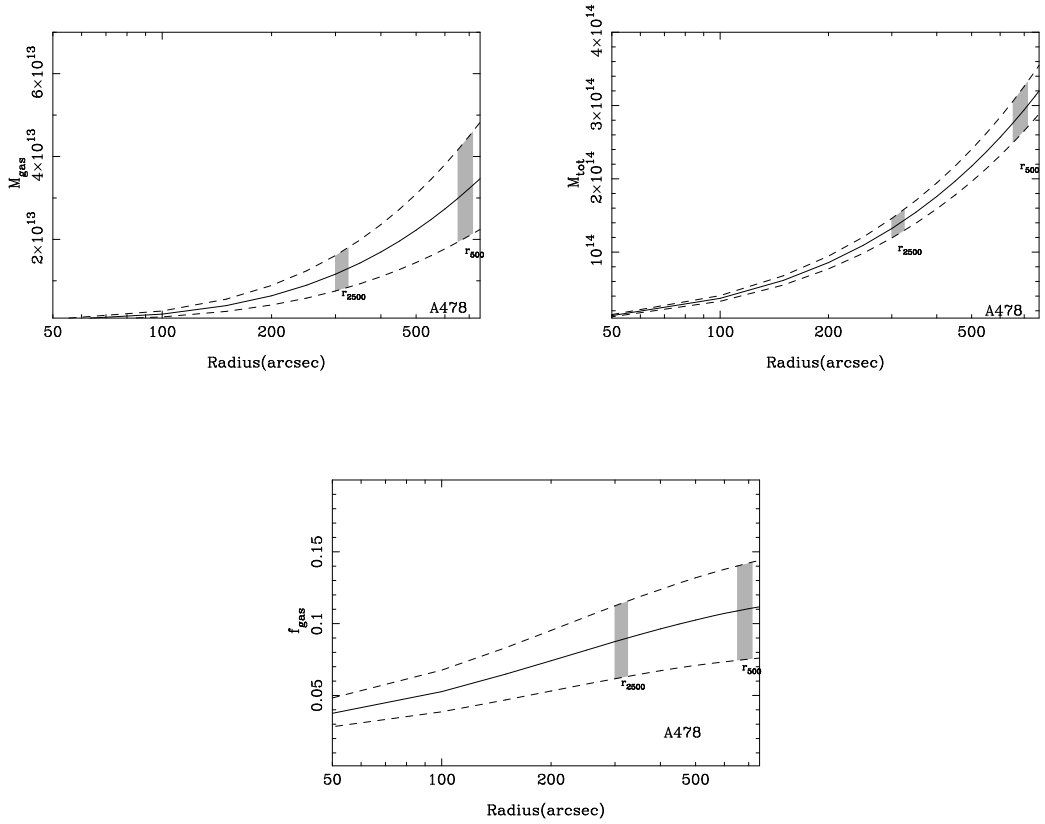

Figure 5.20: Abell 478: Radial gas mass, total mass, and gas mass fraction profiles from joint X-ray/SZE analysis.

5.5.5 MACSJ0429.6-0253

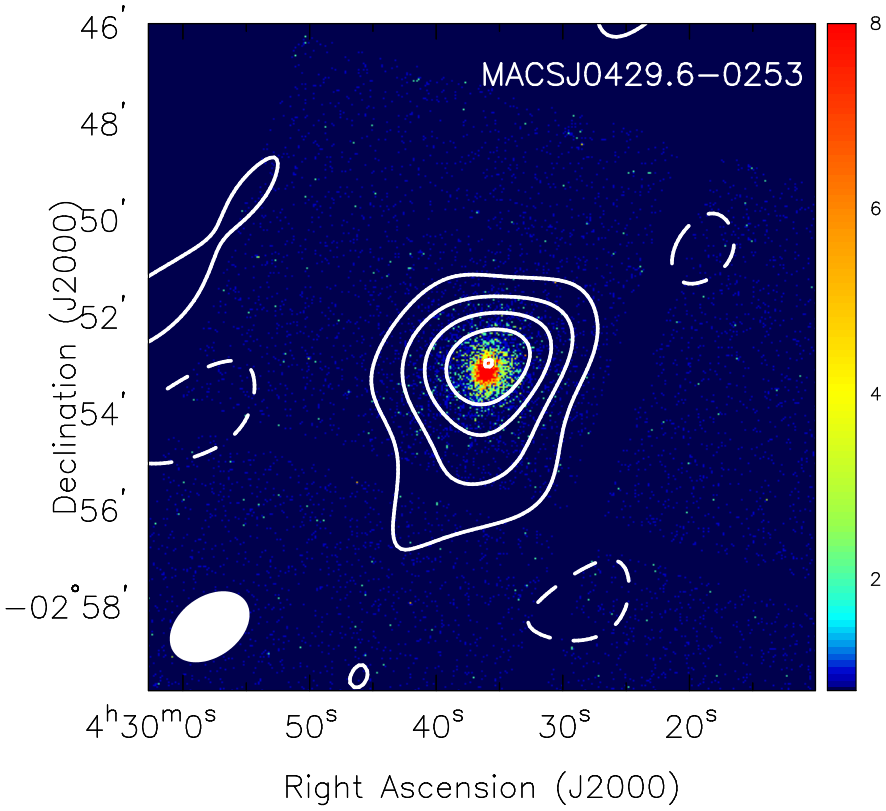

Figure 5.21: MACSJ0429.6-0253: SZE contours overlaid on X-ray false color images. The *Chandra* X-ray surface brightness data are from the energy range 0.7–7.0 keV. The color bars reflect the number of counts detected by Chandra in the 0.7-7 keV band. The SZE data are from the SZA, and the contour levels are (+2,-2,-4,...) times the rms noise (see Table 3.1). The synthesized beams of the SZE observations are shown in the lower left corner of each image.

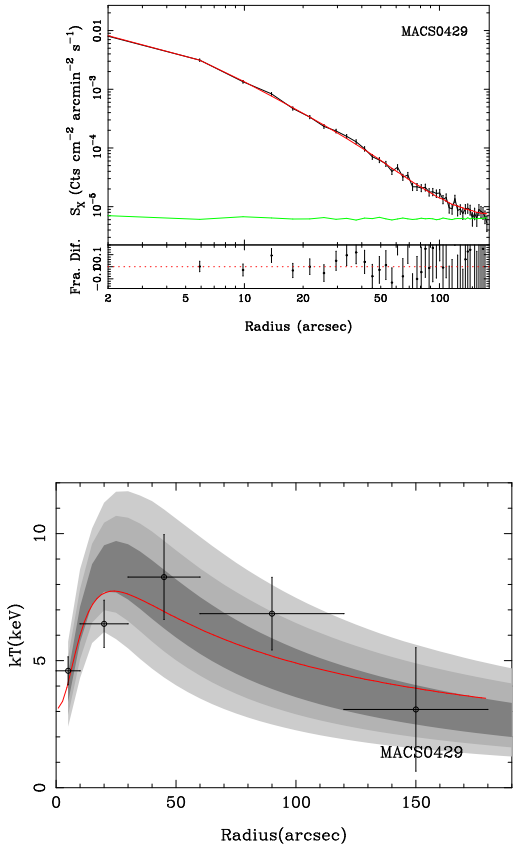

Figure 5.22: MACSJ0429.6-0253: Surface brightness and temperature profile from joint X-ray/SZE analysis.

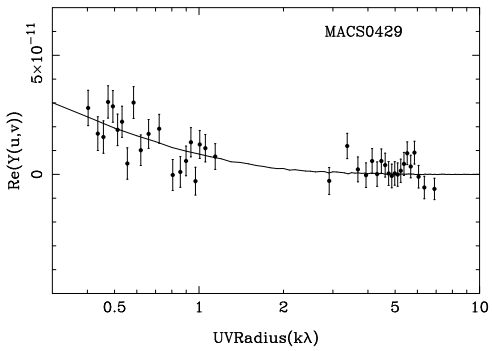

Figure 5.23: MACSJ0429.6-0253: SZE visibility profile plotted as a function of $u-v$ radius ($\sqrt{u^2+v^2}$). The plots show the real components of the measured visibilities along with the best fit model.

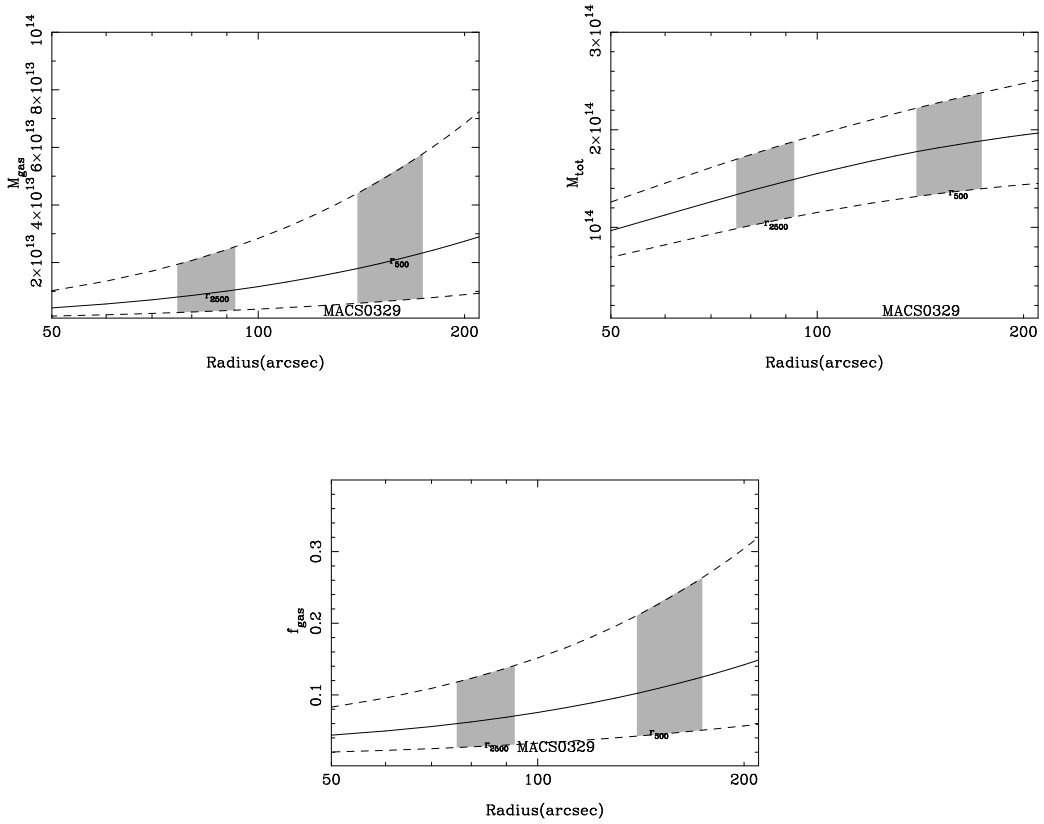

Figure 5.24: MACSJ0429.6-0253: Radial gas mass, total mass, and gas mass fraction profiles from joint X-ray/SZE analysis.

5.5.6 3C186

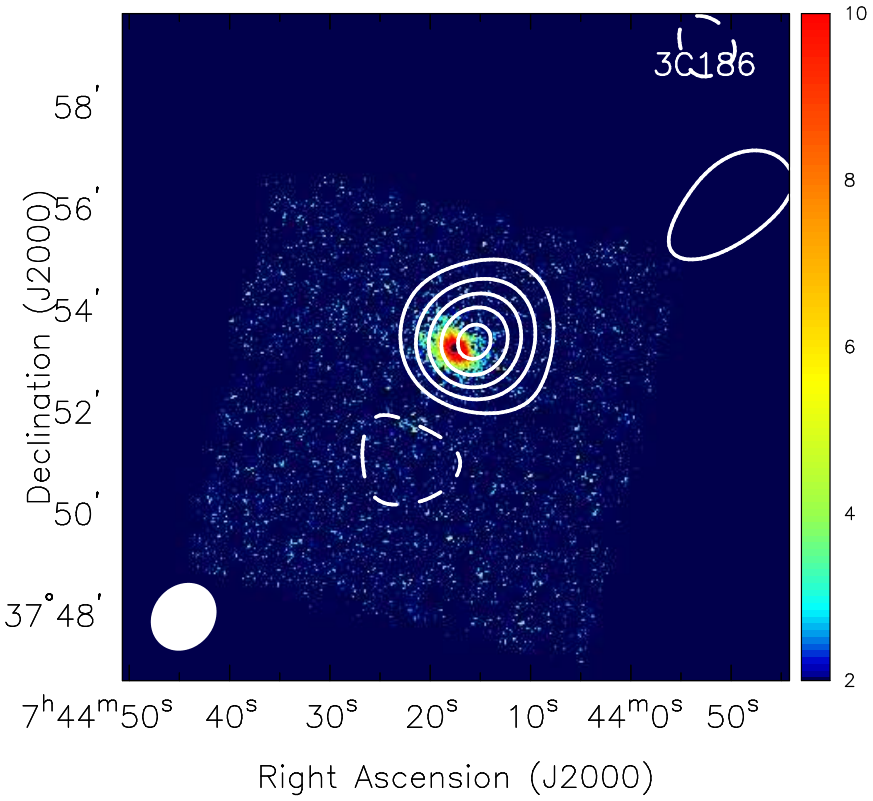

Figure 5.25: 3C186: SZE contours overlaid on X-ray false color images. The *Chandra* X-ray surface brightness data are from the energy range 0.7–7.0 keV. The color bars reflect the number of counts detected by Chandra in the 0.7-7 keV band. The SZE data are from the SZA, and the contour levels are (+2,-2,-4,...) times the rms noise (see Table 3.1). The synthesized beams of the SZE observations are shown in the lower left corner of each image.

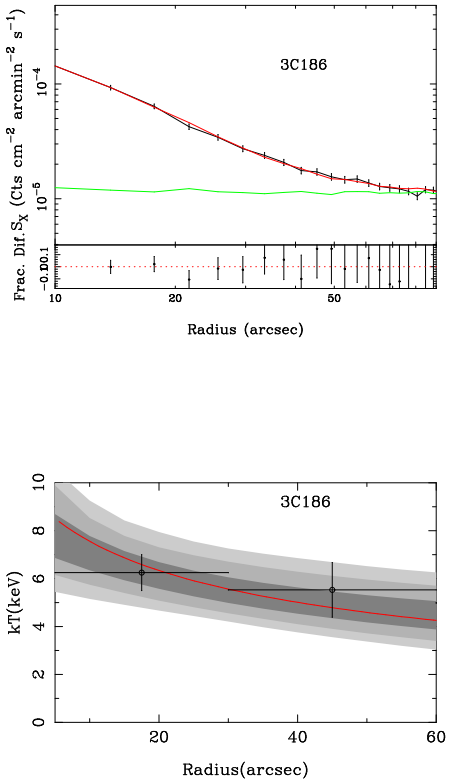

Figure 5.26: 3C186: Surface brightness and temperature profile from joint X-ray/SZE analysis.

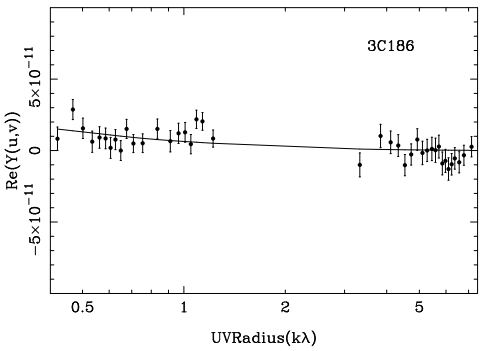

Figure 5.27: 3C186: SZE visibility profile plotted as a function of $u - v$ radius ($\sqrt{u^2 + v^2}$). The plots show the real components of the measured visibilities along with the best fit model.

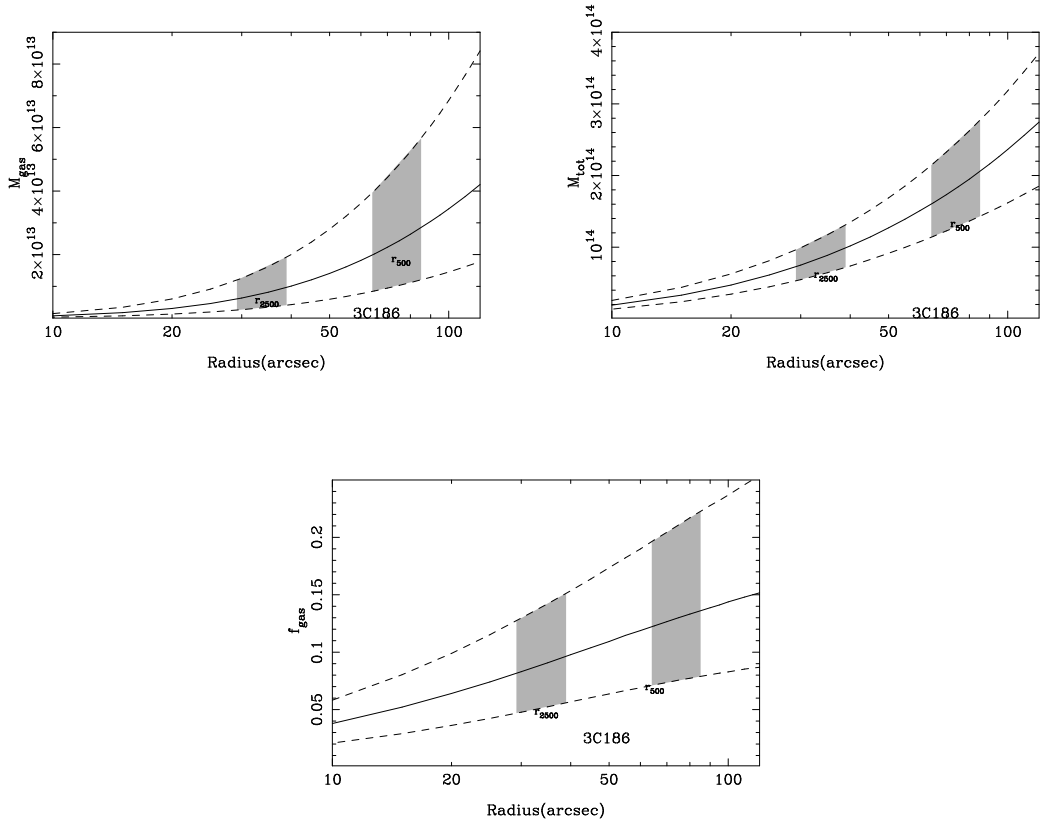

Figure 5.28: 3C186: Radial gas mass, total mass, and gas mass fraction profiles from joint X-ray/SZE analysis.

5.5.7 MACSJ0744.9+3927

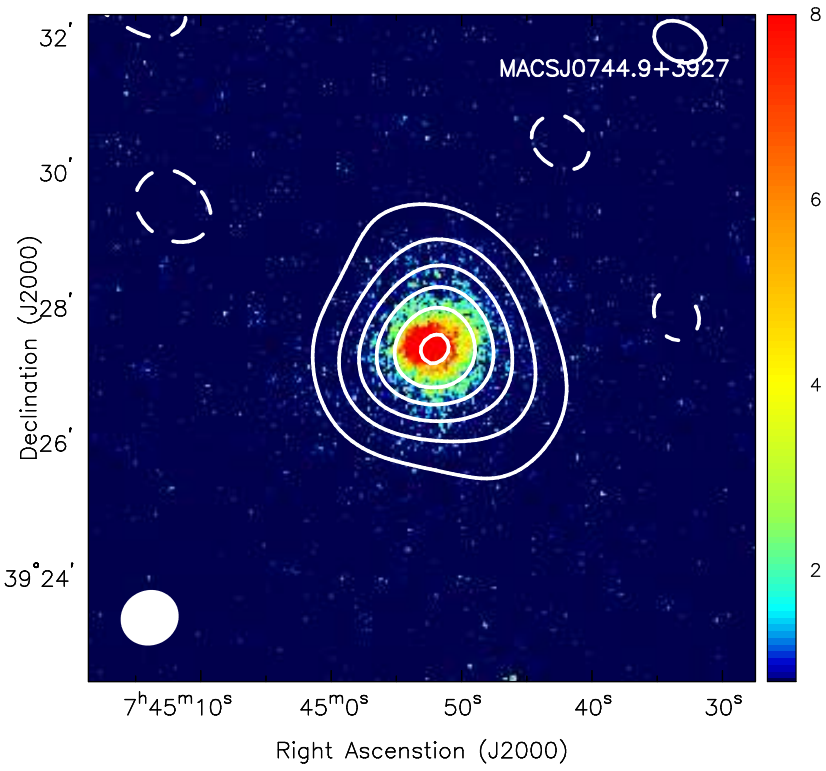

Figure 5.29: MACSJ0744.9+3927: SZE contours overlaid on X-ray false color images. The *Chandra* X-ray surface brightness data are from the energy range 0.7–7.0 keV. The color bars reflect the number of counts detected by Chandra in the 0.7-7 keV band. The SZE data are from the SZA, and the contour levels are (+2,-2,-4,...) times the rms noise (see Table 3.1). The synthesized beams of the SZE observations are shown in the lower left corner of each image.

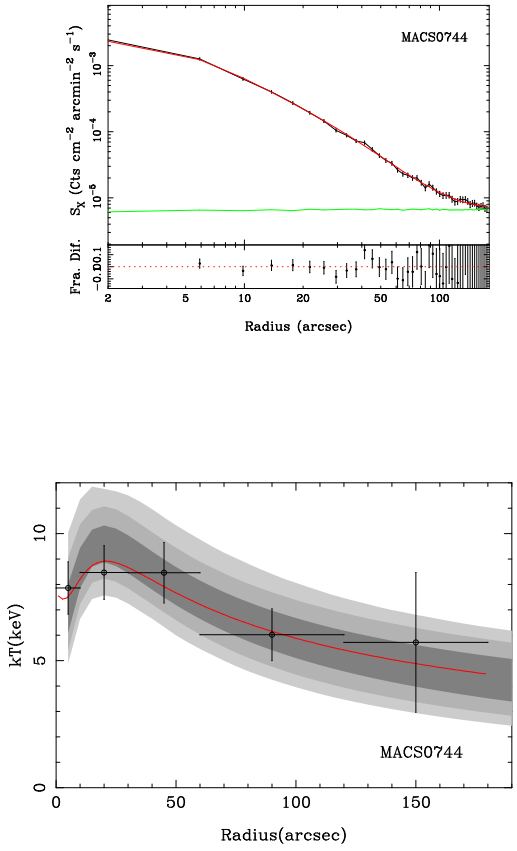

Figure 5.30: MACSJ0744.9+3927: Surface brightness and temperature profile from joint X-ray/SZE analysis.

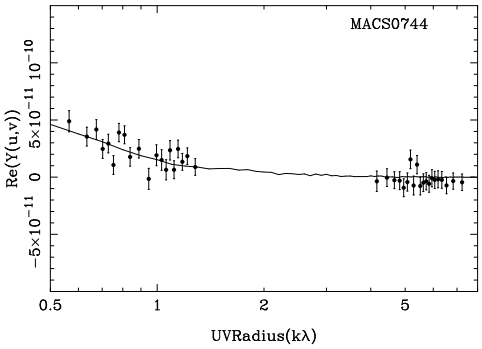

Figure 5.31: MACSJ0744.9+3927: SZE visibility profile plotted as a function of $u-v$ radius ($\sqrt{u^2+v^2}$). The plots show the real components of the measured visibilities along with the best fit model.

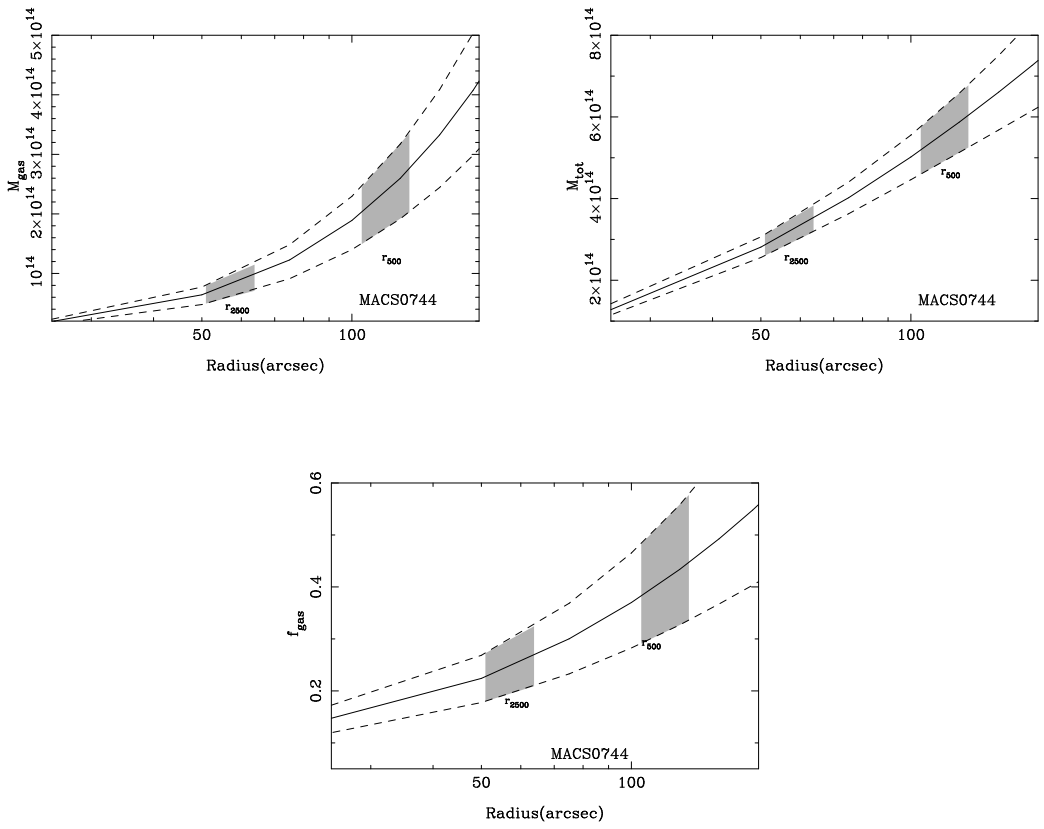

Figure 5.32: MACSJ0744.9+3927: Radial gas mass, total mass, and gas mass fraction profiles from joint X-ray/SZE analysis.

5.5.8 MACSJ0947.2+7623

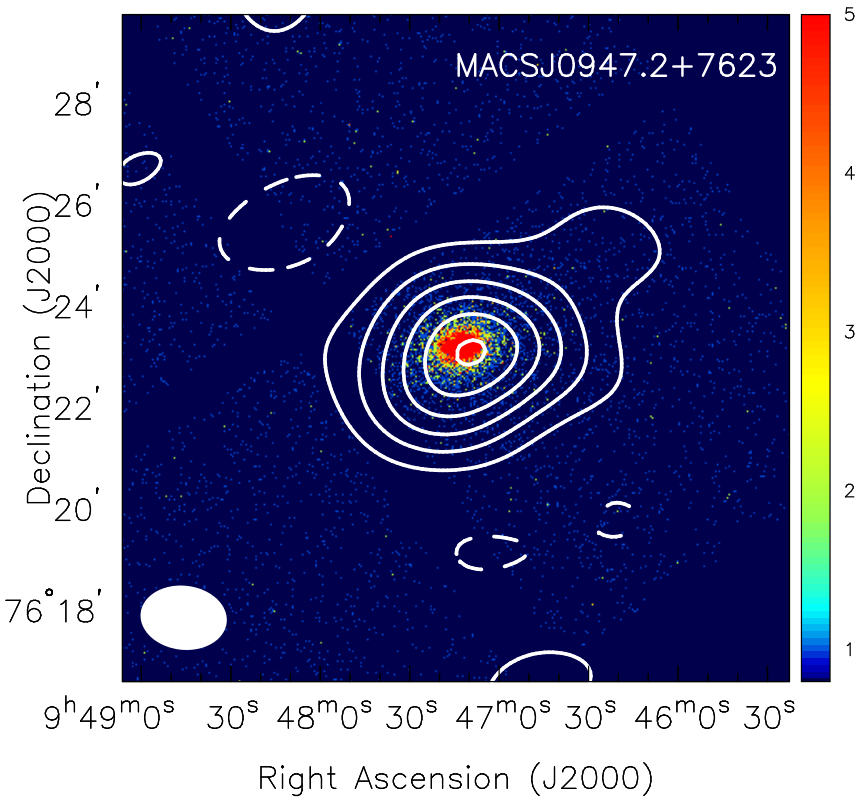

Figure 5.33: MACSJ0947.2+7623: SZE contours overlaid on X-ray false color images. The *Chandra* X-ray surface brightness data are from the energy range 0.7–7.0 keV. The color bars reflect the number of counts detected by Chandra in the 0.7-7 keV band. The SZE data are from the SZA, and the contour levels are (+2,-2,-4,...) times the rms noise (see Table 3.1). The synthesized beams of the SZE observations are shown in the lower left corner of each image.

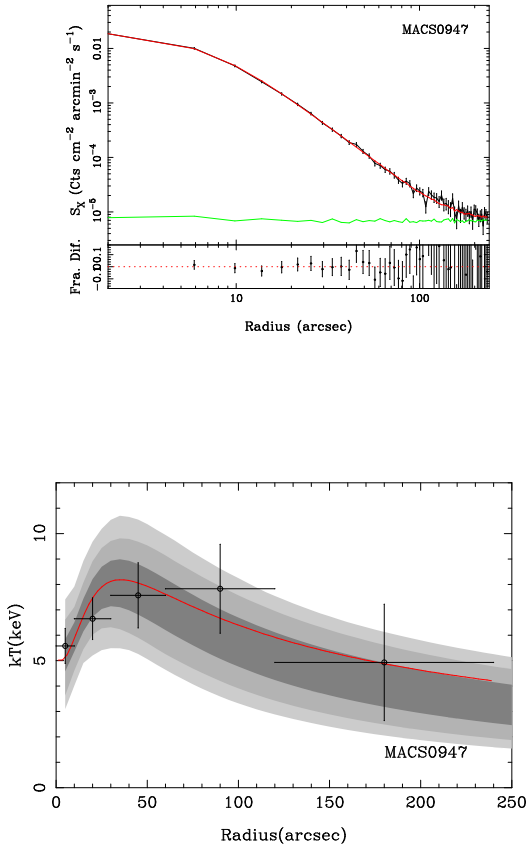

Figure 5.34: MACSJ0947.2+7623: Surface brightness and temperature profile from joint X-ray/SZE analysis.

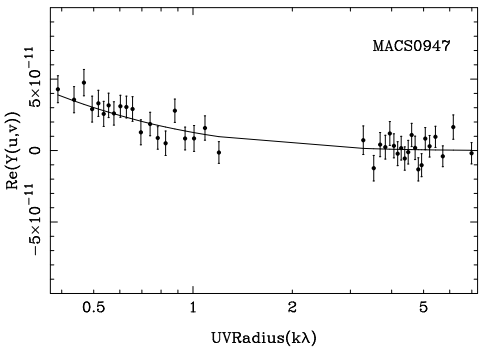

Figure 5.35: MACSJ0947.2+7623: SZE visibility profile plotted as a function of $u-v$ radius ($\sqrt{u^2+v^2}$). The plots show the real components of the measured visibilities along with the best fit model.

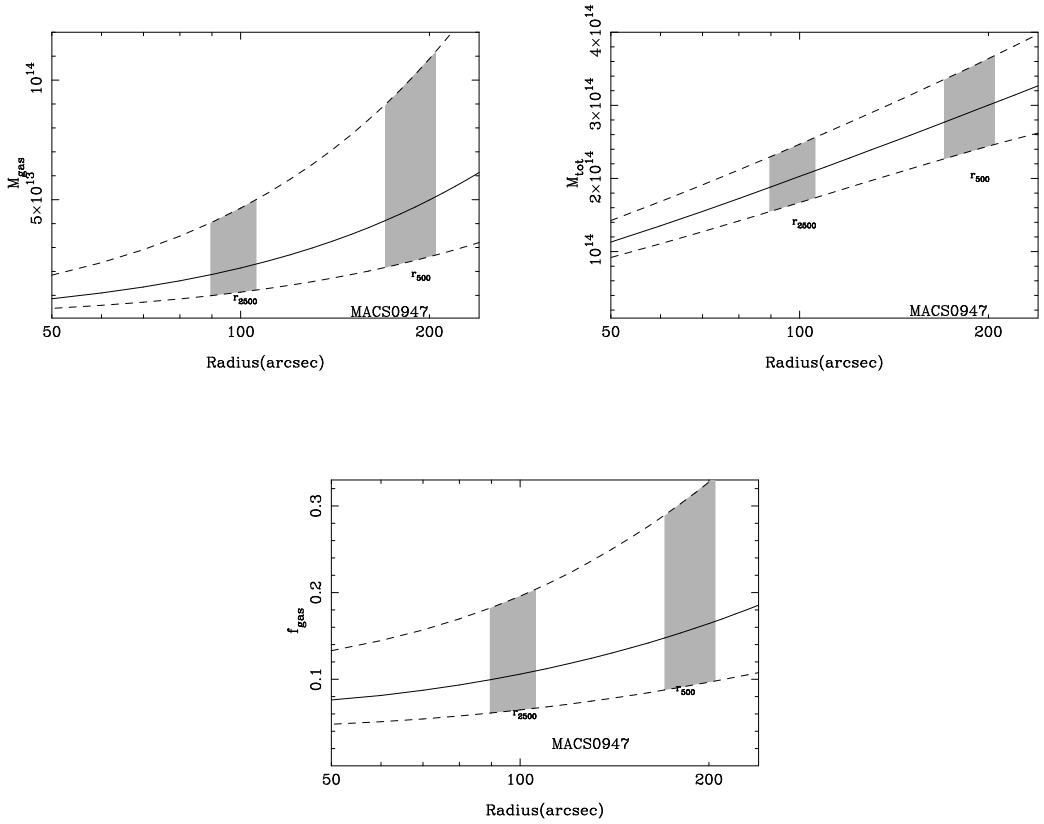

Figure 5.36: MACSJ0947.2+7623: Radial gas mass, total mass, and gas mass fraction profiles from joint X-ray/SZE analysis.

5.5.9 Zwicky 3146

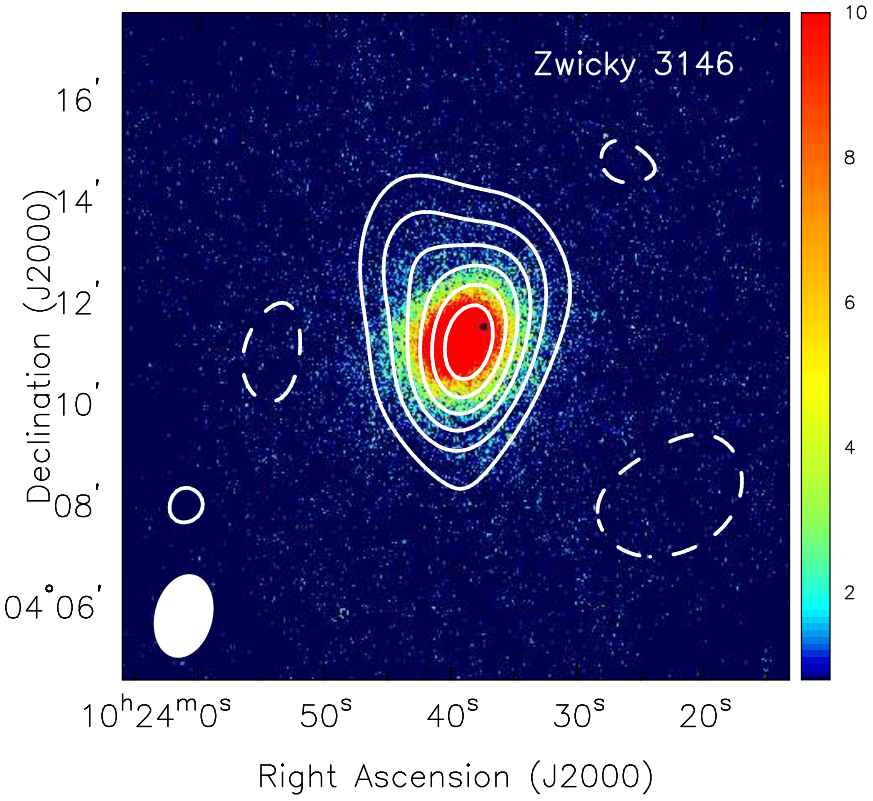

Figure 5.37: Zwicky 3146: SZE contours overlaid on X-ray false color images. The *Chandra* X-ray surface brightness data are from the energy range 0.7–7.0 keV. The color bars reflect the number of counts detected by Chandra in the 0.7-7 keV band. The SZE data are from the SZA, and the contour levels are (+2,-2,-4,...) times the rms noise (see Table 3.1). The synthesized beams of the SZE observations are shown in the lower left corner of each image.

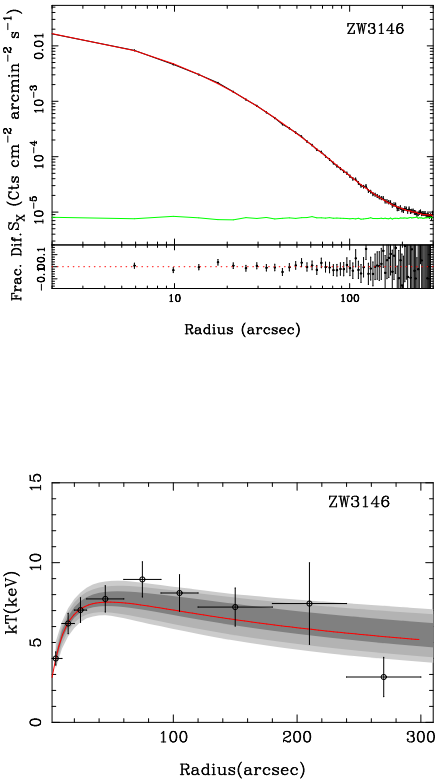

Figure 5.38: Zwicky 3146: Surface brightness and temperature profile from joint X-ray/SZE analysis.

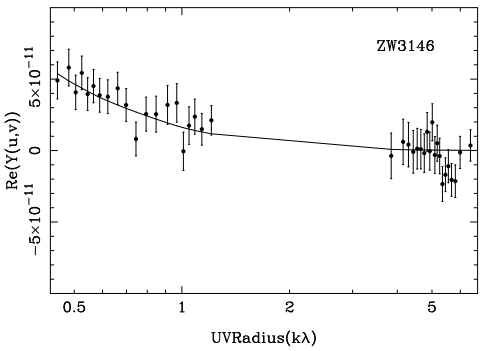

Figure 5.39: Zwicky 3146: SZE visibility profile plotted as a function of $u-v$ radius ($\sqrt{u^2+v^2}$). The plots show the real components of the measured visibilities along with the best fit model.

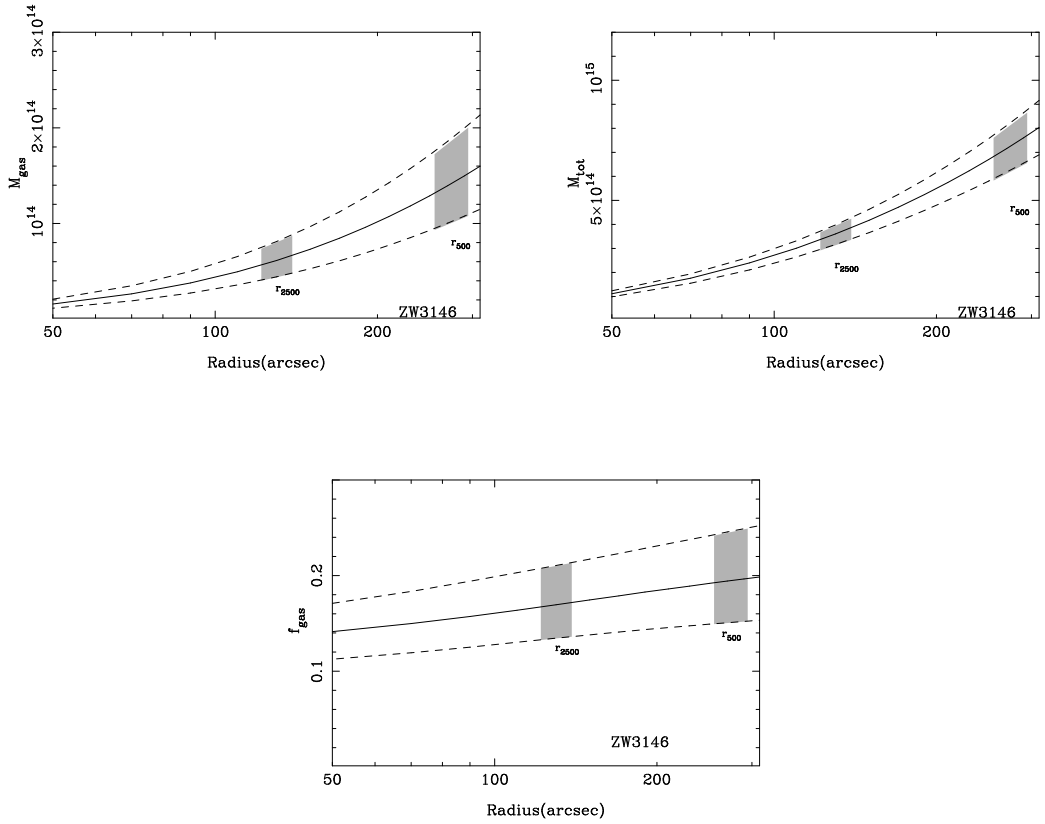

Figure 5.40: Zwicky 3146: Radial gas mass, total mass, and gas mass fraction profiles from joint X-ray/SZE analysis.

5.5.10 MACSJ1115.8+0129

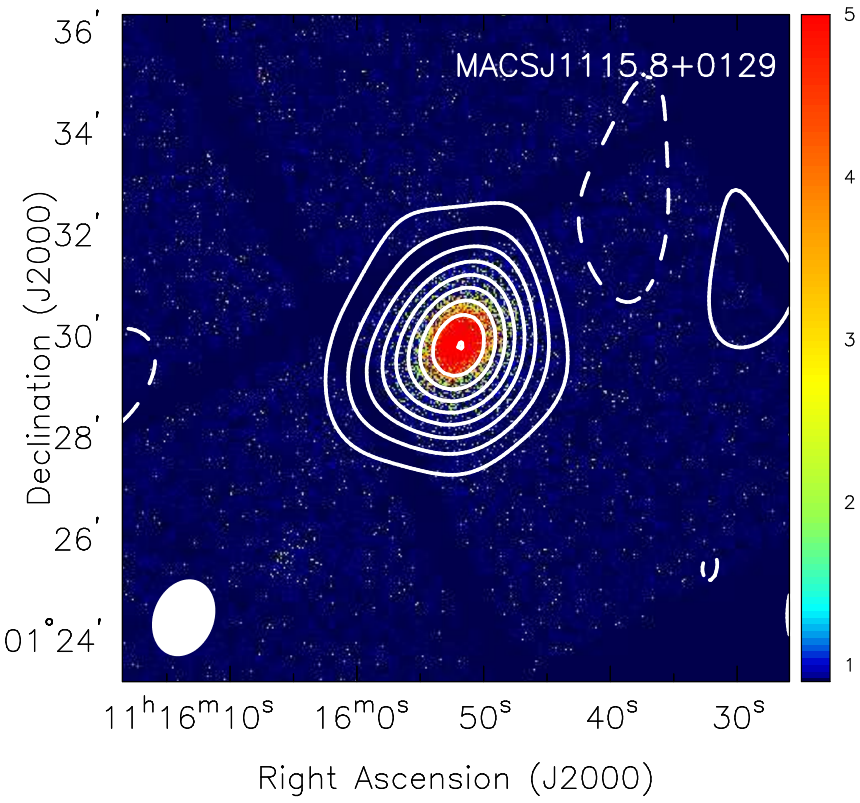

Figure 5.41: MACSJ1115.8+0129: SZE contours overlaid on X-ray false color images. The *Chandra* X-ray surface brightness data are from the energy range 0.7–7.0 keV. The color bars reflect the number of counts detected by Chandra in the 0.7-7 keV band. The SZE data are from the SZA, and the contour levels are (+2,-2,-4,...) times the rms noise (see Table 3.1). The synthesized beams of the SZE observations are shown in the lower left corner of each image.

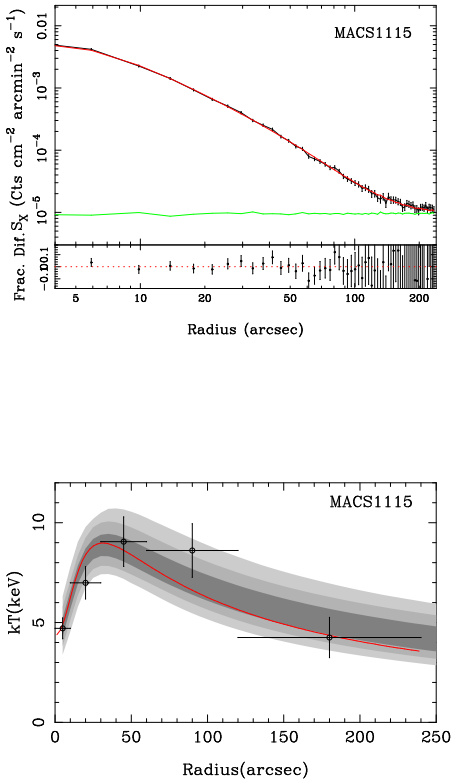

Figure 5.42: MACSJ1115.8+0129: Surface brightness and temperature profile from joint X-ray/SZE analysis.

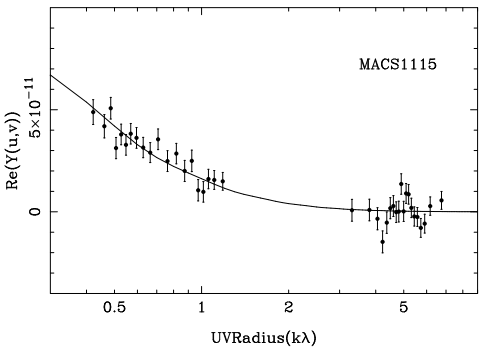

Figure 5.43: MACSJ1115.8+0129: SZE visibility profile plotted as a function of $u-v$ radius ($\sqrt{u^2+v^2}$). The plots show the real components of the measured visibilities along with the best fit model.

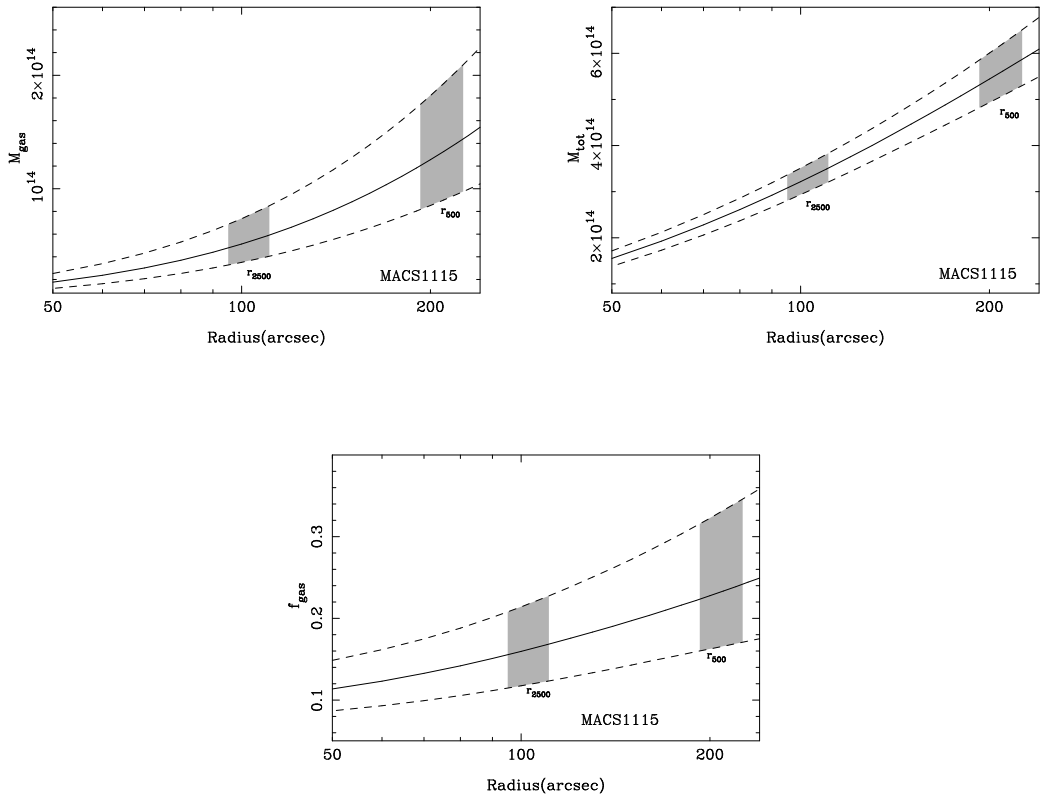

Figure 5.44: MACSJ1115.8+0129: Radial gas mass, total mass, and gas mass fraction profiles from joint X-ray/SZE analysis.

5.5.11 MS1137.5+6625

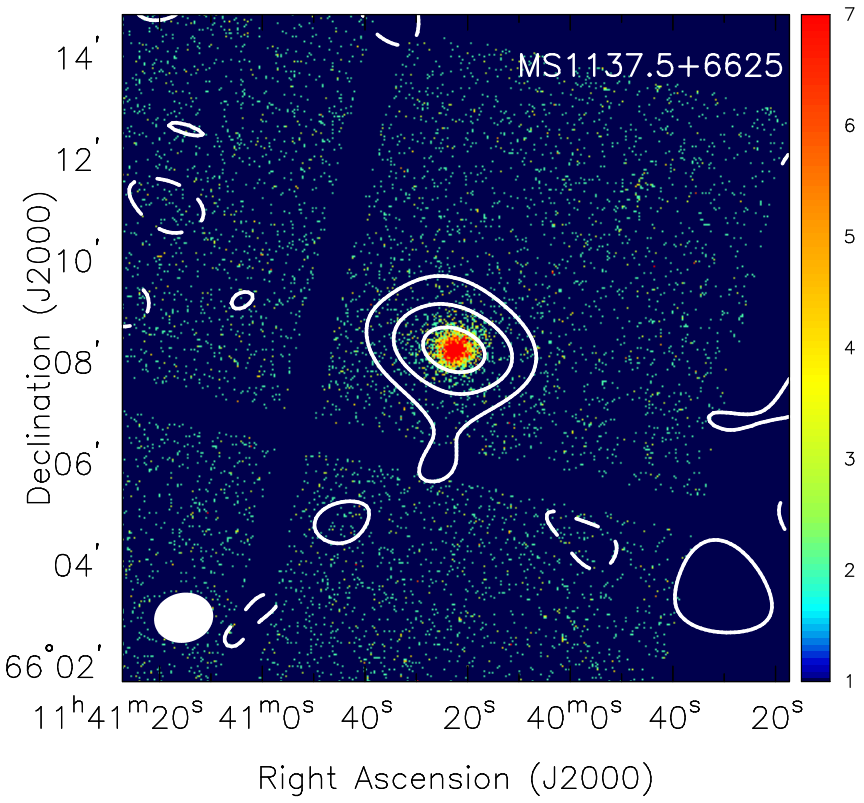

Figure 5.45: MS1137.5+6625: SZE contours overlaid on X-ray false color images. The *Chandra* X-ray surface brightness data are from the energy range 0.7–7.0 keV. The color bars reflect the number of counts detected by Chandra in the 0.7-7 keV band. The SZE data are from the SZA, and the contour levels are (+2,-2,-4,...) times the rms noise (see Table 3.1). The synthesized beams of the SZE observations are shown in the lower left corner of each image.

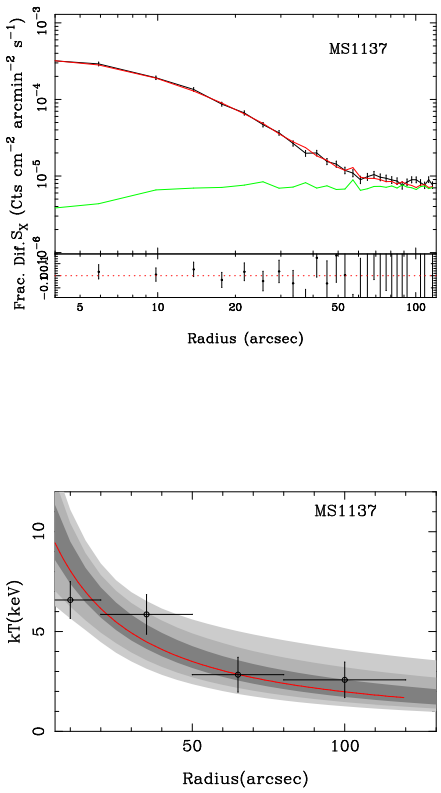

Figure 5.46: MS1137.5+6625: Surface brightness and temperature profile from joint X-ray/SZE analysis.

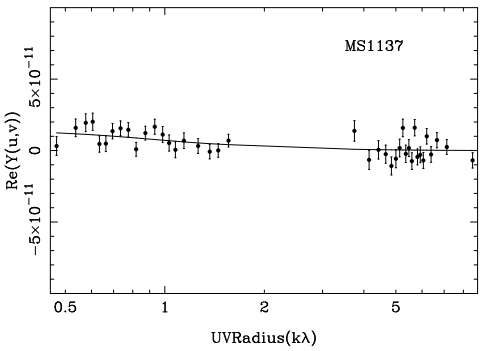

Figure 5.47: MS1137.5+6625: SZE visibility profile plotted as a function of $u - v$ radius ($\sqrt{u^2 + v^2}$). The plots show the real components of the measured visibilities along with the best fit model.

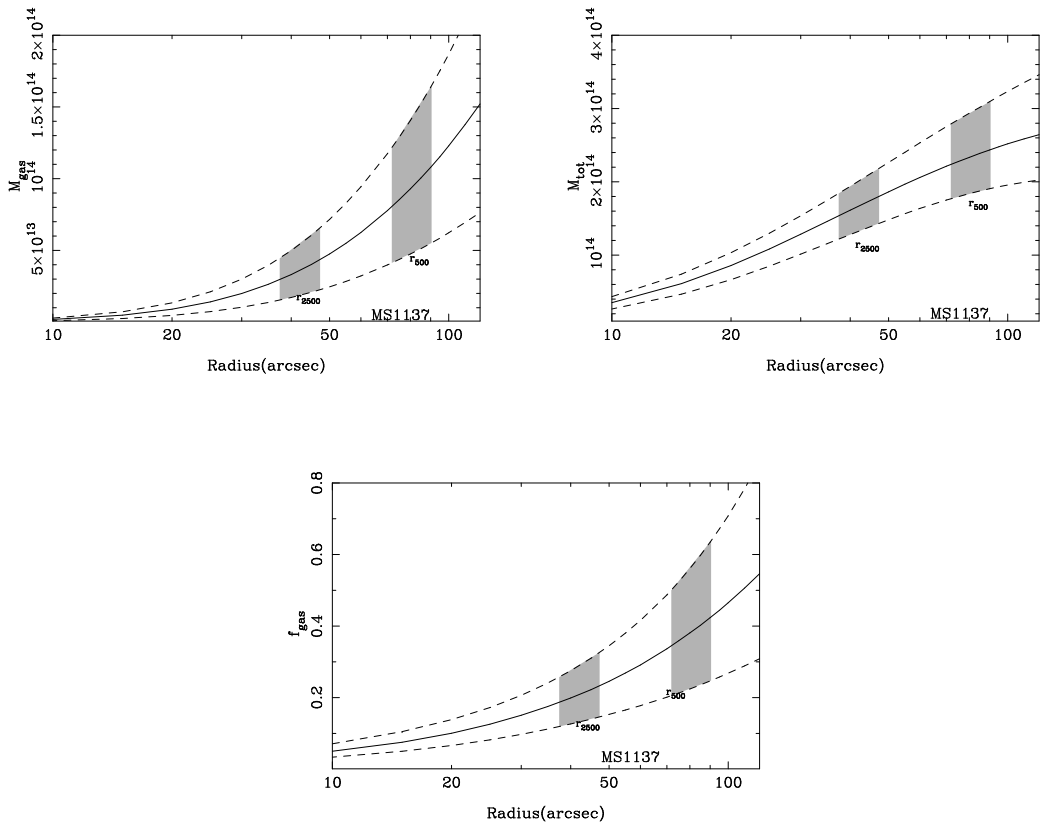

Figure 5.48: MS1137.5+6625: Radial gas mass, total mass, and gas mass fraction profiles from joint X-ray/SZE analysis.

5.5.12 Abell 1413

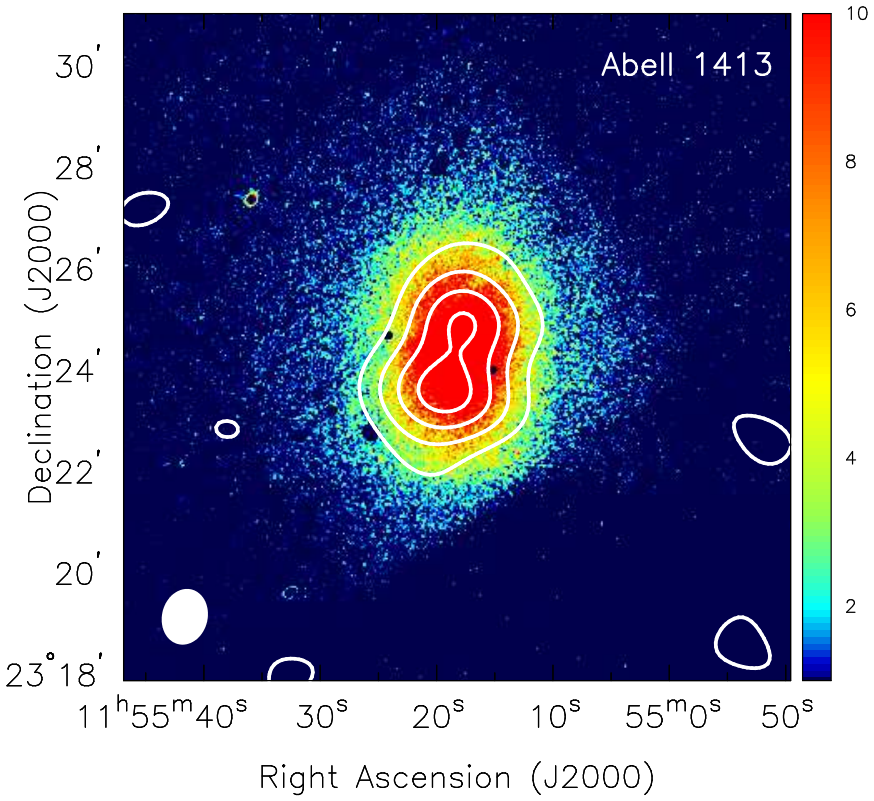

Figure 5.49: Abell 1413: SZE contours overlaid on X-ray false color images. The *Chandra* X-ray surface brightness data are from the energy range 0.7–7.0 keV. The color bars reflect the number of counts detected by Chandra in the 0.7-7 keV band. The SZE data are from the SZA, and the contour levels are (+2,-2,-4,...) times the rms noise (see Table 3.1). The synthesized beams of the SZE observations are shown in the lower left corner of each image.

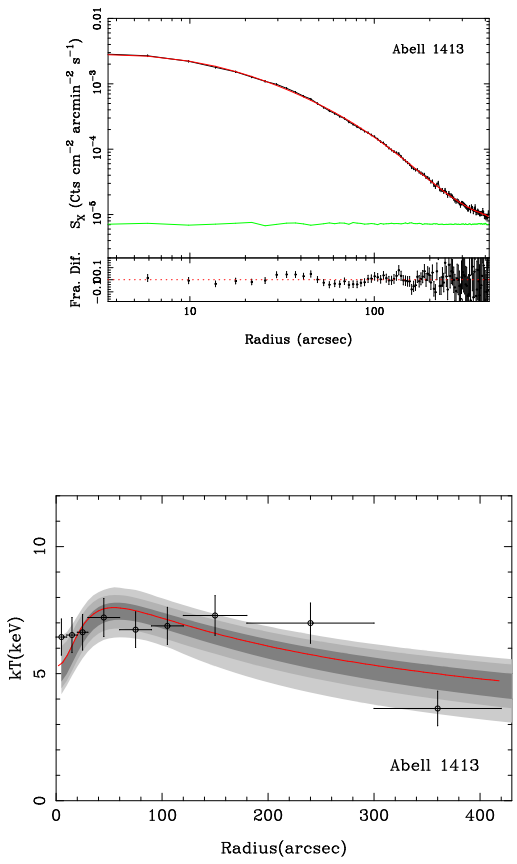

Figure 5.50: Abell 1413: Surface brightness and temperature profile from joint X-ray/SZE analysis.

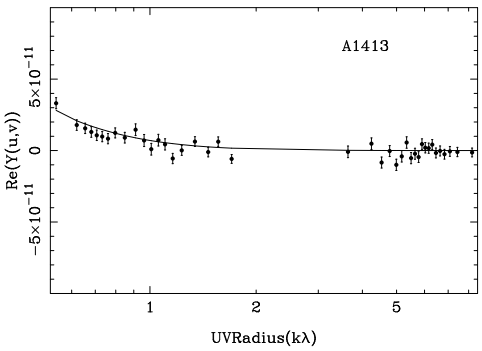

Figure 5.51: Abell 1413: SZE visibility profile plotted as a function of $u-v$ radius ($\sqrt{u^2+v^2}$). The plots show the real components of the measured visibilities along with the best fit model.

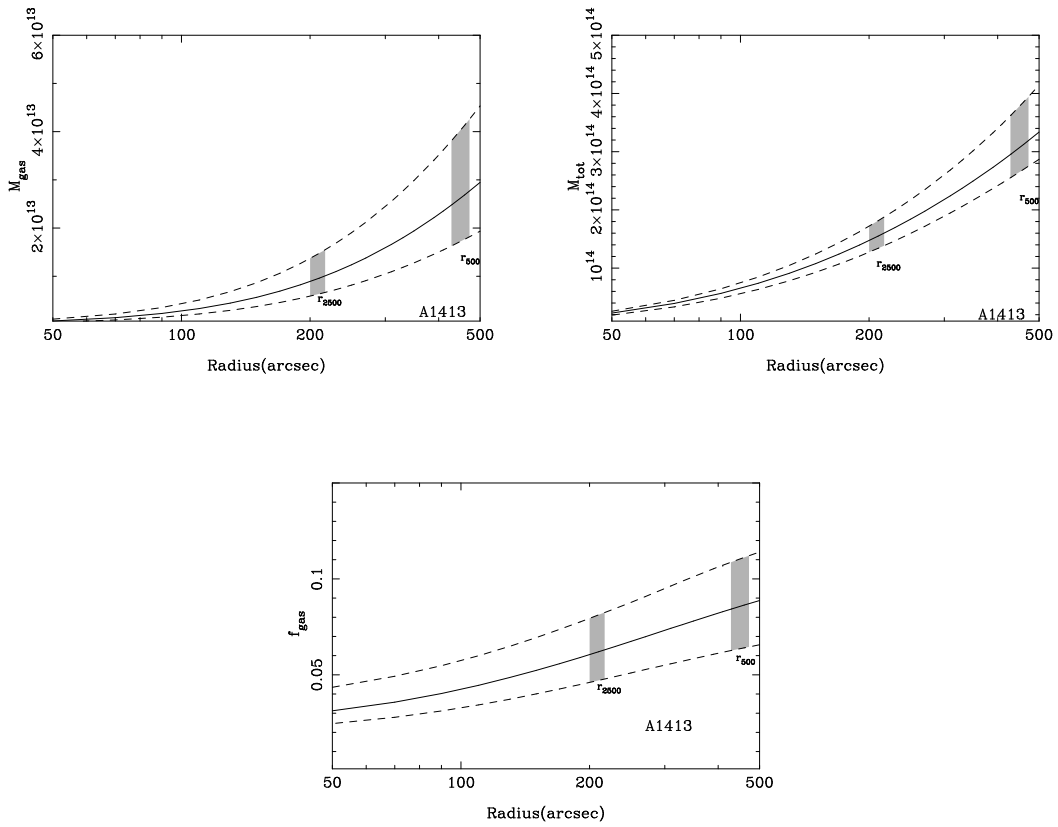

Figure 5.52: Abell 1413: Radial gas mass, total mass, and gas mass fraction profiles from joint X-ray/SZE analysis.

5.5.13 CLJ1226.9+3332

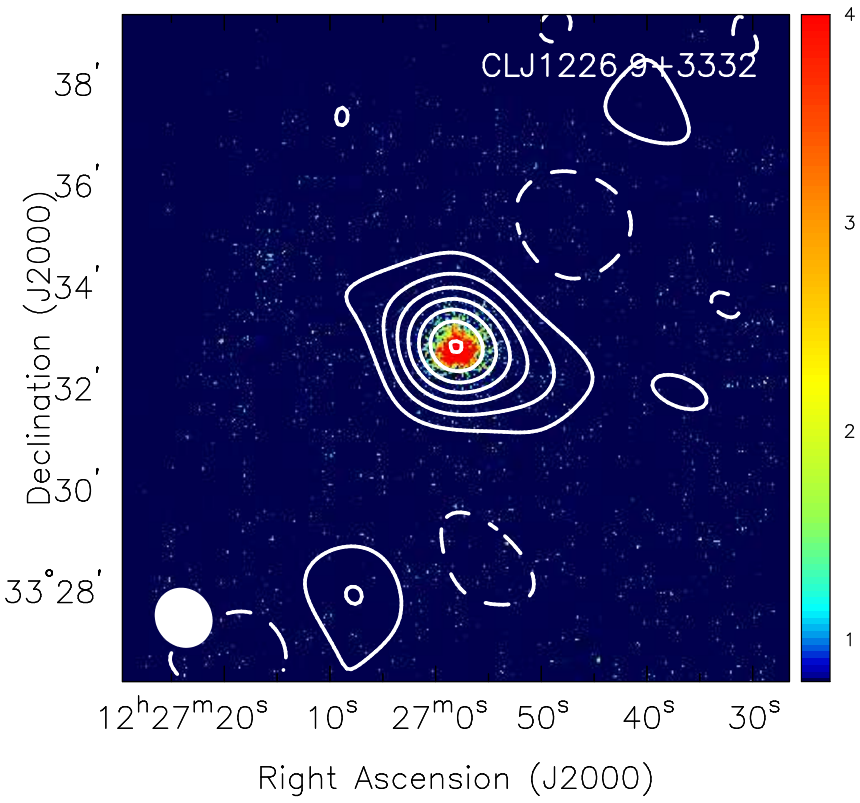

Figure 5.53: CLJ1226.9+3332: SZE contours overlaid on X-ray false color images. The *Chandra* X-ray surface brightness data are from the energy range 0.7–7.0 keV. The color bars reflect the number of counts detected by Chandra in the 0.7-7 keV band. The SZE data are from the SZA, and the contour levels are (+2,-2,-4,...) times the rms noise (see Table 3.1). The synthesized beams of the SZE observations are shown in the lower left corner of each image.

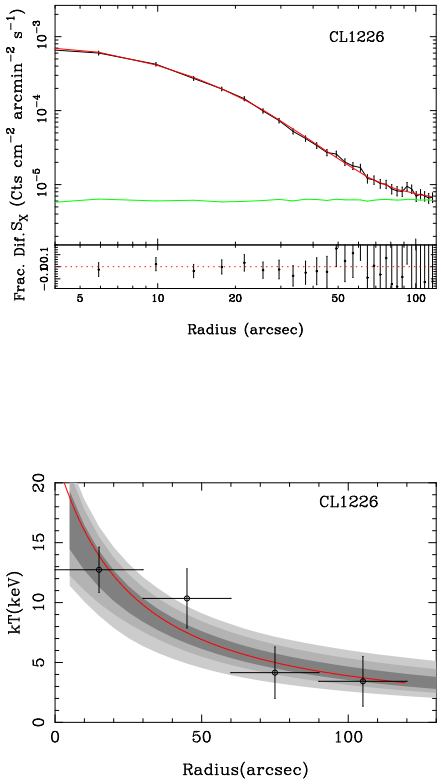

Figure 5.54: CLJ1226.9+3332: Surface brightness and temperature profile from joint X-ray/SZE analysis.

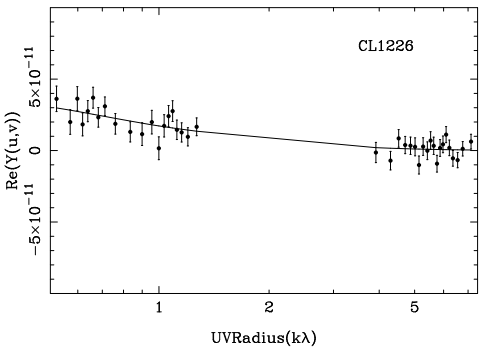

Figure 5.55: CLJ1226.9+3332: SZE visibility profile plotted as a function of $u-v$ radius ($\sqrt{u^2+v^2}$). The plots show the real components of the measured visibilities along with the best fit model.

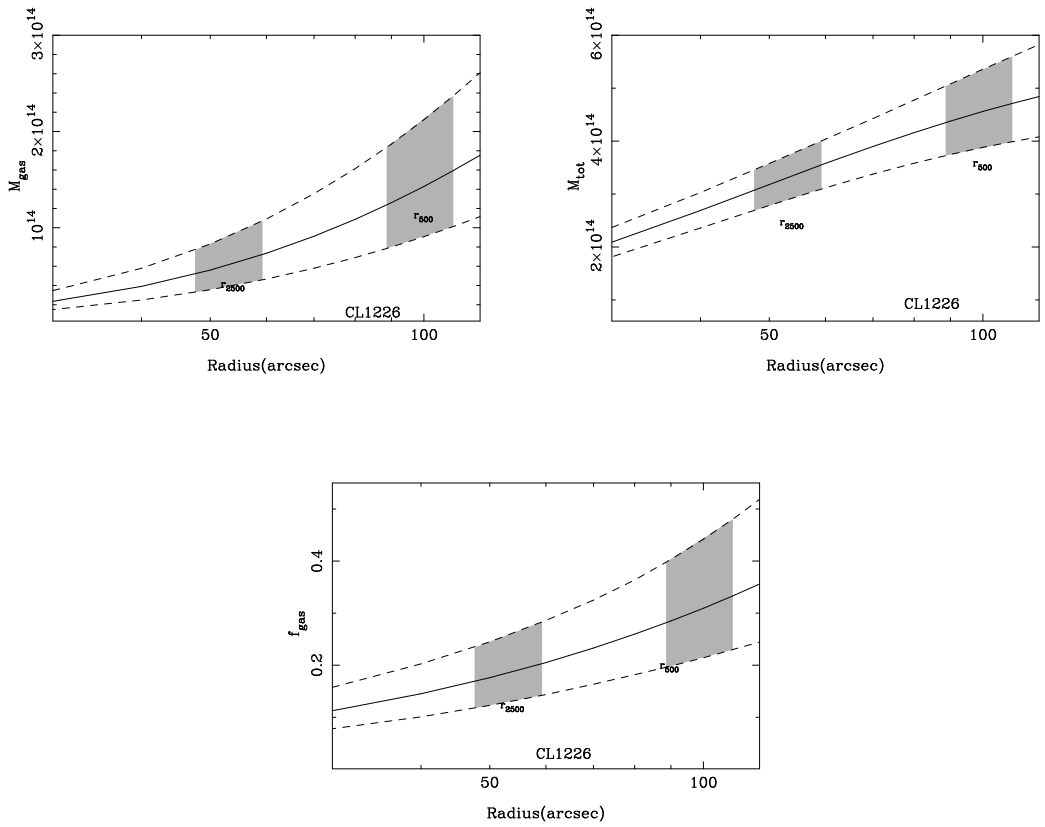

Figure 5.56: CLJ1226.9+3332: Radial gas mass, total mass, and gas mass fraction profiles from joint X-ray/SZE analysis.

5.5.14 MACS1311.0-0311

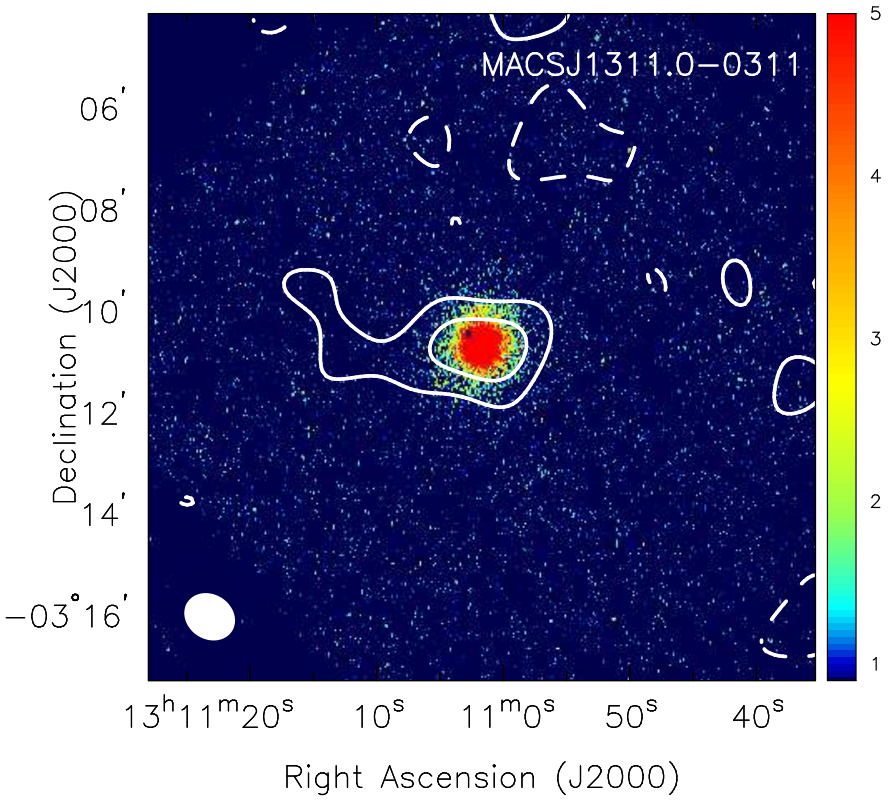

Figure 5.57: MACS1311.0-0311: SZE contours overlaid on X-ray false color images. The *Chandra* X-ray surface brightness data are from the energy range 0.7–7.0 keV. The color bars reflect the number of counts detected by Chandra in the 0.7-7 keV band. The SZE data are from the SZA, and the contour levels are (+2,-2,-4,...) times the rms noise (see Table 3.1). The synthesized beams of the SZE observations are shown in the lower left corner of each image.

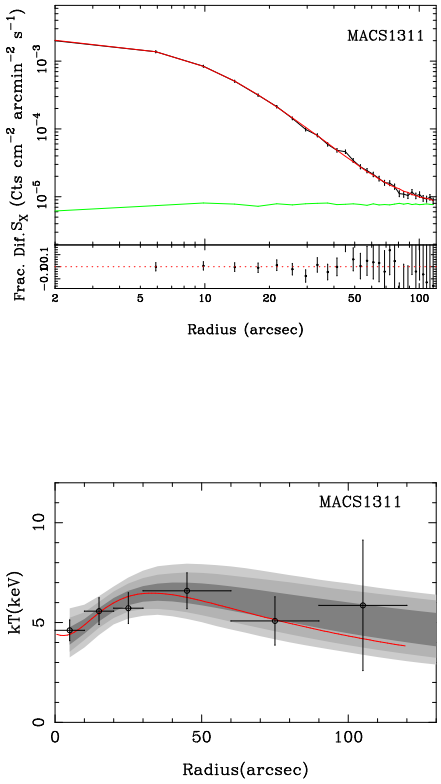

Figure 5.58: MACS1311.0-0311: Surface brightness and temperature profile from joint X-ray/SZE analysis.

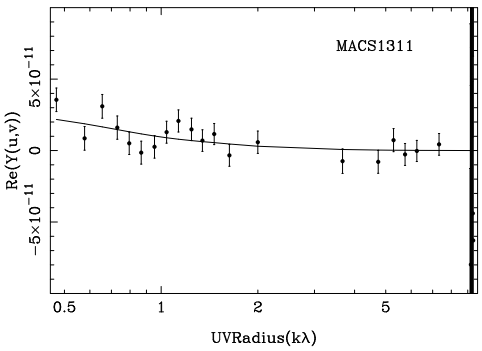

Figure 5.59: MACS1311.0-0311:SZE visibility profile plotted as a function of $u - v$ radius ($\sqrt{u^2 + v^2}$). The plots show the real components of the measured visibilities along with the best fit model.

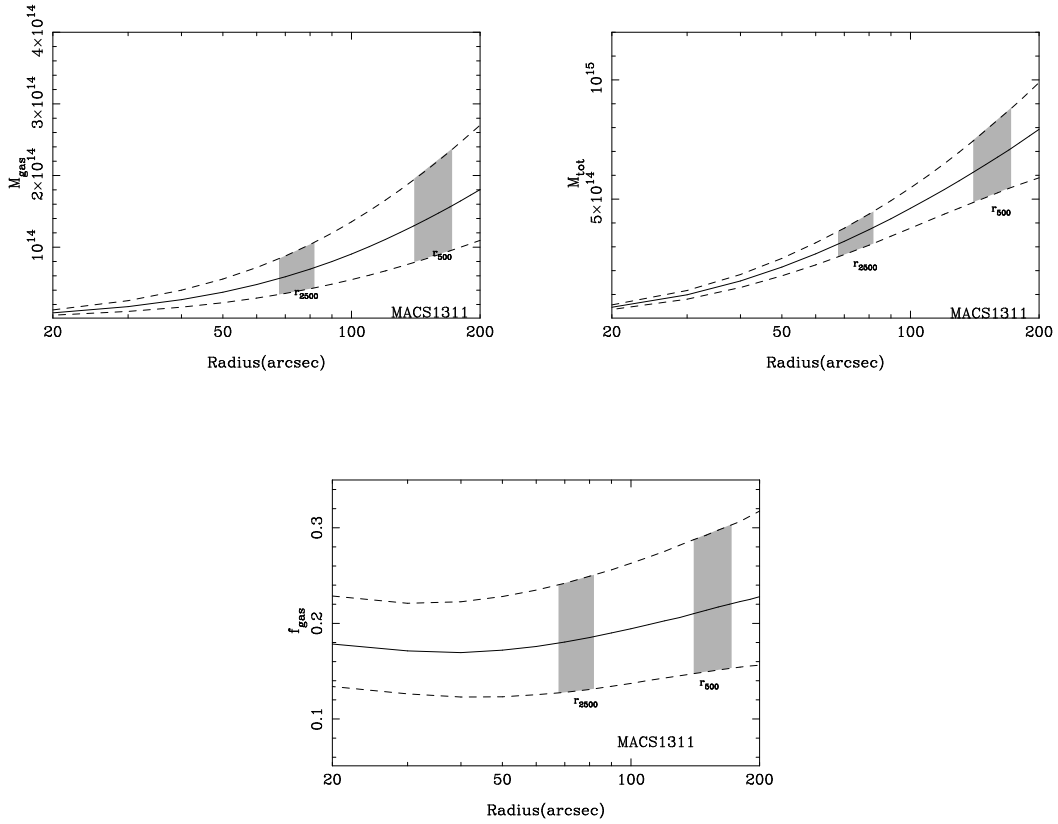

Figure 5.60: MACS1311.0-0311: Radial gas mass, total mass, and gas mass fraction profiles from joint X-ray/SZE analysis.

5.5.15 RXJ1347.5-1145

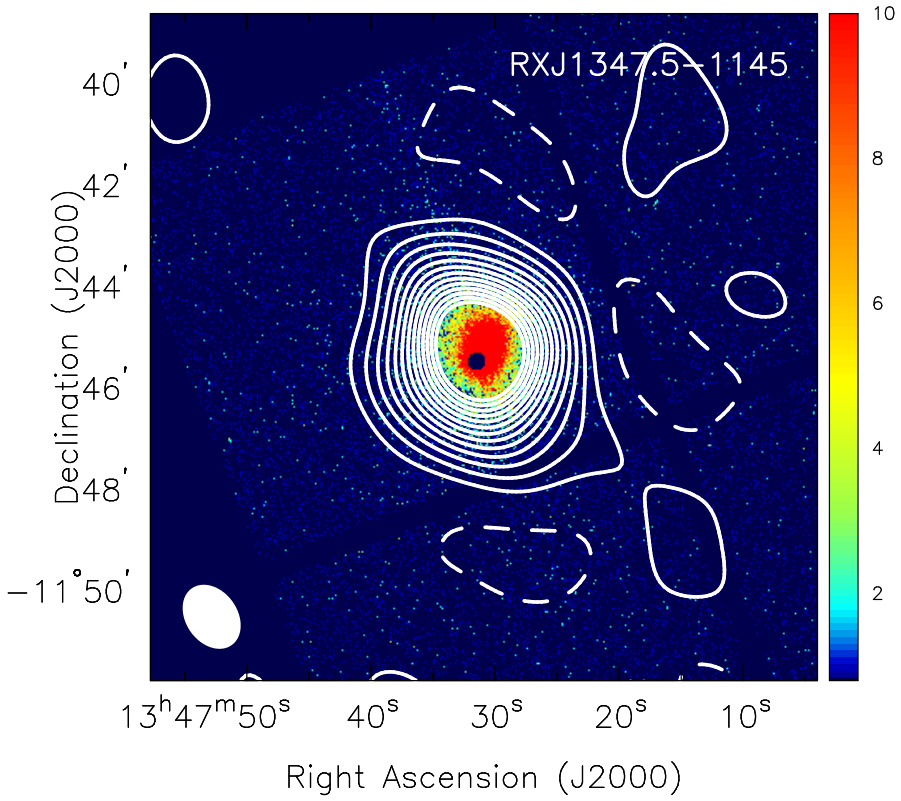

Figure 5.61: RXJ1347.5-1145: SZE contours overlaid on X-ray false color images. The *Chandra* X-ray surface brightness data are from the energy range 0.7–7.0 keV. The color bars reflect the number of counts detected by Chandra in the 0.7-7 keV band. The SZE data are from the SZA, and the contour levels are (+2,-2,-4,...) times the rms noise (see Table 3.1). The synthesized beams of the SZE observations are shown in the lower left corner of each image.

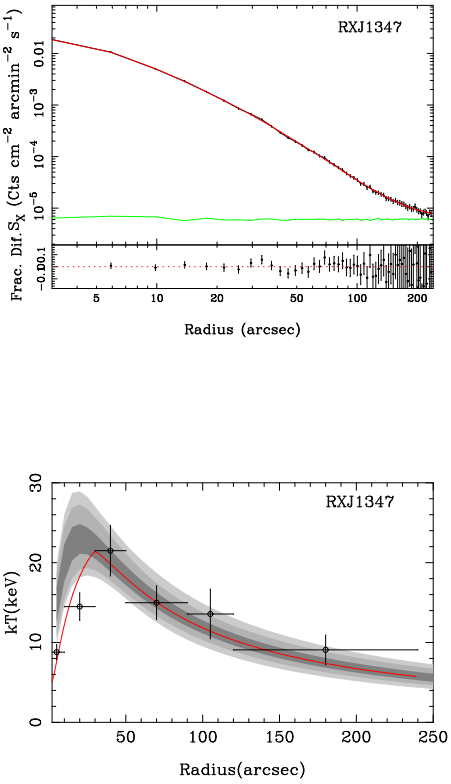

Figure 5.62: RXJ1347.5-1145: Surface brightness and temperature profile from joint X-ray/SZE analysis.

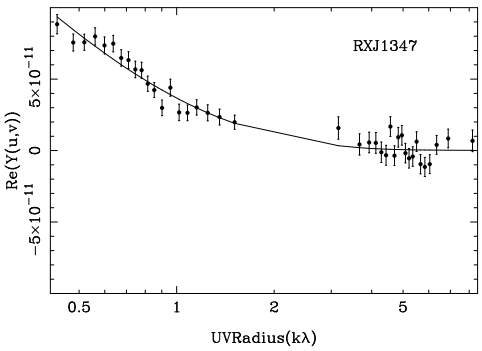

Figure 5.63: RXJ1347.5-1145: SZE visibility profile plotted as a function of $u - v$ radius ($\sqrt{u^2 + v^2}$). The plots show the real components of the measured visibilities along with the best fit model.

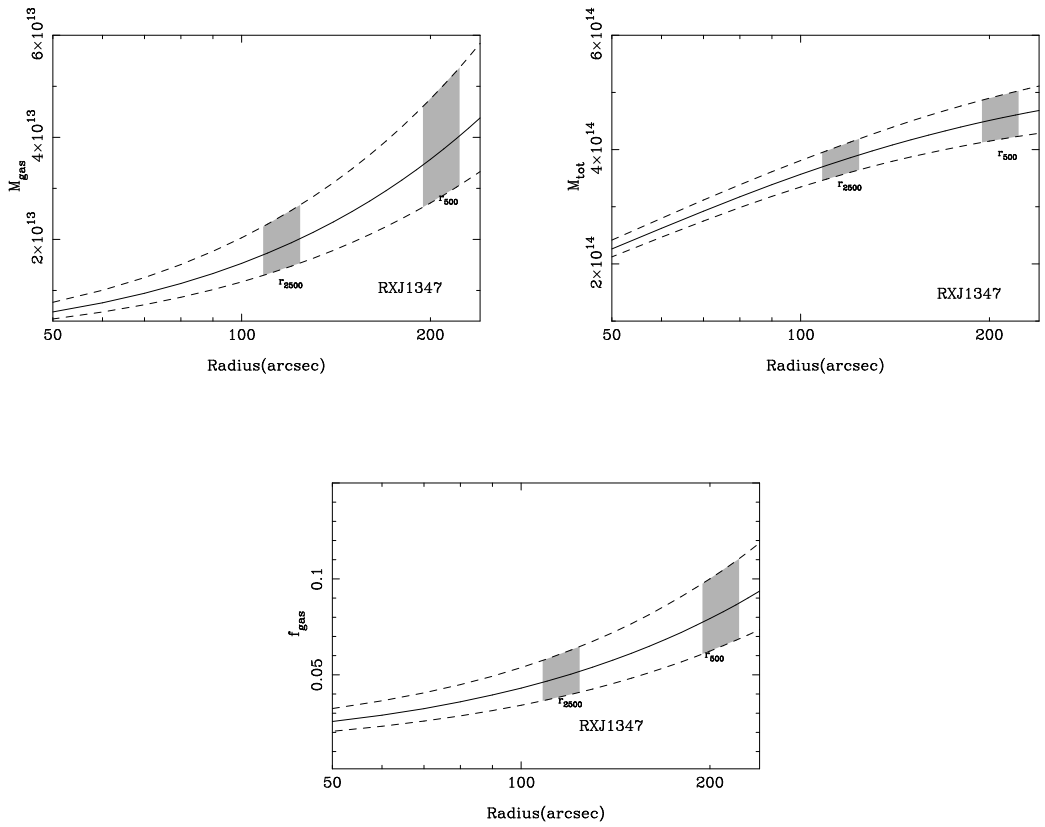

Figure 5.64: RXJ1347.5-1145: Radial gas mass, total mass, and gas mass fraction profiles from joint X-ray/SZE analysis.

5.5.16 Abell 1835

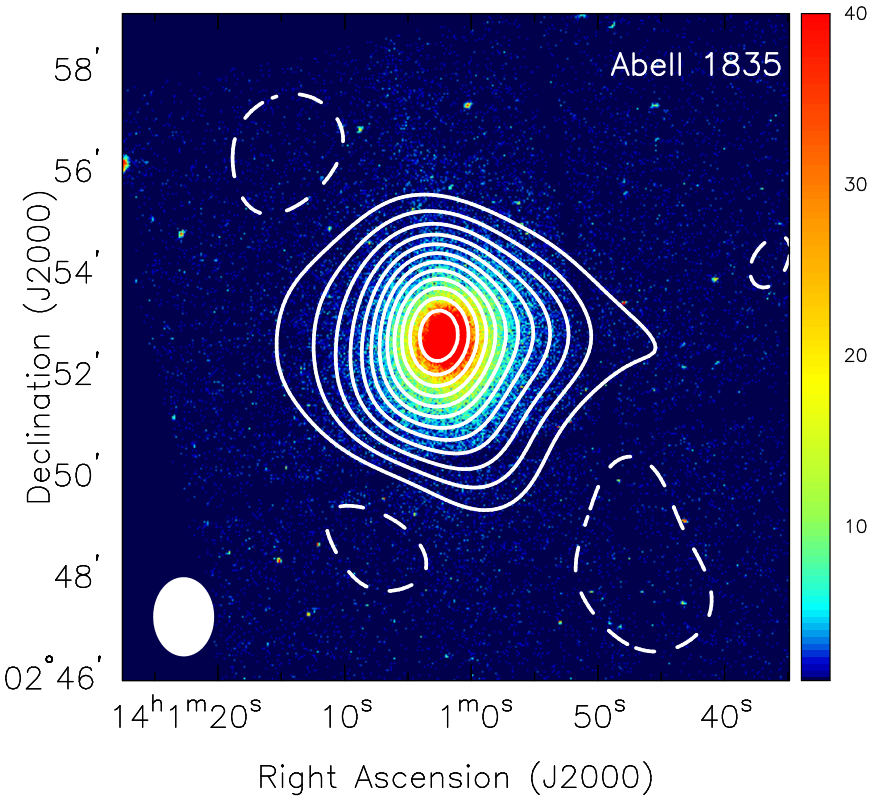

Figure 5.65: Abell 1835: SZE contours overlaid on X-ray false color images. The *Chandra* X-ray surface brightness data are from the energy range 0.7–7.0 keV. The color bars reflect the number of counts detected by Chandra in the 0.7-7 keV band. The SZE data are from the SZA, and the contour levels are (+2,-2,-4,...) times the rms noise (see Table 3.1). The synthesized beams of the SZE observations are shown in the lower left corner of each image.

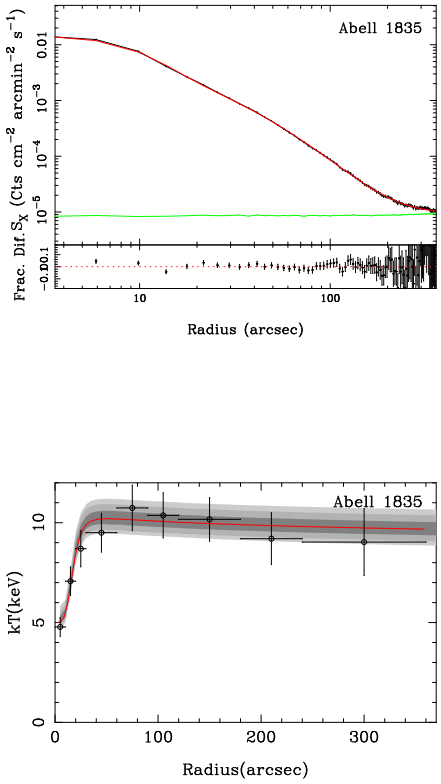

Figure 5.66: Abell 1835: Surface brightness and temperature profile from joint X-ray/SZE analysis.

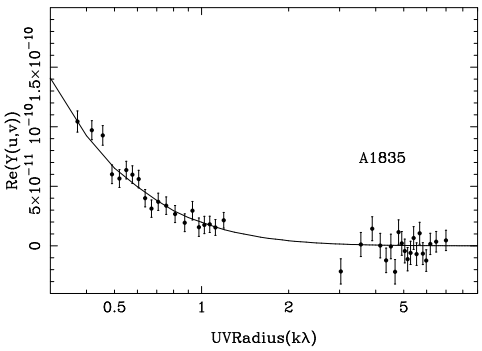

Figure 5.67: Abell 1835: SZE visibility profile plotted as a function of $u - v$ radius ($\sqrt{u^2 + v^2}$). The plots show the real components of the measured visibilities along with the best fit model.

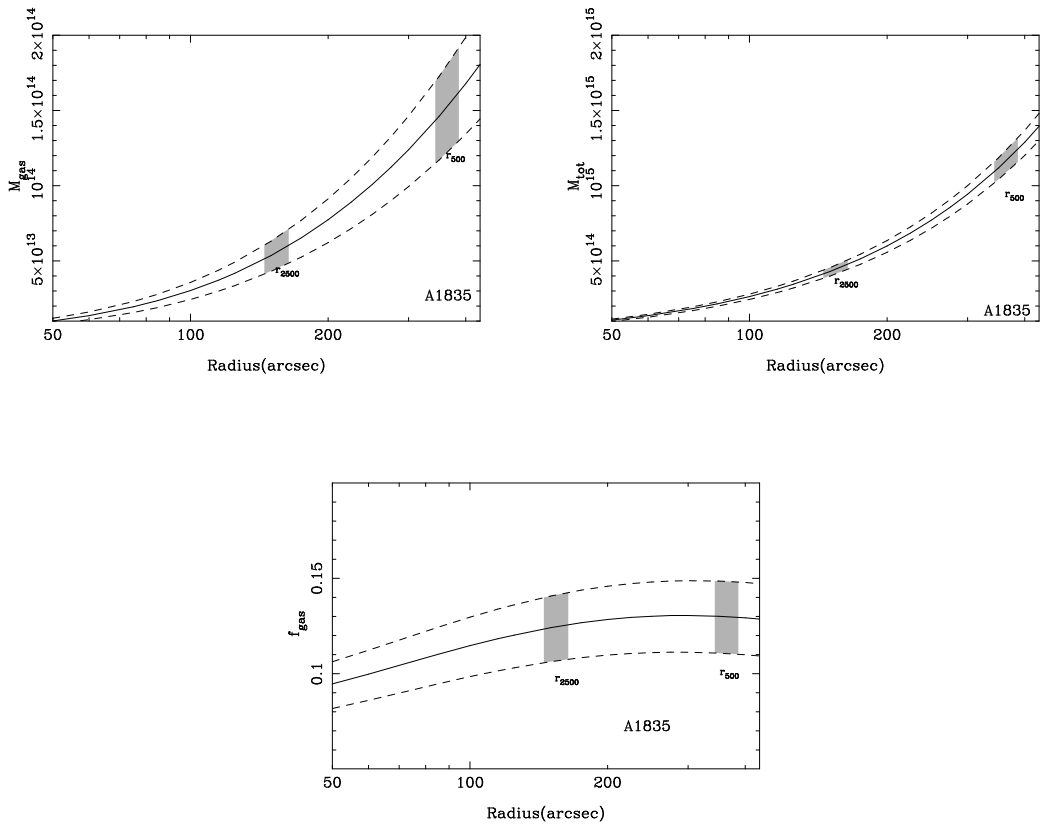

Figure 5.68: Abell 1835: Radial gas mass, total mass, and gas mass fraction profiles from joint X-ray/SZE analysis.

5.5.17 MACSJ1423.8+2404

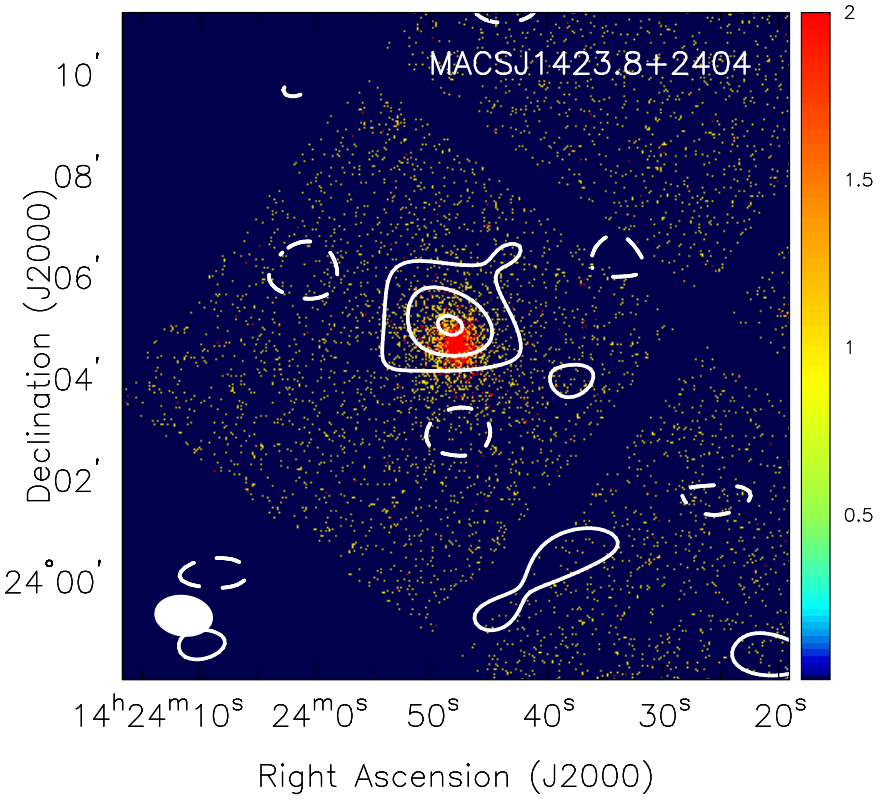

Figure 5.69: MACSJ1423.8+2404: SZE contours overlaid on X-ray false color images. The *Chandra* X-ray surface brightness data are from the energy range 0.7–7.0 keV. The color bars reflect the number of counts detected by Chandra in the 0.7-7 keV band. The SZE data are from the SZA, and the contour levels are (+2,-2,-4,...) times the rms noise (see Table 3.1). The synthesized beams of the SZE observations are shown in the lower left corner of each image.

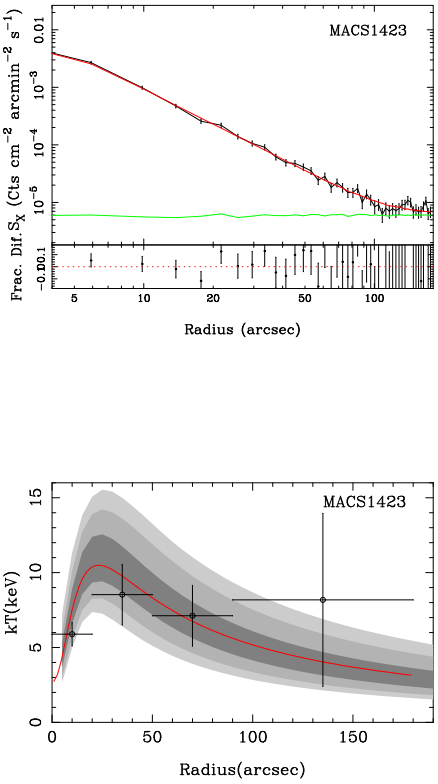

Figure 5.70: MACSJ1423.8+2404: Surface brightness and temperature profile from joint X-ray/SZE analysis.

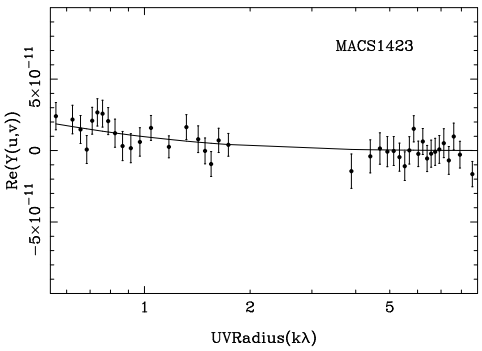

Figure 5.71: MACSJ1423.8+2404: SZE visibility profile plotted as a function of $u-v$ radius ($\sqrt{u^2+v^2}$). The plots show the real components of the measured visibilities along with the best fit model.

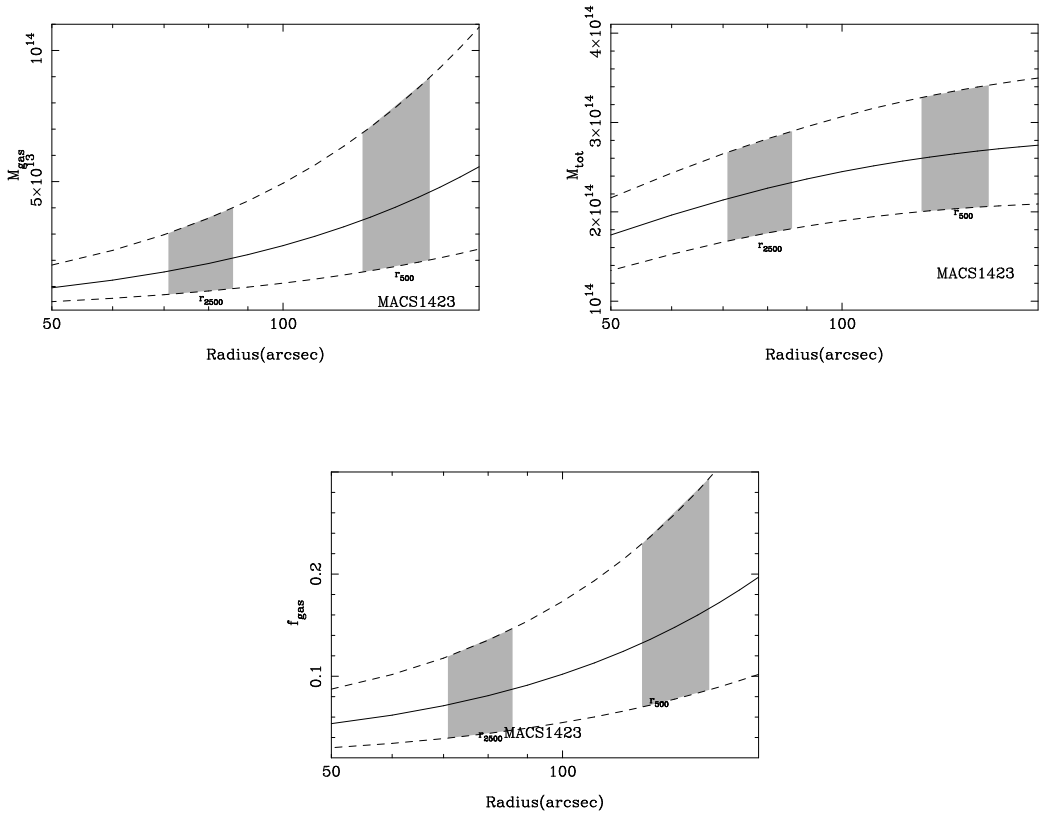

Figure 5.72: MACSJ1423.8+2404: Radial gas mass, total mass, and gas mass fraction profiles from joint X-ray/SZE analysis.

5.5.18 MACSJ1427.3+4408

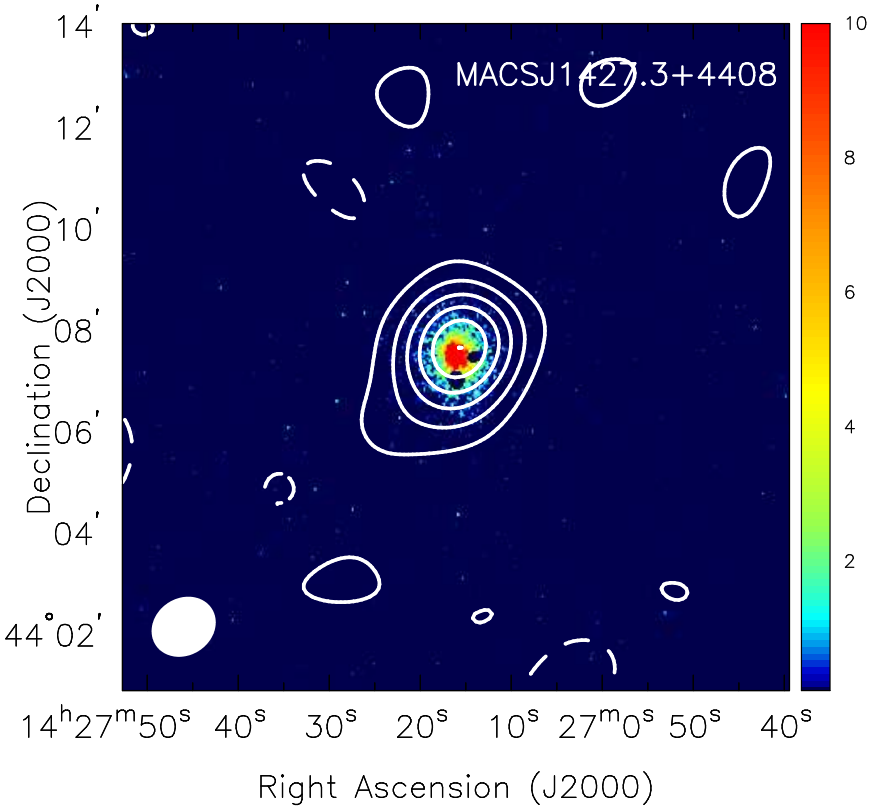

Figure 5.73: MACSJ1427.3+4408: SZE contours overlaid on X-ray false color images. The *Chandra* X-ray surface brightness data are from the energy range 0.7–7.0 keV. The color bars reflect the number of counts detected by Chandra in the 0.7-7 keV band. The SZE data are from the SZA, and the contour levels are (+2,-2,-4,...) times the rms noise (see Table 3.1). The synthesized beams of the SZE observations are shown in the lower left corner of each image.

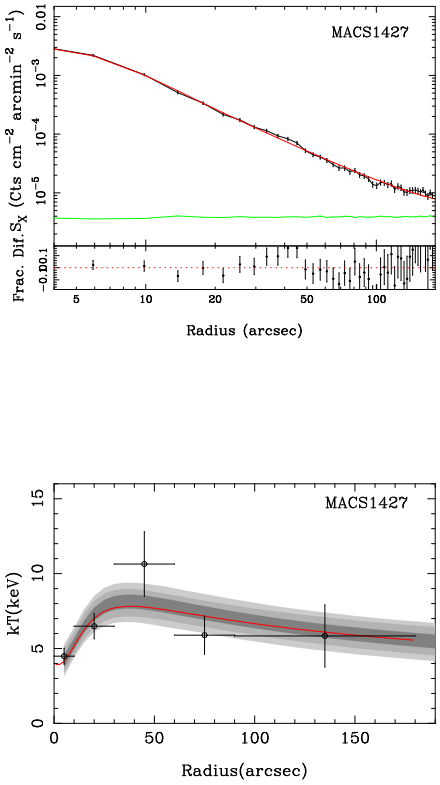

Figure 5.74: MACSJ1427.3+4408: Surface brightness and temperature profile from joint X-ray/SZE analysis.

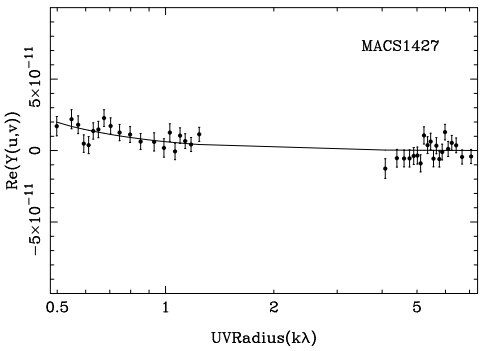

Figure 5.75: MACSJ1427.3+4408: SZE visibility profile plotted as a function of $u-v$ radius ($\sqrt{u^2+v^2}$). The plots show the real components of the measured visibilities along with the best fit model.

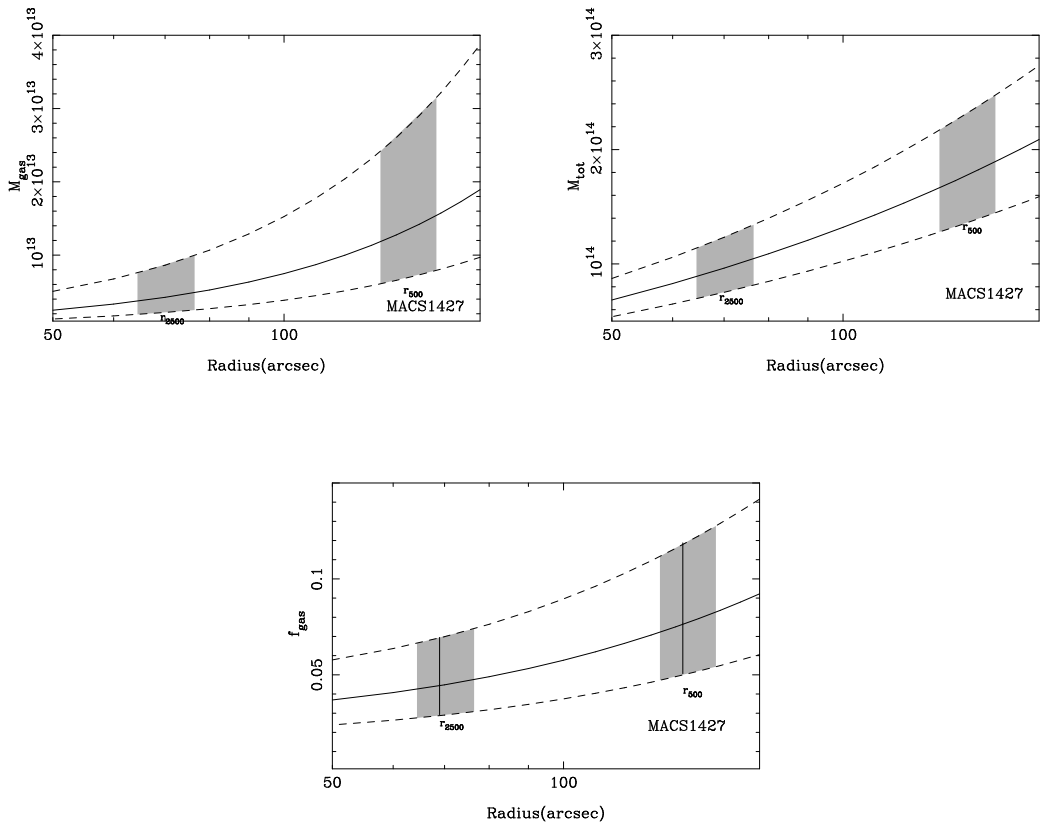

Figure 5.76: MACSJ1427.3+4408: Radial gas mass, total mass, and gas mass fraction profiles from joint X-ray/SZE analysis.

5.5.19 RXJ1504.1-0248

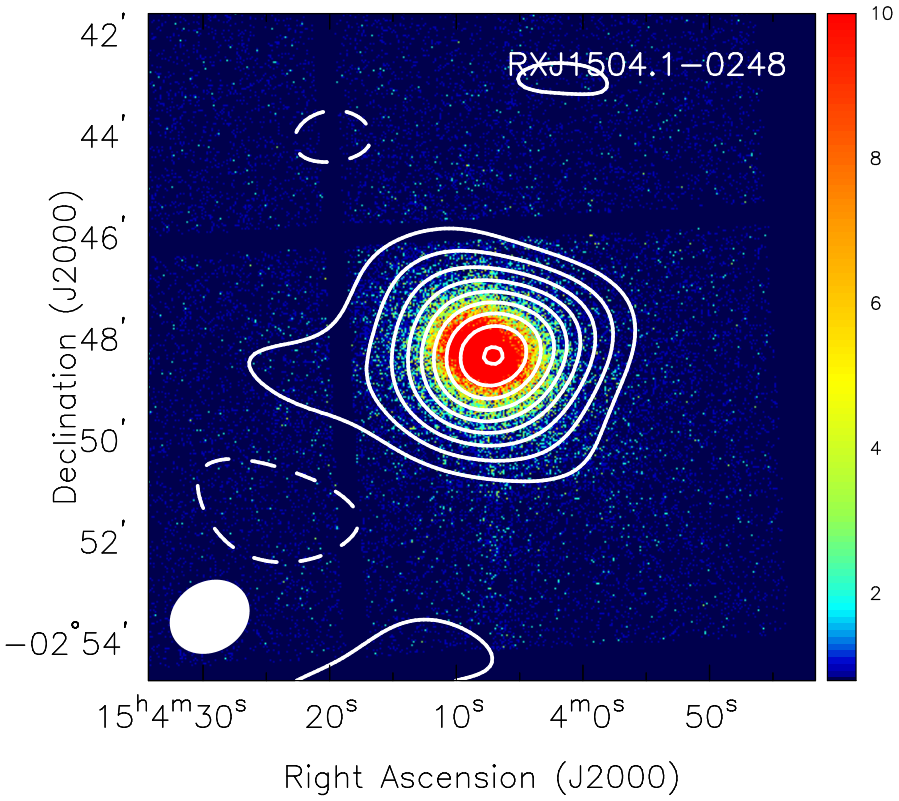

Figure 5.77: RXJ1504.1-0248: SZE contours overlaid on X-ray false color images. The *Chandra* X-ray surface brightness data are from the energy range 0.7–7.0 keV. The color bars reflect the number of counts detected by Chandra in the 0.7-7 keV band. The SZE data are from the SZA, and the contour levels are (+2,-2,-4,...) times the rms noise (see Table 3.1). The synthesized beams of the SZE observations are shown in the lower left corner of each image.

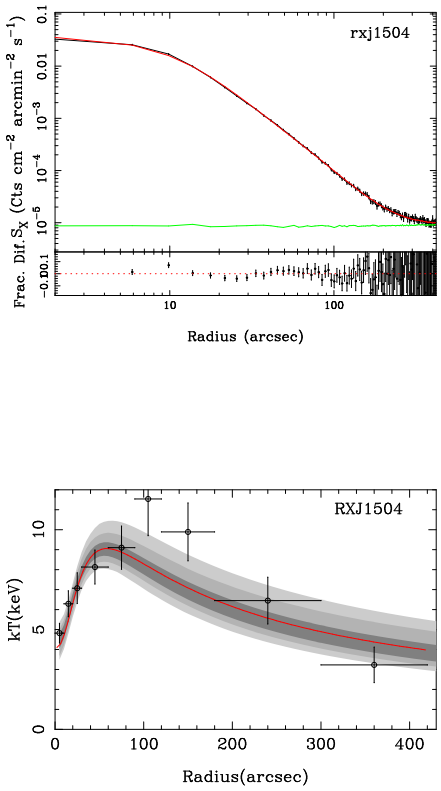

Figure 5.78: RXJ1504.1-0248: Surface brightness and temperature profile from joint X-ray/SZE analysis.

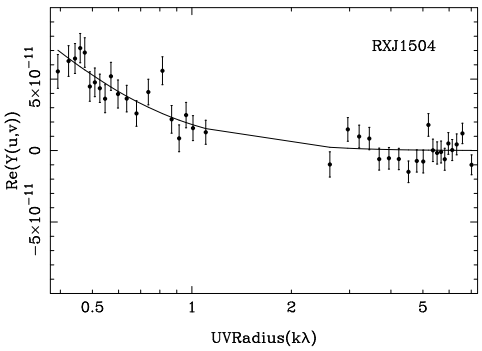

Figure 5.79: RXJ1504.1-0248: SZE visibility profile plotted as a function of $u - v$ radius ($\sqrt{u^2 + v^2}$). The plots show the real components of the measured visibilities along with the best fit model.

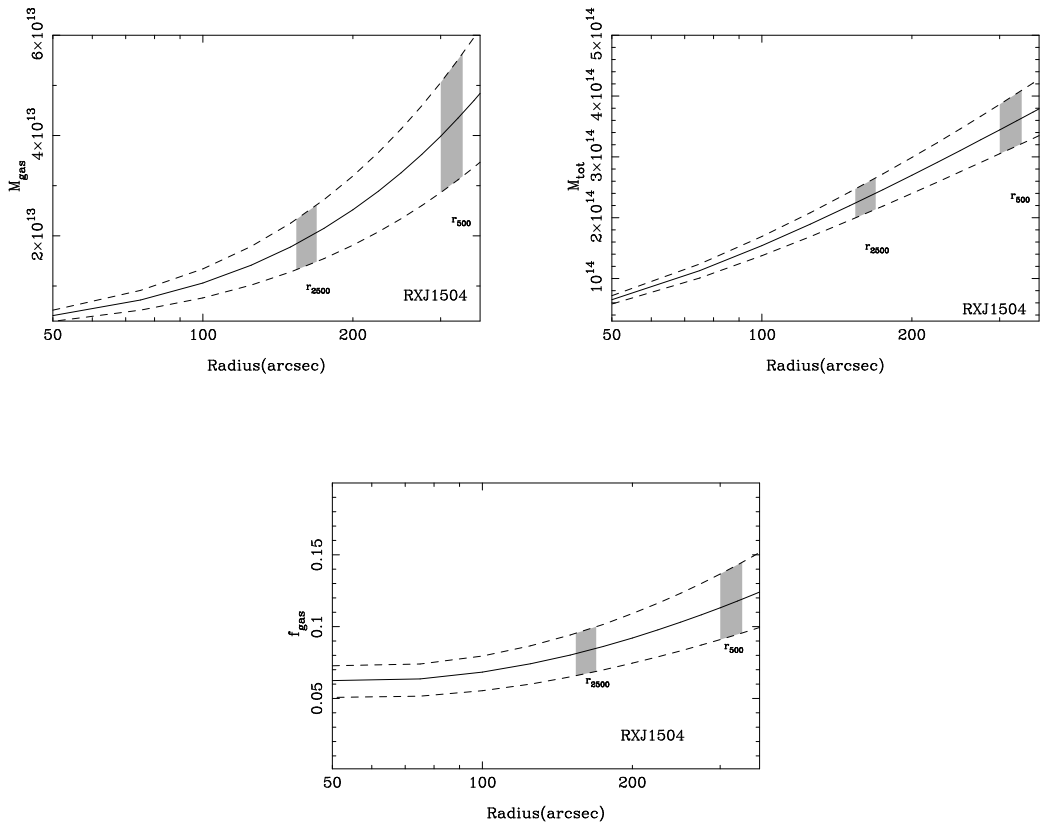

Figure 5.80: RXJ1504.1-0248: Radial gas mass, total mass, and gas mass fraction profiles from joint X-ray/SZE analysis.

5.5.20 MACSJ1523.9+3021

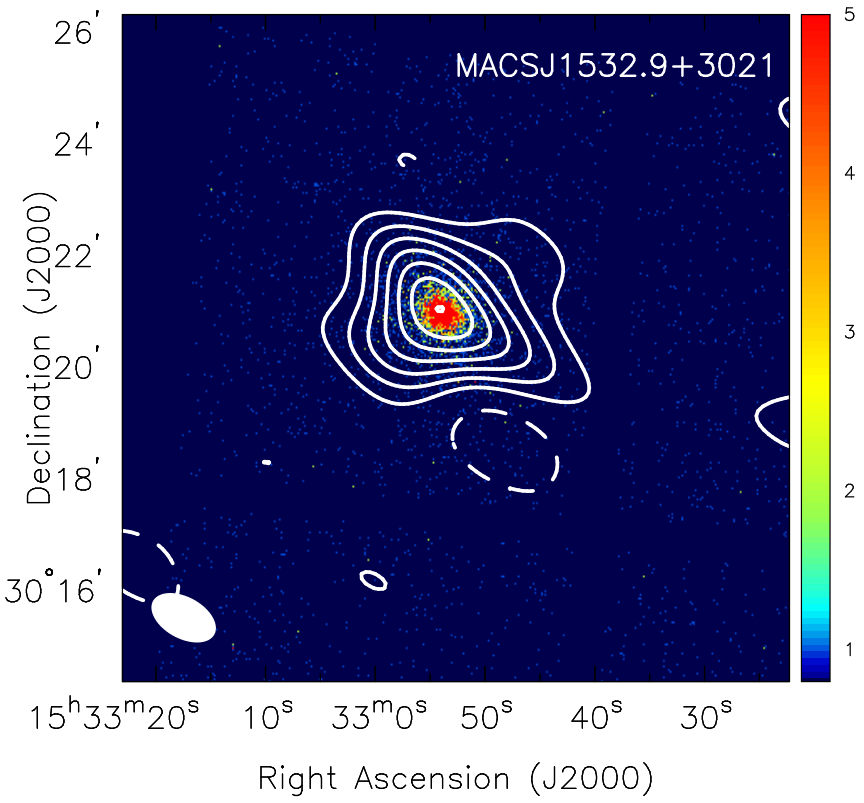

Figure 5.81: MACSJ1532.9+3021: SZE contours overlaid on X-ray false color images. The *Chandra* X-ray surface brightness data are from the energy range 0.7–7.0 keV. The color bars reflect the number of counts detected by Chandra in the 0.7-7 keV band. The SZE data are from the SZA, and the contour levels are (+2,-2,-4,...) times the rms noise (see Table 3.1). The synthesized beams of the SZE observations are shown in the lower left corner of each image.

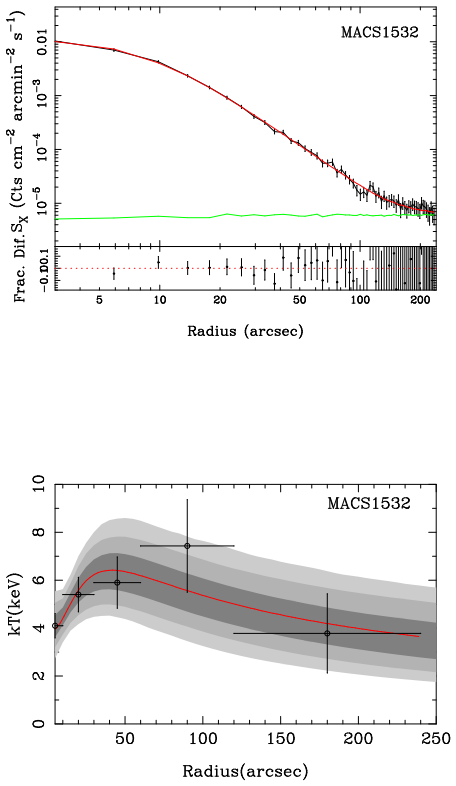

Figure 5.82: MACSJ1532.9+3021: Surface brightness and temperature profile from joint X-ray/SZE analysis.

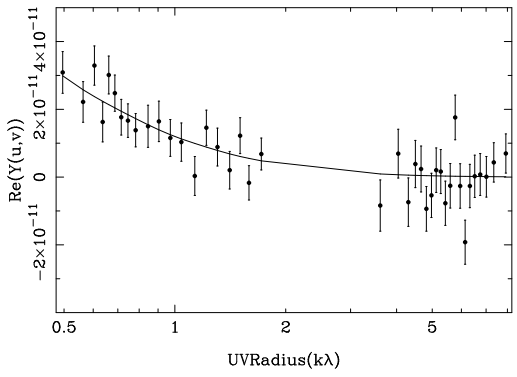

Figure 5.83: MACSJ1532.9+3021: SZE visibility profile plotted as a function of $u-v$ radius ($\sqrt{u^2+v^2}$). The plots show the real components of the measured visibilities along with the best fit model.

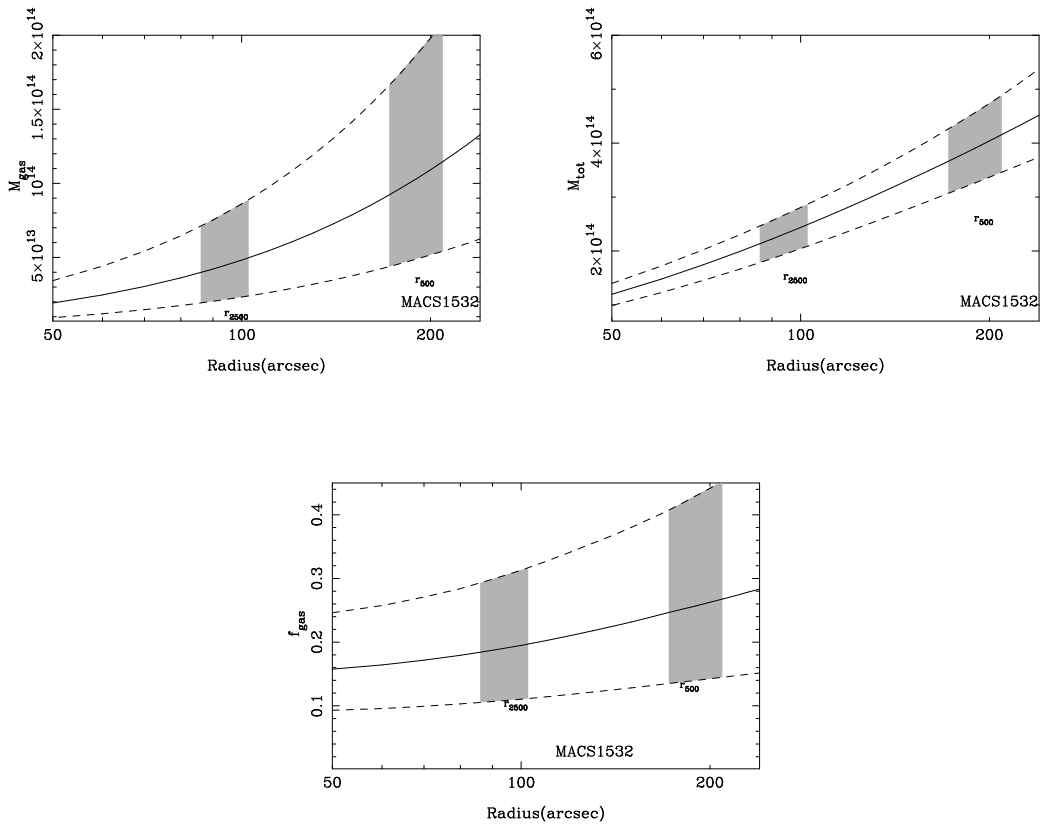

Figure 5.84: MACSJ1532.9+3021: Radial gas mass, total mass, and gas mass fraction profiles from joint X-ray/SZE analysis.

5.5.21 MACSJ1621.6+3810

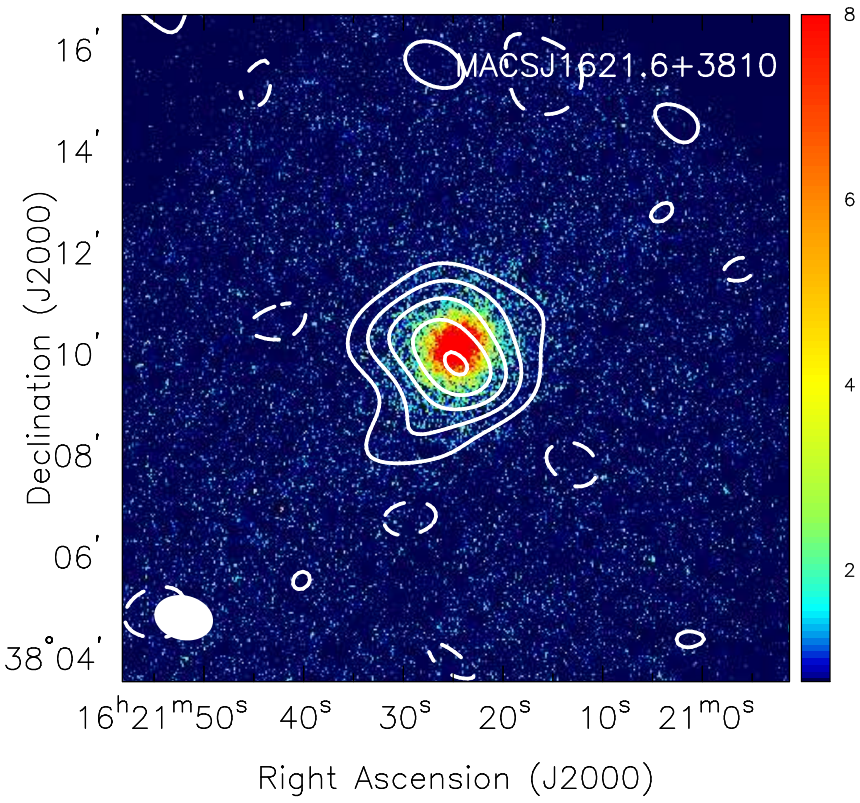

Figure 5.85: MACSJ1621.6+3810: SZE contours overlaid on X-ray false color images. The *Chandra* X-ray surface brightness data are from the energy range 0.7–7.0 keV. The color bars reflect the number of counts detected by Chandra in the 0.7-7 keV band. The SZE data are from the SZA, and the contour levels are (+2,-2,-4,...) times the rms noise (see Table 3.1). The synthesized beams of the SZE observations are shown in the lower left corner of each image.

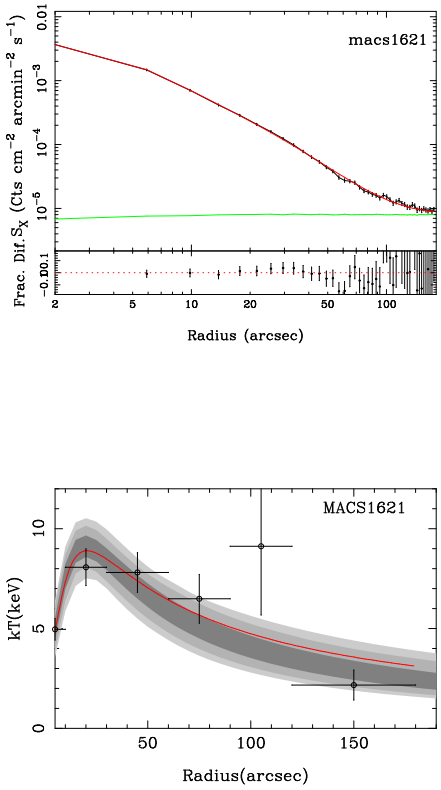

Figure 5.86: MACSJ1621.6+3810: Surface brightness and temperature profile from joint X-ray/SZE analysis.

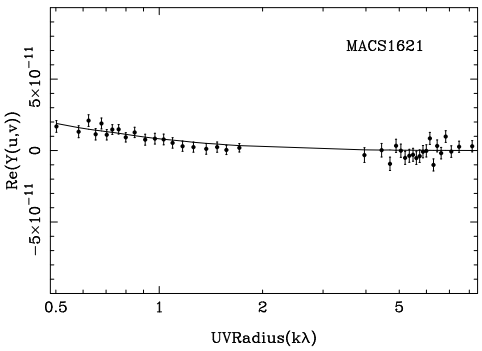

Figure 5.87: MACSJ1621.6+3810: SZE visibility profile plotted as a function of $u-v$ radius ($\sqrt{u^2+v^2}$). The plots show the real components of the measured visibilities along with the best fit model.

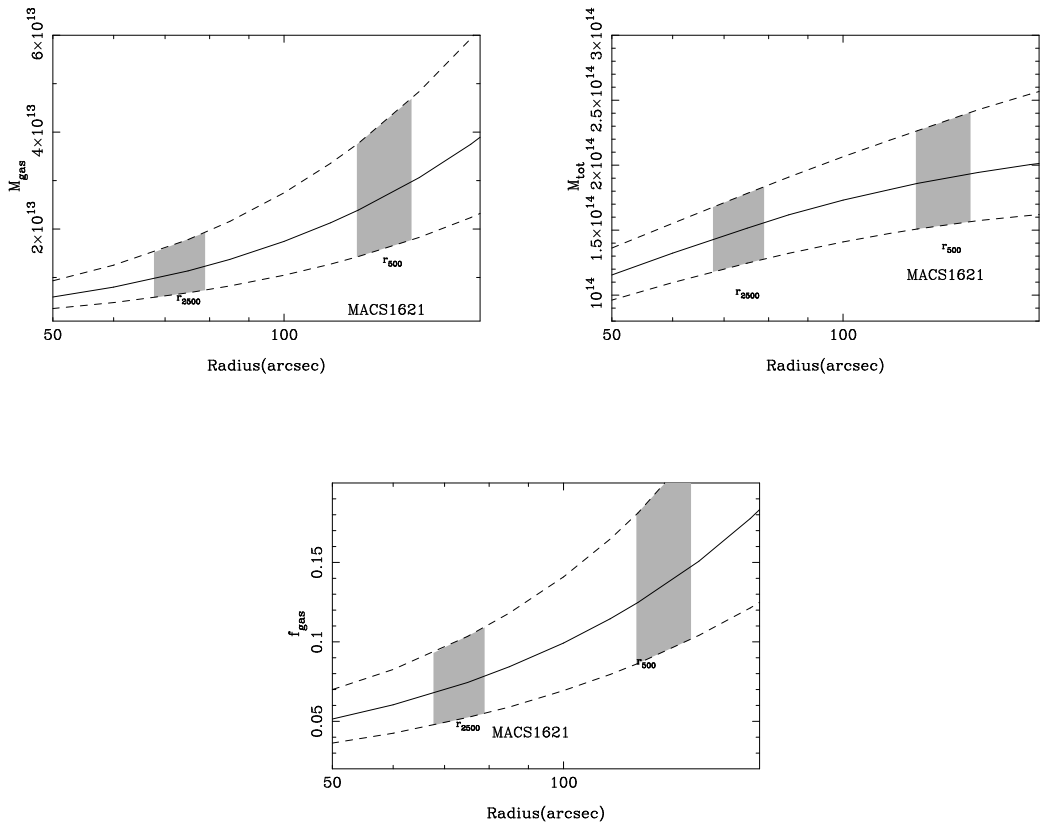

Figure 5.88: MACSJ1621.6+3810: Radial gas mass, total mass, and gas mass fraction profiles from joint X-ray/SZE analysis.

5.5.22 Abell 2204

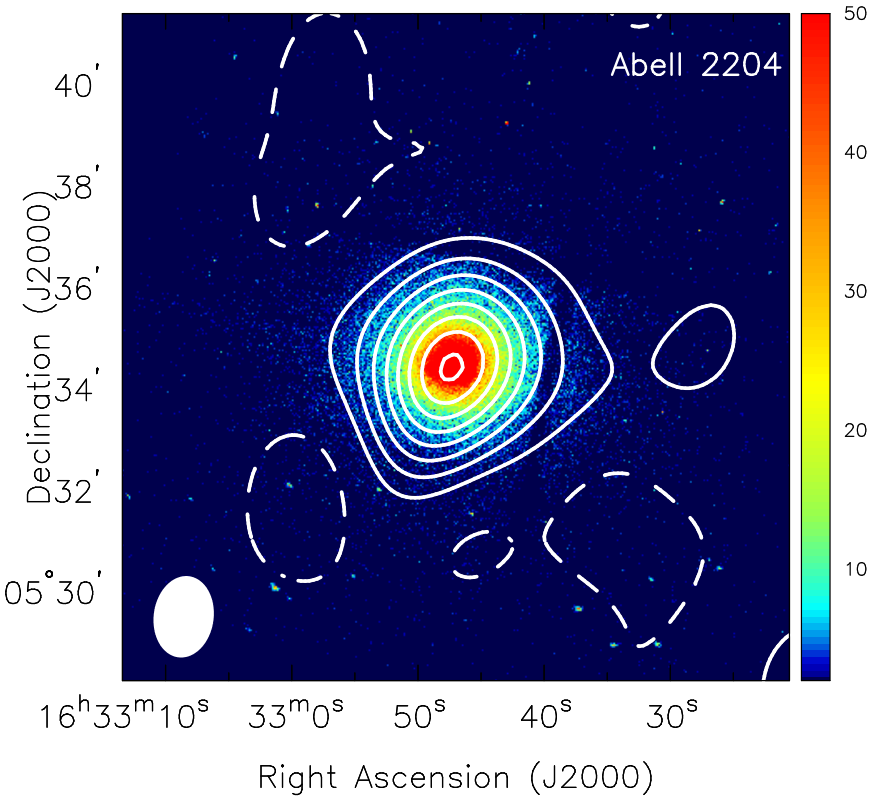

Figure 5.89: Abell 2204: SZE contours overlaid on X-ray false color images. The *Chandra* X-ray surface brightness data are from the energy range 0.7–7.0 keV. The color bars reflect the number of counts detected by Chandra in the 0.7-7 keV band. The SZE data are from the SZA, and the contour levels are (+2,-2,-4,...) times the rms noise (see Table 3.1). The synthesized beams of the SZE observations are shown in the lower left corner of each image.

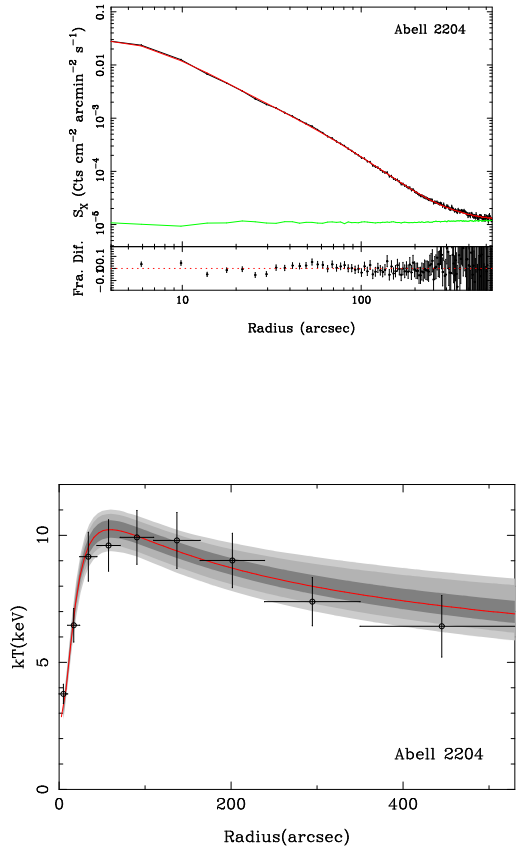

Figure 5.90: Abell 2204: Surface brightness and temperature profile from joint X-ray/SZE analysis.

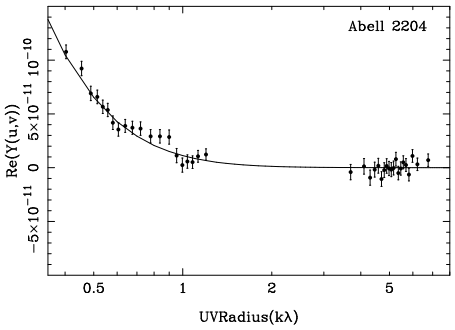

Figure 5.91: Abell 2204: SZE visibility profile plotted as a function of $u - v$ radius ($\sqrt{u^2 + v^2}$). The plots show the real components of the measured visibilities along with the best fit model.

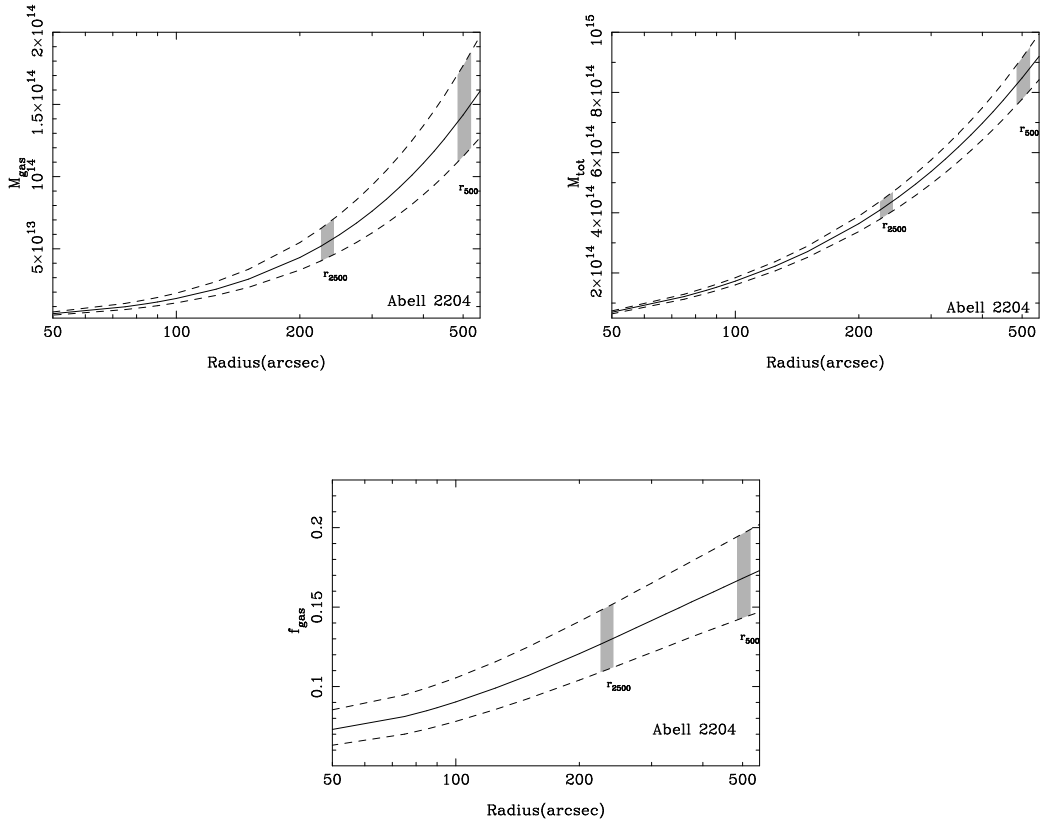

Figure 5.92: Abell 2204: Radial gas mass, total mass, and gas mass fraction profiles from joint X-ray/SZE analysis.

5.5.23 MACSJ1720.3+3536

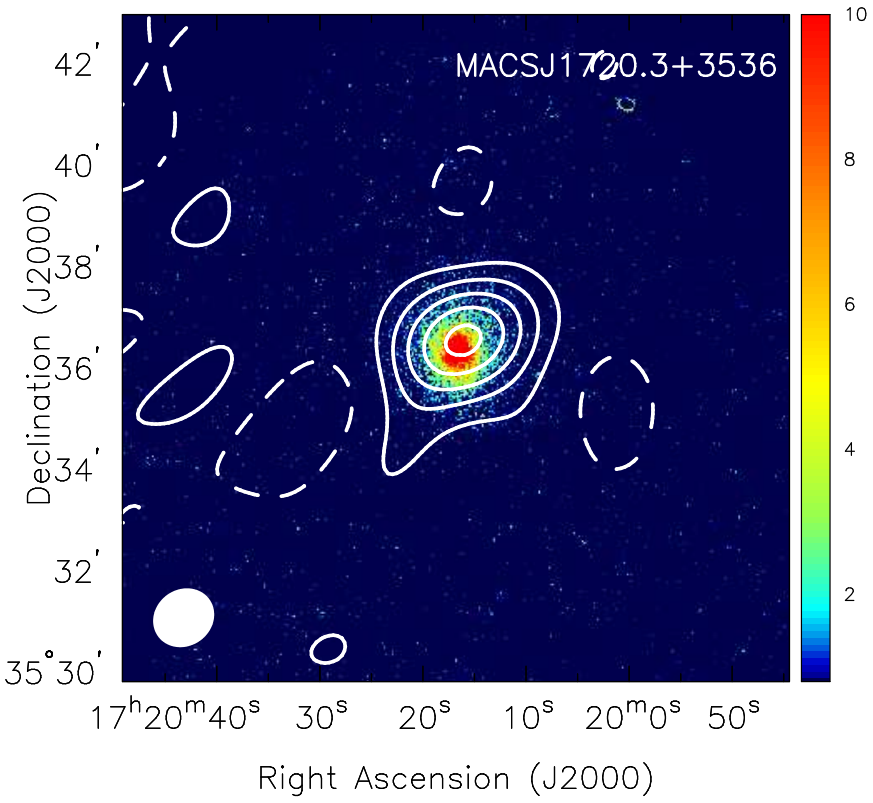

Figure 5.93: MACSJ1720.3+3536: SZE contours overlaid on X-ray false color images. The *Chandra* X-ray surface brightness data are from the energy range 0.7–7.0 keV. The color bars reflect the number of counts detected by Chandra in the 0.7-7 keV band. The SZE data are from the SZA, and the contour levels are (+2,-2,-4,...) times the rms noise (see Table 3.1). The synthesized beams of the SZE observations are shown in the lower left corner of each image.

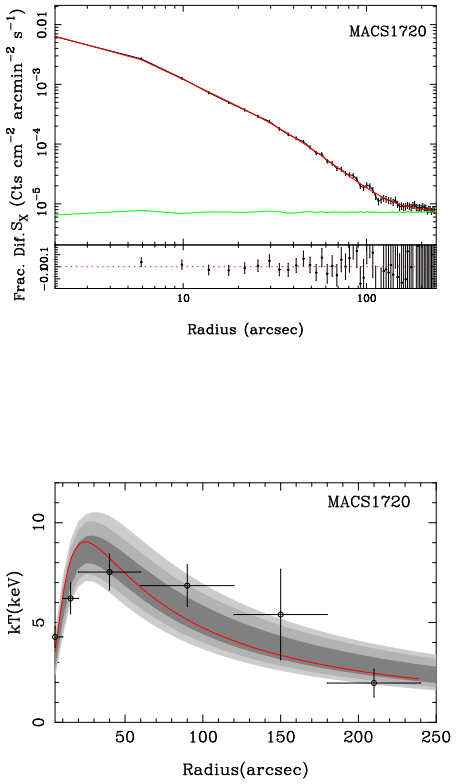

Figure 5.94: MACSJ1720.3+3536: Surface brightness and temperature profile from joint X-ray/SZE analysis.

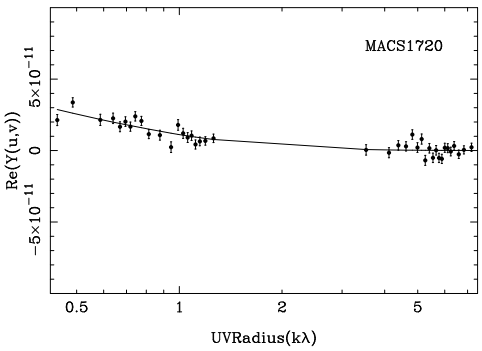

Figure 5.95: MACSJ1720.3+3536: SZE visibility profile plotted as a function of $u-v$ radius ($\sqrt{u^2+v^2}$). The plots show the real components of the measured visibilities along with the best fit model.

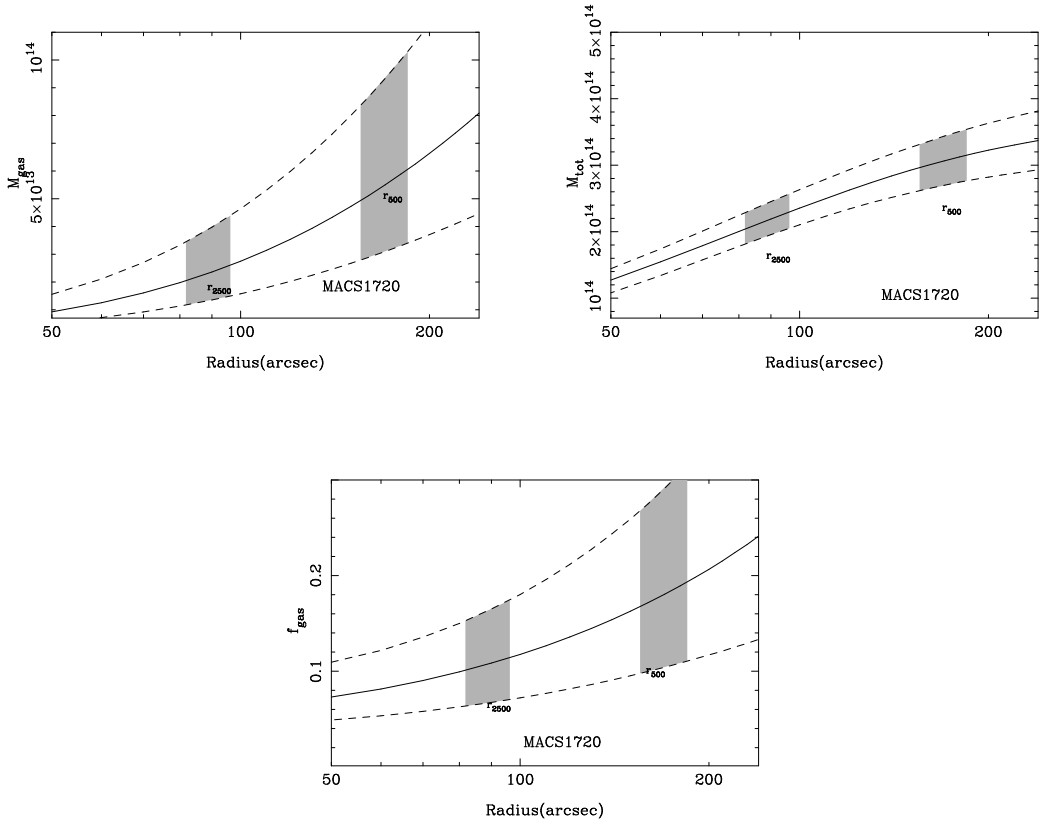

Figure 5.96: MACSJ1720.3+3536: Radial gas mass, total mass, and gas mass fraction profiles from joint X-ray/SZE analysis.

5.5.24 RXJ2129.6+0005

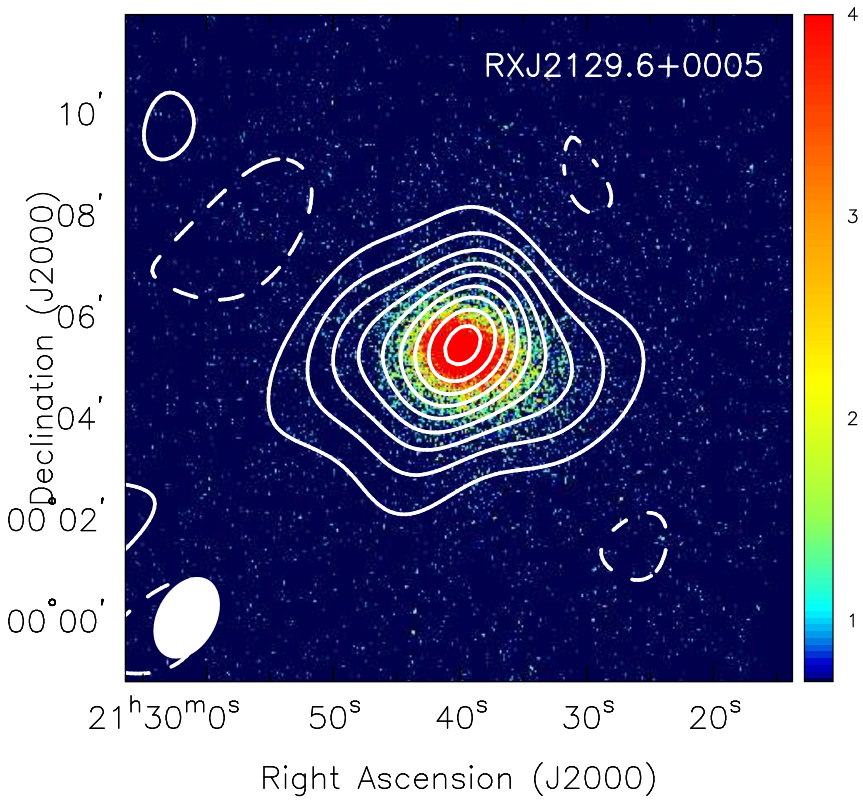

Figure 5.97: RXJ2129.6+0005: SZE contours overlaid on X-ray false color images. The *Chandra* X-ray surface brightness data are from the energy range 0.7–7.0 keV. The color bars reflect the number of counts detected by Chandra in the 0.7-7 keV band. The SZE data are from the SZA, and the contour levels are (+2,-2,-4,...) times the rms noise (see Table 3.1). The synthesized beams of the SZE observations are shown in the lower left corner of each image.

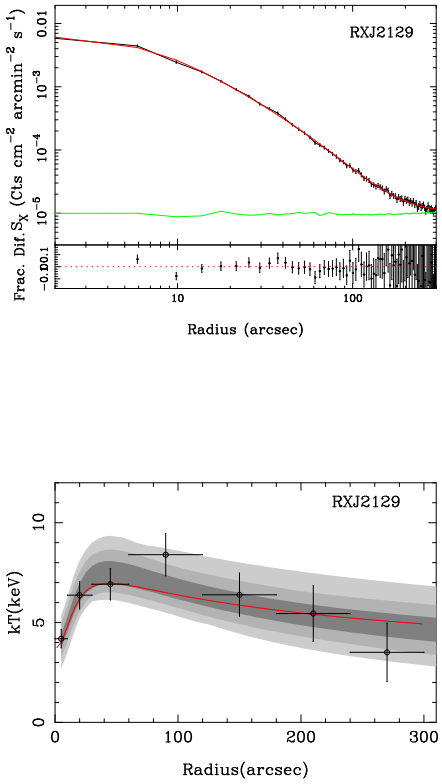

Figure 5.98: RXJ2129.6+0005: Surface brightness and temperature profile from joint X-ray/SZE analysis.

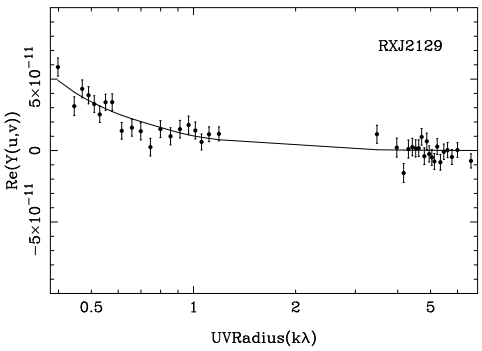

Figure 5.99: RXJ2129.6+0005: SZE visibility profile plotted as a function of $u - v$ radius ($\sqrt{u^2 + v^2}$). The plots show the real components of the measured visibilities along with the best fit model.

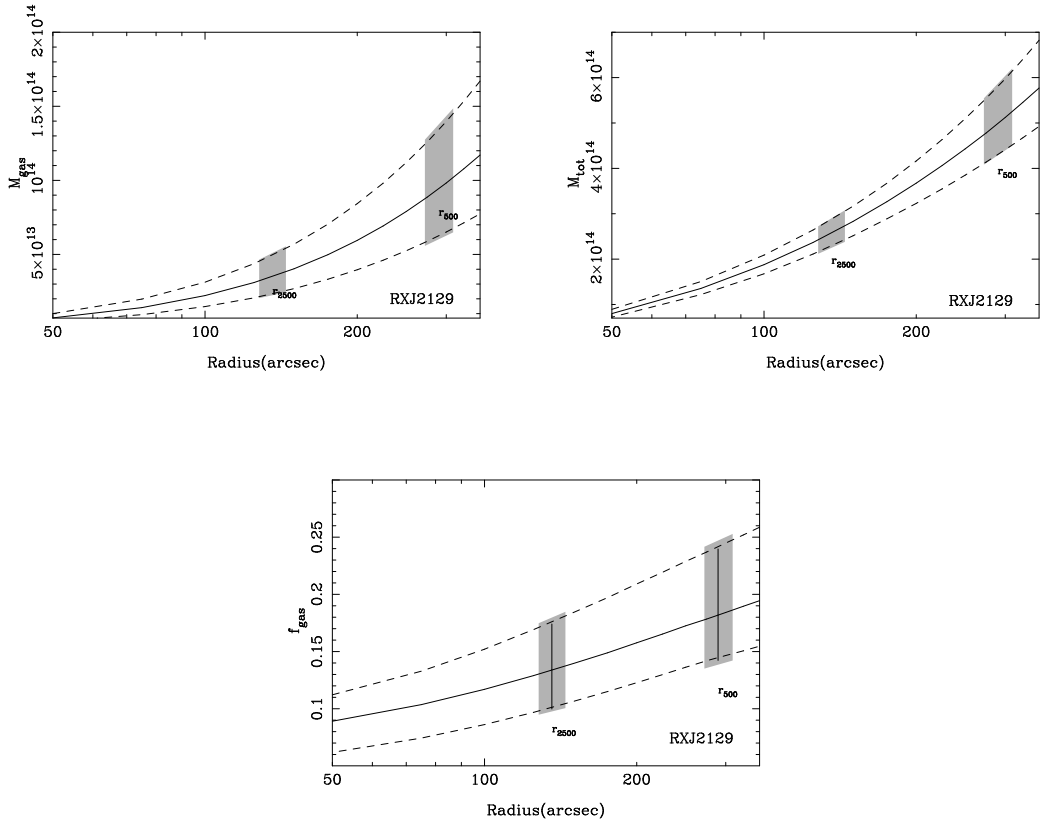

Figure 5.100: RXJ2129.6+0005: Radial gas mass, total mass, and gas mass fraction profiles from joint X-ray/SZE analysis.

5.5.25 Abell 2537

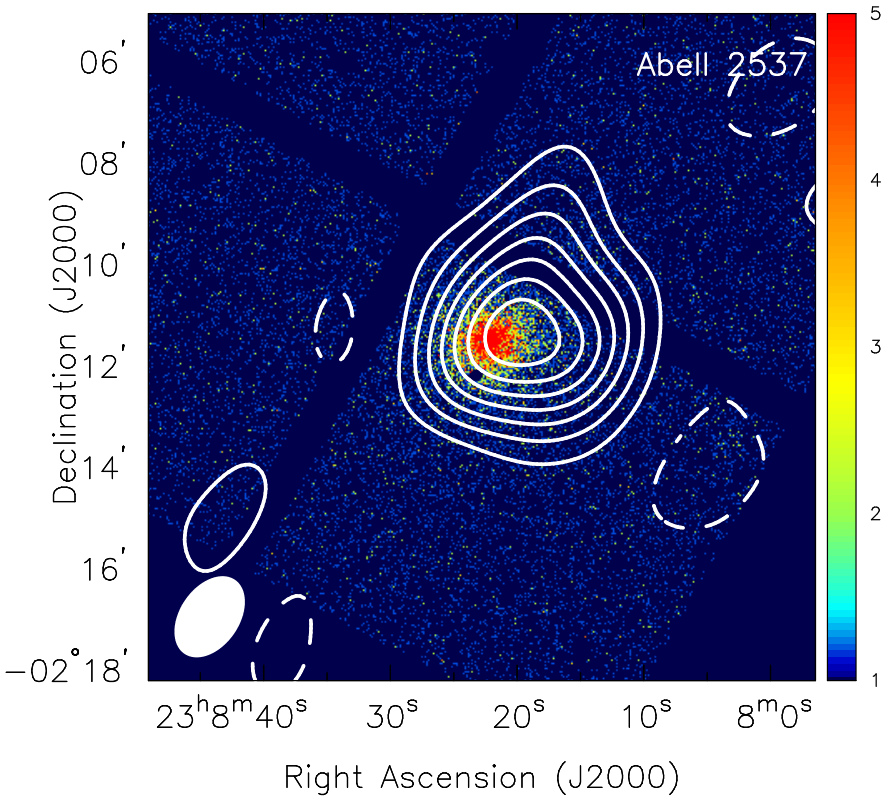

Figure 5.101: Abell 2537: SZE contours overlaid on X-ray false color images. The *Chandra* X-ray surface brightness data are from the energy range 0.7–7.0 keV. The color bars reflect the number of counts detected by Chandra in the 0.7-7 keV band. The SZE data are from the SZA, and the contour levels are (+2,-2,-4,...) times the rms noise (see Table 3.1). The synthesized beams of the SZE observations are shown in the lower left corner of each image.

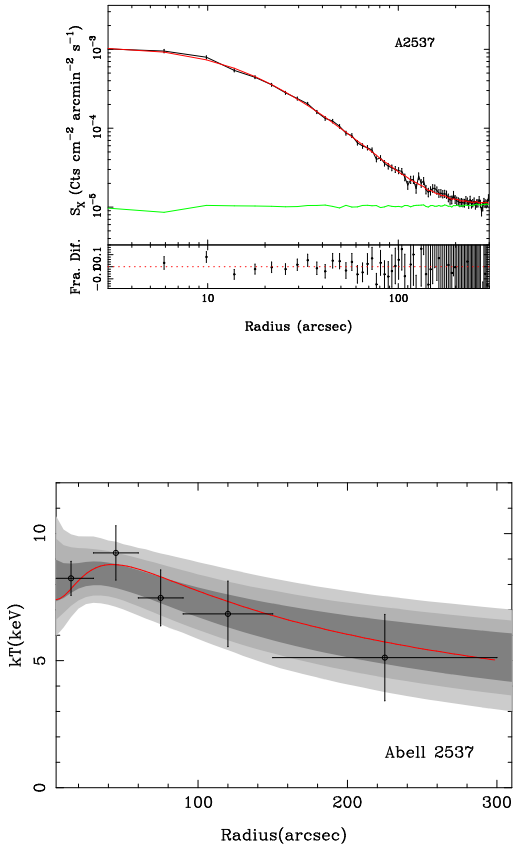

Figure 5.102: Abell 2537: Surface brightness and temperature profile from joint X-ray/SZE analysis.

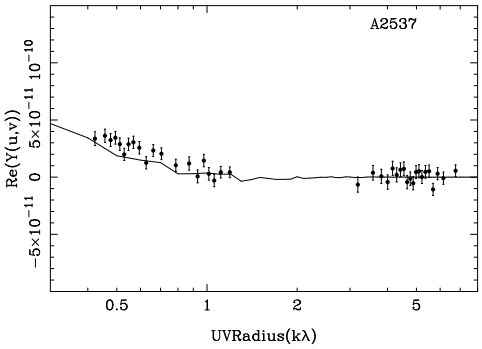

Figure 5.103: Abell 2537: SZE visibility profile plotted as a function of $u - v$ radius ($\sqrt{u^2 + v^2}$). The plots show the real components of the measured visibilities along with the best fit model.

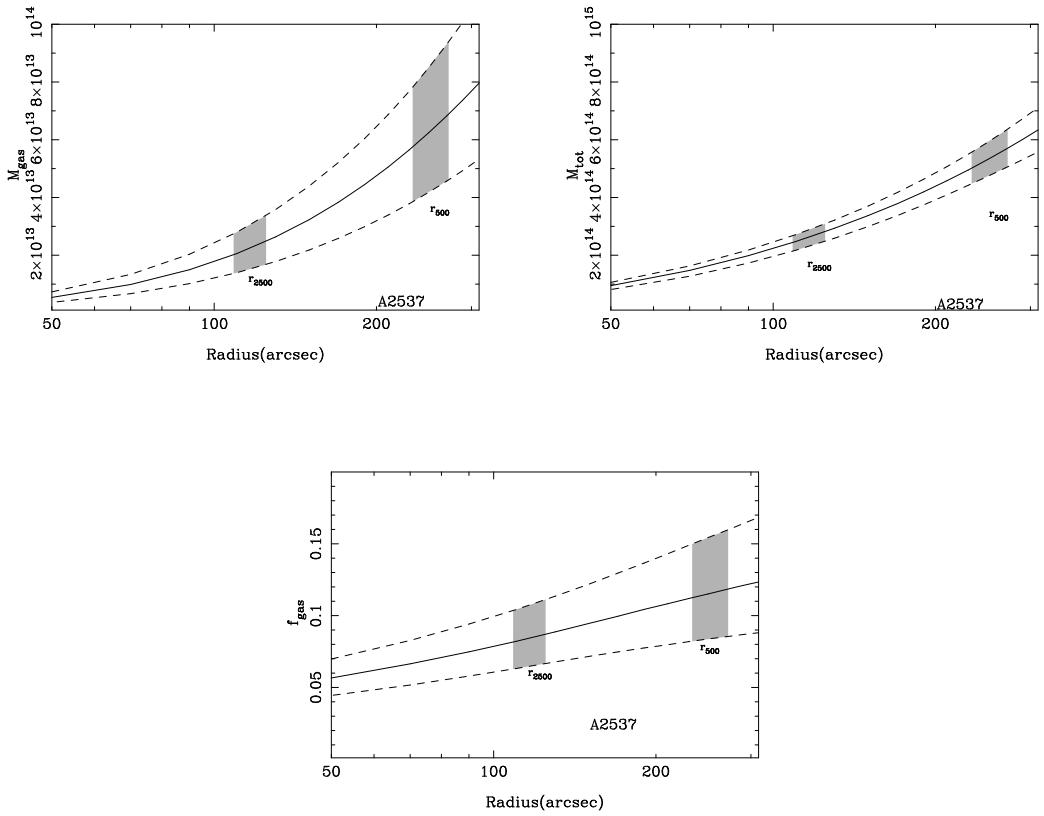

Figure 5.104: Abell 2537: Radial gas mass, total mass, and gas mass fraction profiles from joint X-ray/SZE analysis.

CHAPTER 6

COMPARISON OF X-RAY AND SUNYAEV ZEL'DOVICH EFFECT MEASUREMENTS OF THE ELECTRON PRESSURE

X-ray and Sunyaev Zel'dovich effect observations provide measurements of the electron pressure profile. The X-ray observables are the electron temperature and the surface brightness, $S_X \propto n_e^2$ (Equation 4.1). The SZE observables is proportional to the electron pressure along the line of sight (Equation 3.2).

X-ray observations accurately measure the ICM of galaxy clusters; therefore, the depth of the SZE decrement can be predicted. Each observational technique is subject to unique systematics that may bias their measurements. For example, certain measurements of the electron pressure with WMAP are in disagreement with X-ray predictions (Lieu et al., 2006; Bielby & Shanks, 2007). Lieu et al. (2006) used ROSAT and WMAP observations to compare the radial profiles between X-ray and microwave observations. ROSAT observations of 38 clusters from the Bonamente et al. (2006) sample were used to predict the SZE radial profiles and a discrepancy was found between the expected and measured SZE decrement from WMAP 1-year data. Bielby & Shanks (2007) found the same result when the expected SZE signal was compared to WMAP 3-year data.

Lueker et al. (2010) measured the CMB power-spectrum at 150 and 220 GHz using the South Pole Telescope. They combined the 150 and 220 GHz data to remove

the point source power in order to detect the SZE signal. Using the WMAP 5-year cosmological parameters in the Arnaud et al. (2007) model, and found the SZE signal to be significantly lower than the predicted model. This discrepancy may suggest that the current cluster models overestimate the ICM pressure, particularly in the cluster outskirts (Battaglia et al., 2010; Shaw et al., 2010; Trac et al., 2010). Fowler et al. (2010) also measured the CMB power-spectrum at 148 GHz using the Atacama Cosmology Telescope. Using the full range of the power spectrum $600 < l < 8100$, an upper limit was placed on the model's amplitude, but it has no implication for the interpretation of the pressure comparison.

Both observables can be affect by different systematic effects. For example, in X-ray observations non-thermal emission may be present due to inverse compton scattering between relativistic electrons and the Cosmic Microwave Background (CMB) photons (Sarazin & Lieu, 1998; Bonamente et al., 2005). A relativistic electron with a Lorentz factor γ will scatter a CMB photon to higher energies:

$$E = 75\left(\frac{\gamma}{300}\right)^2 eV, \tag{6.1}$$

where $\gamma = 600 - 1500$ to generate photons detected in the 0.3-2.0 keV energy band (Bonamente et al., 2005). The presence of the non-thermal emission may result in an increase in the X-ray emission above the level of the thermal gas.

The presence of the relativistic electrons in SZE observations may also give rise to a change in its SZE signal. The radiative pressure for non-relativistic electrons is given by,

$$p = \frac{2}{3}u_{NRel}, \tag{6.2}$$

where $u_{NRel} = (Nm_ec^2)/V$, N is the number of electrons, m_e is the electron mass,

c is the speed of light, and V is the volume. For relativistic electrons the radiative pressure,

$$p = \frac{1}{3} u_{Rel}, \tag{6.3}$$

where $u_{Rel} = (N\gamma m_e c^2)/V$. A much smaller number of relativistic electrons are needed to generate the same amount of pressure as the relativistic electrons if $\gamma = 1000$. Therefore the presence of relativistic electrons can lead to an incorrect measurement of the SZE signal (Colafrancesco et al., 2003).

Moreover, radio emission from cluster halos (Brunetti et al., 2007) may partially fill the SZE decrement and this will result in a lower SZE signal. Therefore a joint measurement of the electron pressure profile can be used to determine the presence of systematic effects which can result in a discrepancy between the X-ray and SZE pressure profiles.

Therefore a joint measurement from both X-ray and SZE data is useful for investigating their systematics. For these measurements, the model provides a unique parametrization that consistently describes the X-ray and SZE observables, and therefore mitigates the effect of using different models for X-ray and SZE observables. In order to use the integrated pressure as a cosmological tool it is necessary to check the agreement between independent methods of measurement, in particular with a model that has a consistent parametrization for all observables. A joint fit to the Chandra and Sunyaev Zel'dovich Array observations of 25 cluster is performed in order to measure the integrated pressure at r_{500}.

6.1 Method

A MCMC technique is used to fit the model described in Chapter 2 to the X-ray and SZE data. A joint fit between the X-ray and SZE observations is performed in which all the shape parameters (r_s, n, β) are linked between the dataset. In the model the normalization parameters (n_{eo}, T_0, P_{eo}) be free and a ΛCDM cosmology is assumed for the calculation of the angular diameter distance. This approach lets the X-ray and SZE pressure profiles have the same shape. Therefore the ratio of the SZE to X-ray pressure will be the same at every radius in the cluster. The parameter fits to the datasets can be found in Table 6.1.

Once the model accurately fits to the datasets, the integrated pressure is computed:

$$Y_{sph}(r) = \frac{4\pi\sigma_T}{m_e c^2} \int_0^r P_e(r') r'^2 dr', \tag{6.4}$$

where m_e is the electron mass, P_e is the electron pressure described by the Bulbul et al. (2010) model.

Table 6.1: Best-fit parameters to the joint fit to SZE and X-ray data

Cluster	n_{eo} ($10^{-2} cm^{-3}$)	r_s ($''$)	n	β	T_o (keV)	r_{cool} ($''$)	α	γ	P_{eo} (10^{-10} ergs cm^{-3})
MACSJ0159.8-0849	$2.61\pm^{0.21}_{0.15}$	$23.4\pm^{2.3}_{2.8}$	$5.80\pm^{1.69}_{1.37}$	$1.56\pm^{0.21}_{0.15}$	$15.0\pm^{1.8}_{1.4}$	$12.8\pm^{0.6}_{0.6}$	$0.24\pm^{0.02}_{0.02}$	2.0	$5.47\pm^{0.84}_{0.74}$
Abell 383	$3.20\pm^{0.51}_{0.41}$	$22.1\pm^{5.0}_{4.3}$	$4.50\pm^{1.84}_{1.10}$	$1.69\pm^{0.29}_{0.24}$	$7.8\pm^{1.0}_{1.0}$	$14.5\pm^{1.4}_{1.3}$	$0.28\pm^{0.04}_{0.03}$	2.0	$4.65\pm^{0.89}_{0.72}$
MACS0329.7-0212	$3.52\pm^{0.82}_{0.70}$	$15.9\pm^{11.9}_{4.7}$	$3.22\pm^{1.00}_{0.90}$	$2.01\pm^{0.96}_{0.33}$	$12.1\pm^{2.5}_{1.8}$	$11.5\pm^{0.5}_{0.4}$	$0.36\pm^{0.08}_{0.06}$	2.0	$4.58\pm^{1.54}_{0.80}$
Abell 478	$4.59\pm^{0.41}_{0.31}$	$46.5\pm^{5.6}_{5.6}$	$10.74\pm^{0.88}_{1.18}$	$1.28\pm^{0.03}_{0.02}$	$7.8\pm^{0.4}_{0.4}$	$15.5\pm^{1.5}_{1.3}$	$0.28\pm^{0.03}_{0.03}$	2.0	$4.75\pm^{0.49}_{0.39}$
MACSJ0429.6-0253	$2.83\pm^{0.92}_{0.40}$	$20.7\pm^{5.7}_{7.2}$	$3.26\pm^{1.00}_{0.54}$	$2.01\pm^{0.40}_{0.32}$	$14.9\pm^{1.9}_{2.0}$	$11.7\pm^{1.1}_{1.3}$	$0.19\pm^{0.05}_{0.03}$	2.0	$5.73\pm^{1.90}_{1.33}$
3C186	$4.38\pm^{0.67}_{0.57}$	$10.9\pm^{3.9}_{2.6}$	$3.51\pm^{1.57}_{0.77}$	$1.98\pm^{0.43}_{0.33}$	$10.7\pm^{2.2}_{1.9}$	-	-	-	$9.43\pm^{2.70}_{1.98}$
MACSJ0744.9+3927	$2.58\pm^{0.48}_{0.40}$	$17.9\pm^{5.4}_{4.1}$	$3.05\pm^{0.82}_{0.45}$	$2.08\pm^{0.31}_{0.29}$	$17.5\pm^{2.0}_{2.2}$	$11.4\pm^{1.2}_{1.2}$	$0.32\pm^{0.07}_{0.05}$	2.0	$9.43\pm^{2.70}_{1.98}$
MACSJ0947.2+7623	$4.18\pm^{0.90}_{0.73}$	$14.1\pm^{6.3}_{3.6}$	$2.97\pm^{0.73}_{0.48}$	$2.01\pm^{0.50}_{0.24}$	$21.2\pm^{2.9}_{2.6}$	$23.0\pm^{2.1}_{1.9}$	$0.25\pm^{0.04}_{0.04}$	2.0	$12.29\pm^{3.21}_{2.63}$
Zwicky 3146	$2.89\pm^{0.20}_{0.32}$	$23.3\pm^{2.5}_{2.2}$	$4.05\pm^{0.51}_{0.38}$	$1.80\pm^{0.13}_{0.11}$	$17.6\pm^{1.5}_{1.3}$	$23.0\pm^{3.2}_{2.9}$	$0.07\pm^{0.01}_{0.02}$	$0.91\pm^{0.06}_{0.05}$	$9.30\pm^{0.86}_{0.84}$
MACSJ1115.8+0129	$2.52\pm^{0.51}_{0.36}$	$29.1\pm^{8.8}_{7.1}$	$3.39\pm^{0.52}_{0.34}$	$2.13\pm^{0.27}_{0.25}$	$14.8\pm^{1.7}_{1.6}$	$16.8\pm^{1.5}_{1.5}$	$0.29\pm^{0.05}_{0.04}$	2.0	$7.38\pm^{1.58}_{1.03}$
MS1137.5+6625	$2.60\pm^{0.15}_{0.12}$	$41.3\pm^{8.8}_{11.7}$	$2.21\pm^{0.38}_{0.27}$	$4.64\pm^{1.17}_{1.15}$	$11.9\pm^{2.2}_{2.0}$	-	-	-	$7.36\pm^{1.67}_{1.43}$
Abell 1413	$1.64\pm^{0.11}_{0.09}$	$66.7\pm^{6.6}_{6.2}$	$5.14\pm^{1.19}_{1.03}$	$1.71\pm^{0.27}_{0.15}$	$10.7\pm^{1.1}_{0.8}$	$28.6\pm^{2.3}_{2.6}$	$0.50\pm^{0.03}_{0.03}$	2.0	$2.11\pm^{0.17}_{0.19}$
CLJ1226.9+3332	$3.59\pm^{0.22}_{0.20}$	$25.6\pm^{5.4}_{4.3}$	$4.53\pm^{1.37}_{0.73}$	$2.10\pm^{0.29}_{0.31}$	$14.2\pm^{2.5}_{2.5}$	-	-	-	$8.86\pm^{1.49}_{1.30}$
MACSJ1311.0-0311	$1.68\pm^{0.26}_{0.23}$	$37.1\pm^{12.7}_{9.1}$	$4.24\pm^{0.92}_{1.14}$	$2.22\pm^{0.71}_{0.35}$	$12.3\pm^{2.0}_{1.1}$	$23.8\pm^{2.2}_{2.8}$	$0.35\pm^{0.05}_{0.04}$	2.0	$3.40\pm^{1.12}_{0.85}$
RXJ1347.5-1145	$4.16\pm^{0.38}_{0.36}$	$28.4\pm^{10.4}_{6.1}$	$2.32\pm^{0.22}_{0.19}$	$2.93\pm^{0.74}_{0.34}$	$60.5\pm^{8.3}_{6.7}$	$15.6\pm^{1.0}_{0.9}$	$0.13\pm^{0.02}_{0.02}$	$1.35\pm^{0.13}_{0.11}$	$26.65\pm^{2.80}_{3.67}$
Abell 1835	$5.44\pm^{0.32}_{0.33}$	$16.6\pm^{1.2}_{0.9}$	$61.25\pm^{17.49}_{14.14}$	$1.04\pm^{0.01}_{0.01}$	$10.4\pm^{0.4}_{0.4}$	$17.2\pm^{0.4}_{0.3}$	$0.48\pm^{0.03}_{0.03}$	$4.45\pm^{0.56}_{0.37}$	$9.59\pm^{0.78}_{0.73}$
MACSJ1423.8+2404	$1.65\pm^{0.24}_{0.21}$	$61.2\pm^{21.7}_{20.6}$	$1.84\pm^{0.20}_{0.14}$	$5.57\pm^{1.49}_{1.43}$	$30.0\pm^{4.7}_{4.4}$	$15.2\pm^{1.3}_{1.1}$	$0.10\pm^{0.02}_{0.02}$	2.0	$6.77\pm^{1.85}_{1.50}$
MACSJ1427.3+4408	$2.57\pm^{0.41}_{0.67}$	$5.0\pm^{2.3}_{1.0}$	$3.28\pm^{0.74}_{0.59}$	$1.51\pm^{0.17}_{0.11}$	$19.9\pm^{2.6}_{2.6}$	$20.5\pm^{1.4}_{1.4}$	$0.24\pm^{0.03}_{0.05}$	2.0	$5.55\pm^{1.70}_{1.41}$
RXJ1504.1-0248	$3.78\pm^{0.27}_{0.21}$	$26.3\pm^{2.6}_{2.2}$	$3.44\pm^{0.40}_{0.29}$	$1.95\pm^{0.15}_{0.12}$	$20.5\pm^{1.0}_{1.4}$	$34.5\pm^{0.9}_{0.9}$	$0.22\pm^{0.01}_{0.01}$	2.0	$10.81\pm^{0.97}_{1.07}$
MACSJ1532.9+302	$3.14\pm^{0.69}_{0.47}$	$20.3\pm^{6.4}_{6.3}$	$3.14\pm^{0.57}_{0.48}$	$2.15\pm^{0.31}_{0.34}$	$16.1\pm^{2.3}_{1.8}$	$26.3\pm^{3.4}_{2.6}$	$0.25\pm^{0.05}_{0.03}$	2.0	$9.09\pm^{1.54}_{1.59}$
MACSJ1621.6+3810	$2.33\pm^{0.38}_{0.37}$	$16.9\pm^{6.3}_{3.5}$	$3.00\pm^{0.60}_{0.55}$	$2.08\pm^{0.45}_{0.25}$	$15.4\pm^{1.9}_{1.7}$	$10.1\pm^{1.0}_{0.9}$	$0.23\pm^{0.03}_{0.03}$	2.0	$5.27\pm^{1.22}_{0.88}$
Abell 2204	$4.12\pm^{0.18}_{0.18}$	$22.4\pm^{1.3}_{1.1}$	$7.34\pm^{1.12}_{0.94}$	$1.34\pm^{0.57}_{0.50}$	$14.7\pm^{0.8}_{0.8}$	$19.9\pm^{0.5}_{0.5}$	$0.16\pm^{0.07}_{0.07}$	2.0	$9.90\pm^{0.60}_{0.60}$
MACSJ1720.3+3536	$1.60\pm^{0.10}_{0.10}$	$87.5\pm^{19.2}_{19.5}$	$2.46\pm^{0.20}_{0.16}$	$4.32\pm^{0.79}_{0.62}$	$15.8\pm^{1.3}_{1.1}$	$13.0\pm^{0.6}_{0.7}$	$0.12\pm^{0.01}_{0.01}$	2.0	$3.98\pm^{0.49}_{0.45}$
RXJ2129.6+0005	$2.68\pm^{0.28}_{0.45}$	$21.9\pm^{6.0}_{2.5}$	$6.33\pm^{1.17}_{1.32}$	$1.44\pm^{0.17}_{0.08}$	$10.8\pm^{1.4}_{0.9}$	$18.4\pm^{2.3}_{1.8}$	$0.36\pm^{0.03}_{0.05}$	2.0	$4.78\pm^{0.62}_{0.81}$
Abell 2537	$1.66\pm^{0.40}_{0.34}$	$26.8\pm^{11.9}_{5.8}$	$5.38\pm^{2.63}_{1.29}$	$1.60\pm^{0.25}_{0.23}$	$12.2\pm^{1.9}_{1.6}$	$26.5\pm^{7.4}_{7.3}$	$0.72\pm^{0.12}_{0.12}$	2.0	$3.23\pm^{0.58}_{0.55}$

6.2 Results and Discussion

Using Equation 6.4, the spherical integrated pressure is calculated at r_{500} along with the ratio of the SZE to X-ray integrated pressure at each iteration in the MCMC chain. The values are reported in Table 6.2 along with the 68% confidence levels.

When the ratio of the SZE to X-ray pressure is examined, the average found is 1.02 ± 0.04. Agreement between the pressures indicate that the SZE decrement and X-ray emission in relaxed systems are from the same thermal plasma. Therefore no evidence of significant sources of systematics are detected.

Low mass clusters and groups have a shallow potential well, therefore the presence of strong non-thermal emission is more likely to be present than in massive clusters (Sun et al., 2009). Low mass systems also have low signal-to-noise SZE and X-ray data. The discrepancy in the X-ray and SZE pressure measured by Lieu et al. (2006) and Bielby & Shanks (2007) using ROSAT and WMAP data may be explained by WMAPs low signal-to-noise detection of low mass clusters. The results of this work are consistent with LaRoque et al. (2006) in which the gas mass fraction measured from Chandra observations was the same as the gas mass fraction measured from OVRO and BIMA observations.

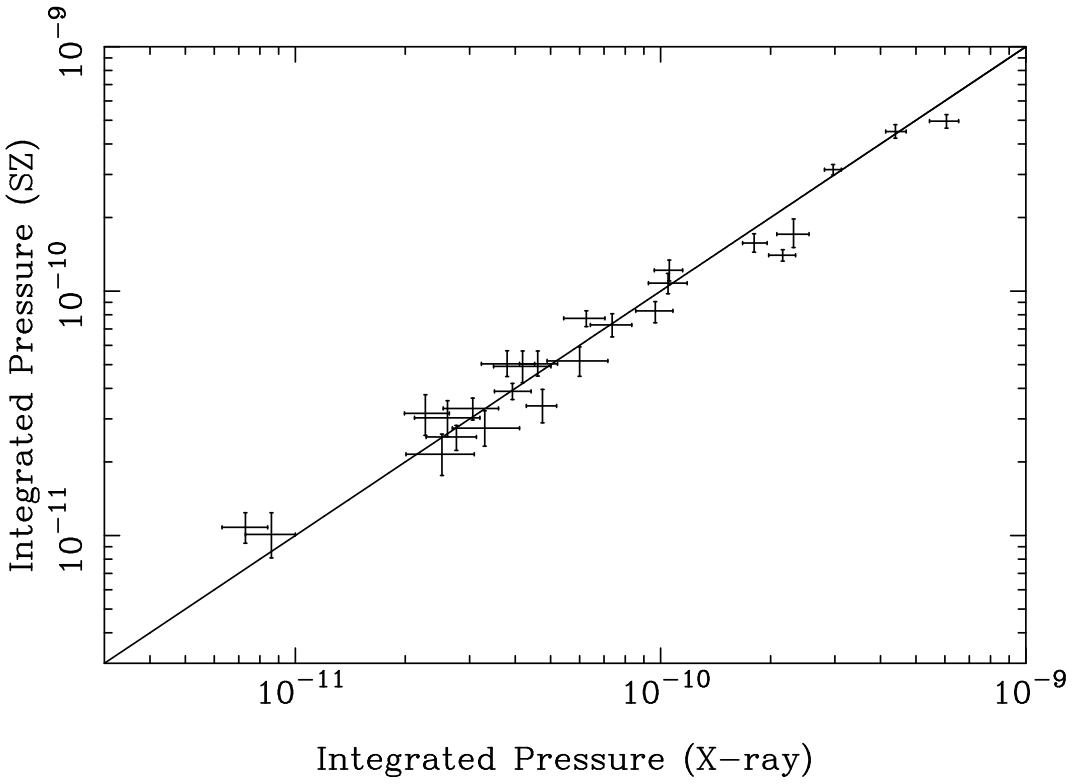

Figure 6.1: Integrated SZE pressure plotted against integrated X-ray pressure. The dotted line is y=x. The weighted mean of SZ/X=1.02±0.04.

Table 6.2: Pressure Comparison Using Polytropic Models at r_{500}

Cluster	r_{500}	$Y_{\rm sph}(r_{500})$		Ratio
		SZ normalization	X-ray normalization	
	($''$)	(10^{-11})	(10^{-11})	
MACSJ0159.8-0849	$221.1\pm^{11.0}_{12.3}$	$8.30\pm^{0.76}_{0.88}$	$9.67\pm^{1.14}_{1.12}$	$0.86\pm^{0.08}_{0.07}$
Abell 383	$268.5\pm^{22.1}_{20.7}$	$4.92\pm^{0.77}_{0.70}$	$4.19\pm^{0.82}_{0.70}$	$1.17\pm^{0.16}_{0.15}$
MACS0329.7-0212	$138.4\pm^{12.7}_{11.9}$	$3.03\pm^{0.53}_{0.49}$	$2.61\pm^{0.59}_{0.49}$	$1.16\pm^{0.20}_{0.18}$
Abell 478	$714.3\pm^{23.5}_{34.5}$	$49.61\pm^{3.15}_{3.19}$	$60.62\pm^{4.84}_{6.13}$	$0.82\pm^{0.06}_{0.05}$
MACSJ0429.6-0253	$182.3\pm^{18.5}_{15.1}$	$2.75\pm^{0.49}_{0.43}$	$3.30\pm^{0.81}_{0.61}$	$0.83\pm^{0.14}_{0.14}$
3C186	$72.1\pm^{5.5}_{5.7}$	$1.01\pm^{0.23}_{0.20}$	$0.86\pm^{0.14}_{0.13}$	$1.17\pm^{0.24}_{0.21}$
MACSJ0744.9+3927	$120.3\pm^{8.6}_{7.5}$	$5.04\pm^{0.66}_{0.57}$	$3.80\pm^{0.72}_{0.57}$	$1.33\pm^{0.16}_{0.15}$
MACSJ0947.2+7623	$196.2\pm^{15.1}_{15.5}$	$5.18\pm^{0.73}_{0.70}$	$6.00\pm^{1.17}_{1.11}$	$0.86\pm^{0.14}_{0.11}$
Zwicky 3146	$265.7\pm^{8.7}_{8.6}$	$12.17\pm^{1.22}_{1.17}$	$10.56\pm^{0.93}_{0.95}$	$1.14\pm^{0.13}_{0.10}$
MACSJ1115.8+0129	$200.0\pm^{9.6}_{10.7}$	$7.74\pm^{0.57}_{0.58}$	$6.26\pm^{0.78}_{0.83}$	$1.24\pm^{0.14}_{0.11}$
MS1137.5+6625	$78.8\pm^{5.6}_{5.1}$	$1.08\pm^{0.16}_{0.15}$	$0.73\pm^{0.11}_{0.10}$	$1.49\pm^{0.26}_{0.24}$
Abell 1413	$454.4\pm^{20.3}_{20.3}$	$17.10\pm^{2.64}_{2.03}$	$23.12\pm^{2.36}_{2.32}$	$0.75\pm^{0.07}_{0.06}$
CLJ1226.9+3332	$109.4\pm^{8.3}_{8.3}$	$3.31\pm^{0.34}_{0.34}$	$3.06\pm^{0.54}_{0.52}$	$1.09\pm^{0.18}_{0.15}$
MACSJ1311.0-0311	$156.5\pm^{11.5}_{10.2}$	$2.36\pm^{0.61}_{0.58}$	$2.31\pm^{0.36}_{0.31}$	$1.02\pm^{0.26}_{0.23}$
RXJ1347.5-1145	$218.0\pm^{6.6}_{5.9}$	$14.02\pm^{0.75}_{0.75}$	$21.59\pm^{1.82}_{1.82}$	$0.65\pm^{0.04}_{0.04}$
Abell 1835	$370.7\pm^{7.6}_{8.0}$	$31.41\pm^{1.56}_{1.56}$	$29.67\pm^{1.56}_{1.57}$	$1.06\pm^{0.06}_{0.06}$
MACSJ1423.8+2404	$189.1\pm^{16.4}_{15.4}$	$2.15\pm^{0.45}_{0.39}$	$2.52\pm^{0.57}_{0.51}$	$0.86\pm^{0.22}_{0.18}$
MACSJ1427.3+4408	$150.5\pm^{4.2}_{4.6}$	$3.39\pm^{0.57}_{0.50}$	$4.75\pm^{0.44}_{0.46}$	$0.72\pm^{0.11}_{0.11}$
RXJ1504.1-0248	$326.7\pm^{12.1}_{9.9}$	$15.73\pm^{1.43}_{1.30}$	$18.03\pm^{1.54}_{1.26}$	$0.87\pm^{0.06}_{0.06}$
MACSJ1532.9+302	$189.1\pm^{9.9}_{9.1}$	$5.04\pm^{0.65}_{0.55}$	$4.61\pm^{0.61}_{0.50}$	$1.09\pm^{0.12}_{0.12}$
MACSJ1621.6+3810	$147.7\pm^{8.0}_{11.1}$	$2.53\pm^{0.29}_{0.30}$	$2.76\pm^{0.37}_{0.48}$	$0.93\pm^{0.12}_{0.10}$
Abell 2204	$504.6\pm^{12.5}_{11.2}$	$44.97\pm^{2.99}_{2.74}$	$43.93\pm^{3.08}_{2.59}$	$1.02\pm^{0.05}_{0.05}$
MACSJ1720.3+3536	$170.5\pm^{8.6}_{8.1}$	$3.89\pm^{0.30}_{0.29}$	$3.93\pm^{0.49}_{0.42}$	$0.98\pm^{0.10}_{0.09}$
RXJ2129.6+0005	$297.6\pm^{13.1}_{13.6}$	$10.78\pm^{1.04}_{1.02}$	$10.48\pm^{1.34}_{1.22}$	$1.04\pm^{0.10}_{0.11}$
Abell 2537	$256.2\pm^{13.4}_{14.4}$	$7.27\pm^{0.81}_{0.77}$	$7.37\pm^{0.97}_{0.95}$	$0.99\pm^{0.09}_{0.09}$

CHAPTER 7

SUMMARY OF DISSERTATION

Galaxy clusters are used to study cosmology since they are tracers of the matter content in the universe. By mass, galaxy clusters are composed of approximately 3% galaxies (Lin et al., 2003; Gonzalez et al., 2007), 15% hot ionized gas, and 83% dark matter. Galaxy clusters contain 30-300 galaxies, have a typical radius of a few mega-parsecs and a mass of $10^{14} - 10^{15}$ $M_{\odot}$ (Borgani & Kravtsov, 2009). The ionized hot gas in galaxy clusters has a temperature of $10^{7} - 10^{8}$ K which emits X-rays primarily through bremsstrahlung radiation. X-ray observations are used to measure the mass of the hot ionized plasma also known as the intra-cluster medium (ICM). In Chapter 1, the motivation for this project was examined.

7.1 Modeling the Intra-cluster Medium

A new analytic model describing the intra-cluster medium of galaxy clusters was investigated in Chapter 2. This model is based on an analytic distribution of the cluster mass density described by the Navarro et al. (1997) distribution, which was generalized following Suto et al. (1998), Ascasibar et al. (2003), and Ascasibar & Diego (2008). The mass density is combined with a polytropic equation of state for the gas to provide self-consistent density, temperature, and pressure profiles for a plasma in hydrostatic equilibrium. This model has a number of features that make

it suitable for the analysis of X-ray and SZE observations of clusters. The model is analytic, and has a limited number of parameters which describe the global properties of clusters. For clusters which do not have a cool core, 5 parameters are sufficient to describe the distribution of the density, temperature, and pressure. The gas density and temperature are linked by the polytropic equation of state, and the total matter density is related to the plasma properties by the hydrostatic equilibrium. The model has the advantage of simultaneously fitting X-ray and SZE data and therefore it is suitable for this project. This model is derived in Chapter 2. The results of this investigation were published in Bulbul, Hasler, Bonamente, and Joy (2010).

7.2 Method of Analysis for X-ray and SZE Data

Galaxy clusters trace the growth of structure of the universe, and their abundance and evolution reflect the underlying cosmological parameters, including Ω_M, σ_8, and the dark energy equation of state parameter w. Many recent works have made use galaxy clusters to constrain cosmology, including dark energy constraints from X-ray measurements of the gas mass fraction (Allen et al., 2008; Ettori et al., 2009), cosmological parameter constraints from the growth of structure via X-ray (Mantz et al., 2008, 2010; Vikhlinin et al., 2009) and SZE cluster surveys (Sehgal et al., 2010; Marriage et al., 2010; Vanderlinde et al., 2010), and gas mass fraction constraints using a combination of SZE and X-ray observations (LaRoque et al., 2006).

In Chapter 3, we presented a method for the joint analysis of X-ray and SZE data using a self-consistent analytic model that to describes physical properties of the intra-cluster medium (Bulbul et al., 2010). The model provides analytic expressions for the radial density, temperature, and pressure profiles, and is therefore simultane-

ously applicable to both X-ray and SZE observables. A joint analysis method was demonstrated and used to measure the cluster gas mass fraction without the need to impose external priors on cosmological parameters such as the Hubble expansion rate $H(z)$ on two relaxed clusters. The models accurately describe the surface brightness and temperature profiles in the X-ray data and fit the 30 GHz SZE data using a minimal number of parameters. The model can therefore be used to jointly fit X-ray and SZE data using a simple analytic parametrization that ensures that the three primary thermodynamic quantities are related by the ideal gas law at all radii. This method was applied to high signal-to-noise data from *Chandra* and Sunyaev-Zel'dovich Array (SZA) observations of two intermediate-redshift clusters, Abell 2204 and Abell 2631 in Chapter 3. These results have been submitted for publication in the Astrophysical Journal, Hasler et al. (2011).

7.3 The Distribution of Baryons in Clusters from X-ray Observations

According to cosmological simulations, slight fluctuations in the density distribution at early epoch decoupled from the Hubble flow. They started to collapse due to gravity and lumps of matter merged together to form larger structures. Galaxy clusters are the largest structures that have undergone gravitational collapse and reached equilibrium (Kravtsov et al., 2005; Borgani & Kravtsov, 2009). Therefore massive relaxed galaxy clusters are expected to trace the matter content of the universe. The cluster gas mass fraction, which is the ratio of the gas to total mass is expected to agree with the cosmic baryon fraction. The cosmic baryon fraction, $\Omega_b/\Omega_M = 0.1675$ (Komatsu et al., 2011) has been measured by the Wilkinson Microwave Anisotropy

Probe (WMAP) using the 7 year data. Komatsu et al. (2011) measured $\Omega_b h^2$ and $\Omega_M h^2$ using WMAP 7 year data including priors on the hubble constant (Riess et al., 2009) and the angular diameter distance (Percival et al., 2010). Previous studies of the gas mass fraction (Allen et al., 2002; Sanderson et al., 2003; Allen et al., 2004; LaRoque et al., 2006; Vikhlinin et al., 2006; Arnaud et al., 2007; Allen et al., 2008; Zhang et al., 2008; Ettori et al., 2009) have fallen short of the cosmic baryon fraction, see Figure 4.2. For example, $f_{gas}(r_{2500}) = 0.119 \pm 0.003 \pm^{0.007}_{0.014}$ (LaRoque et al., 2006) and $f_{gas}(r_{500}) = 0.12 \pm 0.004$ (Zhang et al., 2008).

In Chapter 4, Chandra X-ray observations were used for 25 clusters to measure the gas mass, total mass, and gas mass fraction and therefore determine if the cluster baryon fraction agrees with the cosmic baryon fraction. A ΛCDM cosmology ($H_o = 73 km/s/Mpc$, $\Omega_M = 0.27$, and $\Omega_\Lambda = 0.73$) was assumed in the calculation of the angular diameter distance, which is required for mass measurements. For all 25 clusters, the gas mass fraction was measured at r_{500} and the weighted mean was 0.158 ± 0.024. However, this measurement does not include all the baryons in the cluster.

The cluster baryon fraction is defined as gas mass fraction plus the stellar mass fraction. Giodini et al. (2009) used a sample of 118 galaxies and low mass galaxy clusters to measure the gas mass fraction and concluded that the stellar mass fraction decreases with total mass. The sample used in this project has an average total mass of 3.0×10^{14} solar masses at r_{500} and therefore has a stellar mass fraction of 0.021 ± 0.002 according to Giodini et al. (2009). Therefore the cluster baryon fraction measured was 0.179 ± 0.024 at r_{500} which agrees with the cosmic baryon fraction $\Omega_b/\Omega_M = 0.167 \pm 0.006$ measured by WMAP (Komatsu et al., 2011). It

was confirmed that massive relaxed galaxy clusters accurately trace the primordial content of the universe provided that the measurement of f_{gas} is done at large radii, such as r_{500}.

The measurement at r_{2500} agrees with previous studies of the gas mass fraction (LaRoque et al., 2006; Allen et al., 2008). However, the results found at r_{500} are higher compared to Zhang et al. (2008) and Ettori et al. (2009). One possible explanation for a higher value of $f_{gas}(r_{500})$ than previous measurements is that the sample used for this project consists of massive galaxy clusters. Massive galaxy clusters have a deep potential well which keeps the gas bound despite energy input from supernovae and AGN (Voit, 2005). On the other hand, low mass galaxy clusters and groups have lower gas mass fractions (f_{gas}=0.03-0.07,Sanderson et al. (2003); Vikhlinin et al. (2006); Gastaldello et al. (2007)) because they have shallow potential wells and AGN heating can drive the gas outside the potential well (Sun et al., 2009). Previous studies included low mass systems which will result in a lower measurement of the average gas mass fraction.

Another possible explanation for finding a measurement that agrees with the cosmic baryon fraction is that the sample used for this project consists of relaxed galaxy clusters. These clusters appear spherical in X-ray images and are the mostly likely candidates for being in hydrostatic equilibrium. Therefore masses calculated using hydrostatic equilibrium and a spherically symmetrical model are expected to be accurate at r_{500} (Lau et al., 2009). Some previous studies included unrelaxed systems in their samples which introduce systematics in the measurement of the gas mass fraction.

7.4 Redshift Evolution of the Gas Mass Fraction in Galaxy Clusters

A combined analysis of X-ray and SZE observations of galaxy clusters can be used for a variety of astrophysical applications (Birkinshaw & Hughes, 1994; Hughes & Birkinshaw, 1998; Reese et al., 2002; LaRoque et al., 2006; Bonamente et al., 2006). The joint analysis allows for the direct measurement of the cluster gas mass fraction without the need to impose external priors on cosmological parameters (e.g., the Hubble expansion rate $H(z)$). Such an analysis can directly probe the evolution of cluster gas mass fractions with redshift, providing an important complement to X-ray only cosmological studies that rely on simulations to supply this function (Allen et al., 2008). The joint X-ray and SZE analysis method described in Chapter 3 are applied to 25 relaxed galaxy clusters spanning a redshift range of 0.09-1.06. This joint measurement of the gas mass fraction from a sample of clusters spanning a large redshift range can be used to test the assumption that the gas mass fraction is constant with redshift (Sasaki, 1996; Pen, 1997). Knowledge of the evolution of the gas mass fraction as a function of redshift is required to obtain accurate constraints on cosmological parameters (for example, Allen et al., 2004, 2008; Ettori et al., 2009).

To determine whether there is a difference in the measurement of f_{gas} as a function of redshift, the sample was divided into 2 each bins, low redshift ($z < 0.39$) and high redshift clusters ($z \geq 0.39$). At r_{500} the low redshift clusters have a mean gas mass fraction 0.136 ± 0.010 and the high redshift clusters have a mean gas mass fraction 0.119 ± 0.016. The gas mass fraction at low and high redshift agree within 1σ of each other. Therefore, no significant evidence of the gas mass fraction evolving with redshift was found.

This chapter has shown that measuring the evolution of gas mass fraction with minimal assumptions about the cosmology is possible. Better observations are needed to place tighter constraints on the measurements. Also more clusters at high redshift are required to determine the evolution of the gas mass fraction with redshift. Currently both are happening with other surveys.

7.5 Comparison of X-ray and Sunyaev Zel'dovich Effect Measurements of the Electron Pressure

X-ray and Sunyaev Zel'dovich effect observations provide measurements of the electron pressure profile. Both X-ray and SZE observables can be affected by different systematic effects. For example, in X-ray observations non-thermal emission may be present due to Inverse Compton scattering between relativistic electrons and the Cosmic Microwave Background (CMB) photons (Sarazin & Lieu, 1998; Bonamente et al., 2005). The presence of the non-thermal emission may result in an increase in the X-ray emission above the level of the thermal gas. As for SZE observations, radio emission from cluster halos (Brunetti et al., 2007) may partially fill the SZE decrement which will result in a lower SZE signal.

In this chapter, a joint analysis method was performed in order to measure the integrated pressure from X-ray and SZE observations at r_{500} in order to determine the presence of emission that can result in a discrepancy between the pressure profiles. When we examined the ratio of the SZE to X-ray integrated pressure for all 25 clusters, we found a mean SZ/X=1.02 ± 0.04.

Low mass clusters and groups have a shallow potential well, therefore the presence of strong non-thermal emission is more likely to be present than in massive clusters

(Sun et al., 2009). Low mass systems also have low signal-to-noise SZE and X-ray data. The discrepancy in the X-ray and SZE pressure measured by Lieu et al. (2006) and Bielby & Shanks (2007) using ROSAT and WMAP data may be explained by WMAPs low signal-to-noise detection of low mass clusters. The results of this work are consistent with LaRoque et al. (2006) in which the gas mass fraction measured from Chandra observations was the same as the gas mass fraction measured from OVRO and BIMA observations.

APPENDICES

APPENDIX A

SZE DATA REDUCTION

A software program called Difmap was used to produce images from the SZA. It is a useful tool to inspect visibility data. This section explains the procedurce used for identifing radio point sources and the SZE decrement.

In Difmap the u-v visibility file is loaded. The long baseline are selected to detect radio point sources. In order to identify the point sources, it is helpful to know the beam pattern (see Figure A.1a) because the point source will have the same pattern. After viewing the beam pattern, we can go back to the long baseline dirty map. We use NVSS and FIRST 1.4 GHz point sources to help locate faint sources in the 30 GHz map (Figures A.1d and A.1e). Generally point source have a decreasing flux with increasing frequency. Once the point sources are identified, a small box is drawn around their center (Figure A.1b). Then the point source is modeled out. Table A.1 contains all information about the radio point sources found within $600''$of the cluster. This procedure is repeated until a map of the noise remains (Figure A.1c).

After all radio sources are removed, the short baseline maps are used to located the SZE decrement (Figure A.2b). The SZE decrement is detected in the center of the map. We use a CLEAN algorithm to deconvovle the beam from the decrement. The result is a cleaned map (Figure A.1c).

This procedure was repeated for all 25 clusters. The beam pattern, maps with point sources, maps with NVSS and FIRST markers (when available), map of noise after point sources have been removed are documented for the long baseline data. As for the short baseline data, the beam pattern, map of decrement, and CLEAN map are shown for each cluster.

At the beginning of this project, OVRO (Owens Valley Radio Observatory) and BIMA (Berkeley-Illinois-Maryland Association) data was available for clusters which did not have SZA observations at the time. The OVRO and BIMA observations for some clusters are documented as well. Additional clusters can be found in Appendix B as a possibility of expanding the cluster sample.

Table A.1. Radio Sources in Cluster Field

Cluster	z	Pointing Center		SZ		30 GHz Source				1.4 GHz Flux (mJy)	
		α(J2000)	δ(J2000)	$\Delta\alpha$ (")	$\Delta\delta$ (")	src	$\Delta\alpha$ (")	$\Delta\delta$ (")	Flux (mJy)	NVSS	FIRST
MACSJ0159.8-0849	0.40	01:59:49.4	-08:49:58	30.9	-8.9	1	-0.4	-0.9	84.4±0.2	36.7	31.4
Abell 383	0.19	02:48:03.5	-03:31:45	-0.6	-10.8	1	-2.1	0.7	4.3±0.2	40.9	-
						2	276.1	-160.0	7.5±0.3	54.9	-
MACSJ0329.7-0212	0.45	03:29:41.7	-02:11:48	-20.8	3.5	1	242.4	-93.7	12.7±0.4	37.2	-
Abell 478	0.09	04:13:25.2	+10:27:55	-2.4	-4.2	1	193.0	13.9	2.9±0.1	47.7	-
						2	0.9	-0.1	2.3±0.1	36.9	-
MACSJ0429.6-0253	0.40	04:29:36.1	-02:53:08	-8.2	6.4	1	-1.2	-1.3	18.2±0.2	138.8	-
						2	-293.6	60.3	3.2±0.2	18.3	-
3C186	1.06	07:44:17.5	+37:53:17	-40.6	4.2	1	0.2	0.9	22.6±0.2	1236.4	1244.9
						2	41.0	-90.1	10.6±0.2	105.4	49.2
MACSJ0744.9+3927	0.69	07:44:52.9	+39:27:37	-11	-2.4	1	-226.6	284.3	2.5±0.5	-	4.4
MACSJ0947.2+7623	0.34	09:47:13.1	+76:23:14	-10.4	-11	1	0.7	0.2	2.5±0.3	21.7	-
Zwicky 3146	0.29	10:23:39.3	+04:11:13	-6.2	14.7	1	86.2	-33.8	5.0±0.3	95.8	56.7
						2	2.7	-2.9	1.7±0.2	7.1	2.0
						3	-40.0	-124.0	2.2±0.2	31.5	15.1
MACSJ1115.8+0129	0.35	11:15:52.1	+01:29:53	0.9	-2.4	1	129.6	-362.9	2.7±0.2	11.5	10.5
						2	163.1	-97.9	3.7±0.2	-	2.1
						3	140.6	-67.2	1.8±0.3	-	-
						4	-2.2	0.6	1.4±0.4	6.2	5.6
						5	-168.0	-73.6	2.7±0.2	10.3	6.4
MS1137.5+6625	0.78	11:40:22.3	+66:08:16	7	-2.8	-	-	-	-	-	-
Abell 1413	0.14	11:55:18.0	+23:24:18	-8	-14	1	-125	121.5	2.1±0.1	28.1	19.8
						2	-394.0	-199.2	2.8±0.3	-	-
CLJ1226.9+3332	0.89	12:26:58.0	+33:32:45	-4.4	6.8	1	259.0	-39.2	3.9±0.2	29.8	23.2
MACSJ1311.0-0311	0.49	13:11:01.6	-03:10:40	9	-7	-	-	-	-	-	-
RXJ1347.5-1145	0.45	13:47:30.7	-11:45:09	10.7	-7.1	1	-0.7	-0.8	8.7±0.2	45.9	-
						2	-328.4	244.4	6.9±0.4	365.8	-
						3	-42.6	272.4	2.6±0.3	5.1	-
Abell 1835	0.25	14:01:02.0	+02:52:42	2.3	-7.6	1	0.8	1.6	2.9±0.3	39.3	31.3
						2	-26.7	-55.3	1.0±0.3	-	-
MACSJ1423.8+2404	0.54	14:23:47.9	+24:04:43	11.2	30.6	1	-0.6	-0.9	2.0±0.2	8.0	5.2
MACSJ1427.3+4408	0.49	14:27:16.2	+44:07:31	-6	10.4	1	-1.2	-0.4	16.4±0.2	47.9	41.3
						2	27.6	217.2	1.1±0.2	8.6	8.2
RXJ1504.1-0248	0.21	15:04:07.9	-02:48:16	-11.7	-1.8	1	-6.0	-0.5	15.9±0.2	60.5	40.8
MACSJ1532.9+3021	0.36	15:32:53.9	+30:20:59	0.9	0.0	1	-38.4	-72.9	5.7±0.2	7.9	6.0
						2	-1.8	0.3	3.2±0.2	22.8	15.2
						3	-81.9	-128.4	1.3±0.2	18.0	4.1
MACSJ1621.6+3810	0.46	16:21:24.8	+38:10:09	7.6	-12.1	-	-	-	-	-	-
Abell 2204	0.15	16:32:46.9	+05:34:32			1	0.4	1.2	7.0±0.2	69.3	57.9
						2	-417.8	-360.1	21.6±0.2	41.6	-
						3	195.0	-130.1	0.7±0.1	12.2	1.2
MACSJ1720.3+3536	0.39	17:20:16.8	+35:36:27	-9.7	9.0	1	640.6	349.2	167.7±0.2	-	-
						2	0.6	-0.4	1.8±0.4	18.0	16.8
RXJ2129.6+0005	0.23	21:29:39.9	+00:05:20	3.9	0.9	1	0.7	1.3	2.6±0.2	25.4	23.8
						2	232.0	161.8	3.1±0.2	34.3	6.6
Abell 2537	0.29	23:08:22.1	-02:11:29	-44.2	10	1	94.4	531.6	8.4±0.9	69.9	58.6

A.1 MACSJ0159.8-0849

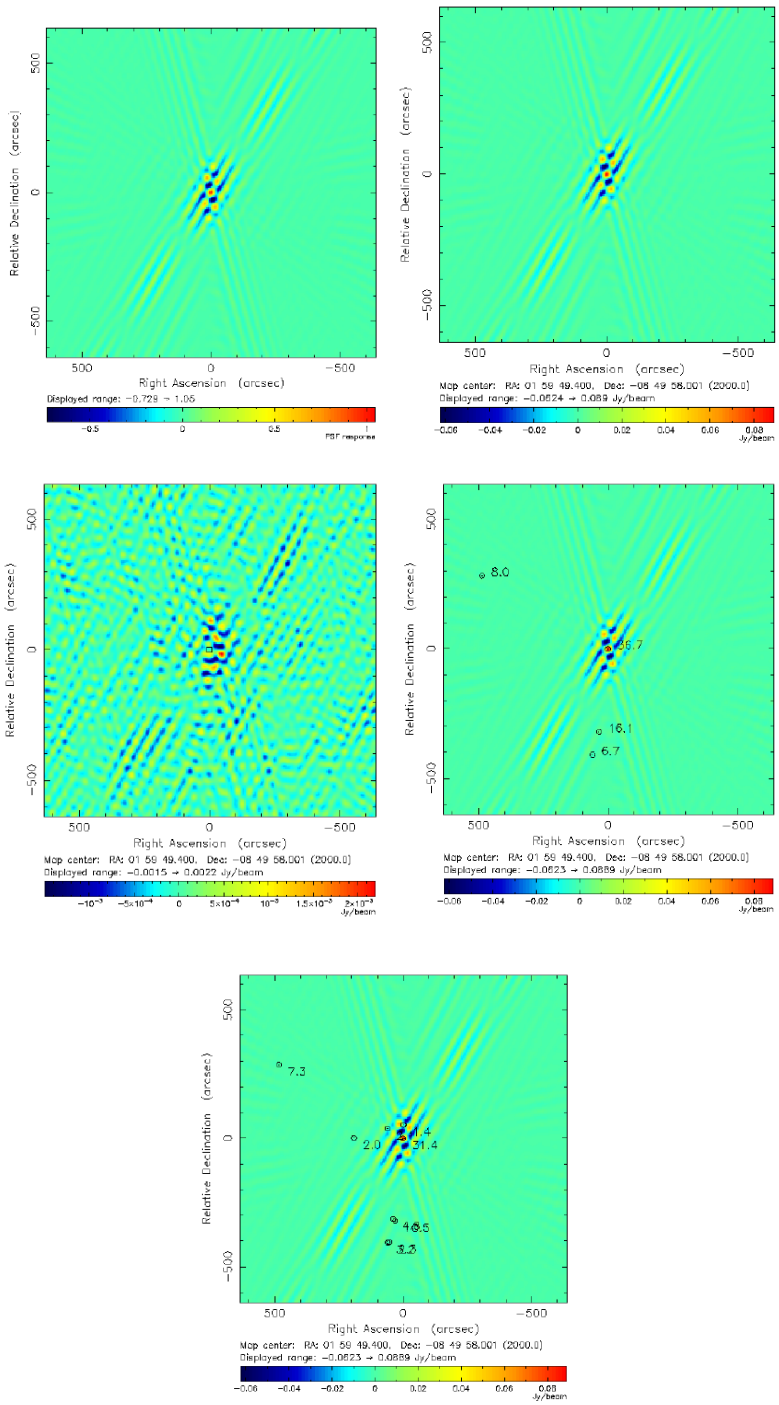

Figure A.1: MACSJ0159.8-0849: (a) Long baseline beam, (b) dirty map, (c) point sources removed map, (d) dirty map with NVSS markers, (e) dirty map with FIRST markers.

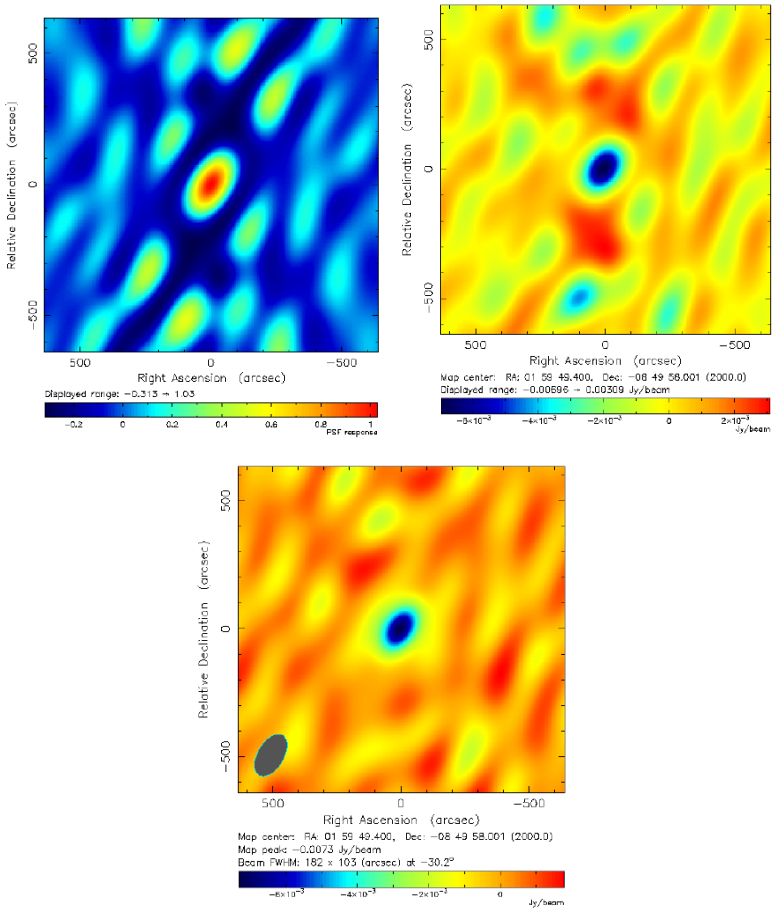

Figure A.2: MACSJ0159.8-0849: (a) Short baseline beam, (b) point sources removed map, and (c) cleaned map. The synthesized beam is 182" x 103" FWHM at -30.2^o.

A.2 Abell 383

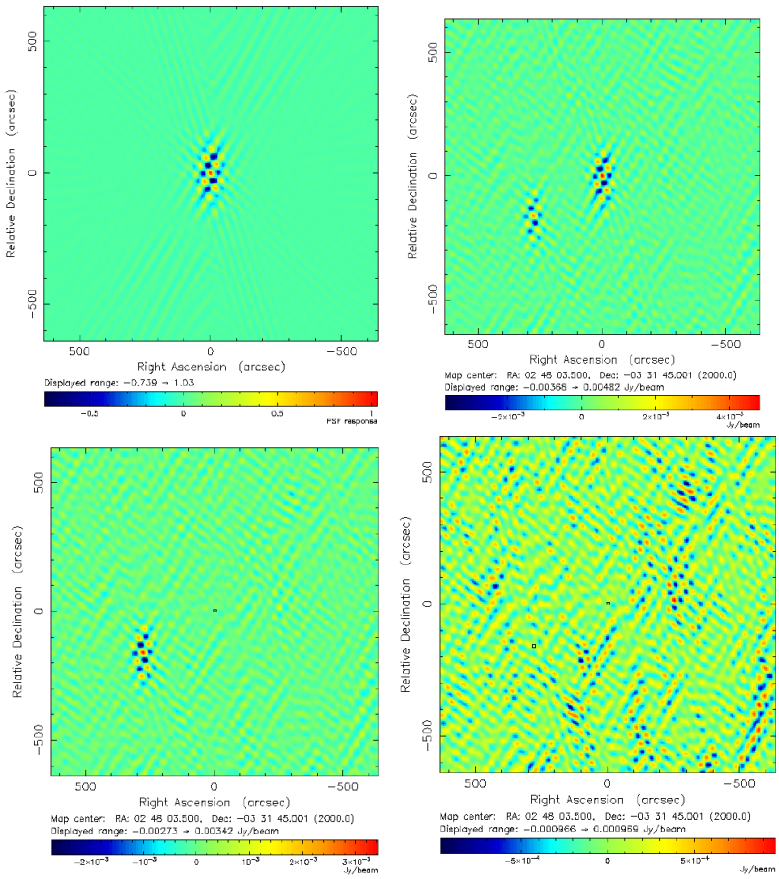

Figure A.3: Abell 383: (a) Long baseline beam, (b) dirty map, (c) 1 point source removed map, (d) 2 point sources removed map.

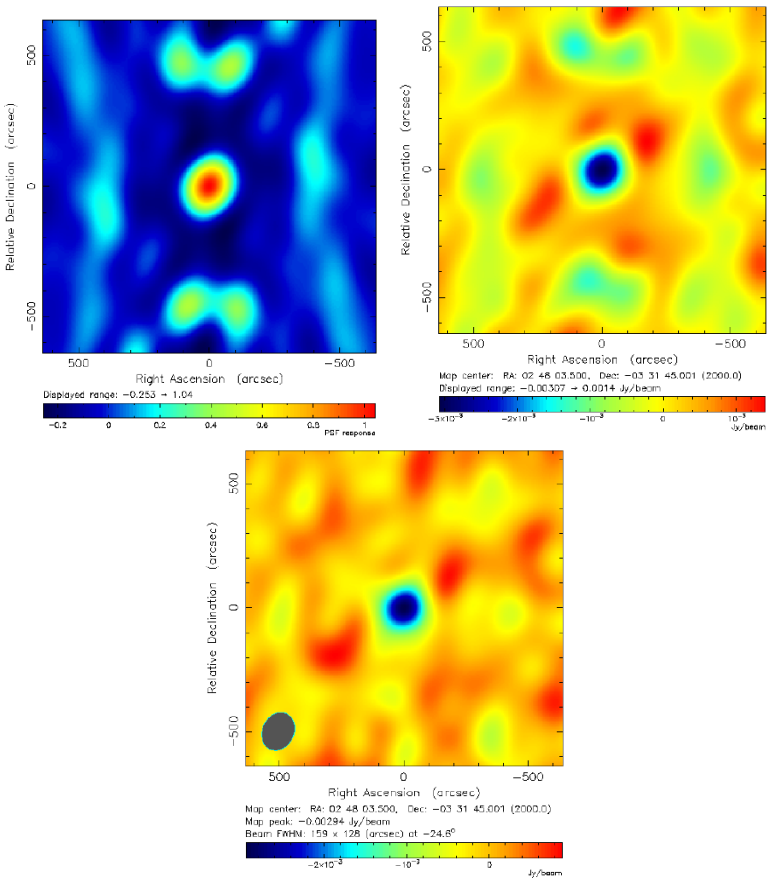

Figure A.4: Abell 383: (a) Short baseline beam, (b) dirty map, and (c) cleaned map. The synthesized beam is 159" x 128" FWHM at -24.6^o.

A.3 MACSJ0329.7-0212

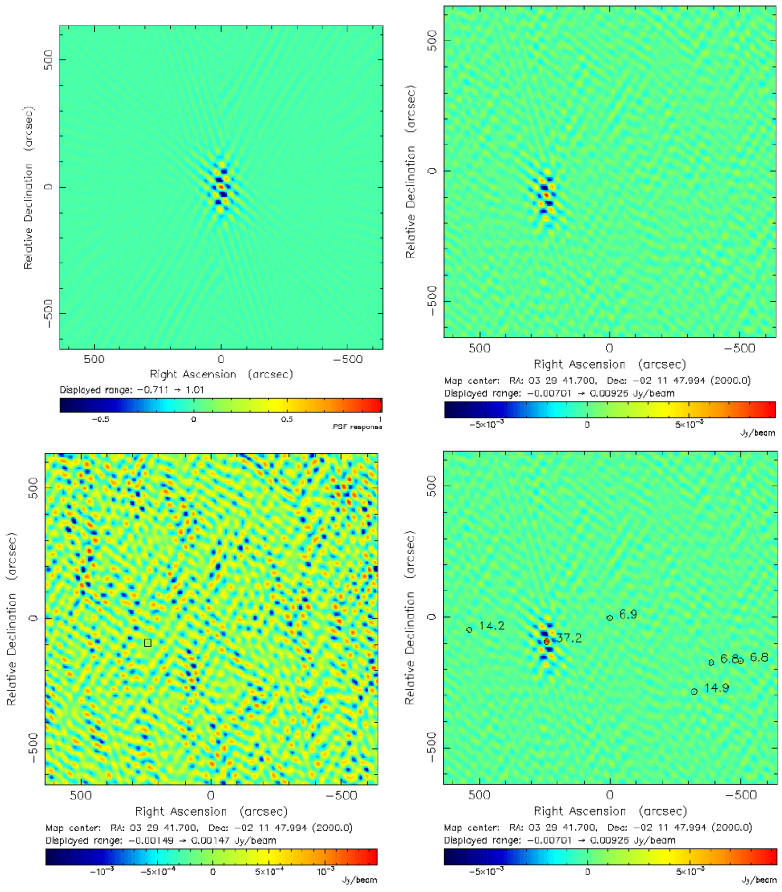

Figure A.5: MACSJ0329.7-0212: (a) Long baseline beam, (b) dirty map, (c) point sources removed map, and (d) dirty map with NVSS markers.

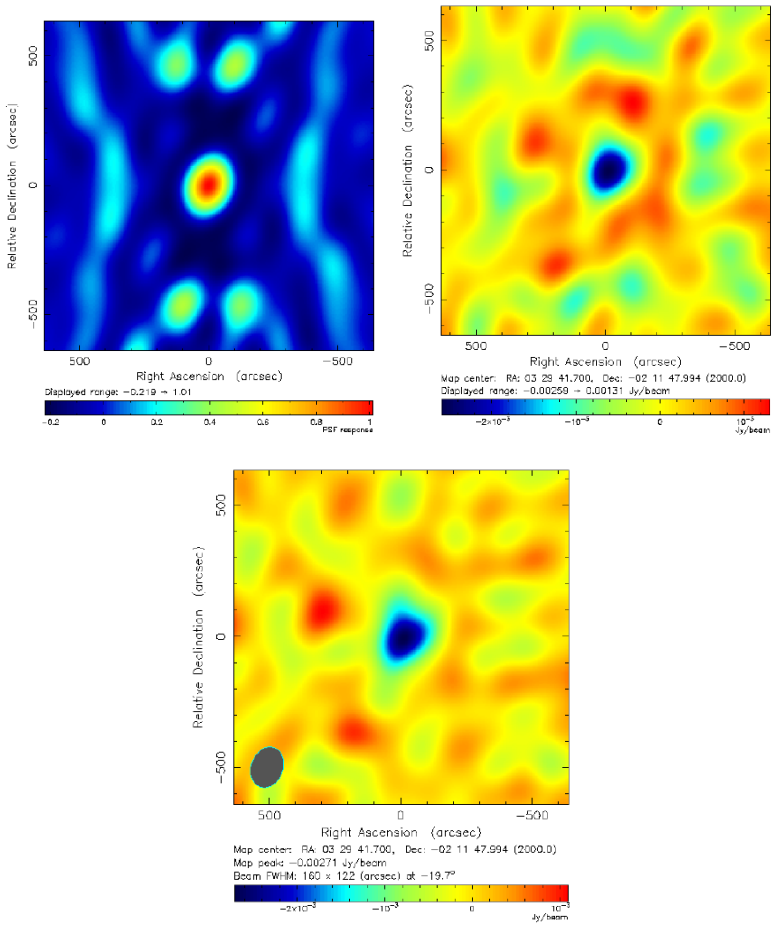

Figure A.6: MACSJ0329.7-0212: (a) Short baseline beam, (b) point sources removed map, and (c) cleaned map. The synthesized beam is 160" x 122" FWHM at -19.7^o.

A.4 Abell 478

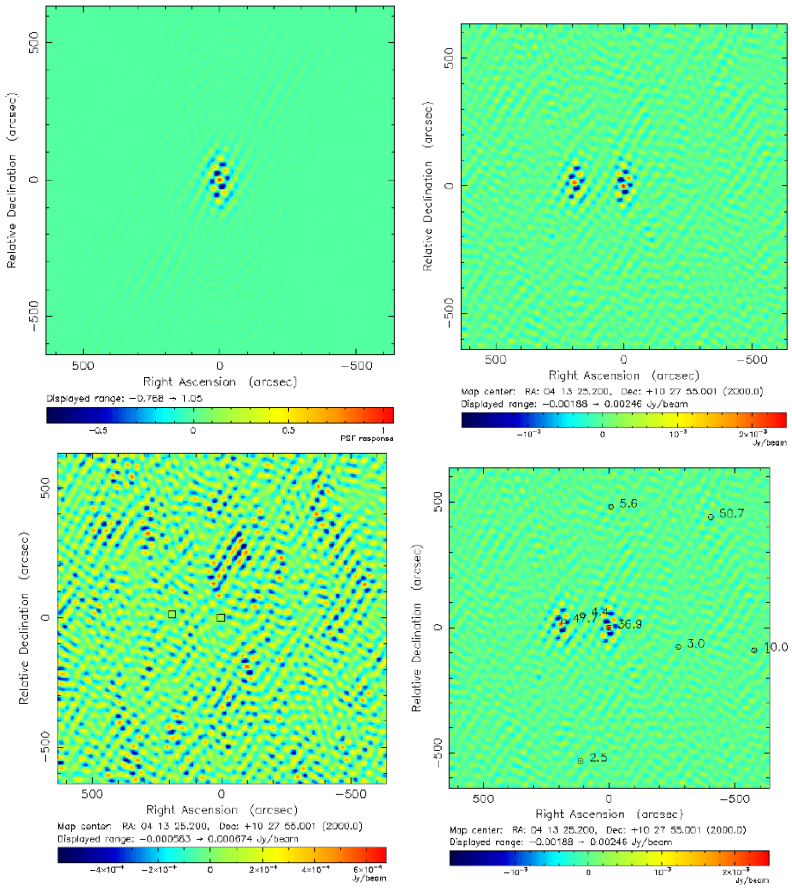

Figure A.7: Abell 478: (a) Long baseline beam, (b) dirty map, (c) 2 point source removed map, and (d) dirty map with NVSS markers.

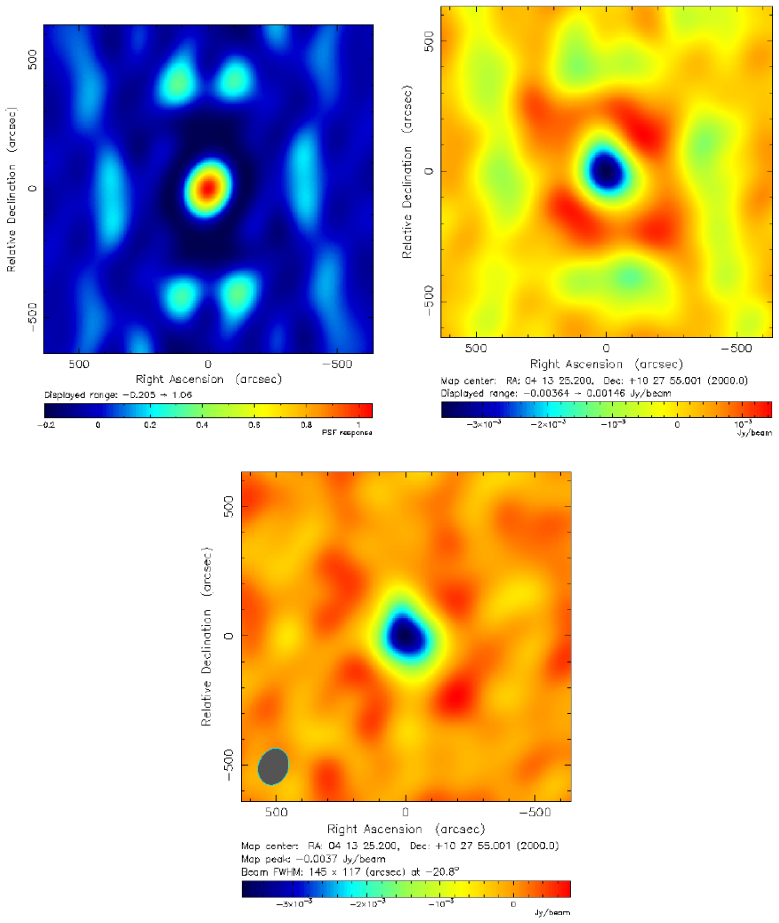

Figure A.8: Abell 478: (a) Short baseline beam, (b) dirty map, and (c) cleaned map. The synthesized beam is 145" x 117" FWHMat -20.8^o.

A.5 MACSJ0429.6-0253

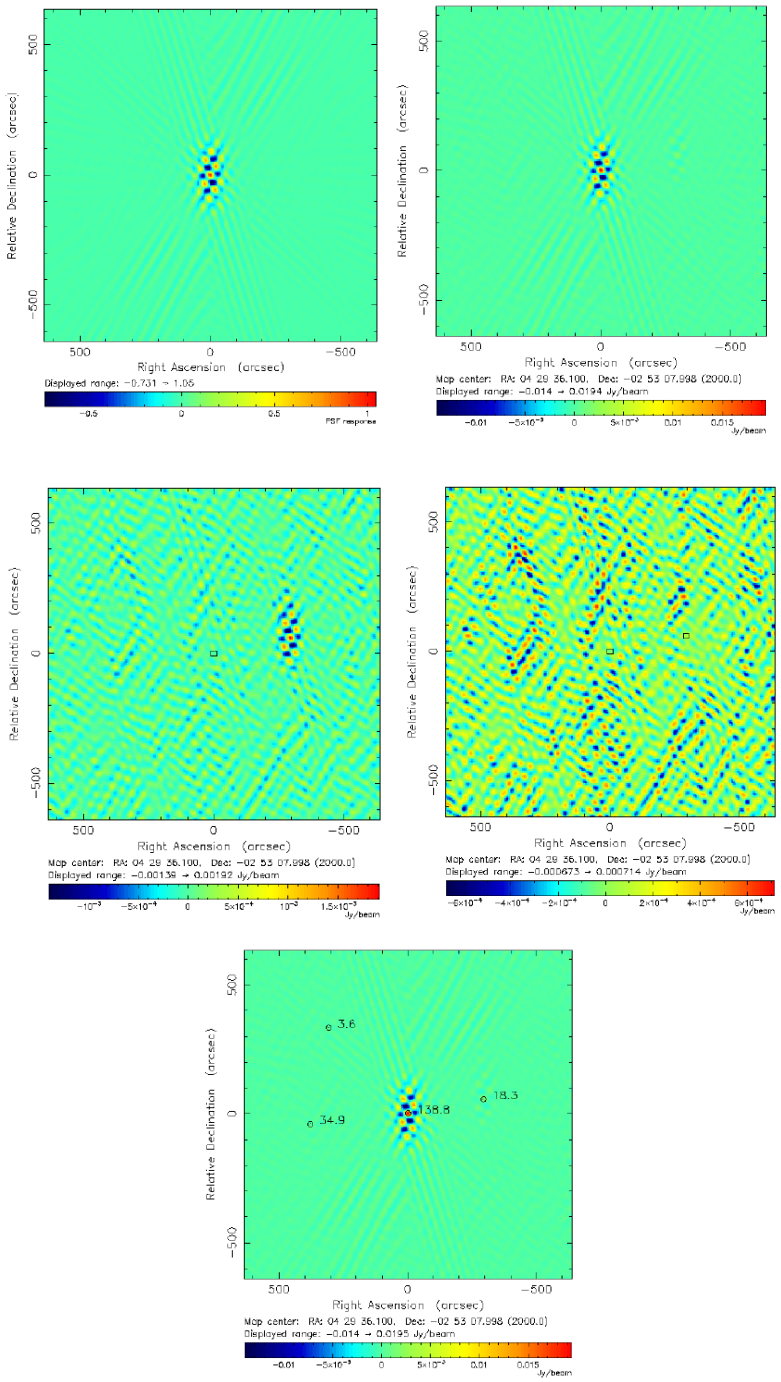

Figure A.9: MACSJ0429.6-0253: (a) Long baseline beam, (b) dirty map, (c) 1 point source removed map , (d) 2 point sources removed map, and (e) dirty map with NVSS markers.

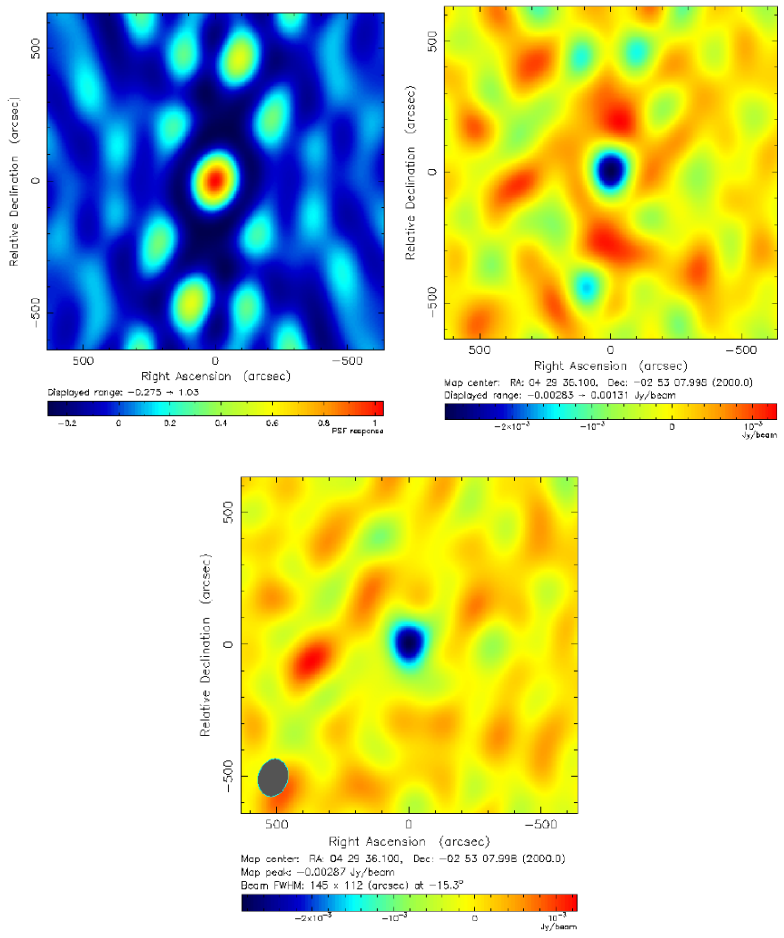

Figure A.10: MACSJ0429.6-0253: (a) Short baseline beam, (b) point sources removed map, and (c) cleaned map. The synthesized beam is 145" x 112" FWHM at -15.3^o.

A.6 3C186

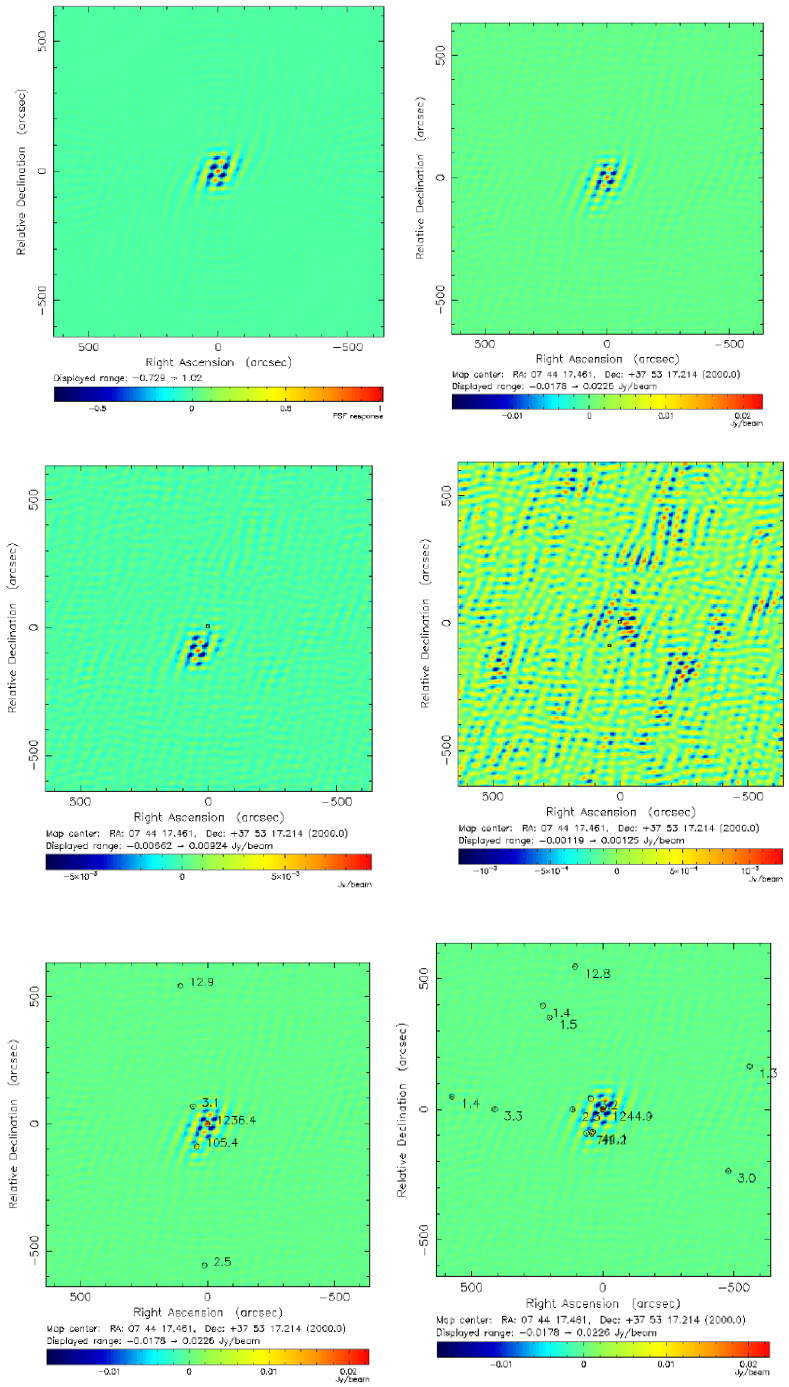

Figure A.11: 3C186: (a) Long baseline beam, (b) dirty map, (c) 1 point source removed map , (d) 2 point sources removed map, and (e) dirty map with FIRST markers and (f) NVSS markers.

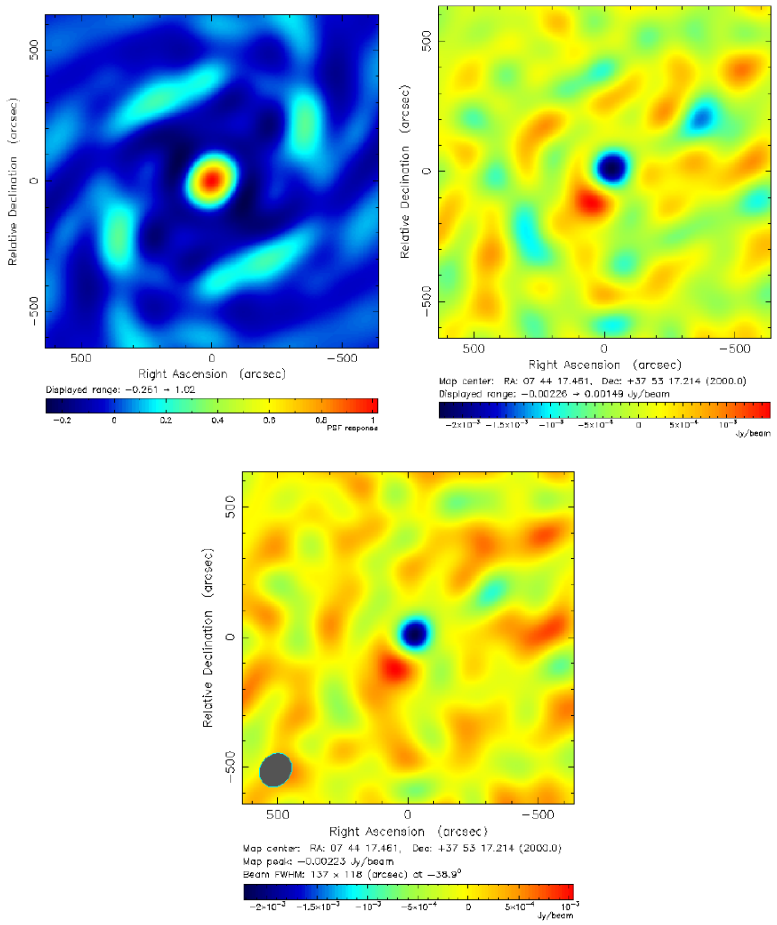

Figure A.12: 3C186: (a) Short baseline beam, (b) point sources removed map, and (c) cleaned map. The synthesized beam is 137" x 118" FWHM at -38.9^o.

A.7 MACSJ0744.9+3927

A.7.1 SZA

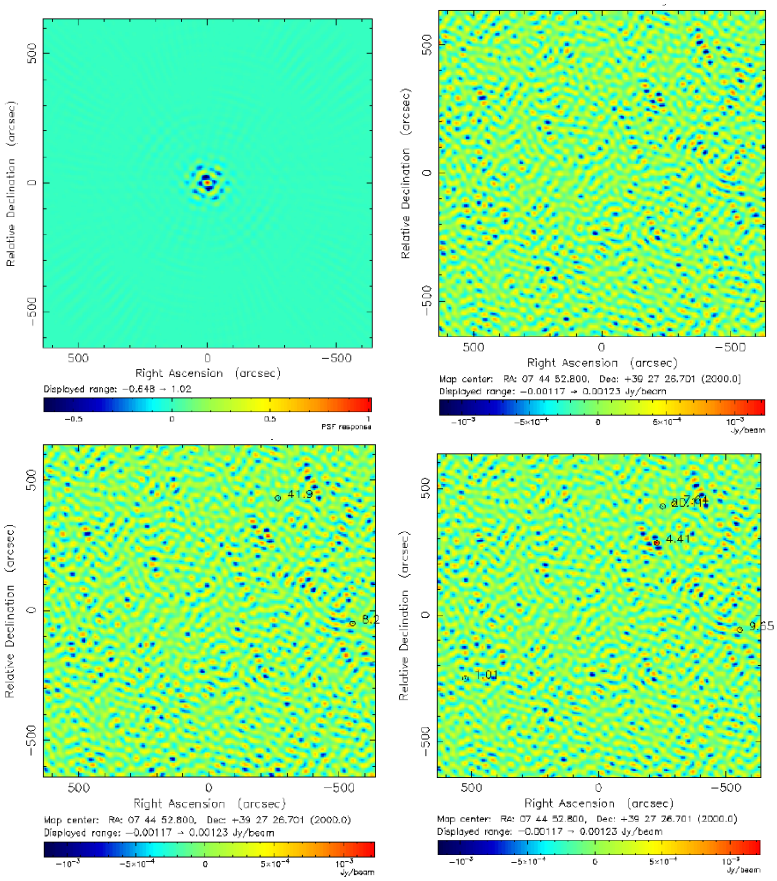

Figure A.13: MACSJ0744.9+3927 SZA: (a) Long baseline beam, (b) dirty map, (c) dirty map with NVSS markers, and (d) dirty map with FIRST markers.

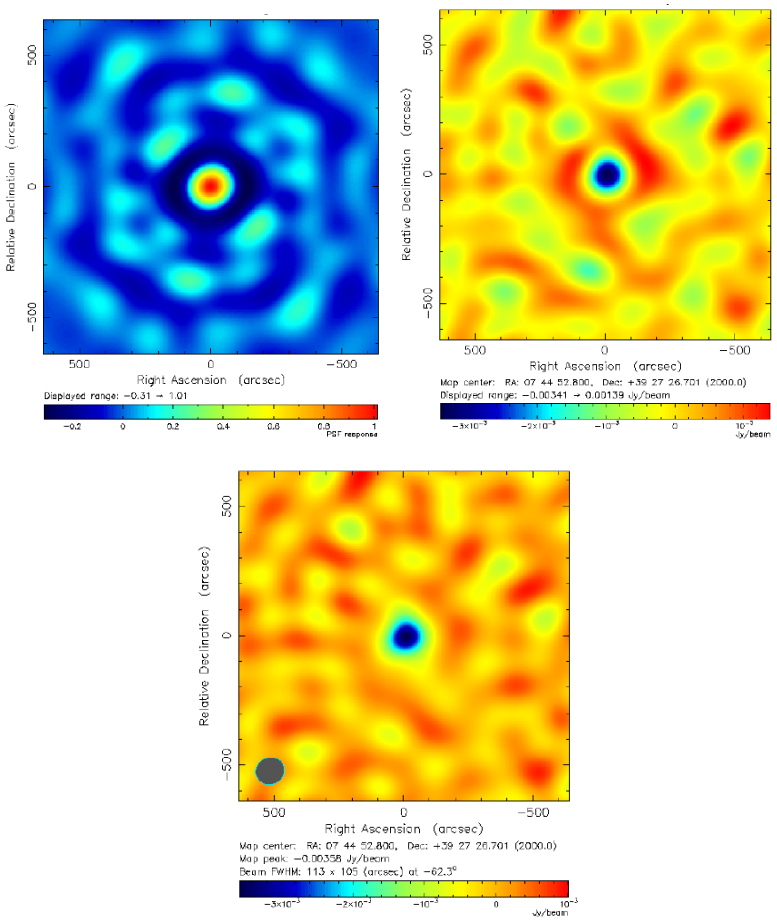

Figure A.14: MACSJ0744.9+3927 SZA: (a) Short baseline beam, (b) dirty map, and (c) cleaned map. The synthesized beam is 113" x 105" FWHM at -62.3^o.

A.7.2 BIMA

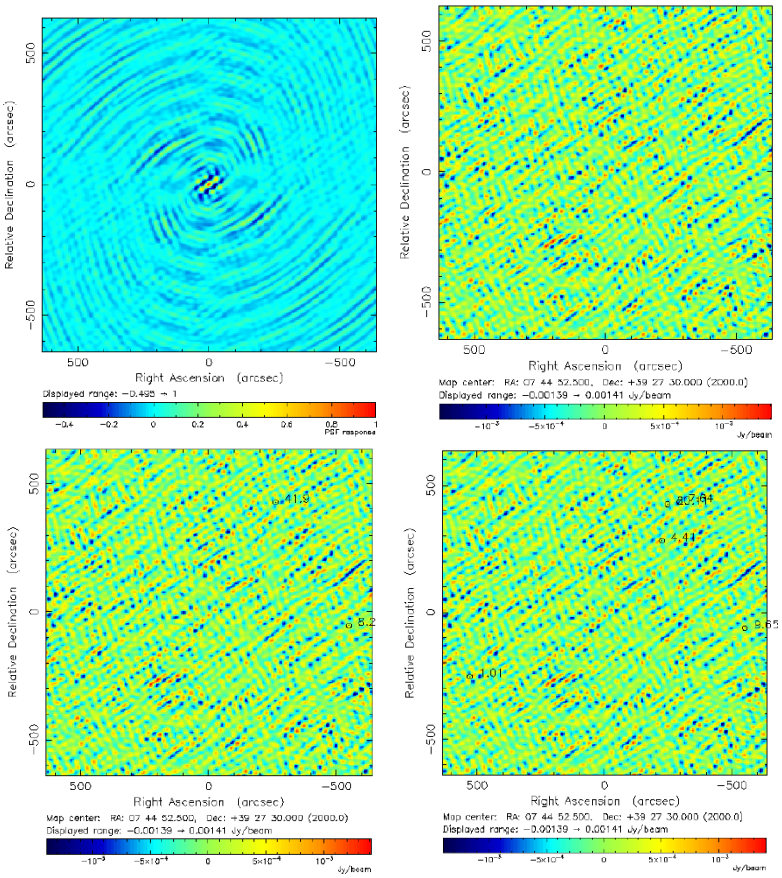

Figure A.15: MACSJ0744.9+3927 BIMA: (a) Long baseline beam, (b) dirty map, (c) dirty map with NVSS markers, and (d) dirty map with FIRST markers.

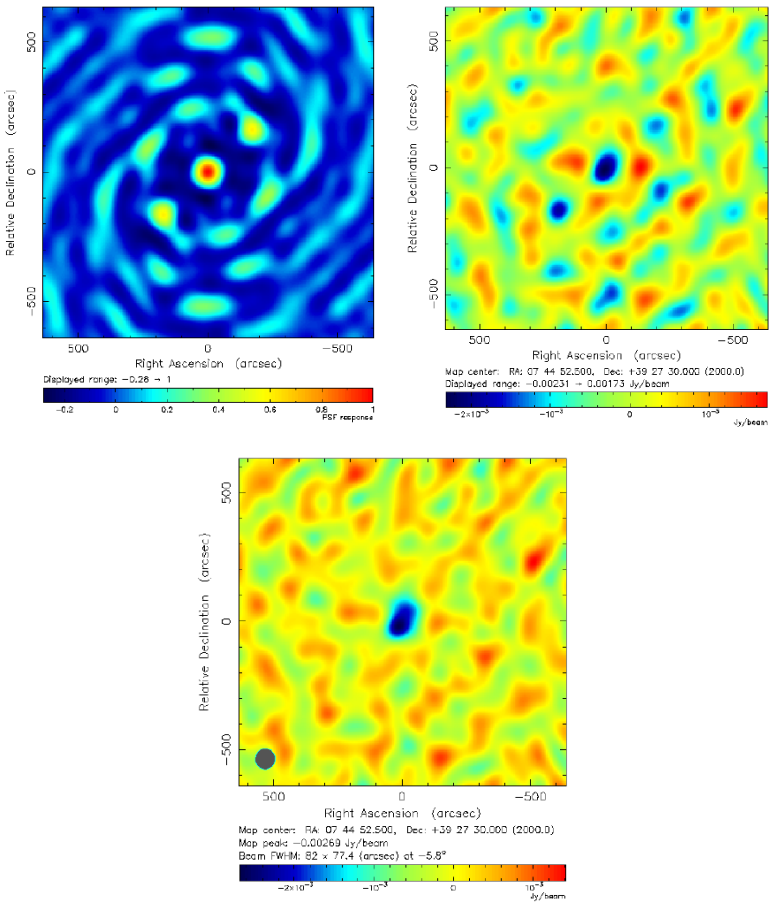

Figure A.16: MACSJ0744.9+3927 BIMA: (a) Short baseline beam, (b) dirty map, and (c) cleaned map. The synthesized beam is 82" x 77.4" FWHM at -5.8^o.

A.7.3 OVRO1

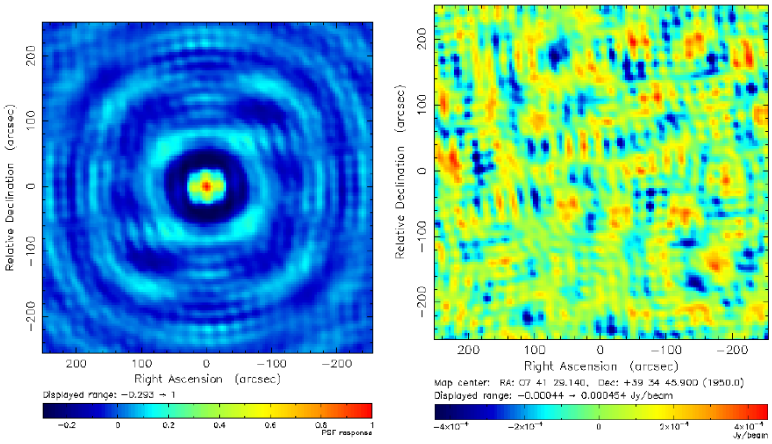

Figure A.17: MACSJ0744.9+3927 OVRO: (a) Long baseline beam and (b) dirty map.

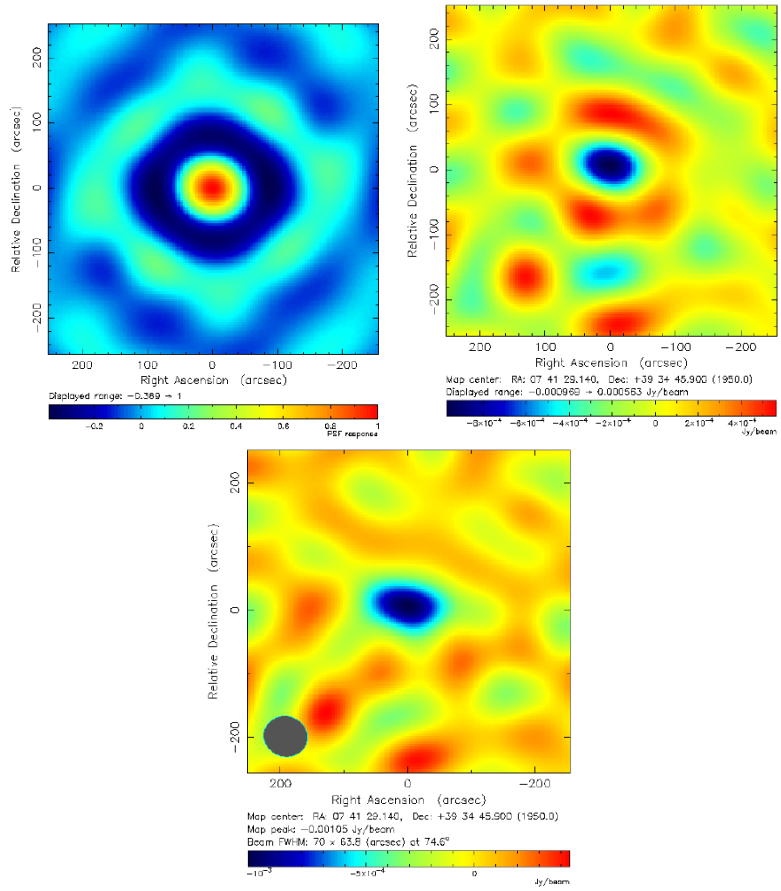

Figure A.18: MACSJ0744.9+3927 OVRO: (a) Short baseline beam, (b) dirty map, and (c) cleaned map. The synthesized beam is 70" x 63.8" FWHM at 74.68°.

A.7.4 OVRO2

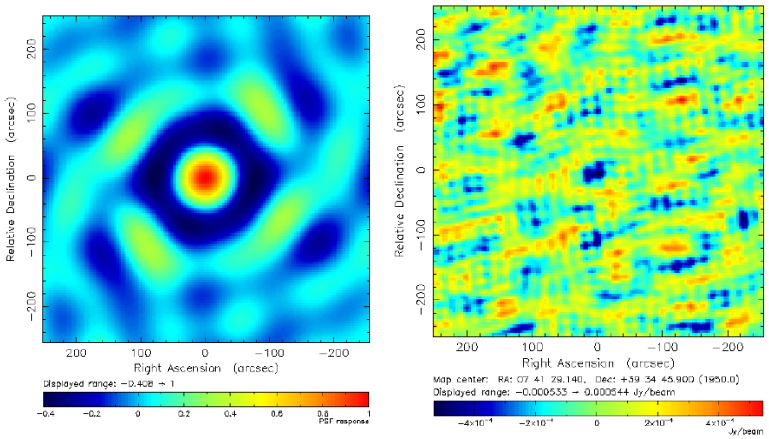

Figure A.19: MACSJ0744.9+3927 OVRO: (a) Long baseline beam and (b) dirty map.

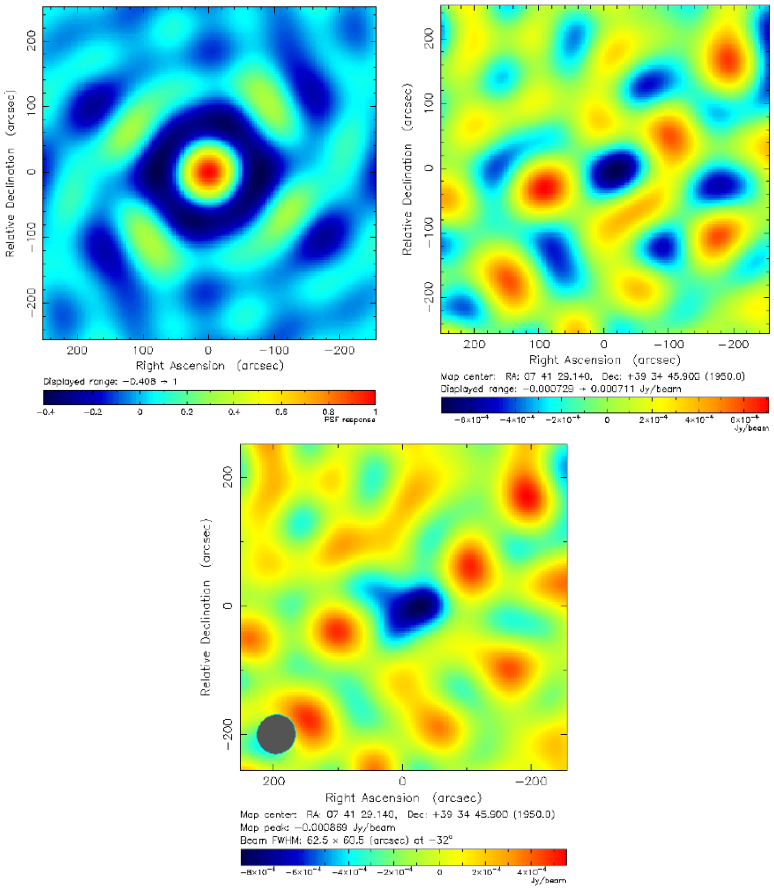

Figure A.20: MACSJ0744.9+3927 OVRO: (a) Short baseline beam, (b) dirty map, and (c) cleaned map. The synthesized beam is 62.5" x 60.5" FWHM at -32.0^o.

A.8 MACS0947.2+7623

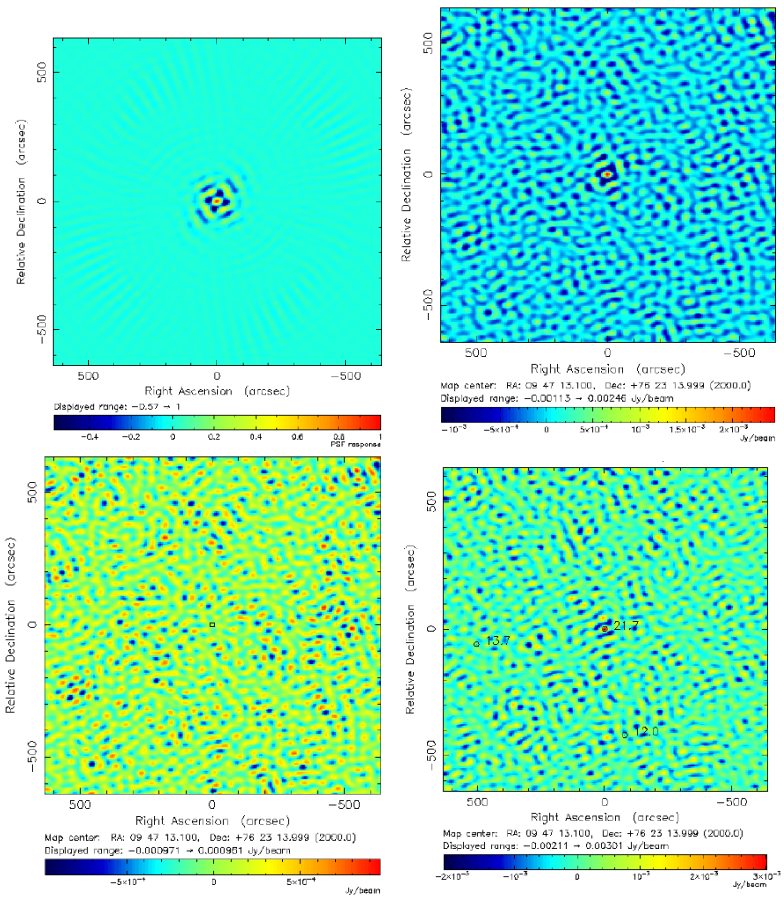

Figure A.21: MACS0947.2+7623: (a) Long baseline beam, (b) dirty map, (c) map after 1 point source removed, and (d) dirty map with NVSS markers.

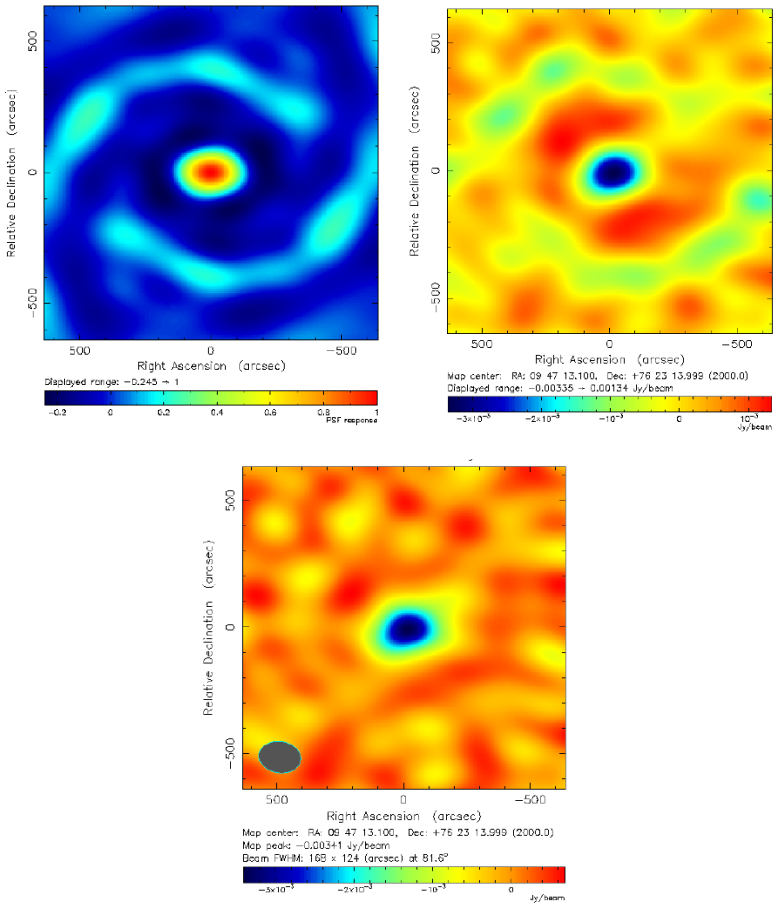

Figure A.22: MACS0947.2+7623: (a) Short baseline beam, (b) dirty map, and (c) cleaned map. The synthesized beam is 167" x 122" FWHM at 83.0^o.

A.9 Zwicky 3146

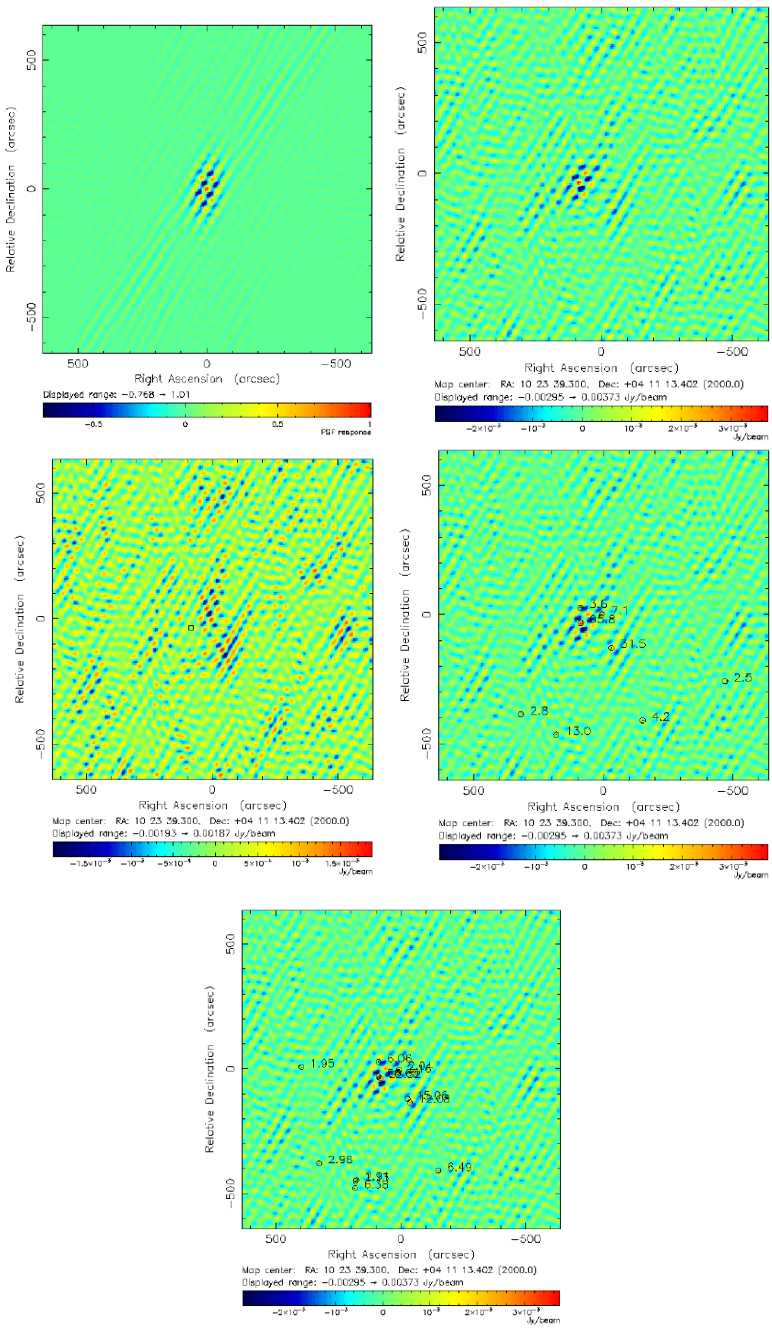

Figure A.23: Zwicky 3146: (a) Long baseline beam, (b) dirty map, (c) point sources removed map, (d) dirty map with NVSS markers, and (e) dirty map with FIRST markers.

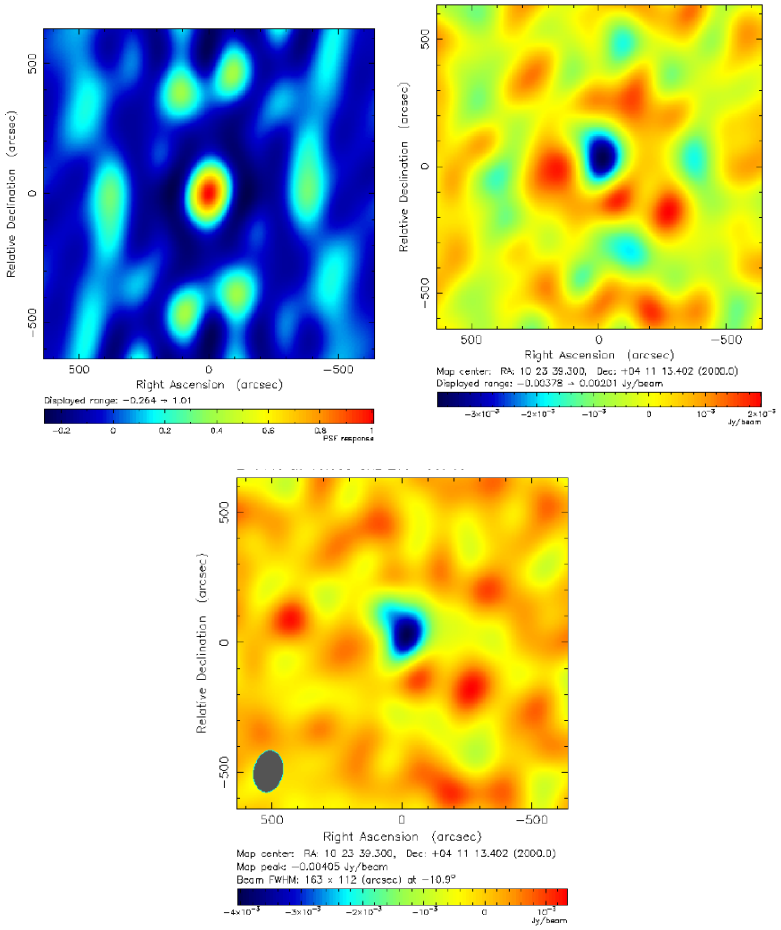

Figure A.24: Zwicky 3146: (a) Short baseline beam, (b) dirty map, and (c) cleaned map. The synthesized beam is 163" x 112" FWHM at -10.9^o.

A.10 MACSJ1115.8+0129

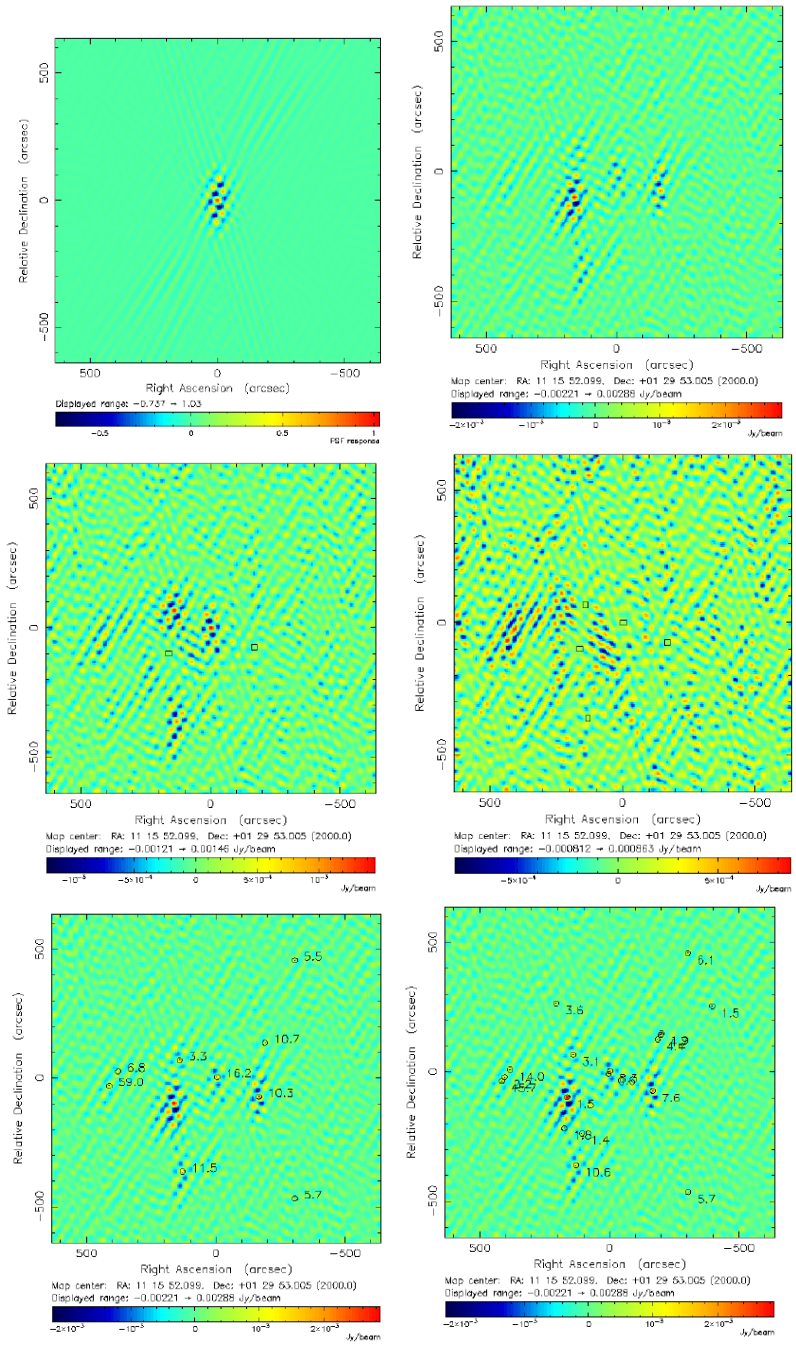

Figure A.25: MACSJ1115.8+0129:(a) Long baseline beam, (b) dirty map, (c) map after 2 point sources are cleaned, (d) map after 5 point sources are cleaned, (e) dirty map with NVSS markers, and (f) dirty map with FIRST markers.

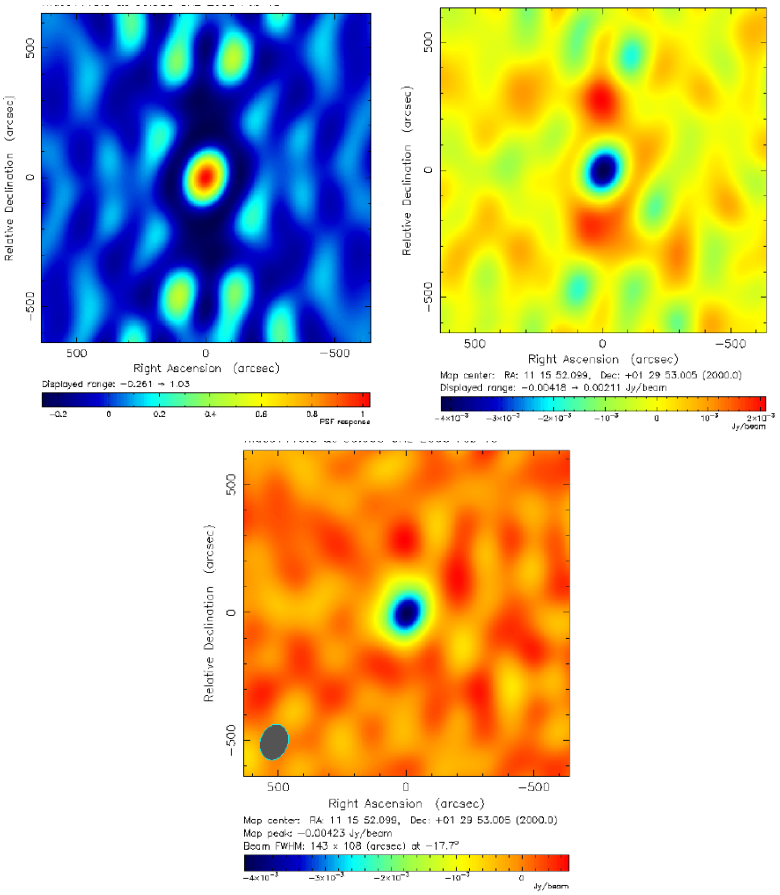

Figure A.26: MACSJ1115.8+0129: (a) Short baseline beam, (b) point sources removed map, and (c) cleaned map. The synthesized beam is 146" x 108" FWHM at -17.7^o.

A.11 MS1137.5+6625

A.11.1 SZA

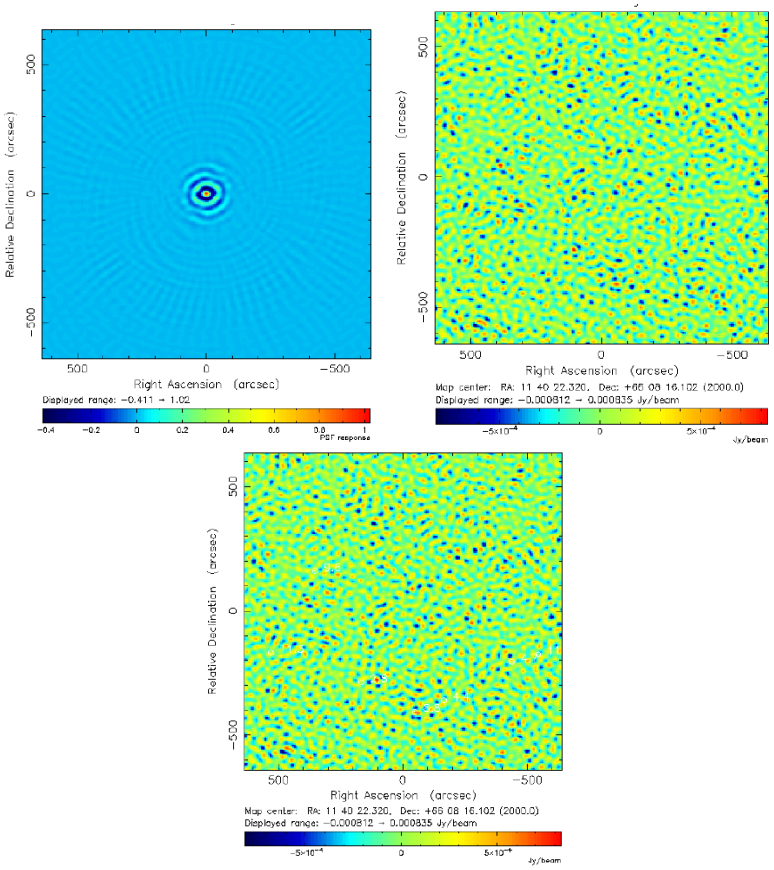

Figure A.27: MS1137.5+6625 SZA: (a) Long baseline beam, (b) dirty map, and (c) dirty map with NVSS markers.

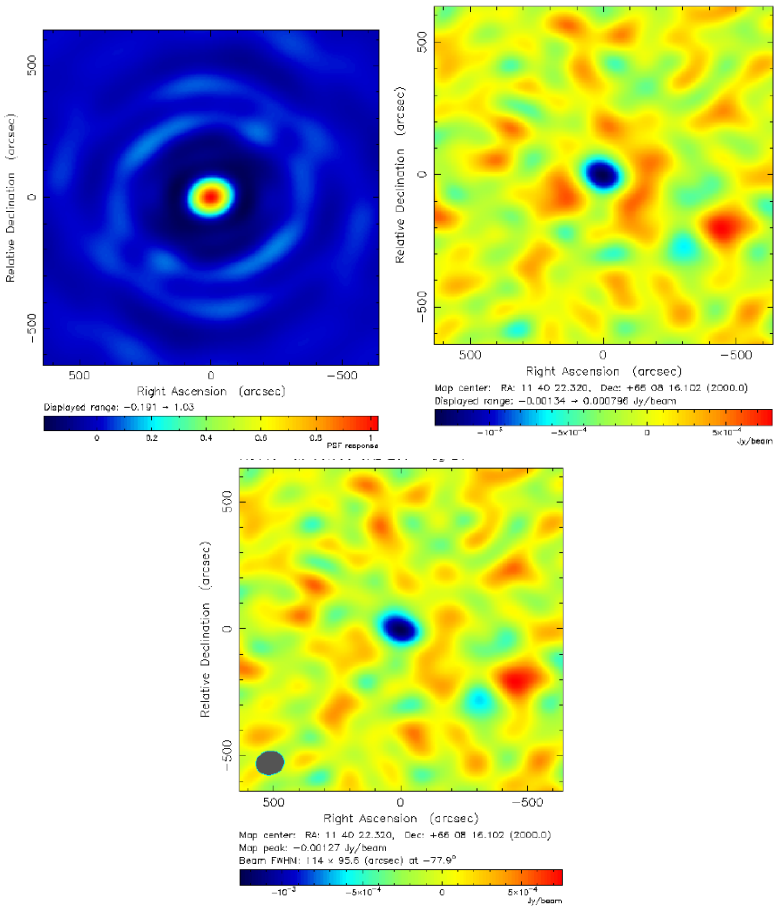

Figure A.28: MS1137.5+6625 SZA: (a) Short baseline beam, (b) dirty map, and (c) cleaned map. The synthesized beam is 80.5" x 76.8" FWHM at 51.5^o.

A.11.2 BIMA

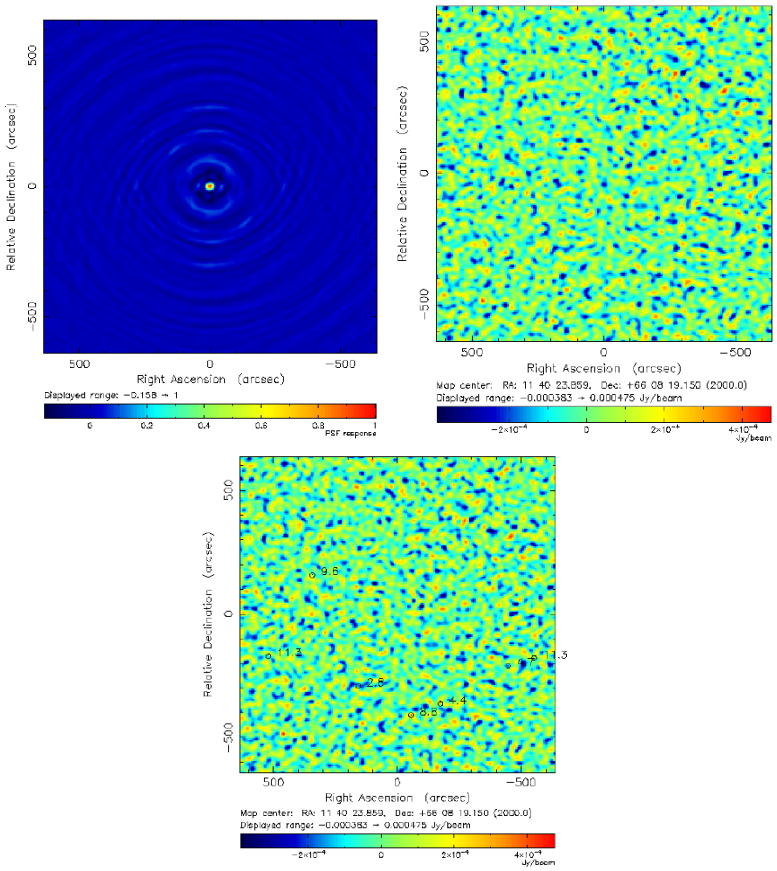

Figure A.29: MS1137.5+6625 BIMA: (a) Long baseline beam, (b) dirty map, and (c) dirty map with NVSS markers.

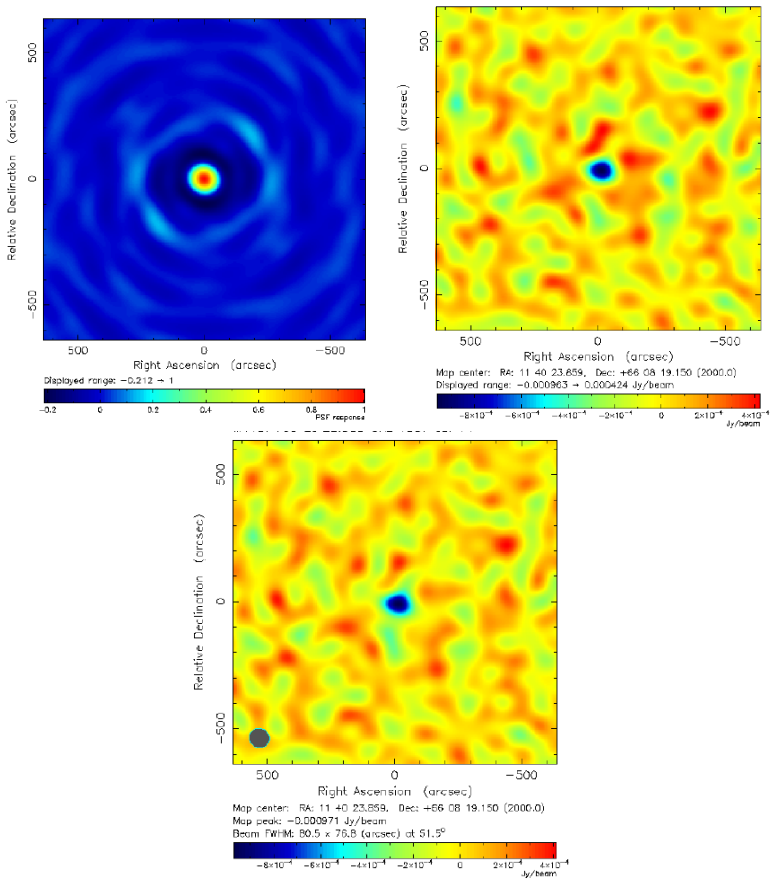

Figure A.30: MS1137.5+6625 BIMA: (a) Short baseline beam, (b) dirty map, and (c) cleaned map. The synthesized beam is 80.5" x 76.8" FWHM at 51.5^o.

A.12 Abell 1413

A.12.1 SZA

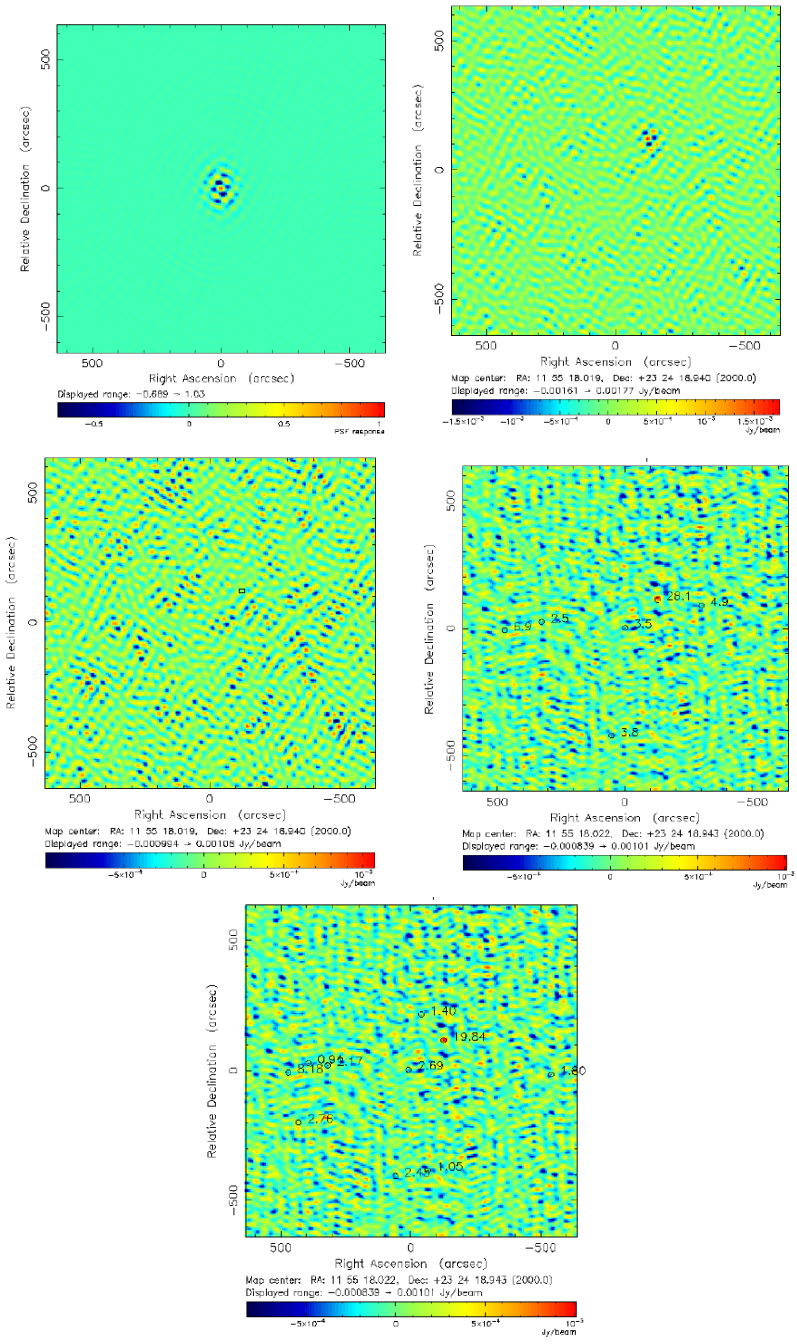

Figure A.31: Abell 1413 SZA: (a) Long baseline beam, (b) dirty map, (c) point source removed map, (d) dirty map with NVSS markers, and (e) dirty map with FIRST markers.

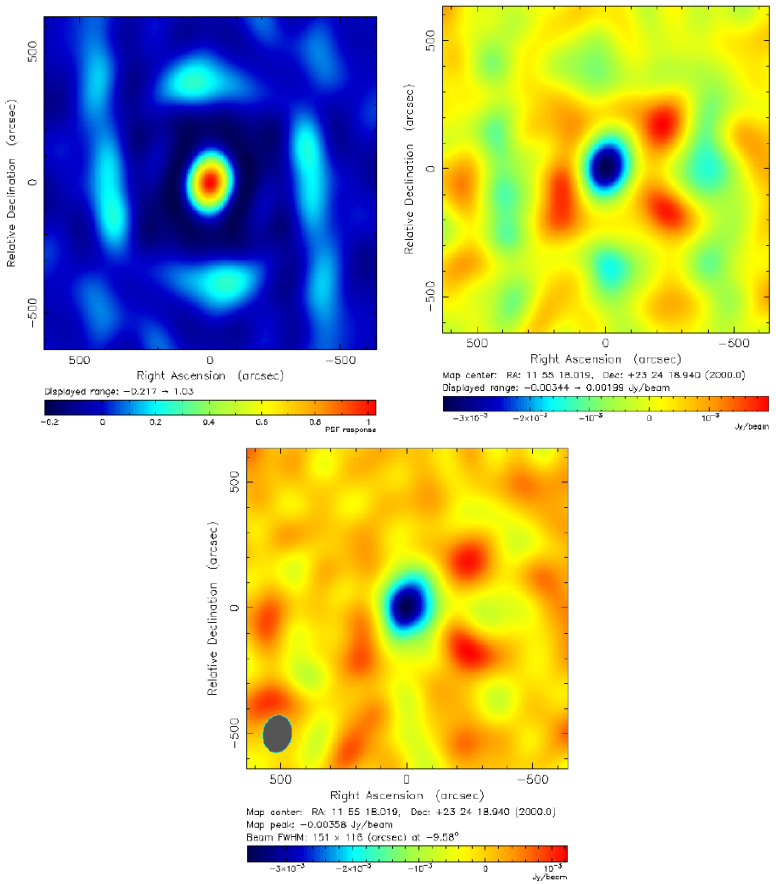

Figure A.32: Abell 1413 SZA: (a) Short baseline beam, (b) dirty map, and (c) cleaned map. The synthesized beam is 151" x 116" FWHM at -9.6^o.

A.12.2 BIMA

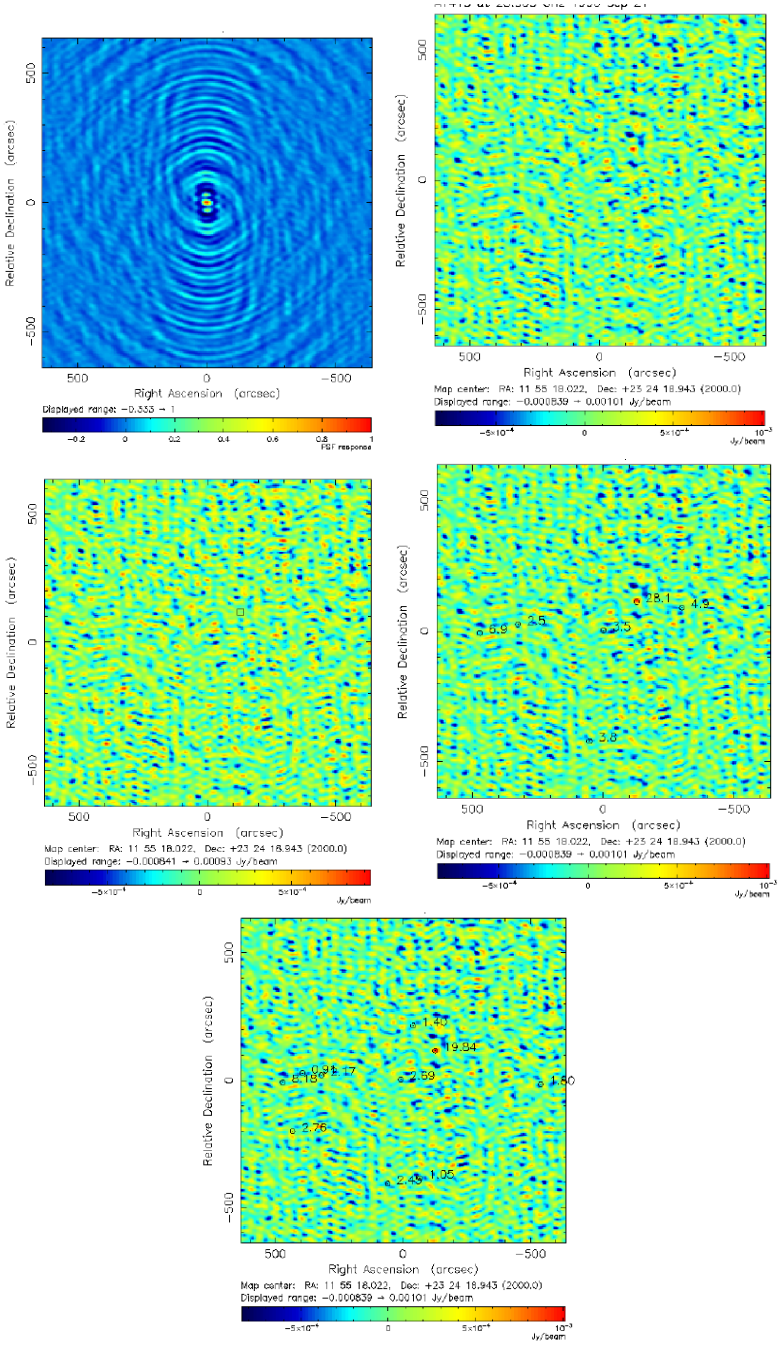

Figure A.33: Abell 1413 BIMA: (a) Long baseline beam, (b) dirty map, (c) 1 point source removed map, (d) dirty map with NVSS markers, and (e) dirty map with FIRST markers.

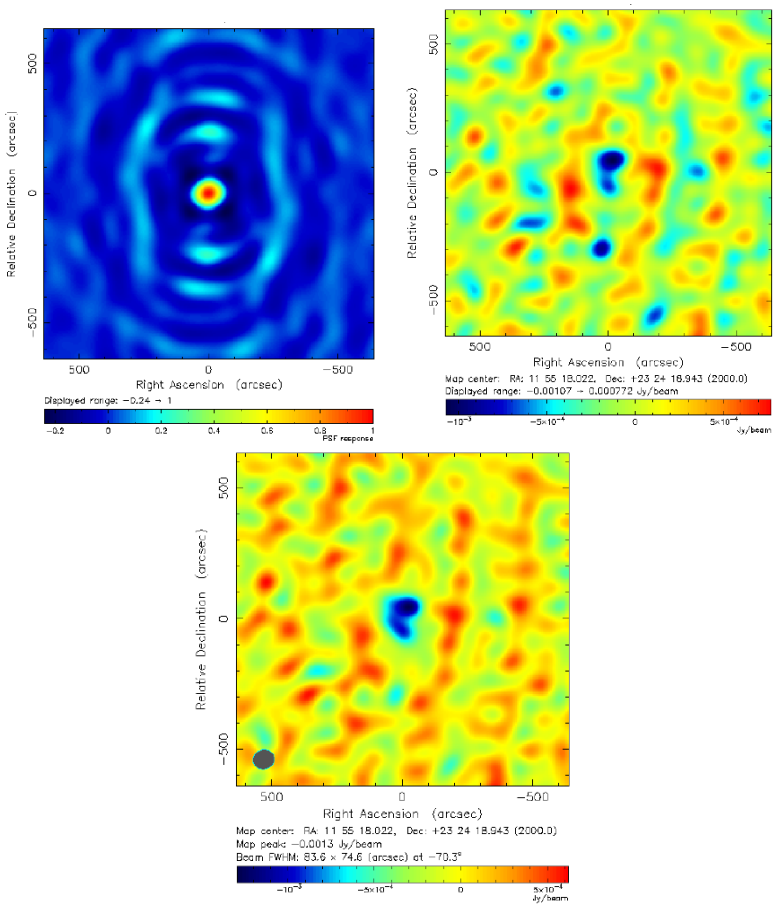

Figure A.34: Abell 1413 BIMA: (a) Short baseline beam, (b) dirty map, and (c) cleaned map. The synthesized beam is 83.6" x 74.6" FWHM at -70.3^o.

A.13 CLJ1226.9+3331

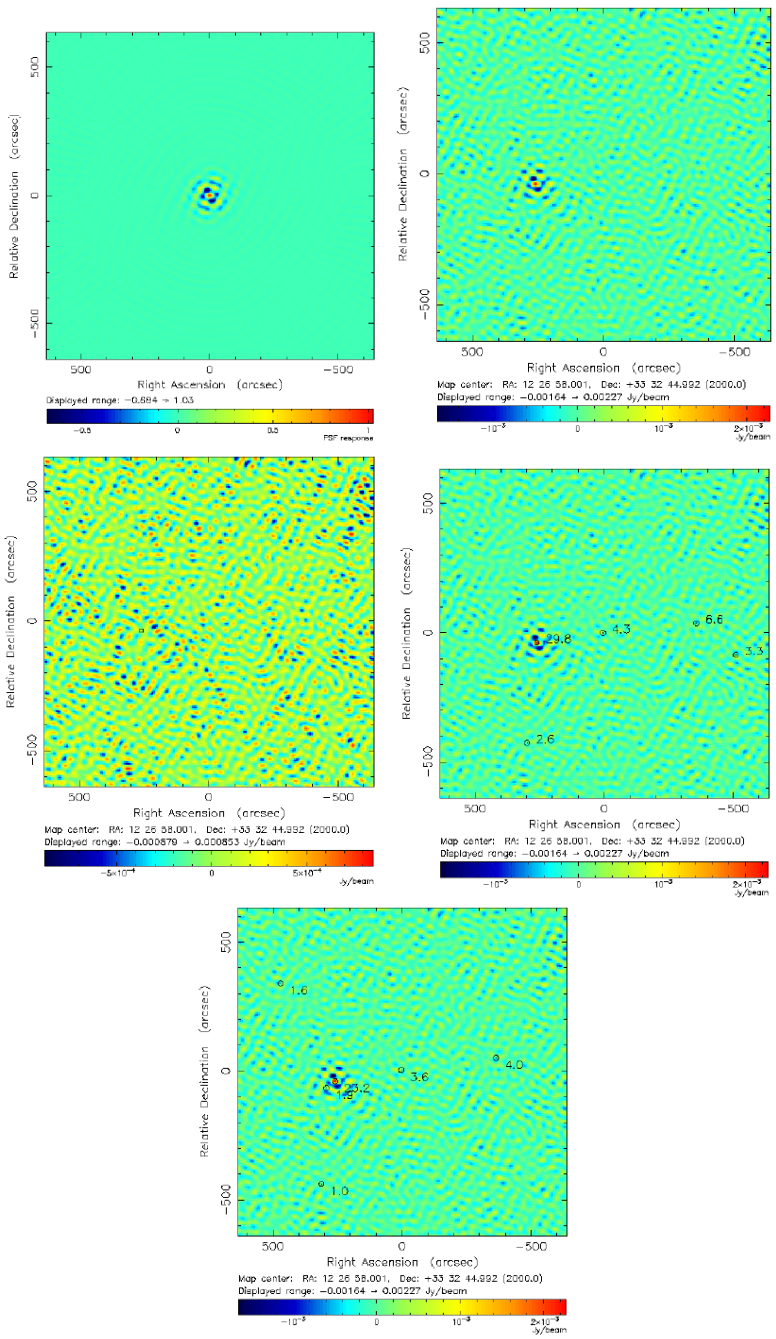

Figure A.35: CLJ1226.9+3331: (a) Long baseline beam, (b) dirty map, and (c) clean, (d) dirty map with NVSS markers, and (e) dirty map with FIRST markers.

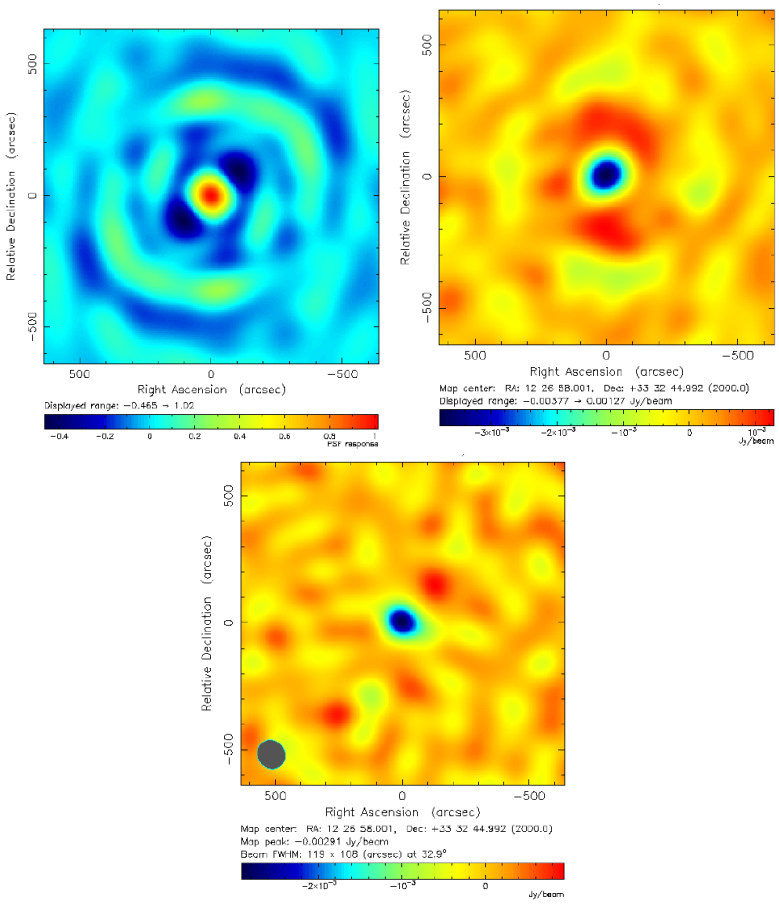

Figure A.36: CLJ1226.9+3331: (a) Short baseline beam, (b) dirty map, and (c) cleaned map. The synthesized beam is 119" x 108" FWHM at 32.9^o.

A.14 MACSJ1311.0-0311

A.14.1 SZA

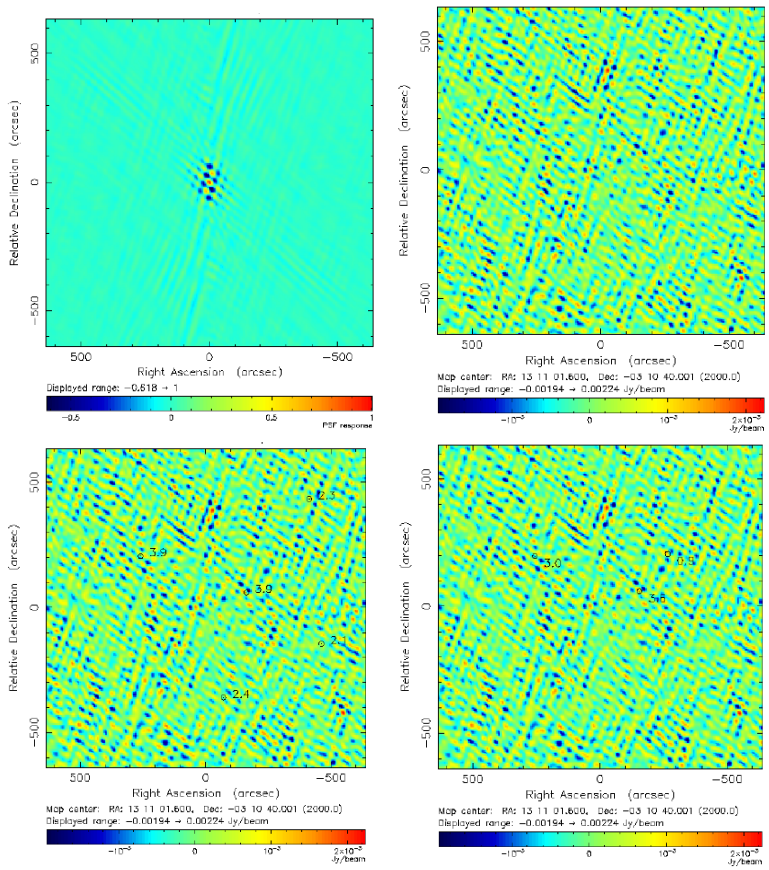

Figure A.37: MACSJ1311.0-0311: (a) Long baseline beam, (b) dirty map, (c) dirty map with NVSS markers, and (d) dirty map with FIRST markers.

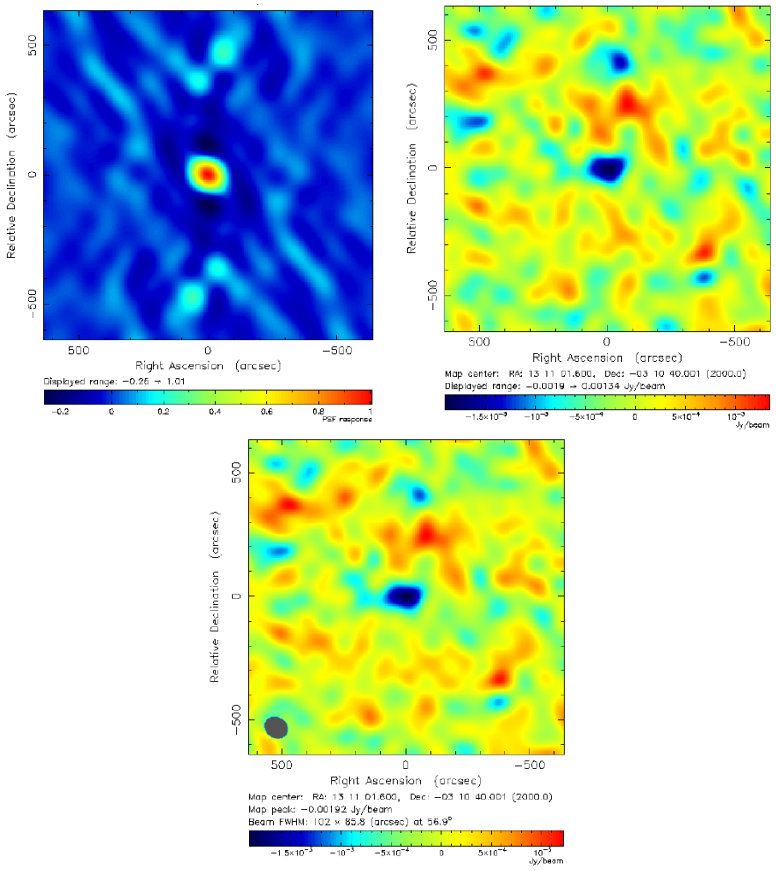

Figure A.38: MACSJ1311.0-0311: (a) Short baseline beam, (b) dirty map, and (c) cleaned map. The synthesized beam is 102" x 85.8" FWHM at 56.9^o.

A.14.2 BIMA

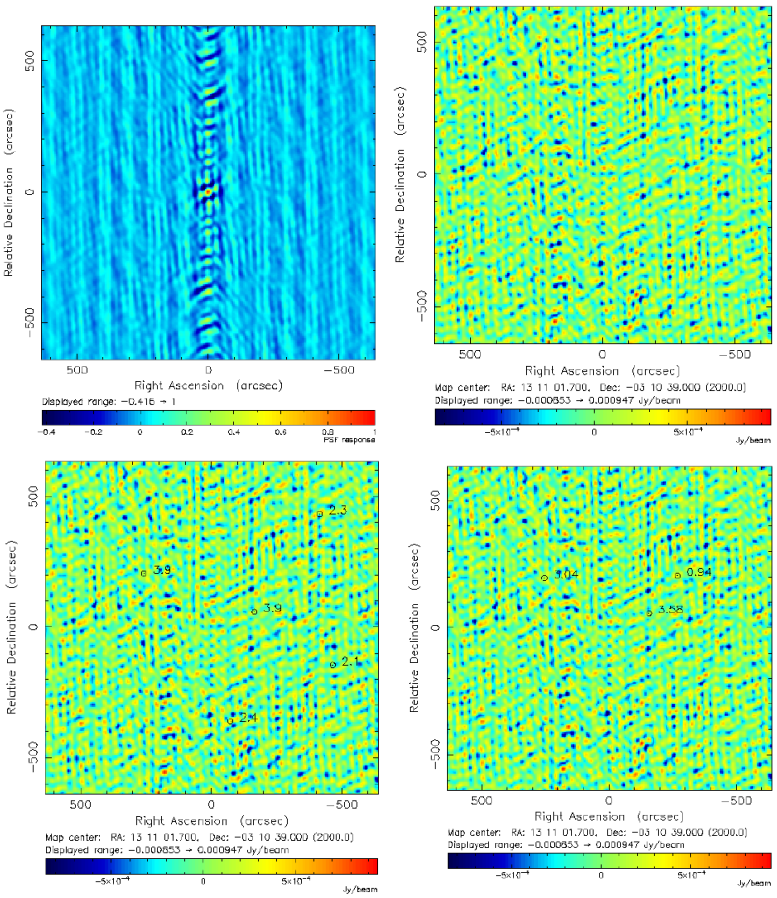

Figure A.39: MACSJ1311.0-0311 BIMA: (a) Long baseline beam, (b) dirty map, (d) dirty map with NVSS markers, and (e) dirty map with FIRST markers.

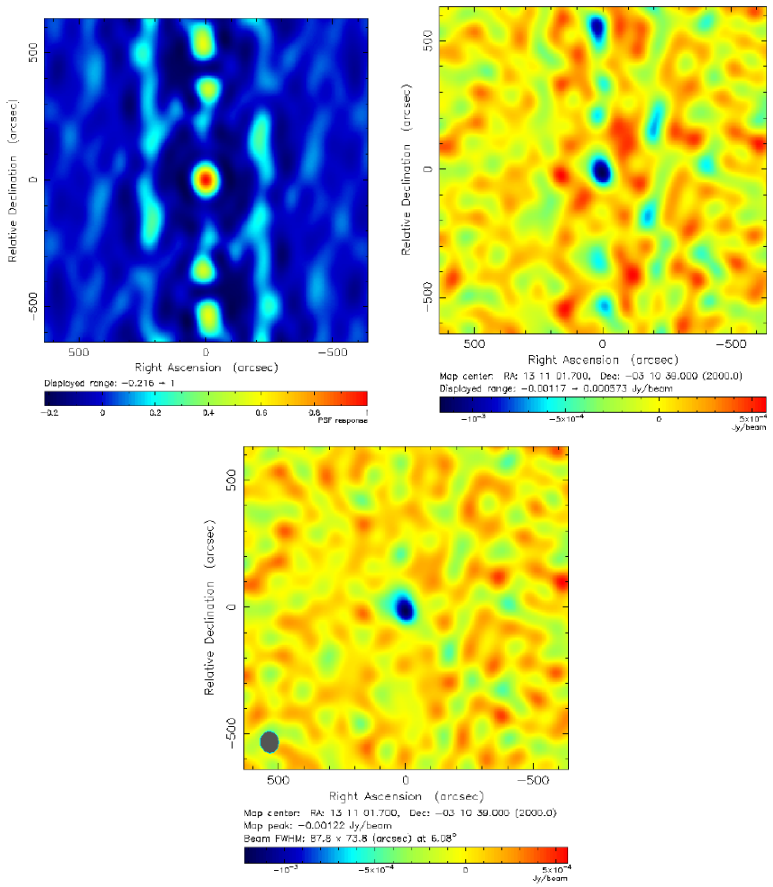

Figure A.40: MACSJ1311.0-0311 BIMA: (a) Short baseline beam, (b) dirty map, and (c) cleaned map. The synthesized beam is 87.8" x 73.8" FWHM at 6.09^o.

A.15 RXJ1347.5-1145

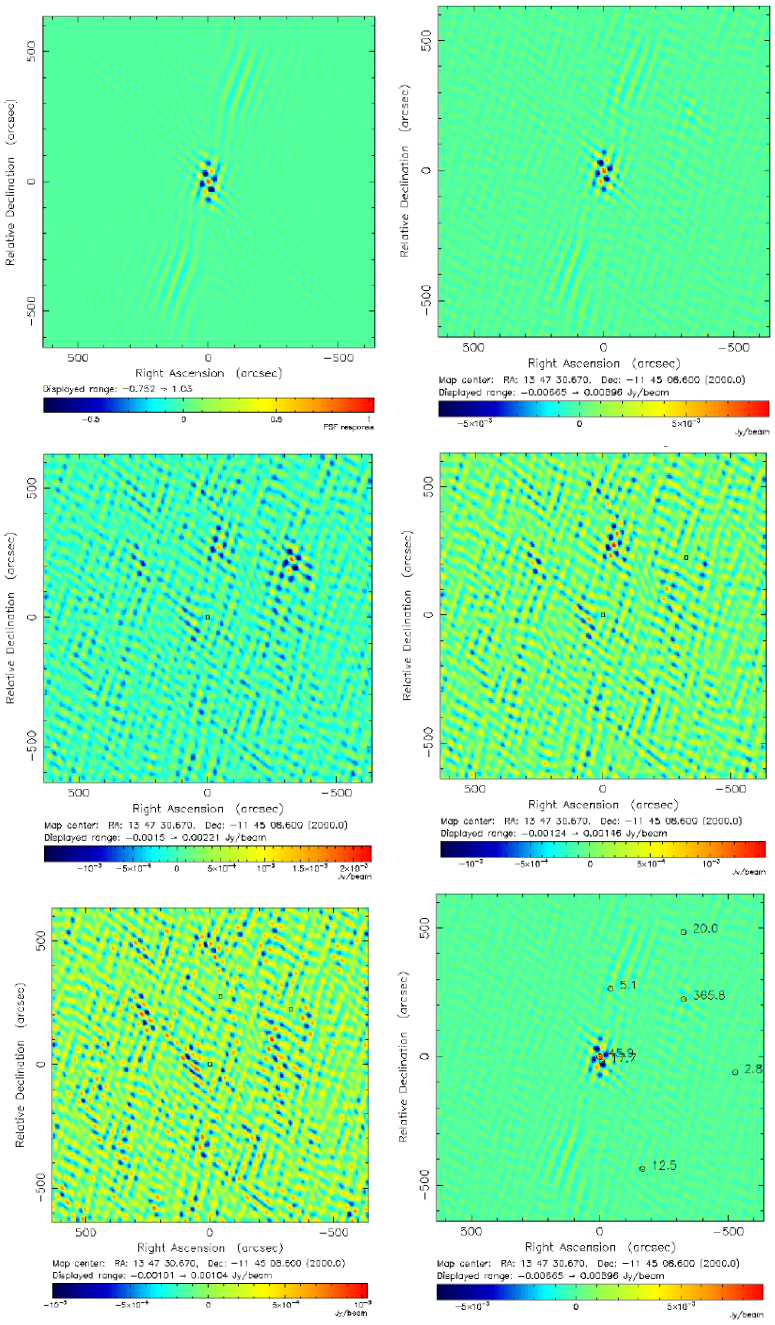

Figure A.41: RXJ1347.5-1145: (a) Long baseline beam, (b) dirty, (c) 1 point source removed map, (d) 2 point sources removed, (e) 3 point sources removed resulting in a map just of the noise and (f) dirty map with NVSS markers.

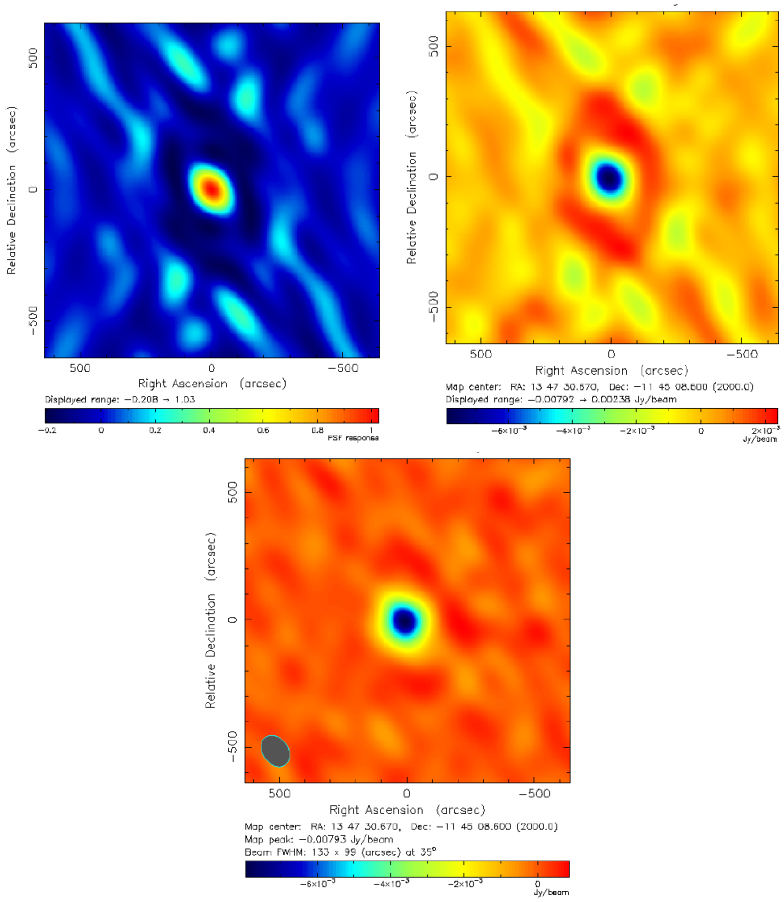

Figure A.42: RXJ1347.5-1145: (a) Short baseline beam, (b) dirty map, and (c) cleaned map. The synthesized beam is 89.2" x 72.8" FWHM at 13.3^o.

A.16 Abell 1835

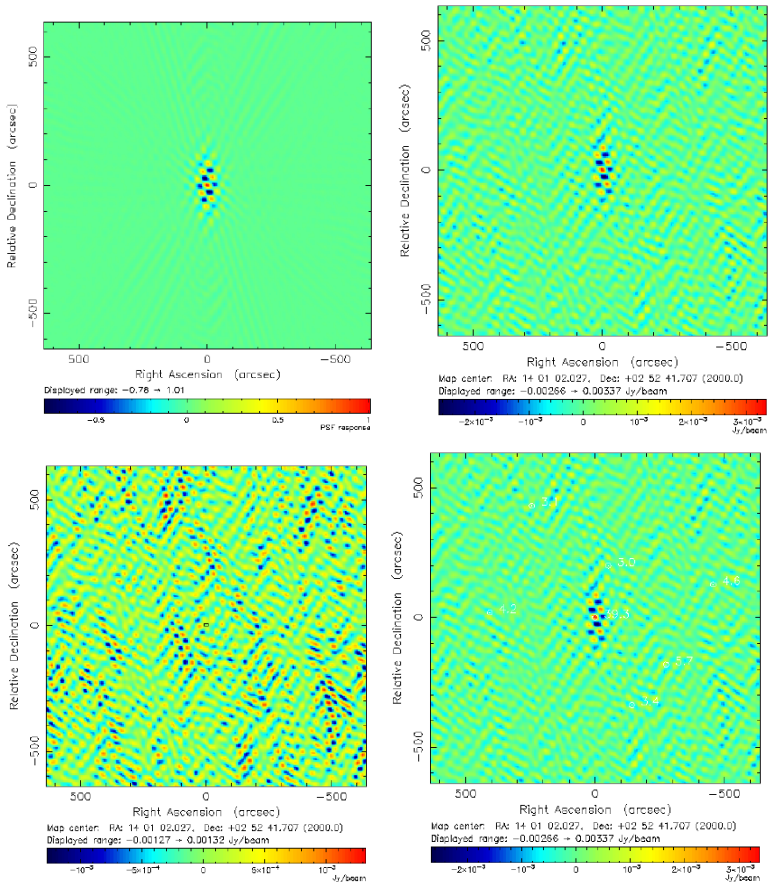

Figure A.43: Abell 1835: (a) Long baseline beam, (b) dirty map, (c) point source removed, and (d) dirty map with NVSS markers.

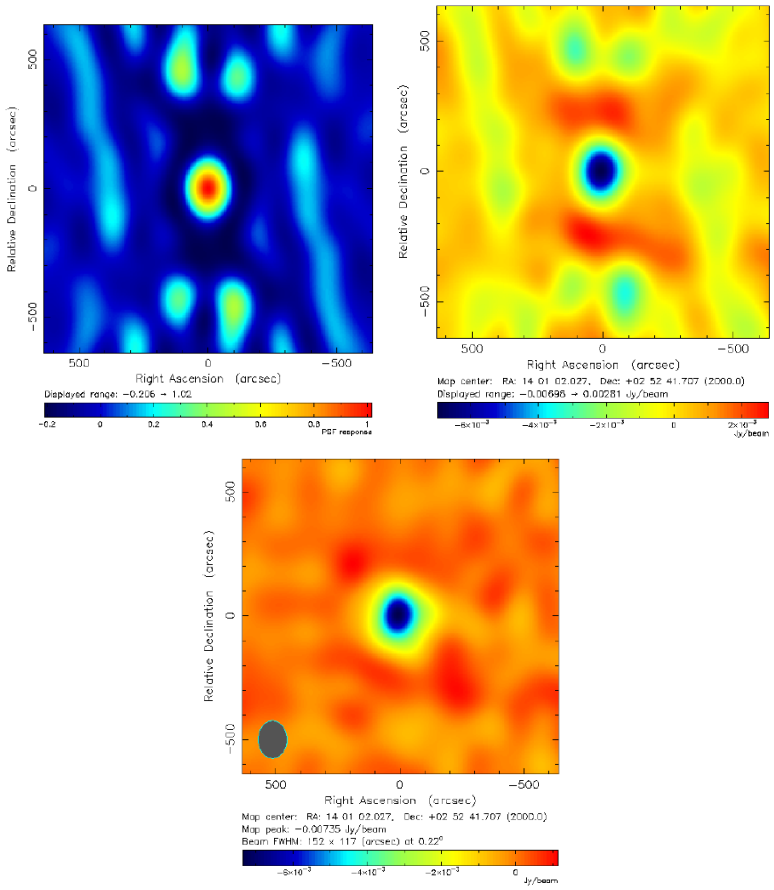

Figure A.44: Abell 1835: (a) Short baseline beam, (b) dirty map, and (c) cleaned map. The synthesized beam is 152" x 117" FWHM at 0.2^o.

A.17 MACSJ1423.8+2404

A.17.1 SZA

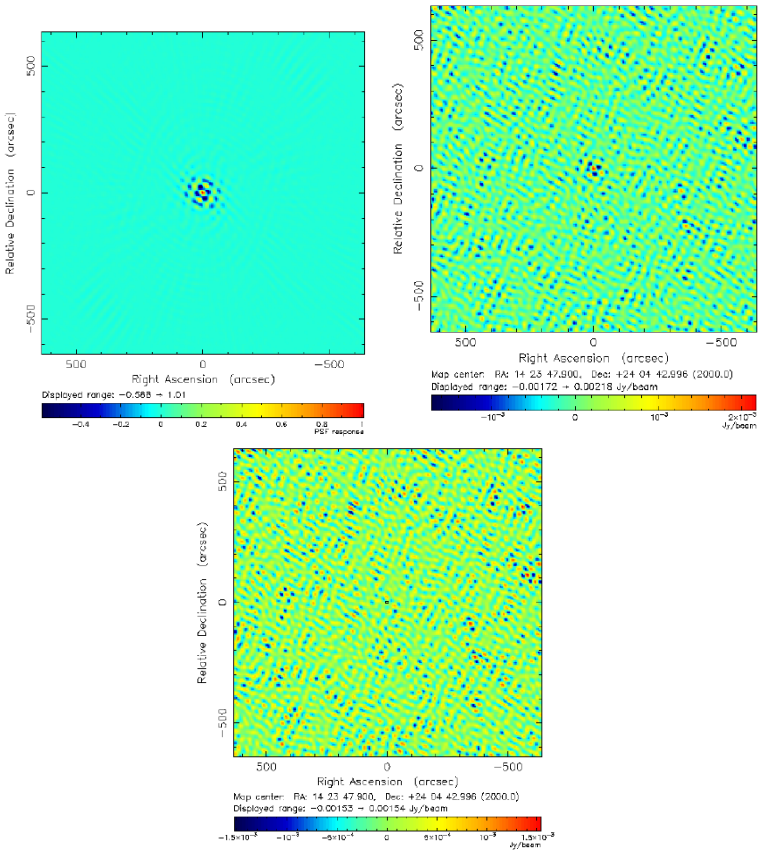

Figure A.45: MACSJ1423.8+2404 SZA: (a) Long baseline beam, (b) dirty map, and (c) clean,

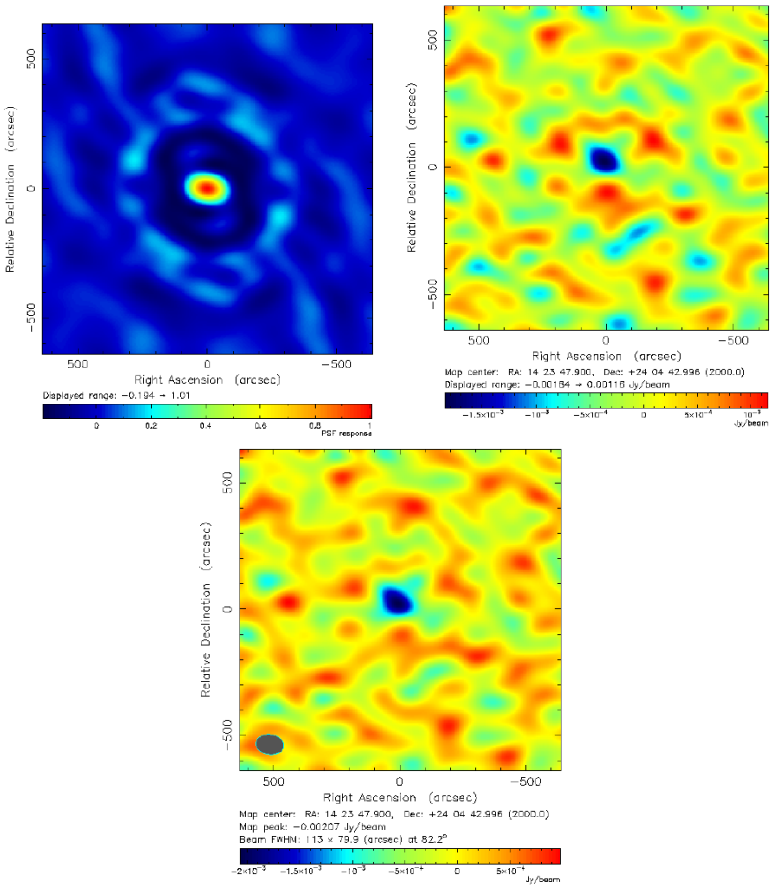

Figure A.46: MACSJ1423.8+2404 SZA: (a) Short baseline beam, (b) dirty map, and (c) cleaned map. The synthesized beam is 113" x 79.9" FWHM at 82.2^o.

A.17.2 BIMA

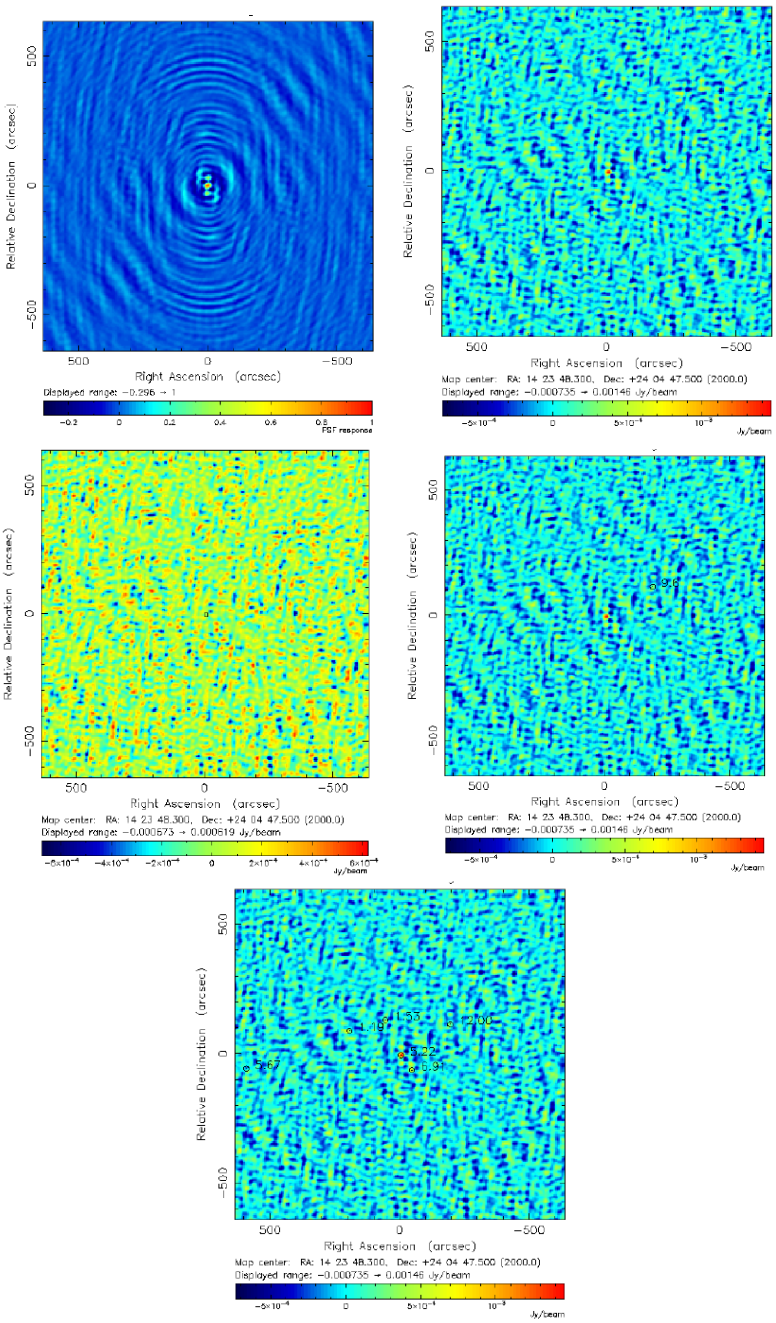

Figure A.47: MACSJ1423.8+2404 BIMA: (a) Long baseline beam, (b) dirty map, and (c) clean, (d) dirty map with NVSS markers, and (e) dirty map with FIRST markers.

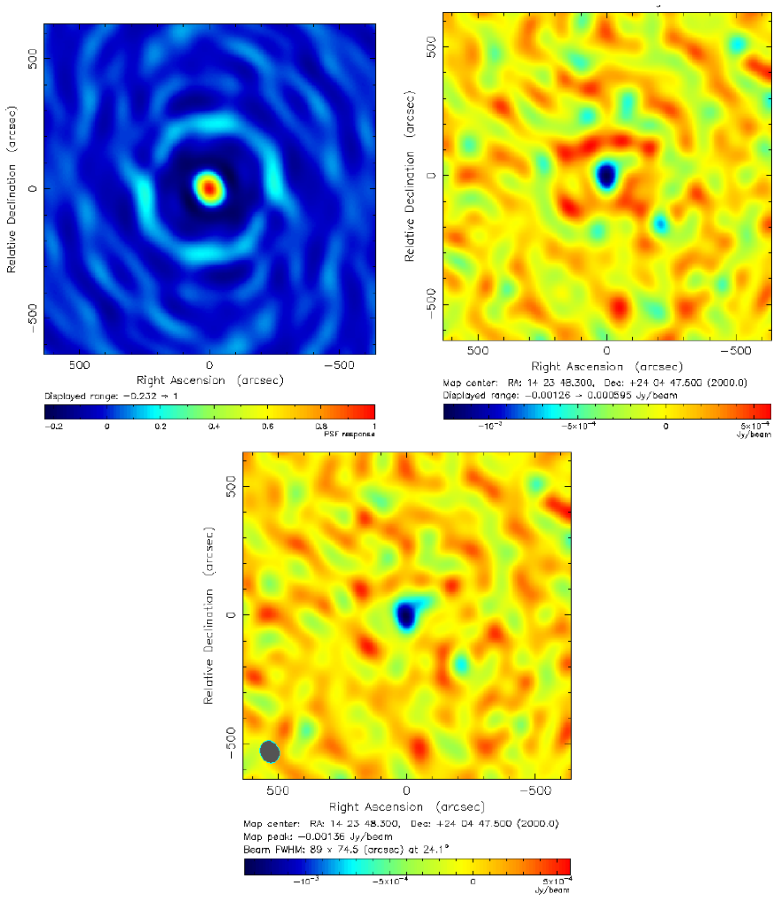

Figure A.48: MACSJ1423.8+2404 BIMA: (a) Short baseline beam, (b) dirty map, and (c) cleaned map. The synthesized beam is 89" x 74.5" FWHM at 24.1^o.

A.18 MACS1427.3+4408

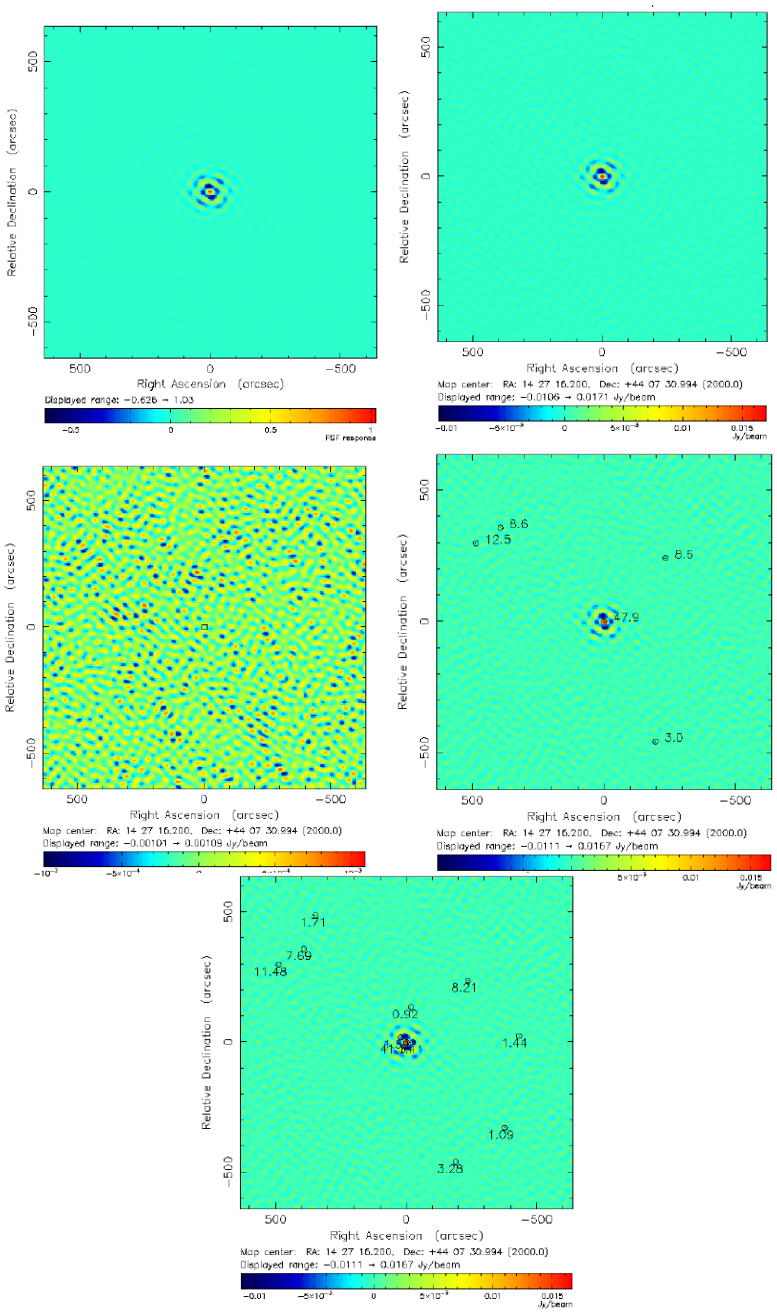

Figure A.49: MACS1427.3+4408: (a) Long baseline beam, (b) dirty map, (c) 1 point source removed map, (d) dirty map with NVSS markers, and (e) dirty map with FIRST markers.

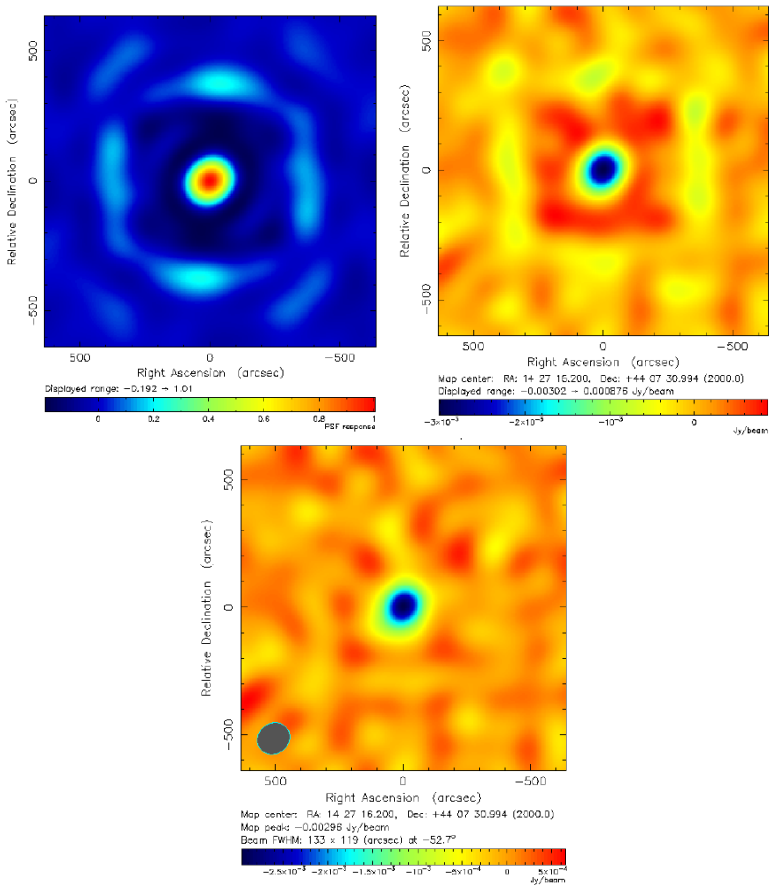

Figure A.50: MACS1427.3+4408: (a) Short baseline beam, (b) dirty map, and (c) cleaned map. The synthesized beam is 133" x 119" FWHM at -52.7^o.

A.19 RXJ1504.1-0248

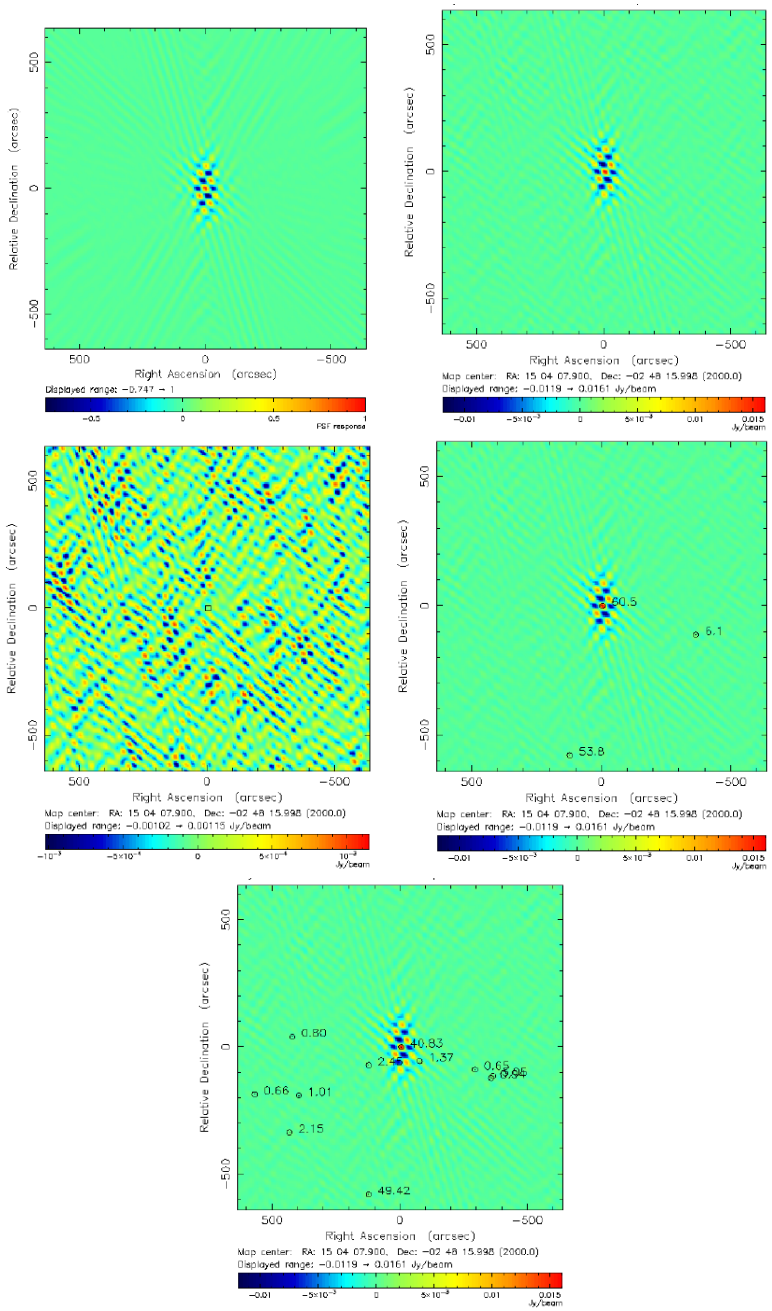

Figure A.51: RXJ1504.1-0248: (a) Long baseline beam, (b) dirty map, (c) 1 point source removed map, (d) dirty map with NVSS markers, and (e) dirty map with FIRST markers.

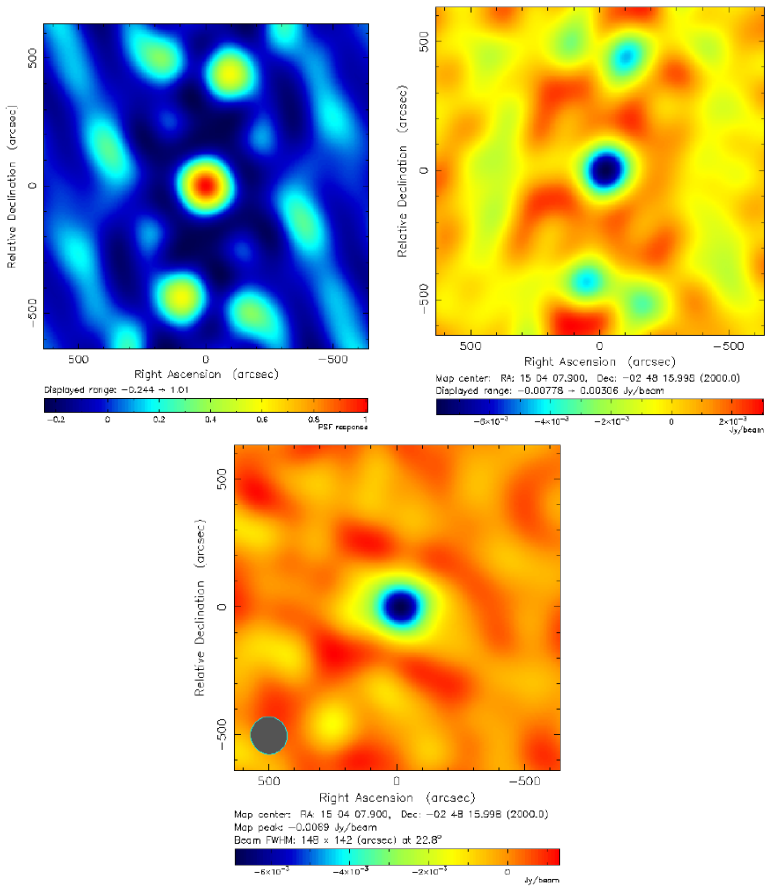

Figure A.52: RXJ1504.1-0248: (a) Short baseline beam, (b) dirty map, and (c) cleaned map. The synthesized beam is 155" x 132" FWHM at -15.8^o.

A.20 MACSJ1532.9+3021

A.20.1 SZA

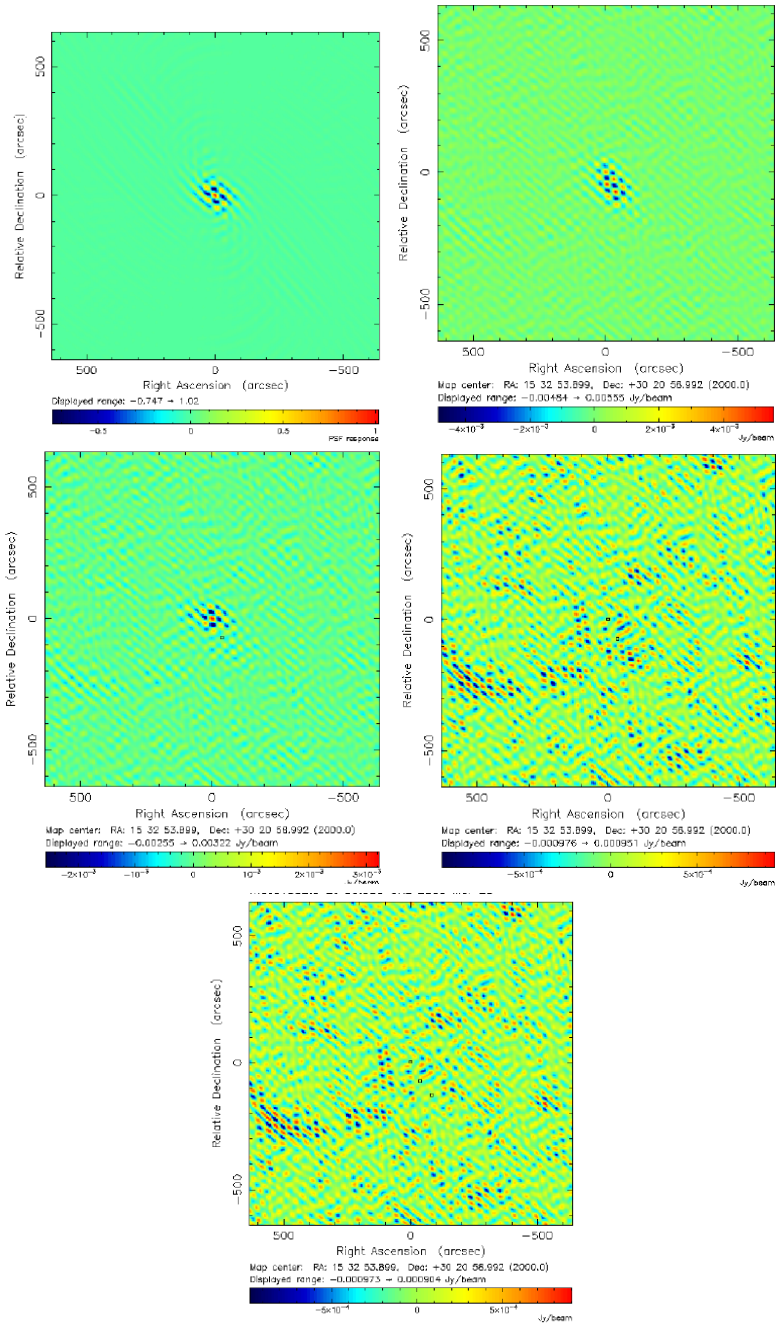

Figure A.53: MACSJ1532.9+3021: (a) Long baseline beam, (b) dirty map, (c) after 1 point source is removed, and (d) after 2 point sources are removed and (e) after 3 point sources are removed.

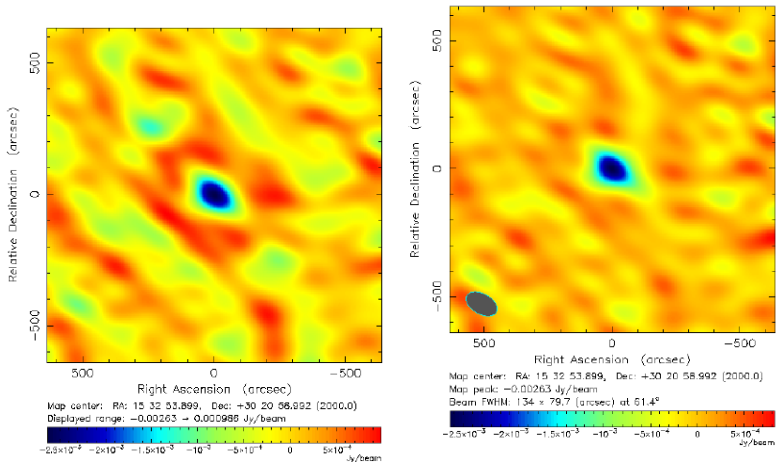

Figure A.54: MACSJ1532.9+3021: (a) Short baseline beam, (b) dirty map, and (c) cleaned map. The synthesized beam is 134" x 79.7" FWHM at 61.4^o.

A.20.2 BIMA

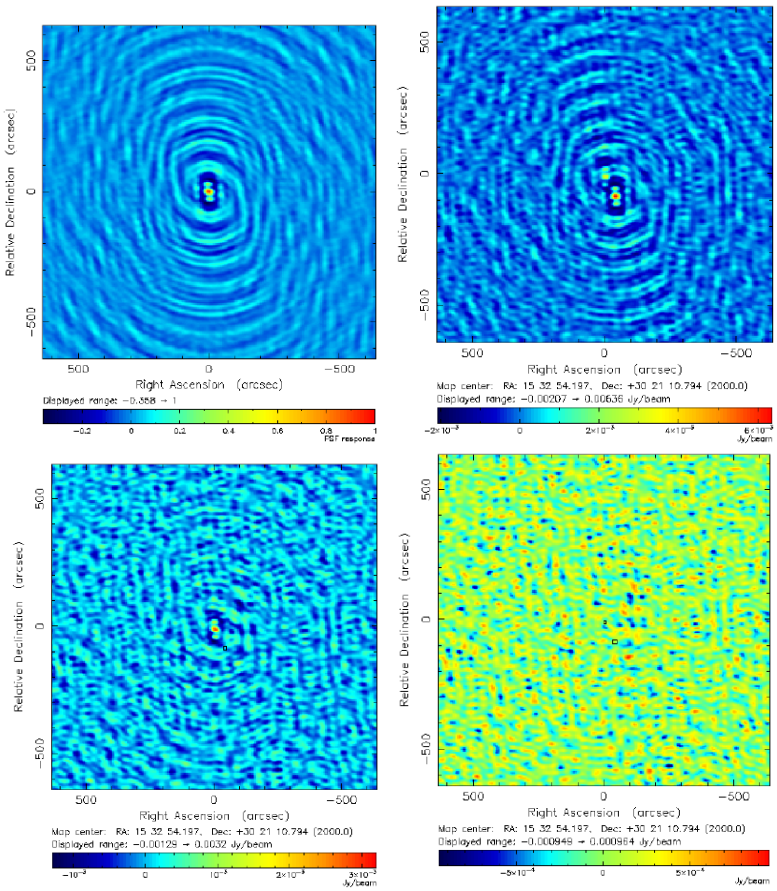

Figure A.55: MACSJ1532.9+3021:BIMA (a) Long baseline beam, (b) dirty map, (c) after 1 point source is removed, and (d) after 2 point sources are removed .

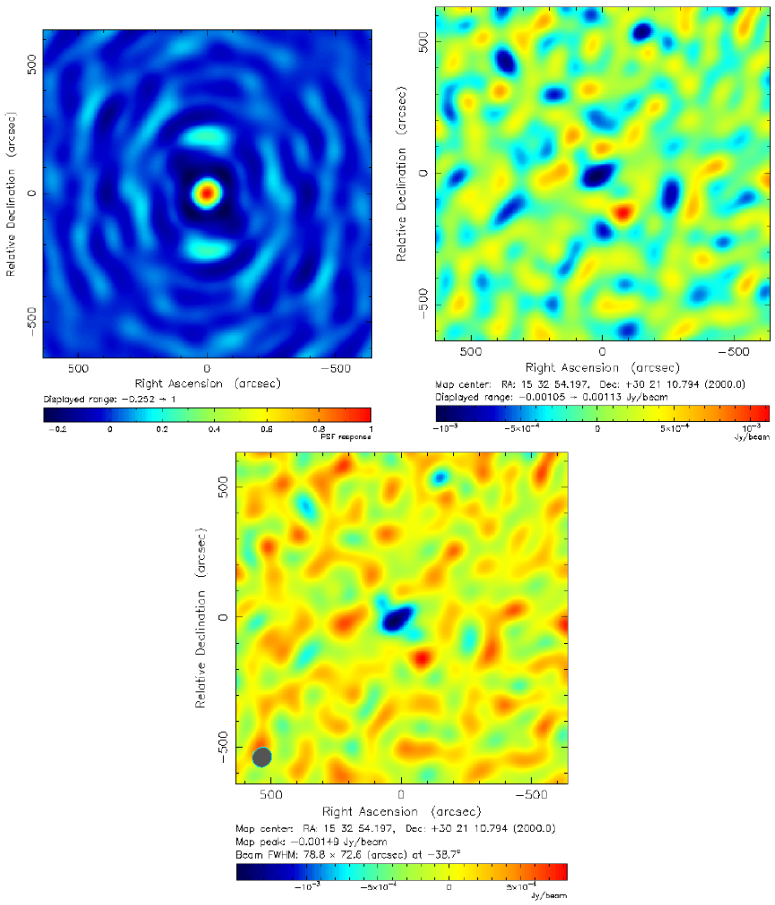

Figure A.56: MACSJ1532.9+3021:BIMA (a) Short baseline beam, (b) dirty map, and (c) cleaned map. The synthesized beam is 78.8" x 72.6" FWHM at -38.7^o.

A.21 MACSJ1621.6+3810

A.21.1 SZA

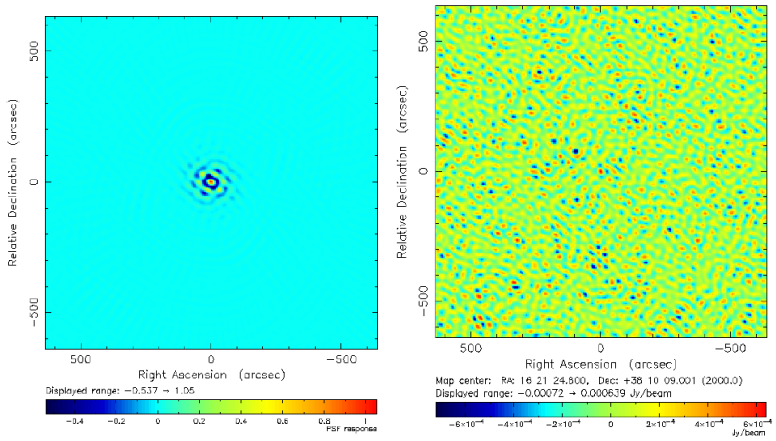

Figure A.57: MACSJ1621.6+3810: (a) Long baseline beam, (b) dirty map,

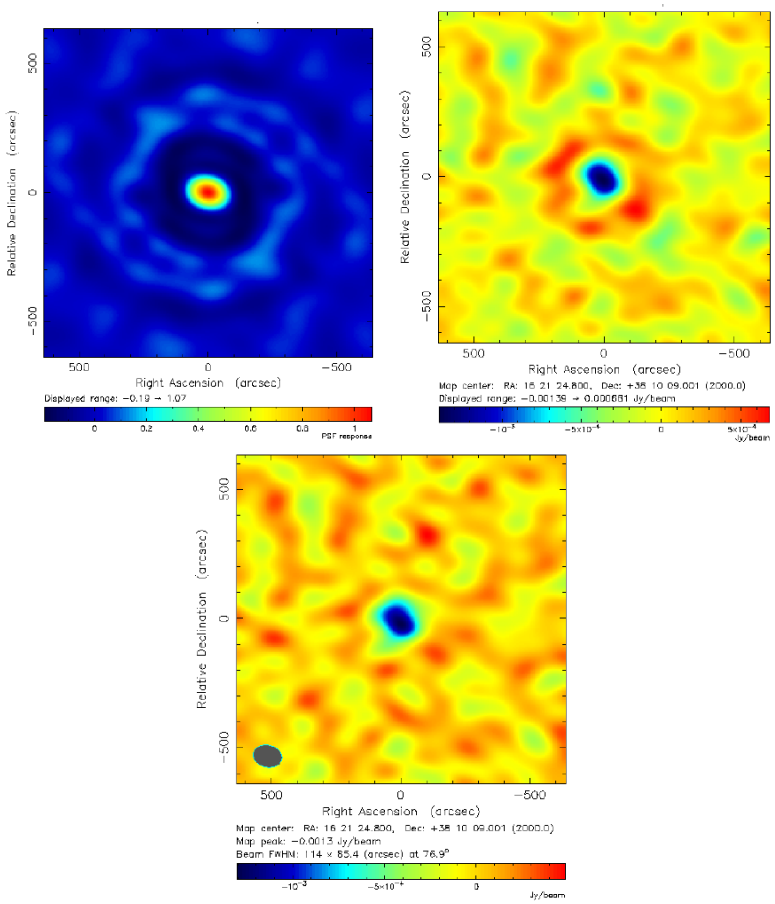

Figure A.58: MACSJ1621.6+3810: (a) Short baseline beam, (b) dirty map, and (c) cleaned map. The synthesized beam is 114" x 85.4" FWHM at 76.9^o.

A.21.2 BIMA

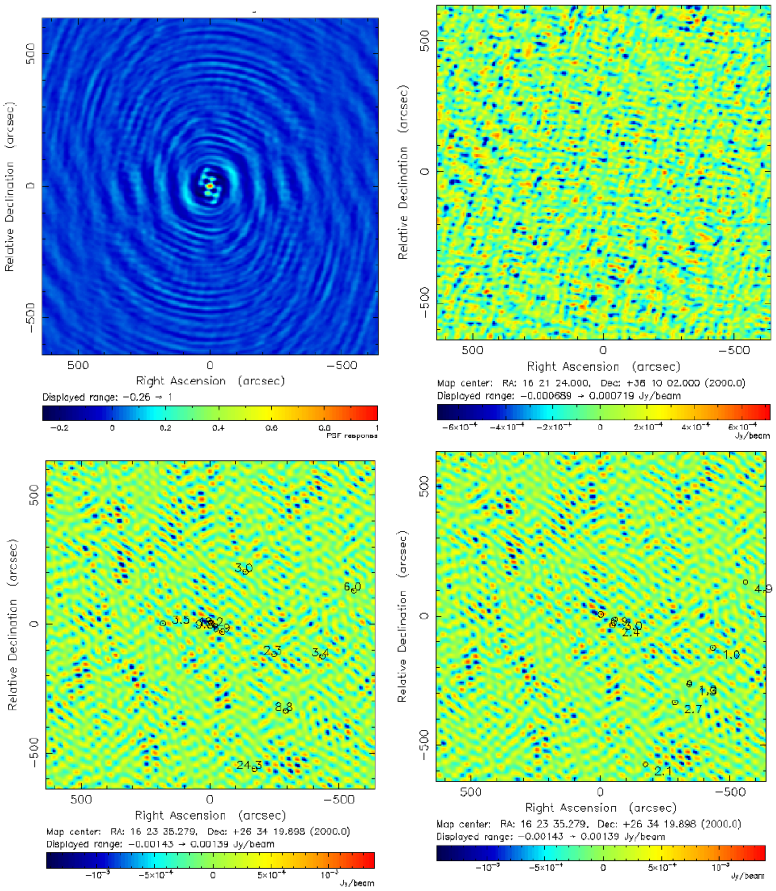

Figure A.59: MACSJ1621.6+3810 BIMA: (a) Long baseline beam, (b) dirty map, (d) dirty map with NVSS markers, and (e) dirty map with FIRST markers.

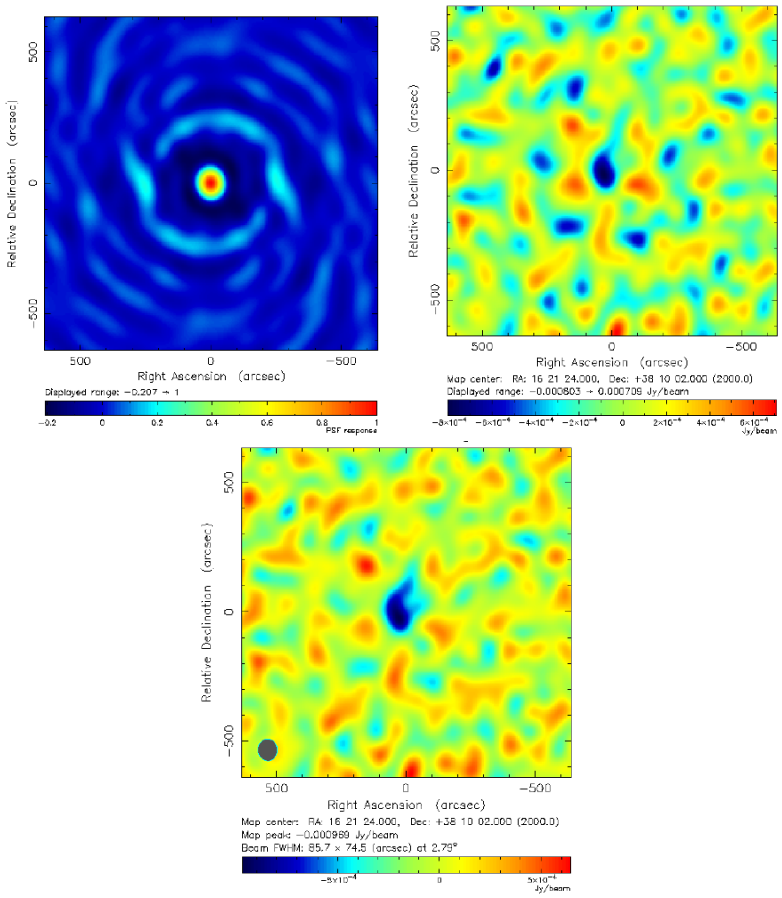

Figure A.60: MACSJ1621.6+3810 BIMA: (a) Short baseline beam, (b) dirty map, and (c) cleaned map. The synthesized beam is 85.7" x 74.5" FWHM at 2.79^o.

A.22 Abell 2204

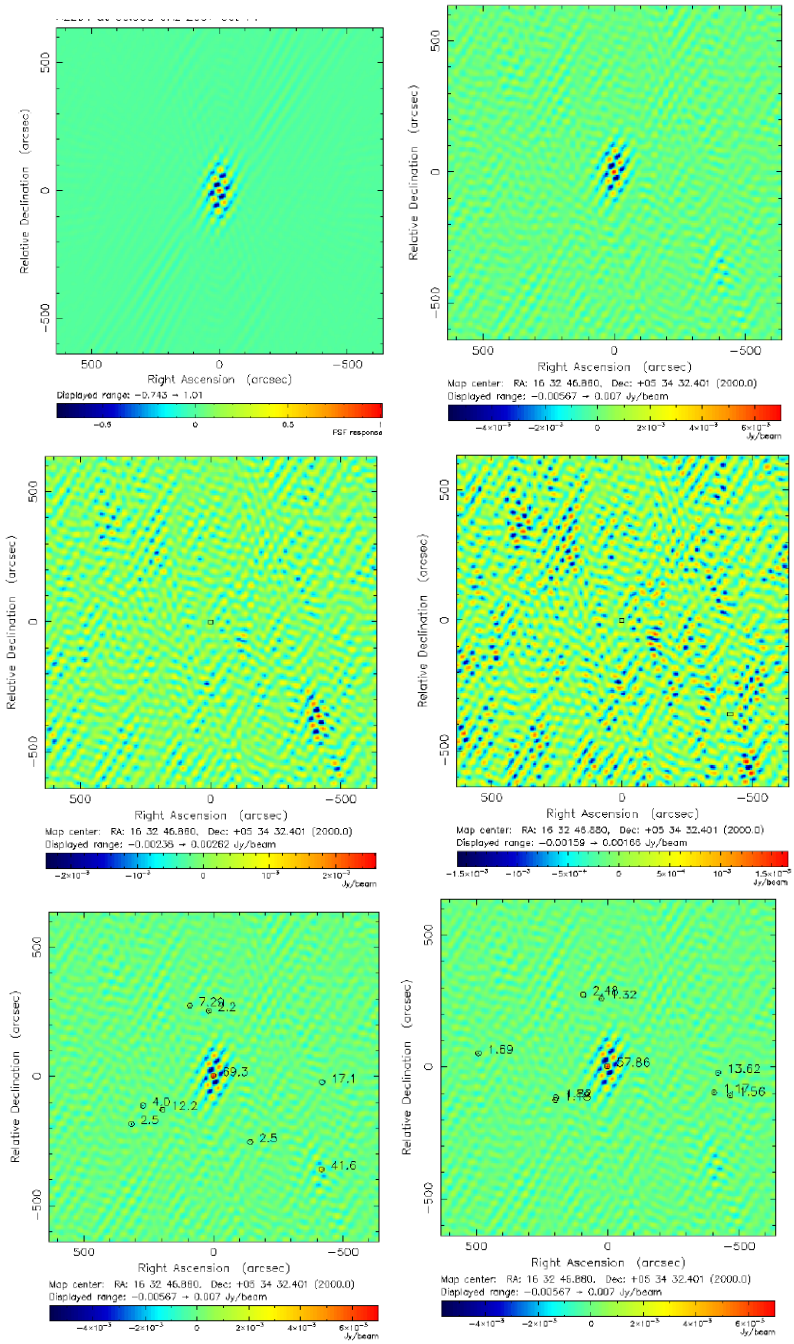

Figure A.61: Abell 2204: (a) Long baseline beam, (b) dirty map, (c) 1 point source removed map, (d) 2 point sourcese removed map, (d) dirty map with NVSS markers, and (e) dirty map with FIRST markers.

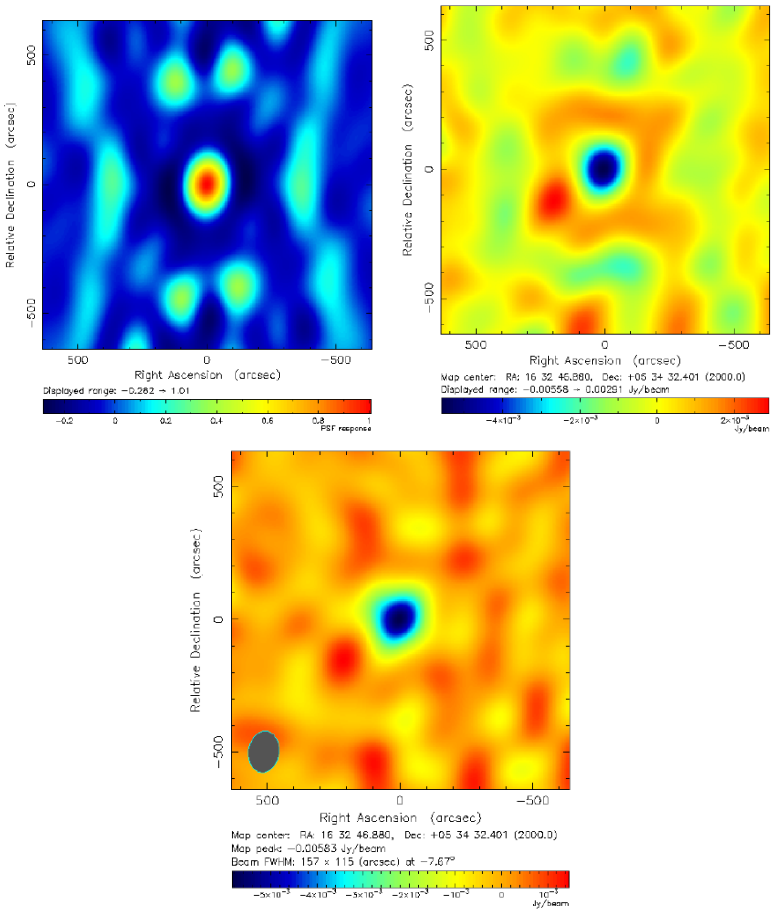

Figure A.62: Abell 2204: (a) Short baseline beam, (b) dirty map, and (c) cleaned map. The synthesized beam is 157" x 115" FWHM at -7.7^o.

A.23 MACSJ1720.3+3536

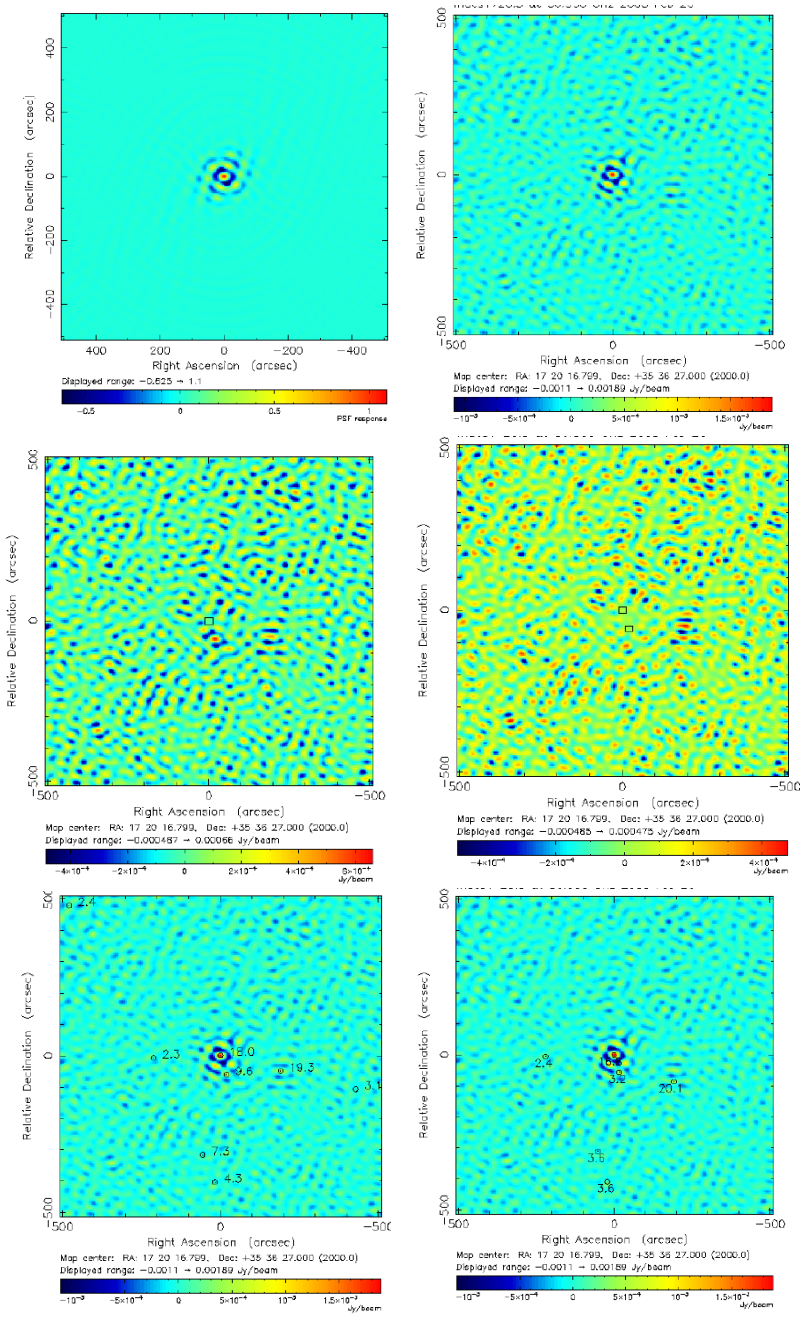

Figure A.63: MACSJ1720.3+3536: (a) Long baseline beam, (b) dirty map, (c) 1 point source removed, (d) 2 point sources removed, (e) dirty map with NVSS markers, and (f) dirty map with FIRST markers.

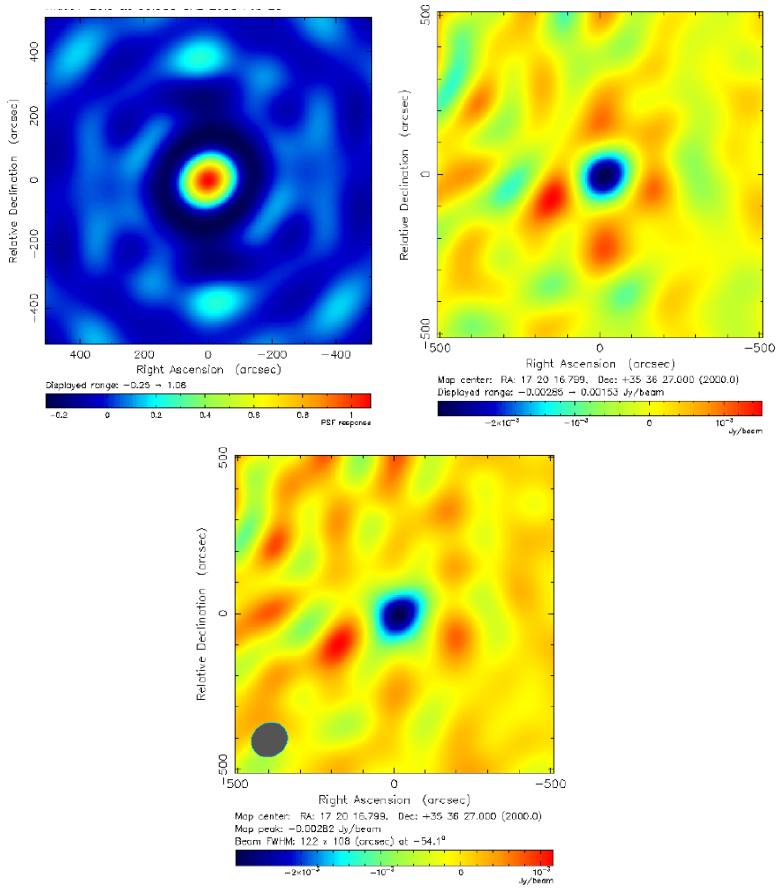

Figure A.64: MACSJ1720.3+3536: (a) Short baseline beam, (b) point sources removed map, and (c) cleaned map. The synthesized beam is 122" x 108" FWHM at -54.1^o.

A.24 RXJ2129.6+0005

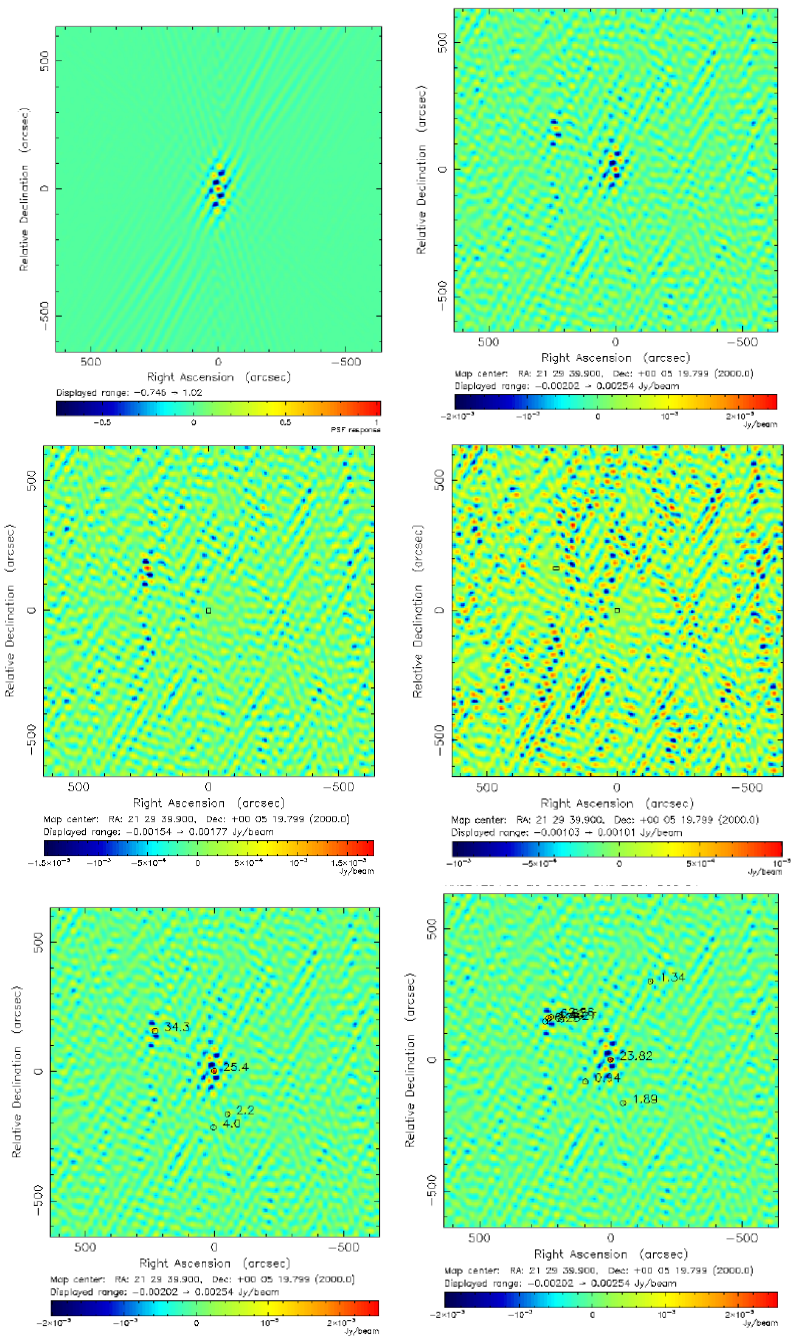

Figure A.65: RXJ2129.6+0005: (a) Long baseline beam, (b) dirty map, (c) after 1 point source is removed, (d) after 2 point sources are removed, (e) dirty map with NVSS markers, and (f) dirty map with FIRST markers.

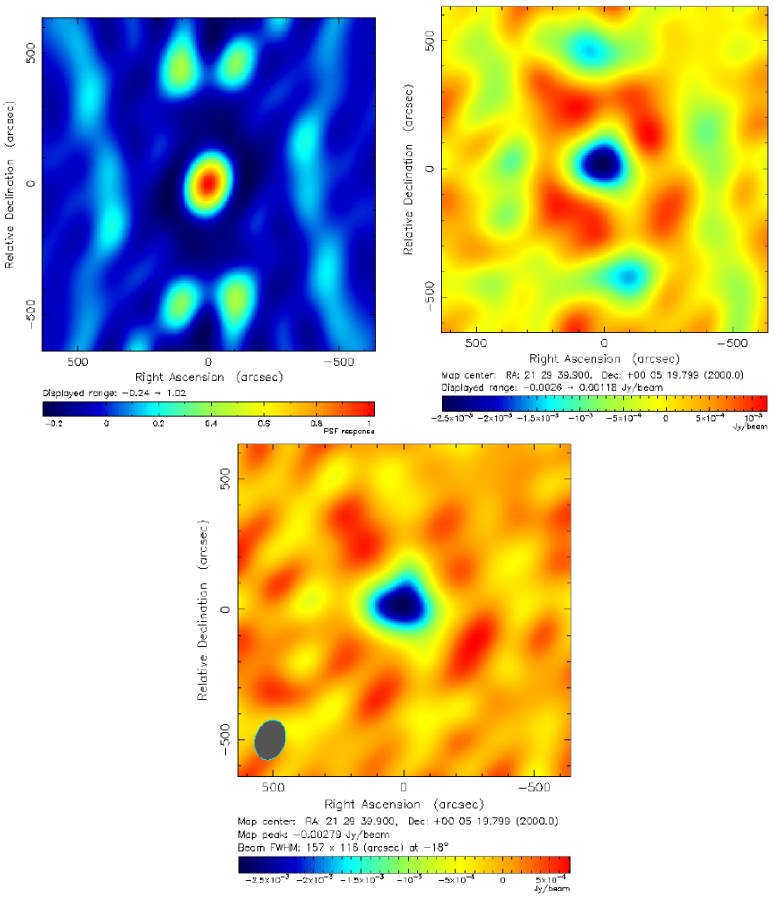

Figure A.66: RXJ2129.6+0005: (a) Short baseline beam, (b) dirty map, and (c) cleaned map. The synthesized beam is 157" x 116" FWHM at -18.0^o.

A.25 Abell 2537

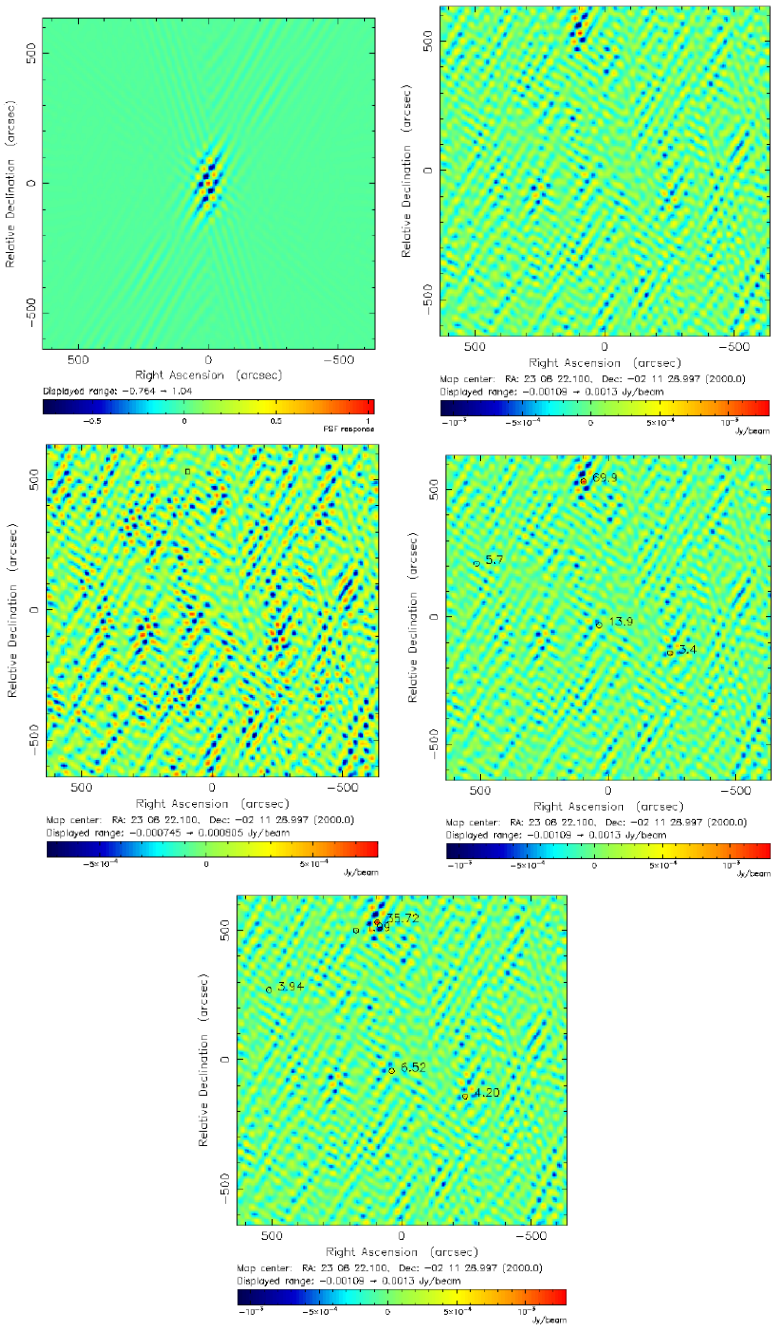

Figure A.67: Abell 2537: (a) Long baseline beam, (b) dirty map, (c) 1 point source is removed map, (d) dirty map with NVSS markers, and (e) dirty map with FIRST markers.

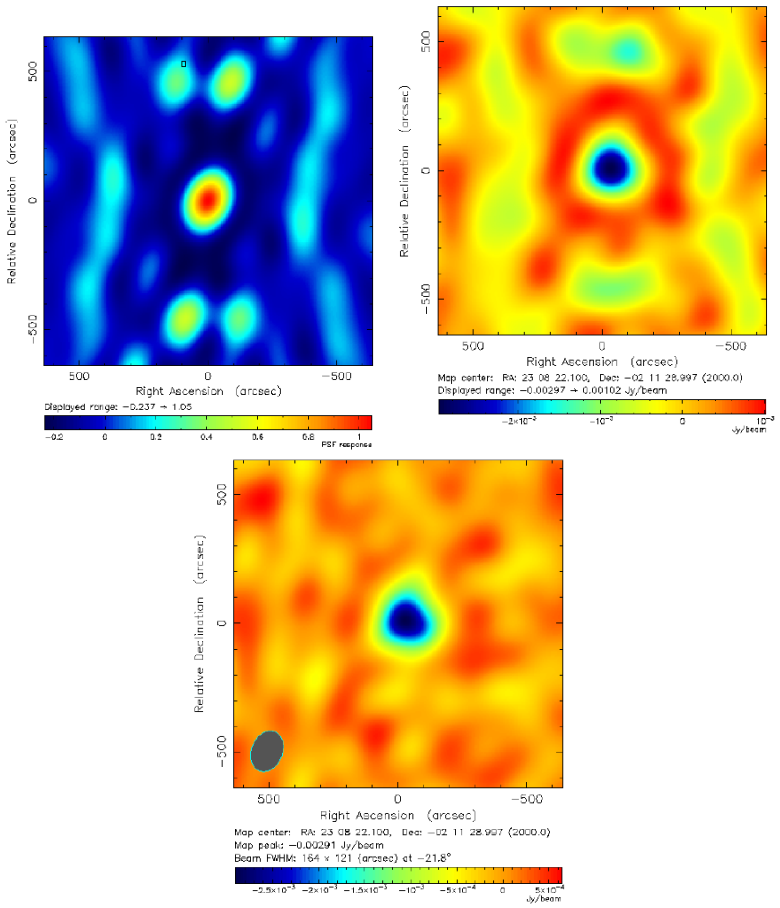

Figure A.68: Abell 2537: (a) Short baseline beam, (b) dirty map, and (c) cleaned map. The synthesized beam is 164" x 121" FWHM at -21.8^o.

APPENDIX B

ADDITIONAL CLUSTERS OBSERVED WITH SZA, BIMA, OVRO

The clusters in this section are additional clusters that were observed with the SZA at the beginning of the project. They may be used to expand the cluster sample.

B.1 Abell 2294

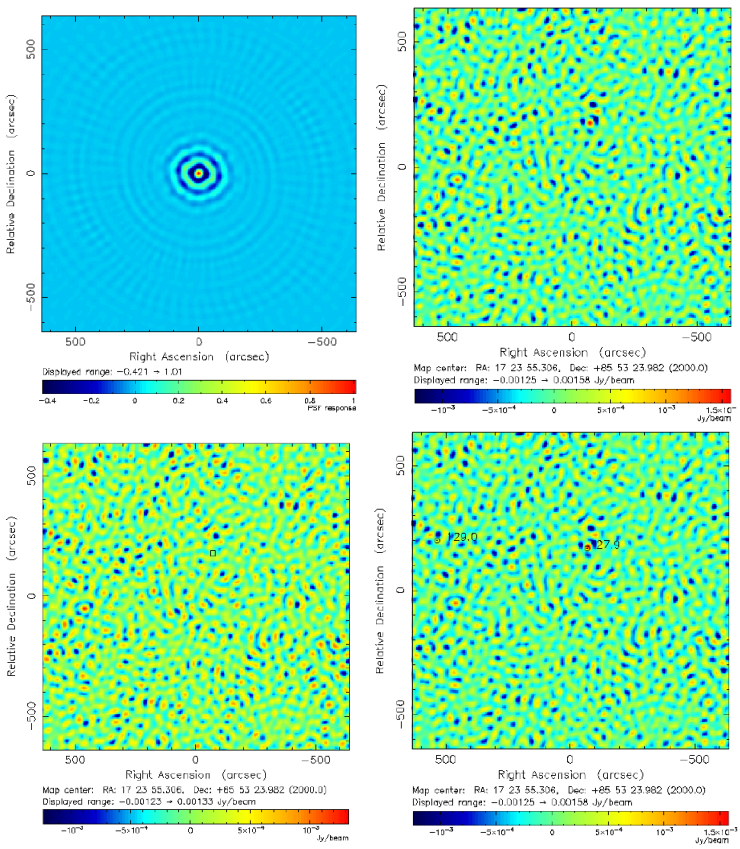

Figure B.1: Abell 2294: (a) Long baseline beam, (b) dirty map, (c) point source removed map, (d) dirty map with NVSS markers.

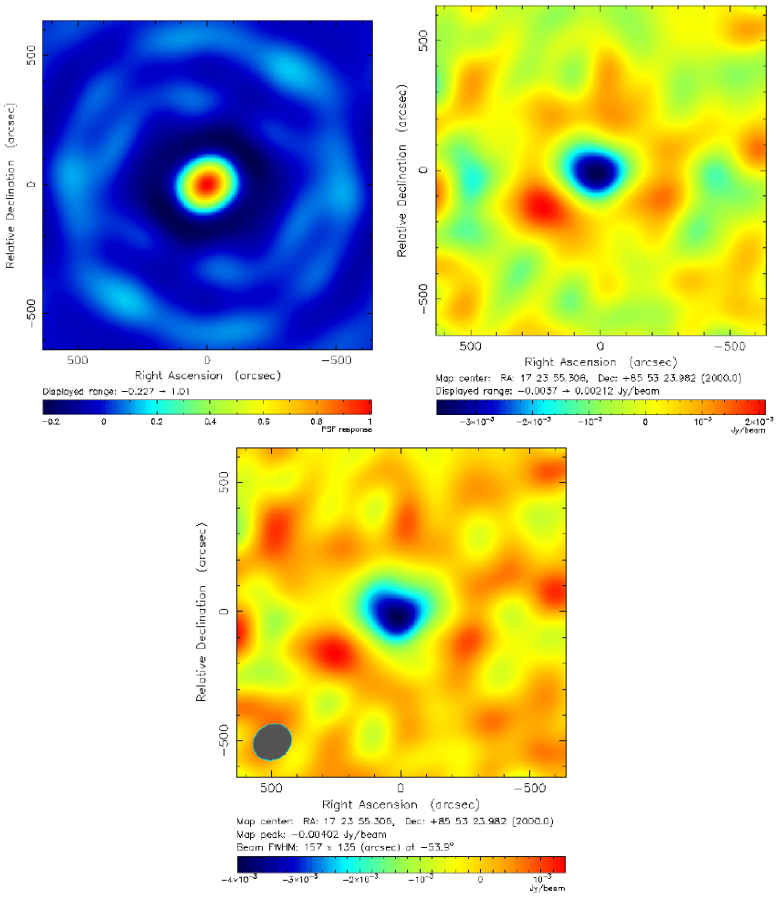

Figure B.2: Abell 2294: (a) Short baseline beam, (b) point source removed, and (c) cleaned map. The synthesized beam is 157" x 135" FWHM at -53.9^o.

B.2 Abell 750

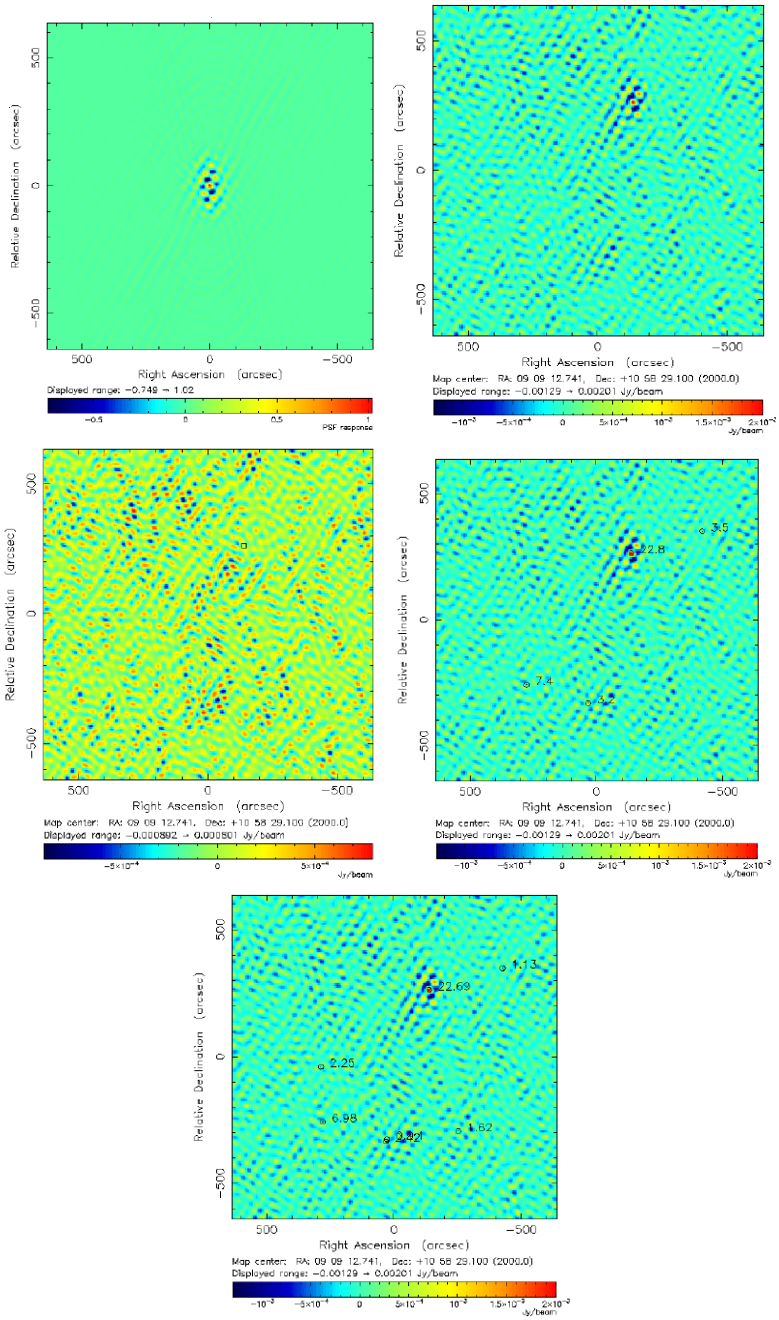

Figure B.3: Abell 750: (a) Long baseline beam, (b) dirty map, (c) map after 1 point source removed, (d) dirty map with NVSS markers, and dirty map with FIRST markers.

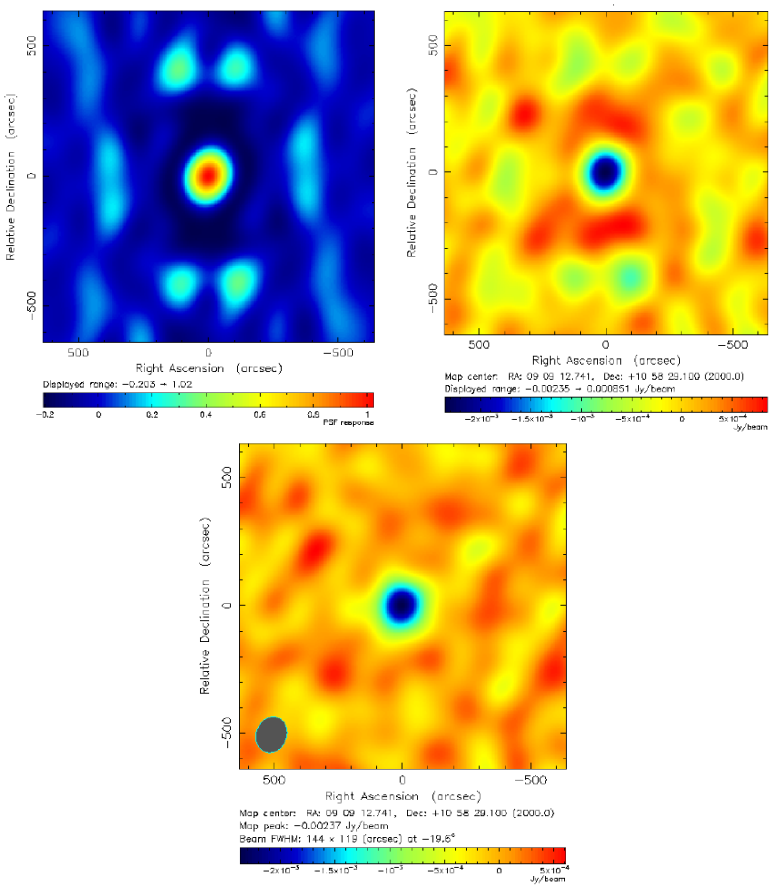

Figure B.4: Abell 750: (a) Short baseline beam, (b) dirty map, and (c) cleaned map. The synthesized beam is 144" x 119" FWHM at -19.6^o.

B.3 Abell 963

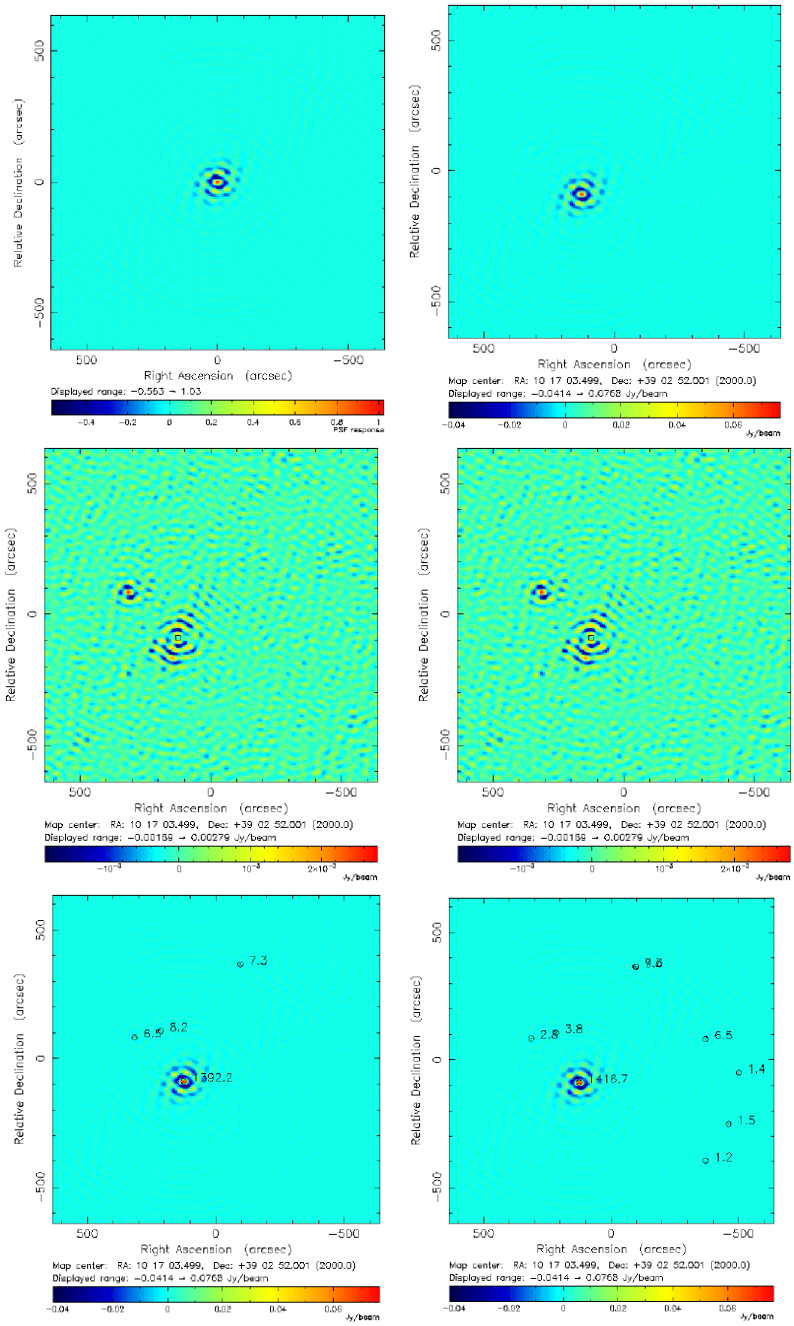

Figure B.5: Abell 963: (a) Long baseline beam, (b) dirty map, (c) map after 1 point source is removed, (d) map after 2 point sources are removed, (e) dirty map with NVSS markers, and (f) dirty map with FIRST markers .

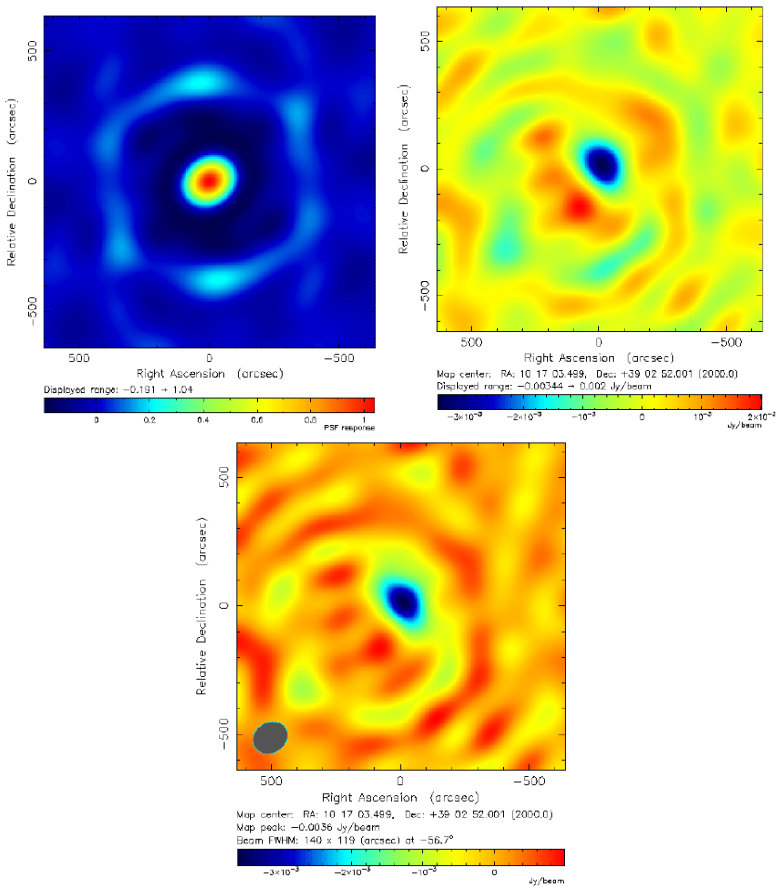

Figure B.6: Abell 963: (a) Short baseline beam, (b) dirty map, and (c) cleaned map. The synthesized beam is 130" x 120" FWHM at -49.4^o.

B.4 Abell 209

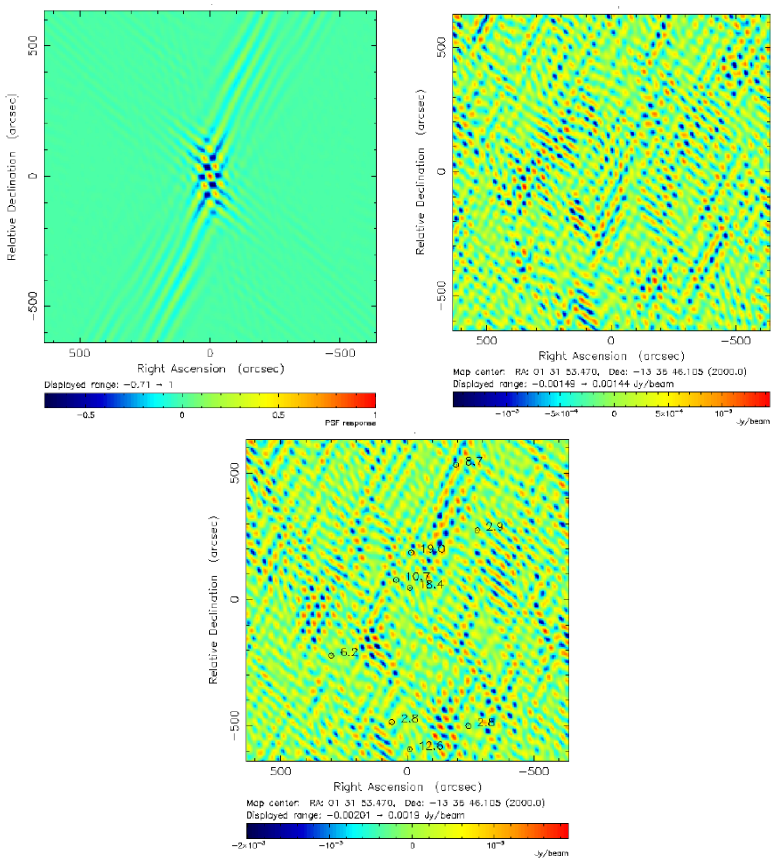

Figure B.7: Abell 209: (a) Long baseline beam, (b) dirty map, and (c) dirty map with NVSS markers.

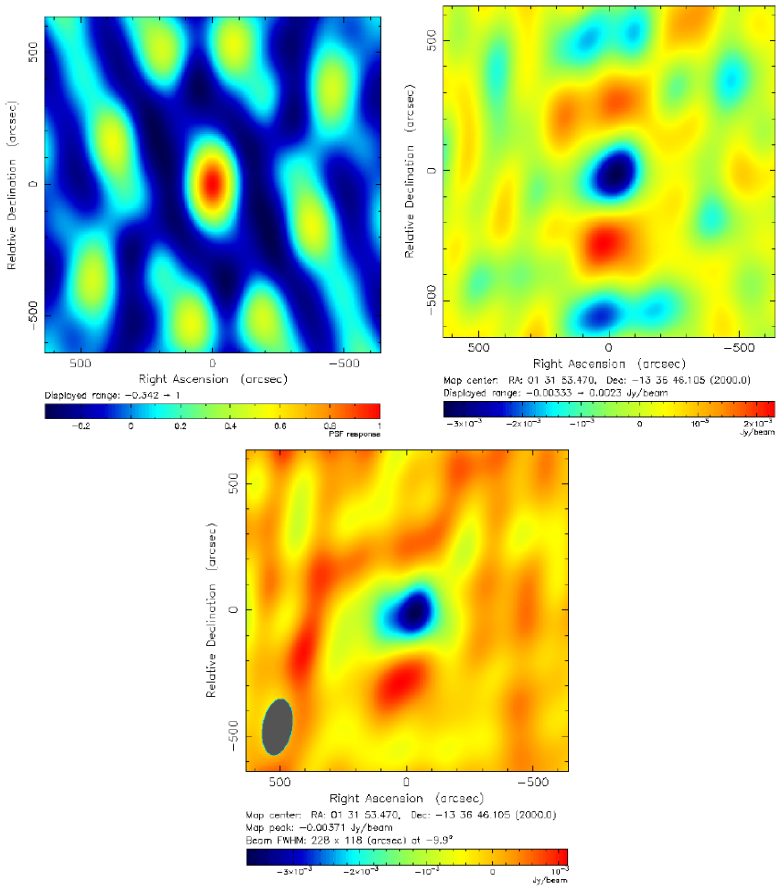

Figure B.8: Abell 209: (a) Short baseline beam, (b) dirty map, and (c) cleaned map. The synthesized beam is 228" x 118" FWHM at -9.9^o.

B.5 Abell 2390

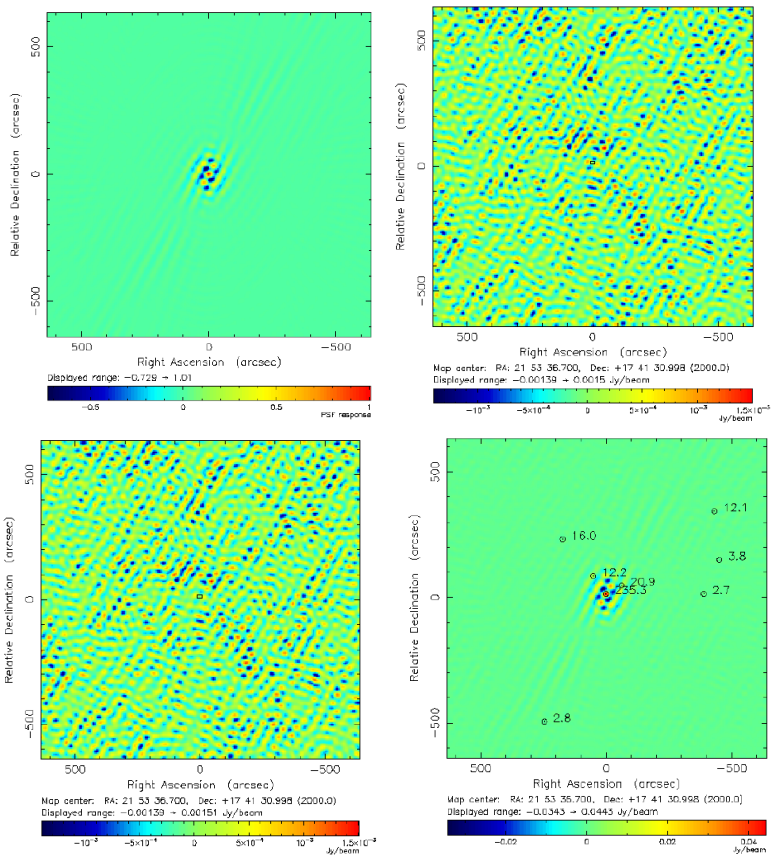

Figure B.9: Abell 2390: (a) Long baseline beam, (b) dirty map, (c) 1 point source is removed map, and (d) dirty map with NVSS markers.

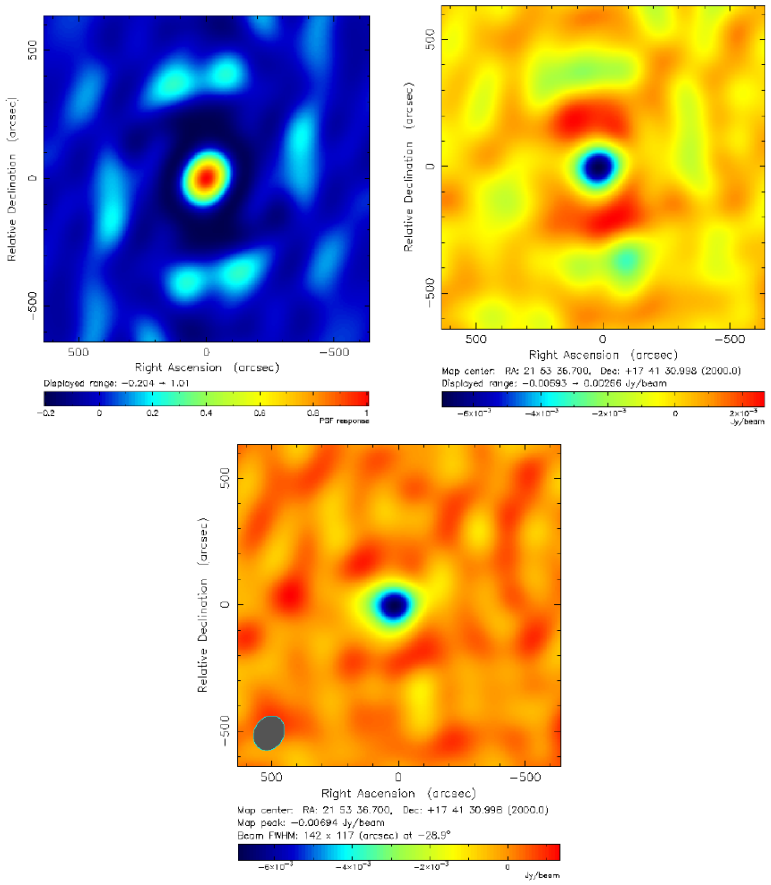

Figure B.10: Abell 2390: (a) Short baseline beam, (b) dirty map, and (c) cleaned map. The synthesized beam is 142" x 117" FWHM at -28.9^o.

B.6 Abell 611

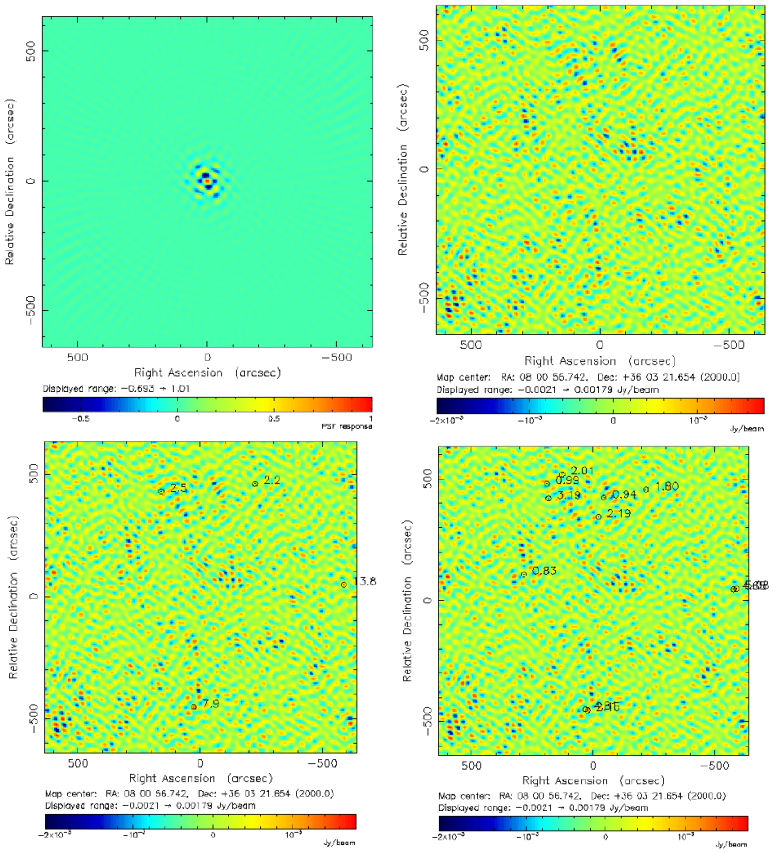

Figure B.11: Abell 611: (a) Long baseline beam, (b) dirty map (no point sources detected), (c) dirty map with NVSS markers, and (d) dirty map with FIRST markers.

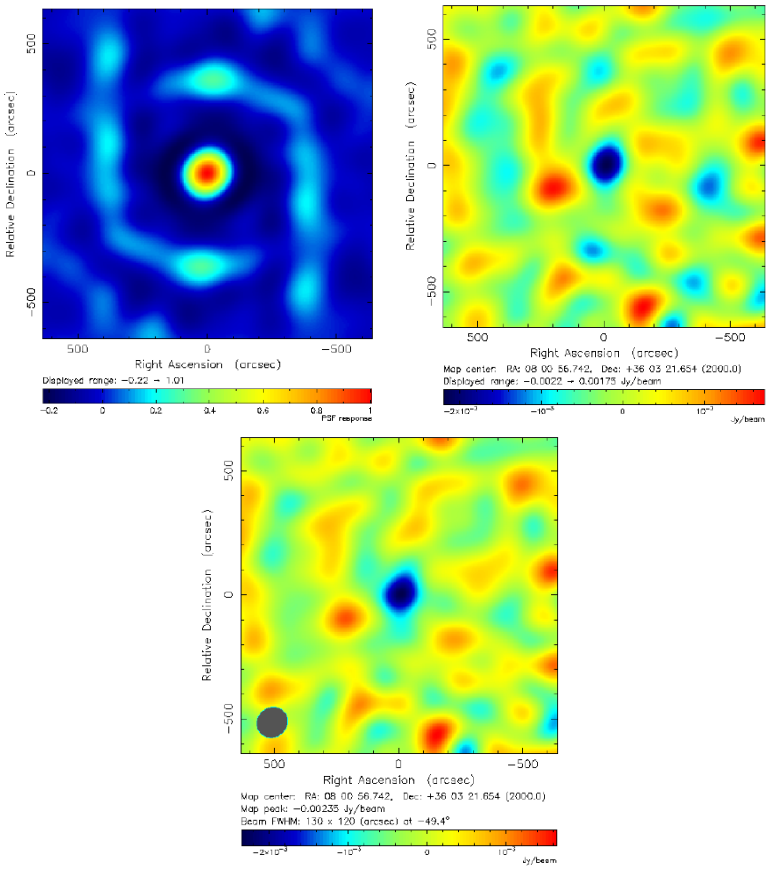

Figure B.12: Abell 611: (a) Short baseline beam, (b) dirty map, and (c) cleaned map. The synthesized beam is 167" x 122" FWHM at 83.0^o.

B.7 MACS0949.8+1708

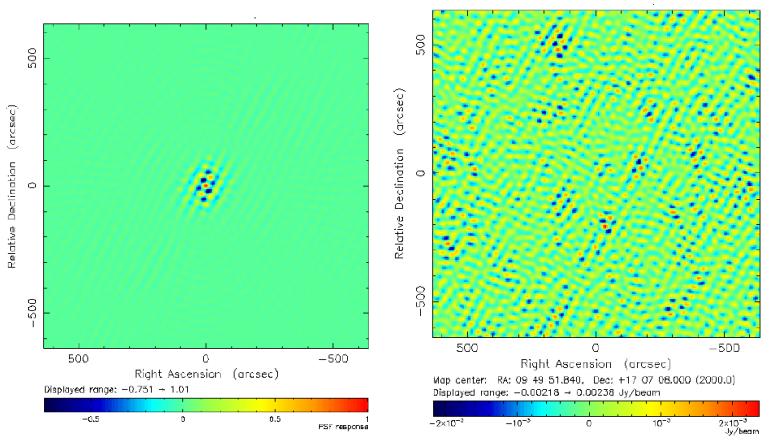

Figure B.13: MACS0949.8+1708: (a) Long baseline beam and (b) dirty map (no point sources were dete cted).

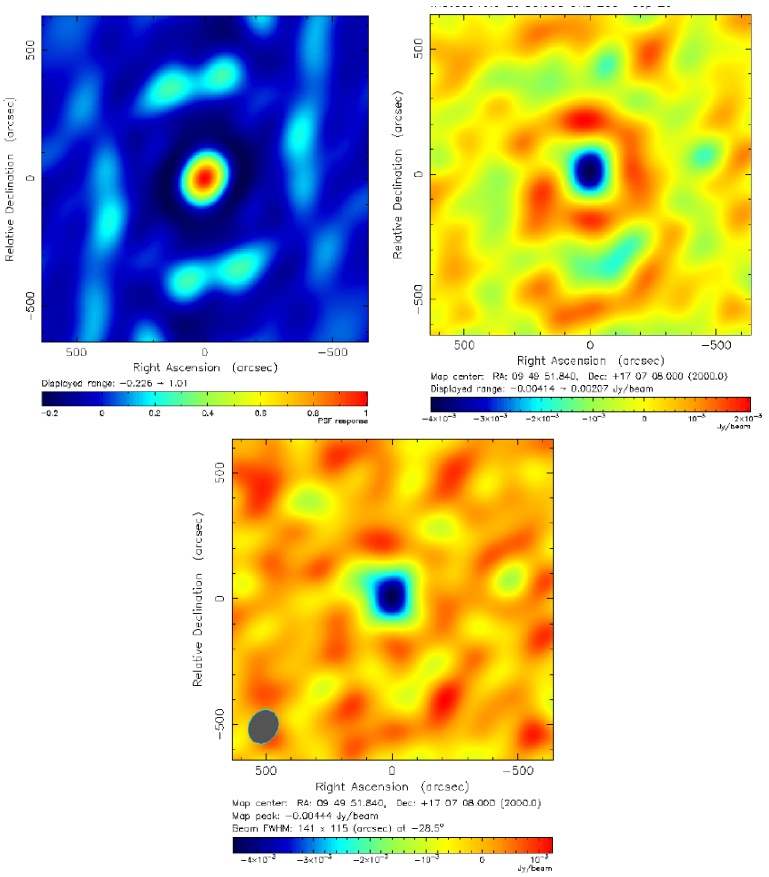

Figure B.14: MACS0949.8+1708: (a) Short baseline beam, (b) dirty map, and (c) cleaned map. The synthesized beam is 141" x 115" FWHM at -28.5^o.

B.8 MS1621.5+2640

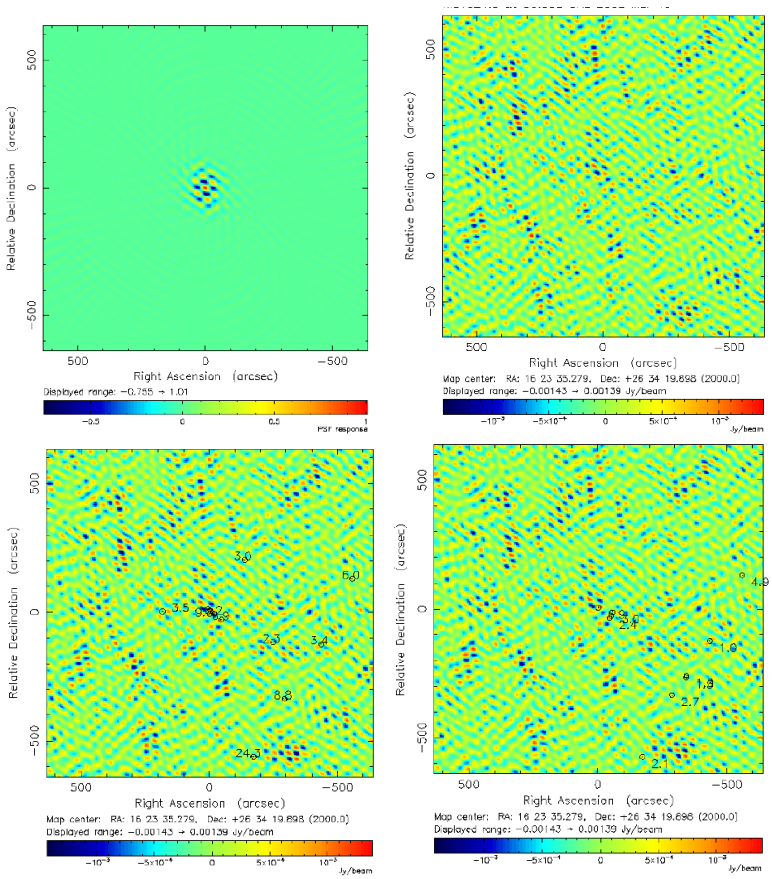

Figure B.15: MS1621.5+2640: (a) Long baseline beam, (b) dirty map (no point sources detected), (c) dirty map with NVSS markers, and (d) dirty map with FIRST markers.

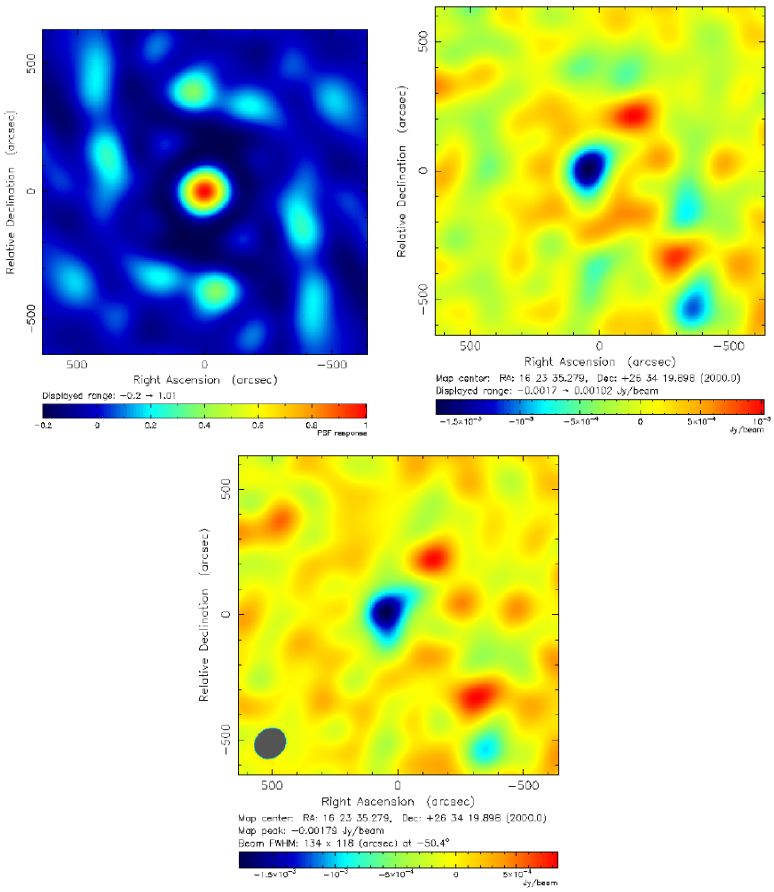

Figure B.16: MS1621.5+2640: (a) Short baseline beam, (b) dirty map (no point sources detected), and (c) cleaned map. The synthesized beam is 134" x 118" FWHM at -50.4^o.

B.9 MACSJ2214.9-1359

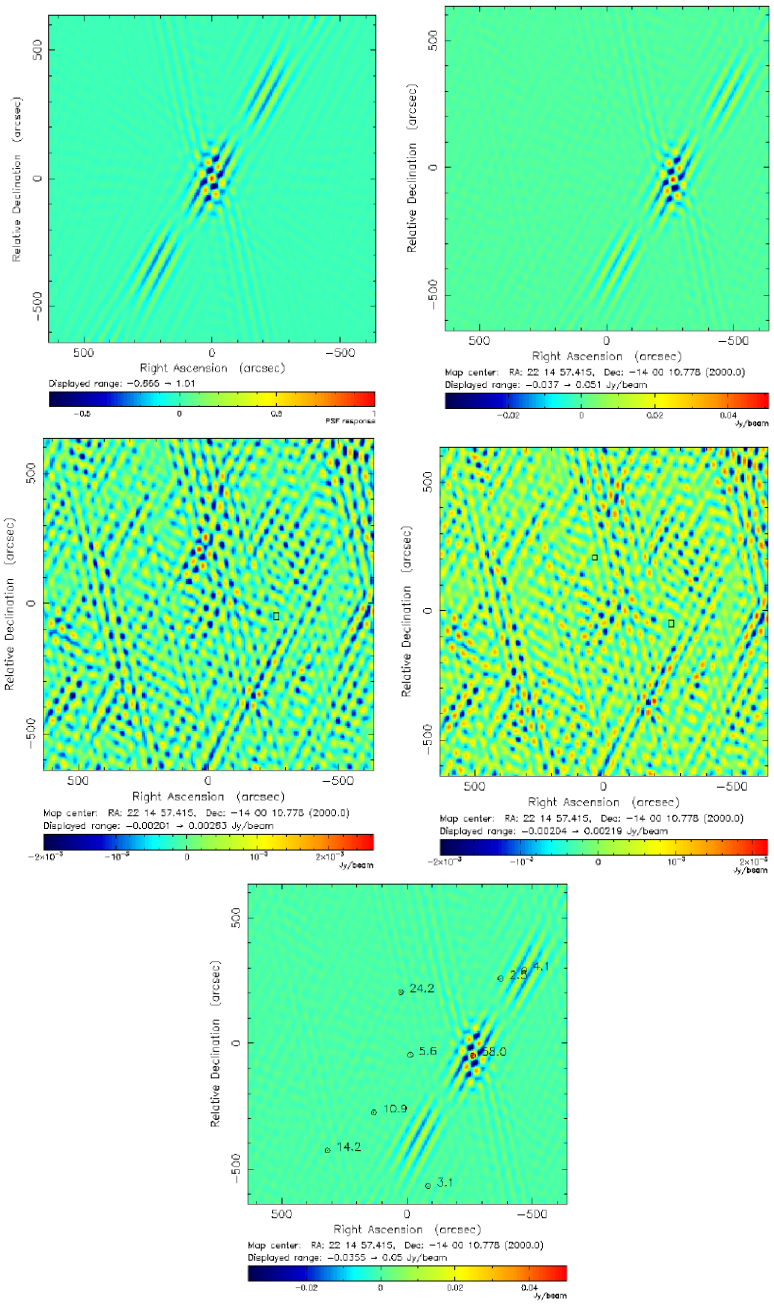

Figure B.17: MACSJ2214.9-1359: (a) Long baseline beam, (b) dirty map, (c) map after 1 point source removed, (d) map after 2 point sources removed, and (e) dirty map with NVSS markers.

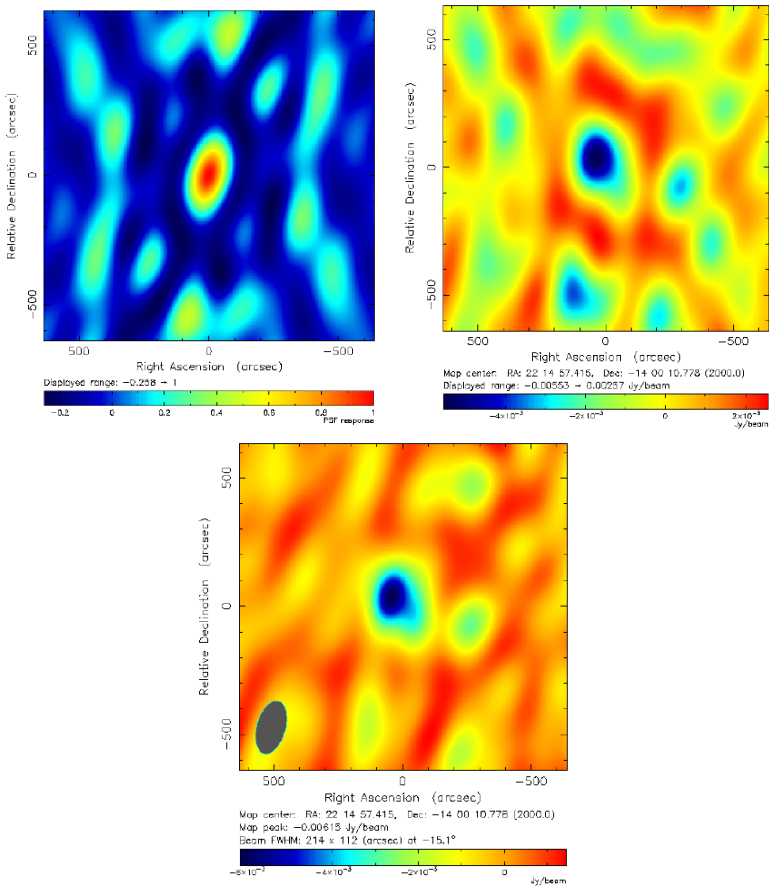

Figure B.18: MACSJ2214.9-1359: (a) Short baseline beam, (b) point sources removed map, and (c) cleaned map . The synthesized beam is 214" x 112" FWHM at -15.1^o.

B.10 MACSJ0454.1-0300

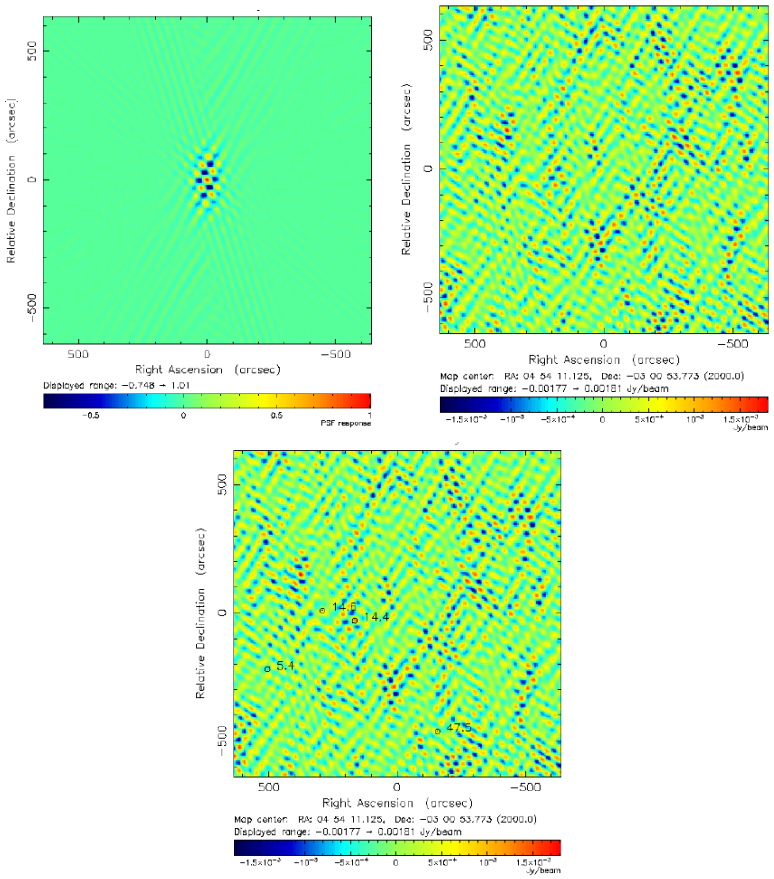

Figure B.19: MACSJ0454.1-0300: (a) Long baseline beam, (b) dirty map (no point sources detected), and (c) dirty map with NVSS markers.

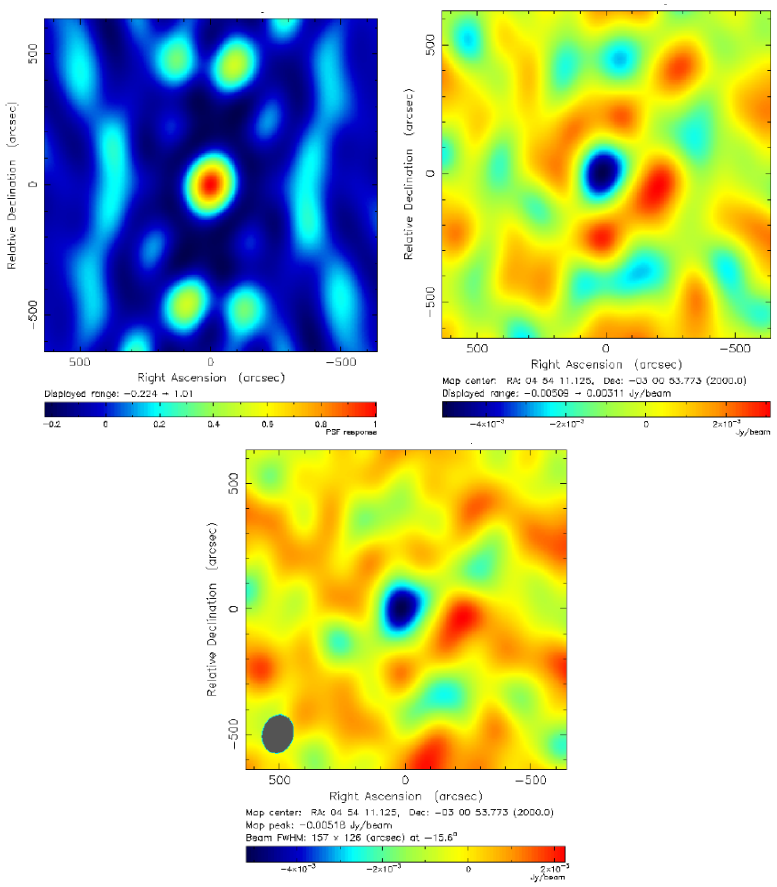

Figure B.20: MACSJ0454.1-0300: (a) Short baseline beam, (b) dirty map, and (c) cleaned map. The synthesized beam is 157" x 126" FWHM at -15.6^o.

APPENDIX C

DIFFRACTION THEORY

In this section diffraction through a single slit and circular aperature are derived from the wave equation.

C.1 Diffraction Pattern

C.1.1 Wave Equation

In order to find the wave equation, the Maxwell's Equations for a vacuum are used:

$$\bigtriangledown \cdot \mathbf{E} = 0 \tag{C.1}$$

$$\bigtriangledown \cdot \mathbf{B} = 0 \tag{C.2}$$

$$\bigtriangledown \times \mathbf{E} = -\frac{\partial \mathbf{B}}{\partial \mathrm{t}} \tag{C.3}$$

$$\bigtriangledown \times \mathbf{B} = \mu_{\mathrm{o}} \epsilon_{\mathrm{o}} \frac{\partial \mathbf{E}}{\partial \mathrm{t}}. \tag{C.4}$$

First take the curl of each side of Maxwell's third equation,

$$\bigtriangledown \times (\bigtriangledown \times \mathbf{E}) = \bigtriangledown \times -\frac{\partial \mathbf{B}}{\partial \mathrm{t}}. \tag{C.5}$$

The left side of the equation is,

$$\bigtriangledown \times (\bigtriangledown \times \mathbf{E}) = \bigtriangledown(\bigtriangledown \cdot \mathbf{E}) - \bigtriangledown^2 \mathbf{E}. \tag{C.6}$$

Applying Maxwell's equation, the first term of the right side of Equation C.6 is zero. Therefore,

$$\bigtriangledown \times (\bigtriangledown \times \mathbf{E}) = - \bigtriangledown^2 \mathbf{E}. \tag{C.7}$$

Now let's look at the right hand side of Equation C.5,

$$\bigtriangledown \times -\frac{\partial \mathbf{B}}{\partial t} = -\frac{\partial}{\partial t}(\bigtriangledown \times \mathbf{B}) = -\mu_\mathrm{o}\epsilon_\mathrm{o}\frac{\partial^2 \mathbf{E}}{\partial \mathrm{t}^2}. \tag{C.8}$$

Combining Equations C.5, C.7 and C.8,

$$\bigtriangledown^2 \mathbf{E} - \mu_\mathrm{o}\epsilon_\mathrm{o}\frac{\partial^2 \mathbf{E}}{\partial \mathrm{t}^2} = 0. \tag{C.9}$$

A generalized form of this equation is the wave equation:

$$\bigtriangledown^2 u - \mu_o\epsilon_o\frac{\partial^2 u}{\partial t^2} = 0. \tag{C.10}$$

The light disturbance at point P at time t is represented by the scalar function

$$u(P,t) = A(P)cos[2\pi\nu t + \phi(P)], \tag{C.11}$$

where $A(P)$ and $\phi(P)$ are the amplitude and phase of the wave the position P, and ν is the frequency. The real part of the previous equation is,

$$u(P,t) = Re\{U(P)exp(-i2\pi\nu t)\}, \tag{C.12}$$

where $U(P)$ is a complex function of position. Using this equation in the wave function equation,

$$\left(\bigtriangledown^2 + k^2 \right) U = 0, \tag{C.13}$$

where $k = 2\pi\frac{\nu}{c}$.

C.1.2 Helmholtz's Kirchhoff's Theorem

Let $U(P)$ and $U'(P)$ be complex functions of position and S is a closed surface surrounding a volume V. If U and U' and their first and second partial derivatives are single-valued and continuous within and on S, then Green's theorem can be applied. Refer to Figure 8.2 in "Principles of Optics by Born.

Green's theorem is,

$$\int\int\int_V (U \bigtriangledown^2 U' - U' \bigtriangledown^2 U) dv = \int\int_S \left(U\frac{\partial U'}{\partial n} - U'\frac{\partial U}{\partial n} \right) ds, \tag{C.14}$$

where $\frac{\partial}{\partial n}$ signifies a partial derivative in the outward normal direction at each point on S.

If U' satisfies the wave equation, then

$$(\bigtriangledown^2 + k^2)U' = 0. \tag{C.15}$$

Combining Equations C.13, C.14, and C.15,

$$\int\int_S \left(U\frac{\partial U'}{\partial n} - U'\frac{\partial U}{\partial n} \right) dS = 0. \tag{C.16}$$

Suppose $U' = \frac{e^{iks}}{s}$, which has a sungularity at $s = 0$. Therefore, P must be excluded from the integration. So a small sphere of radius ϵ is made around the point P. Next, integrate the volume between the surfaces S and S'.

The integral is broken up into parts over S and S'.

$$\int_{S'} \left(U(P)\frac{\partial}{\partial n}\frac{e^{iks}}{s} - \frac{e^{iks}}{s}\frac{\partial U(P)}{\partial n} \right) dS' = -\int_S \left(U(P)\frac{\partial}{\partial n}\frac{e^{iks}}{s} - \frac{e^{iks}}{s}\frac{\partial U(P)}{\partial n} \right) dS. \tag{C.17}$$

Over the surface S', $s = \epsilon$, $\frac{\partial}{\partial n} = \frac{\partial}{\partial s}$, and $dS' = \epsilon^2 d\Omega$, where $d\Omega$ is the solid angle. Therefore,

$$\int_0^{4\pi} \left[U(P)\frac{e^{ik\epsilon}}{\epsilon}\left(ik + \frac{1}{\epsilon} \right) - \frac{e^{ik\epsilon}}{\epsilon}\frac{\partial U(P)}{\partial s} \right] \epsilon^2 d\Omega. \tag{C.18}$$

In the limit ϵ approaches 0, only the last term survives.

$$\int_0^{4\pi} U(P) d\Omega = 4\pi U(P) \tag{C.19}$$

and

$$U(P) = \frac{1}{4\pi}\int\int_S \left(U\frac{\partial}{\partial n}\left(\frac{e^{iks}}{s} \right) - \frac{e^{iks}}{s}\frac{\partial U}{\partial n} \right) dS. \tag{C.20}$$

This is the *Helmholtz-Kirchhoff Integral.*

C.2 Kirchhoff's Diffraction Theory

Consider a monochromatic wave from a point source P_o, propagating through an opening in an opaque screen. Let P be the point where the light disturbance will be measured. Assume the opening on the screen is small compared to r and s. Starting with the Helmholtz and Kirchhoff Integrals,

$$U(P) = \frac{1}{4\pi}\left[\int\int_A + \int\int_B + \int\int_C\right]\left\{U\frac{\partial}{\partial n}\left(\frac{e^{iks}}{s}\right) - \left(\frac{e^{iks}}{s}\right)\frac{\partial U}{\partial n}\right\}dS. \tag{C.21}$$

Applying Boundary conditions. On surface A , opening in the screen:

$$U = \frac{Ae^{ikr}}{r}, \qquad \frac{\partial U}{\partial n} = \frac{Ae^{ikr}}{r}\left[ik - \frac{1}{r}\right]cos(n,r) \sim \frac{Aike^{ikr}}{r}cos(n,r), \tag{C.22}$$

using the fact that $ik >> 1/r$, and $cos(n,r)$ is the angle between the vectors n and r. On surface B , nonilluminated side of the screen,

$$U = 0, \qquad \frac{\partial U}{\partial n} = 0, \tag{C.23}$$

U will never reach the surface B.

On surface C : Assume radius R is so large that at the time of the disturbance the wave never reaches surface C. Therefore there is no contributions on the surface C and the integral will vanish. The integral becomes,

$$U(P) = -\frac{iA}{2\lambda}\int\int_A \frac{e^{ik(r+s)}}{rs}[cos(n,r) - cos(n,s)]dS. \tag{C.24}$$

This is called the *Kirchhoff Diffraction Formula* .

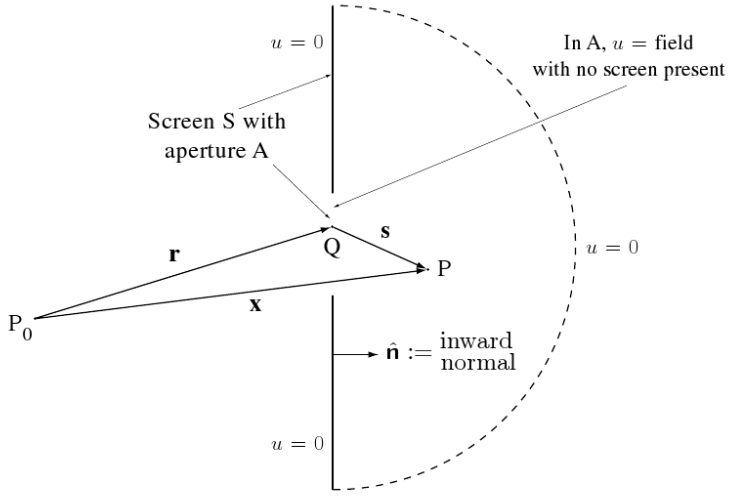

Figure C.1: Kirchhoff Boundary Conditions (*www.utdallas.edu*)

C.2.1 Fraunhofer Diffraction

The Kirchhoff's diffraction formula is used to find the formula for diffraction through a screen. A monochromatic wave is emitted from point, P_o, and propagates through an opening in an opague screen. The goal is to determine the light disturbance at point P. The distance from P_o to the screen and the distance P to the screen is large compared to the opening in the screen.

However, $cos(n,r) = -cos(n,s) = cos\delta$. Also, $1/rs \simeq 1/r's'$. Therefore the Kirchhoff's equation reduces to

$$U(P) \sim -\frac{Aicos\delta}{\lambda r's'} \int\int_A e^{ik(r+s)} dS; \tag{C.25}$$

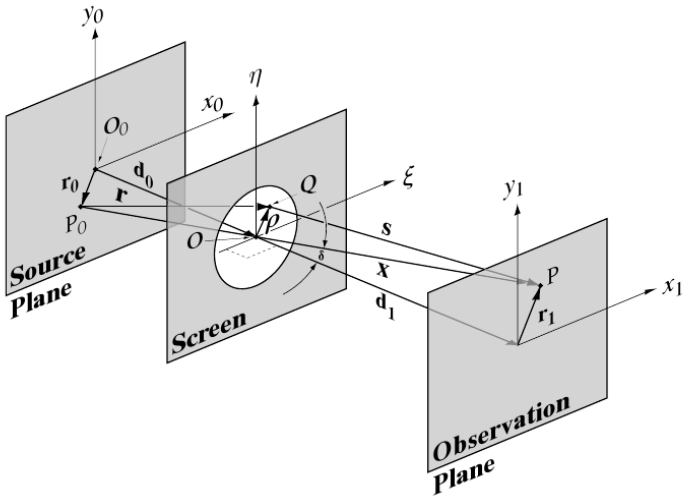

Figure C.2: Diffraction through a plane (*www.utdallas.edu*)

we have

$$\begin{aligned} r^2 &= (x_o - \xi)^2 + (y_o - \eta)^2 + z_o^2, \\ s^2 &= (x - \xi^2 + (y - \eta)^2 + z^2, \\ r'^2 &= x_o^2 + y_o^2 + z_o^2, \\ s'^2 &= x^2 + y^2 + z^2. \end{aligned} \tag{C.26}$$

Hence,

$$\begin{aligned} r &= \sqrt{r'^2 - 2(x_o\xi + y_o\eta) + \xi^2 + \eta^2}, \\ s &= \sqrt{s'^2 - 2(x\xi + y\eta) + \xi^2 + \eta^2}. \end{aligned} \tag{C.27}$$

The linear dimensions of the aperture are small compared to both r' and s', therefore a power expansion for the previous equations in terms of ξ/r', η/r',ξ/s', and η/s' is applied

$$\begin{aligned} r &\sim r' - \frac{x_o\xi + y_o\eta}{r'} + \frac{\xi^2 + \eta^2}{2r'} - \frac{(x_o\xi + y_o\eta)^2}{2r'^3} - ... \\ s &\sim s' - \frac{x\xi + y\eta}{s'} + \frac{\xi^2 + \eta^2}{2s'} - \frac{(x\xi + y\eta)^2}{2s'^3} - .... \end{aligned} \tag{C.28}$$

Substituting this into Equation C.25

$$U(P) = -\frac{icos\delta}{\lambda} A e^{ik(r'+s')} r's' \int\int_A e^{ikf(\xi,\eta)} d\xi d\eta, \tag{C.29}$$

where

$$f(\xi,\eta) = -\frac{x_o\xi + y_o\eta}{r'} - \frac{x\xi + y\eta}{s'} + \frac{\xi^2+\eta^2}{2r'} + \frac{\xi^2+\eta^2}{2s'} - \frac{(x_o\xi + y_o\eta)^2}{2r'^3} - \frac{(x\xi + y\eta)^2}{2s'^3} .... \tag{C.30}$$

We will use first two direction cosines

$$\begin{aligned} l_o = -\frac{x_o}{r'}, \qquad m_o = -\frac{y_o}{r'}, \\ l = \frac{x}{s'}, \qquad m = \frac{y}{s'}, \end{aligned} \tag{C.31}$$

which can be rewritten as,

$$f(\xi,\eta) = (l_o - l)\xi + (m_o - m)\eta + \frac{1}{2}\left[\left(\frac{1}{r'} + \frac{1}{s'}\right)(\xi^2+\eta^2) - \frac{(l_o\xi + m_o\eta)^2}{r'} - \frac{l\xi + m\eta)^2}{s'}\right]. \tag{C.32}$$

All quadratic terms can be neglected for Fraunhoffer diffraction.

$$U(P) = C \int\int_A e^{ik(l_o-l)\xi + ik(m_o-m)\eta} d\xi d\eta, \tag{C.33}$$

where $C = -\frac{icos\delta}{\lambda}\frac{Ae^{ik(r'+s')}}{r's'}$

Let $p = l - l_o$ and $q = m - m_o$, which are the axes on the observation plane, and the previous equation can be written as

$$U(P) = C \int\int_A e^{-ik(p\xi+q\eta)} d\xi d\eta. \tag{C.34}$$

This is the *Fraunhofer Diffraction formula.*

C.2.2 Diffraction through a Single Slit

A monochromatic wave with pass through a one-dimensional slit of width 2a. Using Fraunhoffer diffraction formula,

$$U(P) = C\int_{-a}^{a} e^{-ikp\xi}d\xi = \frac{C}{-ikp}\left[e^{-ikpa} - e^{ikpa}\right]. \tag{C.35}$$

It can be rewritten as

$$U(P) = \frac{2Csin(kpa)}{kp}. \tag{C.36}$$

Intensity is

$$I = |U(P)|^2 = \left(\frac{Sin(kpa)}{kpa}\right)^2 I_o, \tag{C.37}$$

where $I_o = 4C^2a^2$.

Let $x = kpa$ and $y = \left(sin(x)/x\right)^2$.

The distance from the peak to the first null is

$$p = 1.01\frac{\lambda}{D}, \tag{C.38}$$

where $2a = D$ and D is the width of the slit.

For a $D = 3.5$ meters and $\lambda = 1$ cm, $p = 9.9'$

The HWHM is when x=1.390.

$$p = 0.89\frac{\lambda}{D}FWHM. \tag{C.39}$$

For example, $D = 3.5$ meters and $\lambda = 1$ cm. Therefore, $p = 8.6'FWHM$.

C.2.3 Diffraction through a Circular Aperture

In order to find the diffraction pattern through a circular aperture, the Fraunhoffer diffraction formula is required,

$$U(P) = C \int_0^a \int_0^{2\pi} e^{-ik(p\xi+q\eta)} d\xi d\eta. \tag{C.40}$$

Use polar coordinate

$$\rho cos\theta = \xi,$$

$$\rho sin\theta = \eta,$$

$$\omega cos\phi = p,$$

$$\omega sin\phi = q.$$

After substituting the above equations into Equation C.40,

$$U(P) = C \int_0^a \int_0^{2\pi} e^{-ik(\omega\rho cos\theta cos\phi+\omega\rho sin\theta sin\phi)} \rho d\rho d\theta. \tag{C.41}$$

After using a trig identity,

$$U(P) = C \int_0^a \int_0^{2\pi} e^{-ik\omega\rho cos(\theta-\phi)} \rho d\rho d\theta. \tag{C.42}$$

Bessel function:

$$J_n(x) = \frac{i^{-n}}{2\pi} \int_0^{2\pi} e^{ixcos\alpha} e^{in\alpha} d\alpha, \tag{C.43}$$

for $n = 0$,

$$J_0(x) = \frac{1}{2\pi} \int_0^{2\pi} e^{ixcos\alpha} d\alpha. \tag{C.44}$$

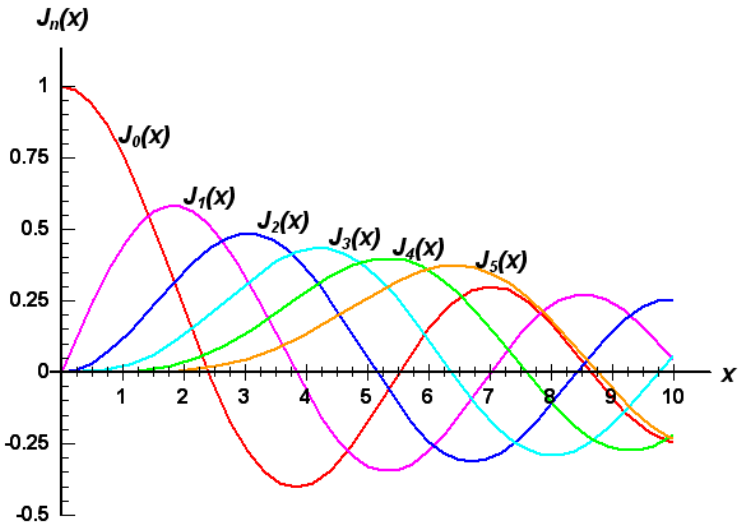

Figure C.3: Bessel Function (*www.efunda.com*)

Apply the above equation to Equation C.42, where $x = k\rho\omega$, $\alpha = \theta - \phi$, and $dx = k\omega d\rho$,

$$U(P) = \frac{4\pi^2 C}{k^2\omega^2}\int_0^{ka\omega} xJ_0(x)dx \tag{C.45}$$

$$\frac{d}{dx}[x^{n+1}J_{n+1}(x)] = x^{n+1}J_n(x), \tag{C.46}$$

when $n = 0$,

$$\int_0^x x'J_0(x')dx' = xJ_1(x). \tag{C.47}$$

Therefore,

$$U(P) = \frac{4\pi^2 C}{k\omega}[J_1(ka\omega)]. \tag{C.48}$$

Intensity is equal to the square of the previous equation: therfore,

$$I = |U(P)|^2 = I_0 \left(\frac{2J_1(ka\omega)}{ka\omega} \right)^2, \tag{C.49}$$

where $k = \frac{2\pi}{\lambda}$.

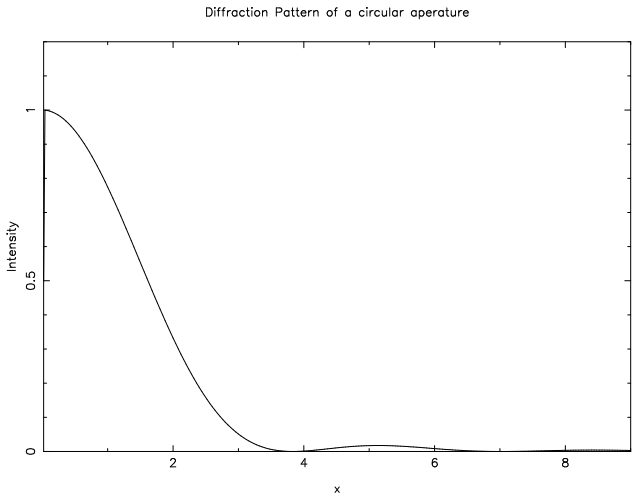

Figure C.4: Diffraction pattern from a wave passing through a circular aperature.

The first zero of this function occurs at $ka\omega = 3.833$. Also $2a = D$, where D is the diameter. Therefore, the angle from the peak to the first zero is,

$$\omega = 1.22 \frac{\lambda}{D}. \tag{C.50}$$

For $D = 3.5$ meters and $\lambda = 1$cm, $\omega = 11.98'$. The FWHM occurs when $ka\omega = 1.830$. For $\lambda = 1$cm and $D = 3.5$meters, $\omega = 11.44'$ FWHM.

C.2.4 Rayleigh Criterion

The Rayleigh Criterion is used to specify when two sources can be distinguished. This occurs when the peak intensity of one source is located at the first minimum of the second source, see Figure C.6.

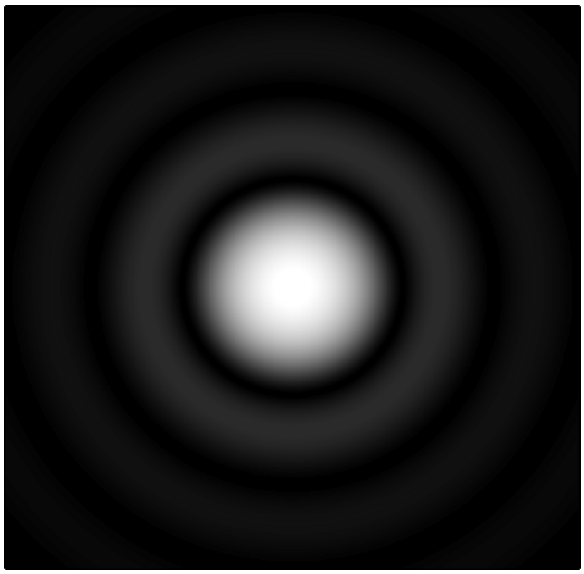

Figure C.5: Diffraction pattern of a circular aperture (*commons.wikimedia.org*).

The angular separation is defined as

$$\theta = 1.22\frac{\lambda}{D}. \tag{C.51}$$

When $\lambda = 1$cm and $D = 3.5$ meters, then the minimum angular separation is $12'$. If the peak intensity of two sources are closer than this, it is difficult to distinguish the two sources from each other.

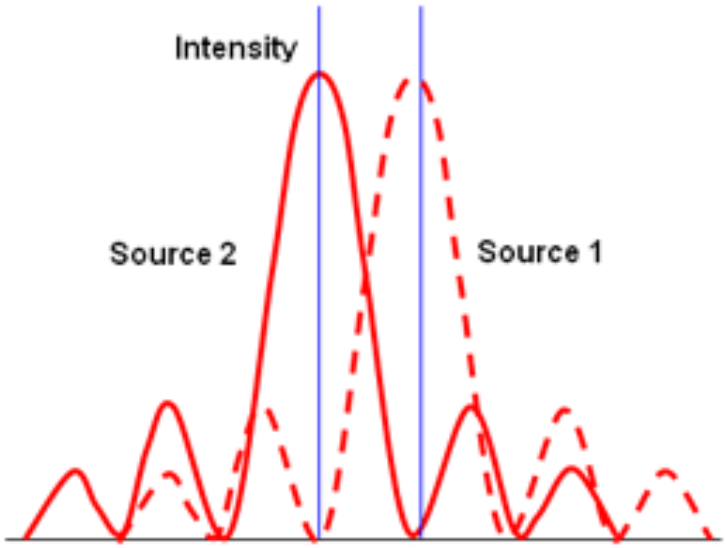

Figure C.6: Rayleigh Criterion (*www.iop.org*)

APPENDIX D

INTERFEROMETRY BASICS

This section discusses the basics of interferometry and the importance of long and short baselines.

D.1 Diffraction Pattern of a Two-Element Interferometer

Young's double slit experiment can be used to illustrate the diffraction pattern of a two-element interferometer. A propagating wave is emitted in the direction of a barrier with two small slits. The slits are very close together and located a distance d apart, see Figure D.1. The waves emitting from the two slits will form a diffraction pattern on a screen that is located a distace L from the slits.

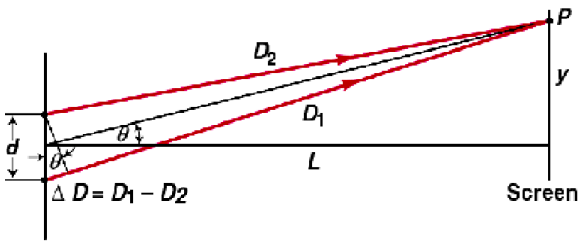

Figure D.1: A diffraction pattern will be created on the screen located at a distance L from the two slits. $(http://www.physics.sc.edu/\ rjones/phys153/0129.GIF)$.

In Figure D.2, D_1 is the distance from slit 1 to a point P on the screen, D_2 is the distance from slit 2 to a point P on the screen, and ΔD is the path difference,

$$\Delta D = D_1 - D_2 = dsin\theta. \tag{D.1}$$

In order to have constructive interference on the screen, the two emitting waves must be in phase; therefore, the path difference will be

$$dsin\theta = n\lambda, \tag{D.2}$$

where λ is the wavelength and $n = 0, \pm1, \pm2, ...$ Since $d << L$, θ is small, and the small angle approximation can be applied, $sin\theta \approx \theta$. Therefore Equation D.2 can be rewritten as,

$$\theta \simeq \frac{n\lambda}{d}. \tag{D.3}$$

Destructive interference occurs when the two waves are out of phase. This happens when the path difference is equal to $(n + 1/2)\lambda$; therefore,

$$\theta \simeq \left(n + \frac{1}{2}\right)\frac{\lambda}{d}, \tag{D.4}$$

where $n = 0, \pm1, \pm2, ...$ Therefore the diffraction pattern on the screen can be seen in Figure D.2.

Young's double slit experiment can be used to describe the diffraction pattern of a two-element interferometer. The antennas were represented by the slits in the experiment and the baseline, B , of the two antennas was length d in the experiment. Constructive interference occurs at,

$$\theta \simeq \frac{n\lambda}{B}, \tag{D.5}$$

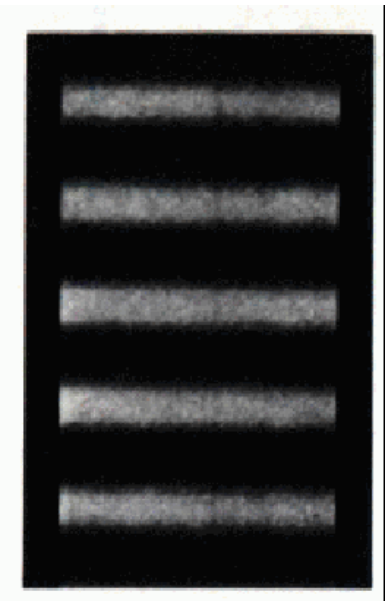

Figure D.2: Diffraction pattern of Young's double slit experiment. This image has been taken from $http://psi.phys.wits.ac.za/img21.png$

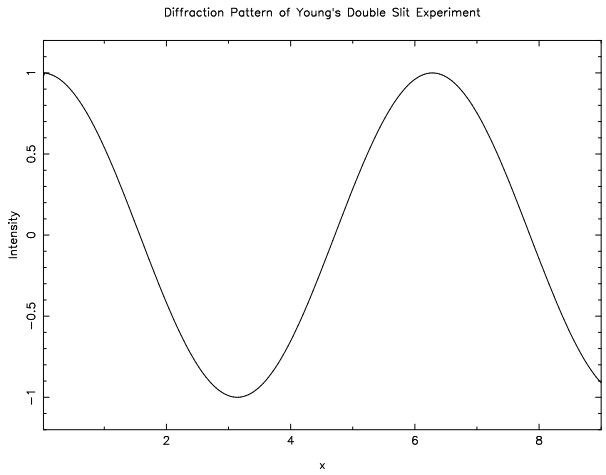

Figure D.3: The Diffraction pattern of Young's double slit experiment.

and destructive interference at

$$\theta \simeq \left(n + \frac{1}{2}\right)\frac{\lambda}{B}. \tag{D.6}$$

The central bright fringe occurs when $n = 0$, therefore $\theta = 0$ according to Equation D.3. According to Equation D.4, the first null occurs when $n = 0$; therefore,

the angular separation between the peak and the first null is,

$$\theta = \frac{\lambda}{2B}. \tag{D.7}$$

For a wavelengh of 1 centimeter the angular separation, θ between the peak and first null can be found in Table D.1 for different baselines.

Baseline (meters)	θ (arcmin)
3.5	4.9
4.5	3.8
50.0	0.3

Point sources contaminate measurements of the Sunyaev Zel'dovich decrement. So, a two-element interferometer needs to be sensitive to small angular scales in order to locate and measure the flux of point sources. For a baseline of 50 meters the two-element interferometer is sensitive to angular scales of approximately $0.6'$. Therefore, sources that are larger than $0.6'$, begin to resolve out. The short baselines are sensitive to large angular scales, for examples a baseline of 4.5 meters, is sensitive to angular scales of 7.4', which is able to detect the SZE decrement.

The synethesized beam of an interferometer is a combination of the diffraction pattern of many two-element interferometers.

D.2 Visibility Equation

The visibility equaton is

$$V(u,v) \approx \int B(x,y) e^{[i2\pi(xu+vy)]} dxdy, \tag{D.8}$$

where $B(x,y)$ is the Intensity of the source, u and v are the coordinates of the uv plane, and x and y are the coordinates of the plane the source is in (Burke and Graham-Smith 2002). The exponent looks like a wave equation.

The visibility equation is the intensity integrated over the source. It can also be written in the form of a fourier transform,

$$V(u,v) \rightleftharpoons B(x,y). \tag{D.9}$$

The Fourier transform is,

$$F(k) = \int f(x) e^{-2\pi i x k} dx. \tag{D.10}$$

D.3 UV Plane

The UV plane is the plane that is perpendicular to the line of sight of the source. The coordinates of the uv plane are u, v, and w. All 3 coorindates are perpendicular to each other. The w coordinate is in the direction along the line of sight. The u coordinate is in the northerly direction (which is also the direction of right ascension), and the v coordinate is in the easterly (which is also the direction of declination).

The baseline of the a two-element interferometer is plotted in the uv plane. A snapsnot of the baseline at a single instance in time will yield one point in the uv plane. Figure D.4 shows the uv coverage for the SZA during an observation. Ideally, complete coverage of the uv plane is preferred, so the image is fully constrained when you take the Fourier Transform.

D.4 Response of a Two-element Interferometer

The equation for the response of a two-element interferometer is,

$$S_{xy}(\nu) = A(\mathbf{s})\mathrm{Sexp}(\mathrm{i}2\pi\nu\tau_{\mathrm{g}}), \tag{D.11}$$

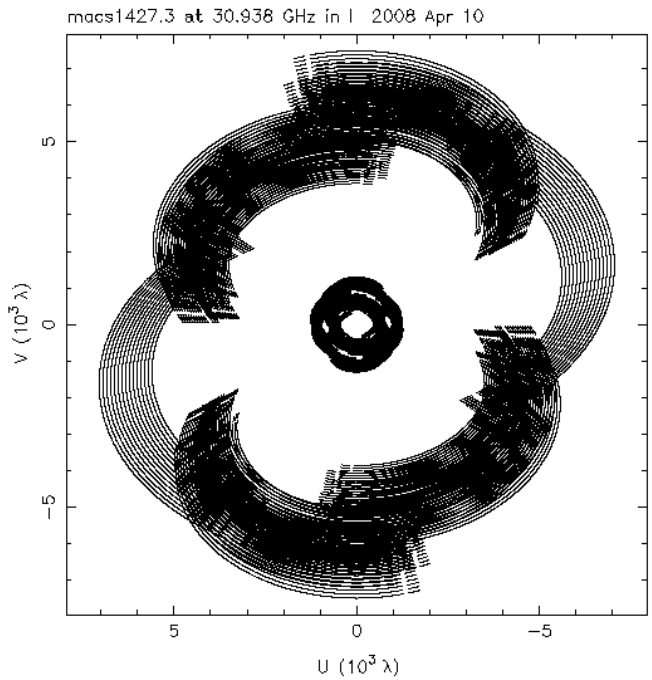

Figure D.4: UV plot of MACS1427

where $A(\mathbf{s})$ is the primary beam pattern, S is the source flux, ν is the frequency and τ_g is the time delay. The response of a two-element interferometer is the convolution of the primary beam and the diffraction patter of a two-element interferometer, see Figure D.5.

D.5 Importance of Long and Short Baselines

The Sunyaev Zel'dovich Array (SZA) is an eight element interferometer that will be used in this example for examining long and short baselines. The array is in a hybrid configuration, where 6 antennas are closely packed together, and 2 antennas are further apart. The distance between two antennas are referred to as a baseline. There are 15 baseline between the antennas 0-5, known as short baselines.

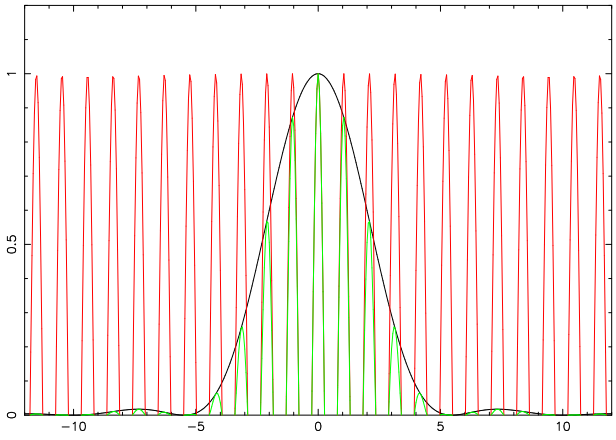

Figure D.5: The red line (cosine) is the diffraction pattern of a two-element interferometer, the white line is the primary beam, and the green line is the response pattern of a two-element interferometer.

Antenna 6 and 7 each create 6 long baselines with antennas 0-5, and another long baseline between them; therefore, the SZA has 13 long baselines.

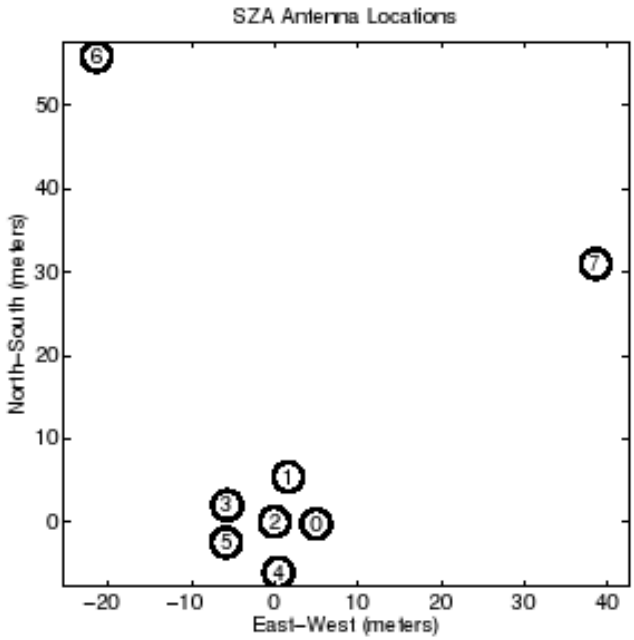

Figure D.6: The location of the eight antennas of the SZA (Muchovej et al. 2008).

Point sources in cluster fields can contaminate the measurements of the SZE decrement by filling in part of the decrement. Therefore, the interferometer needs to be sensitive to small angular scales so the point sources can be located, measured, and removed from the cluster field. The long baseline data is used to locate and remove point sources. A two-element interferometer is sensitive to angular scales,

$$\frac{\lambda}{B}, \tag{D.12}$$

where λ is the wavelength and B is the baseline. For example, a two-element interferometer with a wavelength of 1 cm and a baseline of 50 meters is sensitive to angular scales of 0.7'. Sources larger than this will be resolved out, such as the cluster. Figure D.7 shows the long baseline data for CL1226 before and after the point source is removed from the cluster field. After the point source is removed, a map of noise remains.

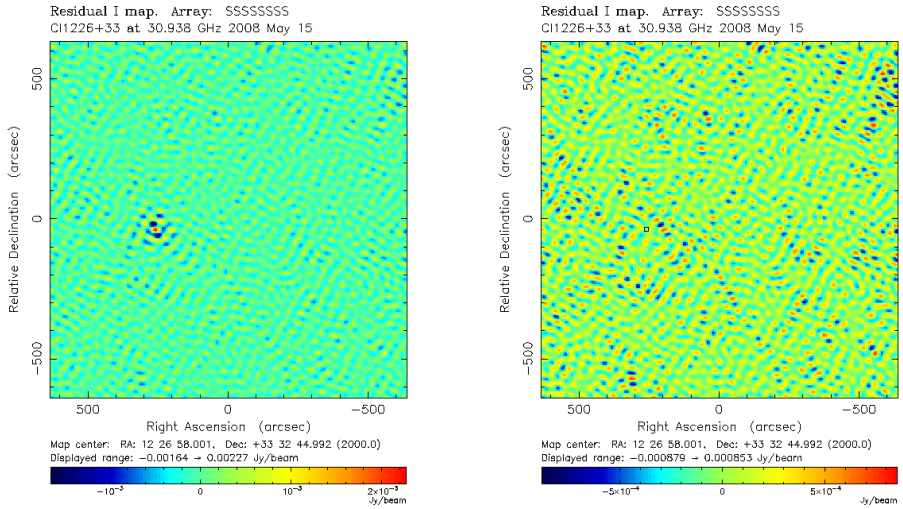

Figure D.7: CL1226: (a) Map of the long baseline data. An off center point source is visible in the field. (b) Map of the long baseline data after the point source has been removed, only noise is present in the map

After the point sources have been removed, the short baseline data are used to detect the SZE decrement. A two-element interferometer with a wavelength of 1 cm and a baseline of 5 meters is sensitive to angular scales of 7'.

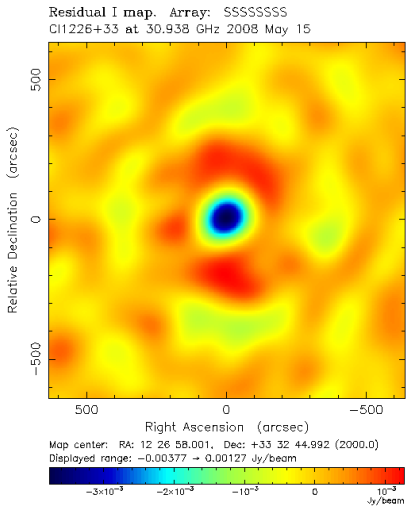

Figure D.8: CL1226: Map of the short baseline data. The SZE decrement is visible in the middle of the map (blue region).

The SZA antennas are 3.5 meters in diameter, this allows the antennas to be closely packed together so the interferometer can be sensitive to large angular scales in order to detect galaxy clusters.

APPENDIX E

HYDROSTATIC EQUILIBRIUM AND PRESSURE RELATIONSHIP

In this section, the relationship between hydrostatic equilibrium and thermodynamical properties are explored.

E.1 Relationship Between Hydrostatic Equilibrium and Central Pressure of a Sphere

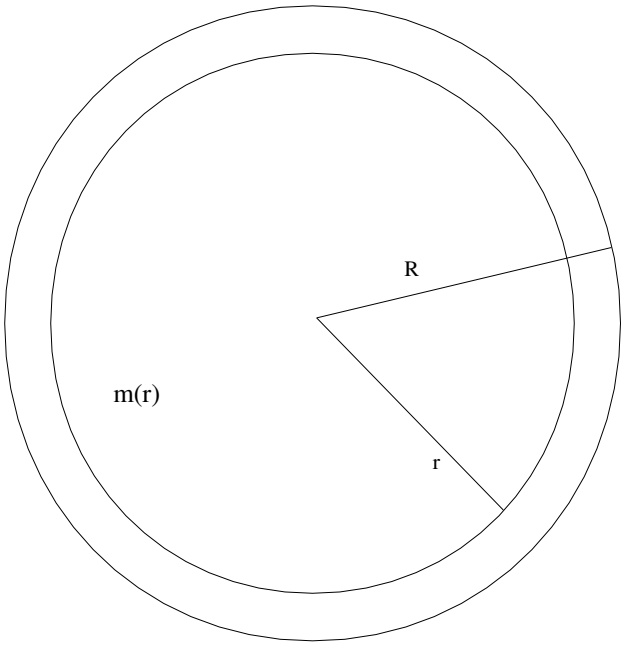

Starting with the equation for hydrostatic equilibrium,

$$\frac{dP(r)}{dr} = -\frac{GM(r)\rho(r)}{r^2}$$

and the mass conservation equation,

$$\frac{dM(r)}{dr} = 4\pi r^2 \rho(r),$$

in which $M(r)$ is the mass within the radius r, $\rho(r)$ is the gas density, and $P(r)$ is the gas pressure. The hydrostatic equilibrium equation can be written as,

$$\frac{dP}{dr} = -\frac{GM(r)}{4\pi r^4}\frac{dM(r)}{dr}. \tag{E.1}$$

Then, consider the following equation:

$$\frac{d}{dr}\left[P + \frac{GM^2(r)}{8\pi r^4}\right] = \frac{dP}{dr} + \frac{GM(r)}{4\pi r^4}\frac{dM(r)}{dr} - \frac{GM^2(r)}{2\pi r^5}. \tag{E.2}$$

The first two terms on the right hand side are equal to zero by Equation E.1, then Equation E.2 can be written as,

$$\frac{d}{dr}\left[P + \frac{GM^2(r)}{8\pi r^4}\right] = -\frac{GM^2(r)}{2\pi r^5} < 0, \tag{E.3}$$

where P_c the central pressure, $P(r)$ the pressure of the sphere at r, P_s the pressure at the surface, M_c the mass at the center of the sphere, $M(r)$ the mass of the sphere at r, r is a radius within the sphere, and R is the radius to the surface of the sphere. Therefore, since $P + \frac{GM^2(r)}{8\pi r^4}$ decreases with radius according to Equation E.3,

$$P_c + \frac{GM_c^2(r)}{8\pi r_c^4} > P(r) + \frac{GM^2(r)}{8\pi r^4} > P_s + \frac{GM^2}{8\pi R^4}.$$

Apply the boundary conditions, $P_s = 0$ and $M_c = 0$; therefore,

$$P_c > P + \frac{GM^2(r)}{8\pi r^4} > \frac{GM^2}{8\pi R^4} \tag{E.4}$$

$$P_c > \frac{GM^2}{8\pi R^4}.$$

For $M = 10^{14} M_\odot$, $R = 1 Mpc$, and $\mu = 0.62$ for an ionized hot gas of 90% H and 10% He, the values on the right hand side of the inequalities are

$P_c > 1.3 \times 10^{-12}$ *dyne* cm^{-2}.

E.2 Relationship Between Hydrostatic Equilibrium and the Potential Energy of a Sphere

Starting with the followng equation since $-\Omega = \int \frac{GM(r)dM(r)}{r}$,

$$I_\nu = \int_0^R \frac{GM(r)dM(r)}{r^\nu}.$$

Using Equation E.1, this is equivalent to

$$I_\nu = -4\pi \int_0^R \frac{dP}{dr} r^{4-\nu} dr.$$

Using integration by parts,

$$-4\pi \int_0^R \frac{dP}{dr} r^{4-\nu} dr = -4\pi P r^{4-\nu}|_0^R + 4\pi(4-\nu) \int_0^R P r^{3-\nu} dr.$$

The first term on the right hand side is zero because $P(R) = P_s = 0$; therefore,

$$I_\nu = 4\pi(4-\nu) \int_0^R P r^{3-\nu} dr.$$

Using the relationship found in Equation E.4,

$$4\pi(4-\nu) \int_0^R P_c r^{3-\nu} dr > I_\nu + 4\pi(4-\nu) \int_0^R \frac{GM^2(r)}{8\pi r^4} r^{3-\nu} dr > 4\pi(4-\nu) \int_0^R \frac{GM^2}{8\pi R^4} r^{3-\nu} dr$$

$$4\pi P_c R^{4-\nu} > I_\nu + \frac{4-\nu}{2} \int_0^R \frac{GM^2(r)}{r^{1+\nu}} dr > \frac{GM^2}{2R^\nu}. \tag{E.5}$$

Now evaluate the integral in the previous equation,

$$\int_0^R \frac{GM^2(r)}{r^{1+\nu}}dr = -\frac{1}{\nu}\int_0^R GM^2(r)\frac{d}{dr}\left(\frac{1}{r^\nu}\right)dr.$$

Using integration by parts,

$$-\frac{1}{\nu}\int_0^R GM^2(r)\frac{d}{dr}\left(\frac{1}{r^\nu}\right)dr = -\frac{GM^2}{\nu R^2} + \frac{2}{\nu}I_\nu,$$

where $I_\nu = \int_0^R \frac{GM(r)}{r^\nu}dr$. Putting the above result into Equation E.5,

$$4\pi P_c R^{4-\nu} > I_\nu + \frac{4-\nu}{2}\left[-\frac{GM^2}{\nu R^\nu} + \frac{2}{\nu}I_\nu\right] > \frac{GM^2}{2R^\nu},$$

which can be simplified,

$$\nu\pi P_c R^{4-\nu} + \frac{4-\nu}{8}\frac{GM^2}{R^\nu} > I_\nu > \frac{GM^2}{2R^\nu}.$$

The case $\nu = 1$ is relevant to the present question, since $I_1 = -\Omega$. For $\nu = 1$,

$$\pi P_c R^3 + \frac{3GM^2}{8R} > -\Omega > \frac{GM^2}{2R}.$$

Therefore,

$$-\Omega > \frac{GM^2}{2R}.$$

For $M = 10^{14}M_\odot$, $R = 1Mpc$, and $\mu = 0.62$ for an ionized hot gas of 90% H and 10% He, the values on the right hand side of the inequalities are

$-\Omega > 4.4 \times 10^{62}$ *dyne cm.*

E.3 Relationship Between the Mean Temperature and Hydrostatic Equilibrium of a Sphere

Start with the ideal gas law, $P(r) = nkT(r)$; using the fact that $\rho(r) = \mu m_H n$, the ideal gas law can be rewritten,

$$P(r) = \frac{kT(r)\rho(r)}{\mu m_H}, \tag{E.6}$$

solving for T and substituting in to $\overline{T} = \frac{1}{M}\int_0^M T dM(r)$,

$$\overline{T} = \frac{1}{M}\int_0^M \frac{P(r)\mu m_H}{\rho k} dM(r).$$

Using the relation $dM(r) = \rho dV(r)$

$$\overline{T} = \frac{\mu m_H}{kM}\int_0^M P(r) dV(r). \tag{E.7}$$

Equation E.3 is used to evaluate the integral above,

$$\frac{dP(r)}{dM(r)} = -\frac{GM(r)}{4\pi r^4}$$

$$4\pi r^3 dP(r) = -\frac{GM(r)}{r} dM(r).$$

Using the fact $V = -4/3\pi r^3$, where V is the volume of a sphere.

$$\int 3V(r) dP(r) = -\int \frac{GM(r)}{r} dM(r).$$

Use integration by parts,

$$3\int V(r) dP(r) = 3VP|_c^s - 3\int P(r) dV(r).$$

The boundary conditions where $V_c = 0$ and $P_s = 0$ is applied. Therefore the first term on the right hand side is zero.

$$3\int_0^V P(r) dV(r) = \int_{)}^M \frac{GM(r)}{r} dM(r) = -\Omega. \tag{E.8}$$

Now substitute the right hand side of Equation E.8 into Equation E.7.

$$\overline{T} = -\frac{\mu m_H}{3kM}\Omega.$$

Using the inequalitiy found in the last problem $-\Omega > (GM^2)/(2R)$,

$$\overline{T} > \frac{1}{6}\frac{\mu m_H}{k}\frac{GM}{R}.$$

For $M = 10^{14} M_{\odot}$, $R = 1 Mpc$, and $\mu = 0.62$ for an ionized hot gas of 90% H and 10% He, the values on the right hand side of the inequalities are

$\overline{T} > 5.5 \times 10^{6} K$.

REFERENCES

Allen, S. W., Rapetti, D. A., Schmidt, R. W., Ebeling, H., Morris, R. G., & Fabian, A. C. 2008, *Mon. Not. Royal Astron. Soc.*, 383, 879

Allen, S. W., Schmidt, R. W., Ebeling, H., Fabian, A. C., & van Speybroeck, L. 2004, *Mon. Not. Royal Astron. Soc.*, 353, 457

Allen, S. W., Schmidt, R. W., & Fabian, A. C. 2002, *Mon. Not. Royal Astron. Soc.*, 335, 256

Arnaud, M., Pointecouteau, E., & Pratt, G. W. 2007, A&A, 474, L37

Ascasibar, Y., & Diego, J. M. 2008, *Mon. Not. Royal Astron. Soc.*, 383, 369

Ascasibar, Y., Yepes, G., Müller, V., & Gottlöber, S. 2003, *Mon. Not. Royal Astron. Soc.*, 346, 731

Battaglia, N., Bond, J. R., Pfrommer, C., Sievers, J. L., & Sijacki, D. 2010, ArXiv e-prints: astro-ph/1003.4256B

Bielby, R. M., & Shanks, T. 2007, *Mon. Not. Royal Astron. Soc.*, 382, 1196

Birkinshaw, M. 1999, Physics Reports, 310, 97

Birkinshaw, M., & Hughes, J. P. 1994, *Astrophysical Journal*, 420, 33

Bonamente, M., Joy, M. K., Carlstrom, J. E., Reese, E. D., & LaRoque, S. J. 2004, *Astrophysical Journal*, 614, 194

Bonamente, M., Joy, M. K., LaRoque, S. J., Carlstrom, J. E., Reese, E. D., & Dawson, K. S. 2006, *Astrophysical Journal*, 647, 25

Bonamente, M., Lieu, R., Mittaz, J. P. D., Kaastra, J. S., & Nevalainen, J. 2005, *Astrophysical Journal*, 629, 192

Borgani, S., & Kravtsov, A. 2009, ArXiv e-prints

Brunetti, G., Venturi, T., Dallacasa, D., Cassano, R., Dolag, K., Giacintucci, S., & Setti, G. 2007, ApJ, 670, L5

Bulbul, G. E., Hasler, N., Bonamente, M., & Joy, M. 2010, *Astrophysical Journal*, 720, 1038

Carlstrom, J. E., Holder, G. P., & Reese, E. D. 2002, ARA&A, 40, 643

Colafrancesco, S., Marchegiani, P., & Palladino, E. 2003, A&A, 397, 27

Colberg, J. M., White, S. D. M., MacFarland, T. J., Jenkins, A., Pearce, F. R., Frenk, C. S., Thomas, P. A., & Couchman, H. M. P. 2000, *Mon. Not. Royal Astron. Soc.*, 313, 229

Crain, R. A., Eke, V. R., Frenk, C. S., Jenkins, A., McCarthy, I. G., Navarro, J. F., & Pearce, F. R. 2007, *Mon. Not. Royal Astron. Soc.*, 377, 41

Eke, V. R., Cole, S., Frenk, C. S., & Patrick Henry, J. 1998, *Mon. Not. Royal Astron. Soc.*, 298, 1145

Ettori, S., Morandi, A., Tozzi, P., Balestra, I., Borgani, S., Rosati, P., Lovisari, L., & Terenziani, F. 2009, A&A, 501, 61

Fowler, J. W. et al. 2010, ArXiv e-prints astro-ph/1001.2934

Freedman, W. L. et al. 2009, *Astrophysical Journal*, 704, 1036

Gastaldello, F., Buote, D. A., Humphrey, P. J., Zappacosta, L., Bullock, J. S., Brighenti, F., & Mathews, W. G. 2007, *Astrophysical Journal*, 669, 158

Giodini, S. et al. 2009, *Astrophysical Journal*, 703, 982

Gonzalez, A. H., Zaritsky, D., & Zabludoff, A. I. 2007, *Astrophysical Journal*, 666, 147

Grainge, K., Grainger, W. F., Jones, M. E., Kneissl, R., Pooley, G. G., & Saunders, R. 2002, *Mon. Not. Royal Astron. Soc.*, 329, 890

Grego, L., Carlstrom, J., Reese, E., Holder, G., Holzapfel, W., Joy, M., Mohr, J., & Patel, S. 2001, *Astrophysical Journal*, 552, 2

Grego, L., Carlstrom, J. E., Joy, M. K., Reese, E. D., Holder, G. P., Patel, S., Cooray, A. R., & Holzapfel, W. L. 2000, *Astrophysical Journal*, 539, 39

Hasler, N., Bulbul, E., Bonamente, M., & Joy, M. 2011, in prep

Hickox, R. C., & Markevitch, M. 2006, *Astrophysical Journal*, 645, 95

Hughes, J. P., & Birkinshaw, M. 1998, *Astrophysical Journal*, 501, 1

Itoh, N., Kohyama, Y., & Nozawa, S. 1998, *Astrophysical Journal*, 502, 7

Komatsu, E. et al. 2011, ApJS, 192, 18

Kravtsov, A. V., Nagai, D., & Vikhlinin, A. A. 2005, *Astrophysical Journal*, 625, 588

Kravtsov, A. V., Vikhlinin, A., & Nagai, D. 2006, *Astrophysical Journal*, 650, 128

Landry, D., Hasler, N., Bonamente, M., & Joy, M. 2011, in prep

LaRoque, S. J., Bonamente, M., Carlstrom, J. E., Joy, M. K., Nagai, D., Reese, E. D., & Dawson, K. S. 2006, *Astrophysical Journal*, 652, 917

Lau, E. T., Kravtsov, A. V., & Nagai, D. 2009, *Astrophysical Journal*, 705, 1129

Lieu, R., Mittaz, J. P. D., & Zhang, S.-N. 2006, *Astrophysical Journal*, 648, 176

Lin, Y., Mohr, J. J., & Stanford, S. A. 2003, *Astrophysical Journal*, 591, 749

Lueker, M. et al. 2010, *Astrophysical Journal*, 719, 1045

Mantz, A., Allen, S. W., Ebeling, H., & Rapetti, D. 2008, *Mon. Not. Royal Astron. Soc.*, 387, 1179

Mantz, A., Allen, S. W., Rapetti, D., & Ebeling, H. 2010, *Mon. Not. Royal Astron. Soc.*, 406, 1759

Marriage, T. A. et al. 2010, ArXiv e-prints

Maughan, B. J., Jones, C., Forman, W., & Van Speybroeck, L. 2008, ApJS, 174, 117

McCarthy, I. G., Bower, R. G., & Balogh, M. L. 2007, *Mon. Not. Royal Astron. Soc.*, 377, 1457

Menanteau, F. et al. 2010, ArXiv e-prints: astro-ph/1006.5126

Million, E. T., & Allen, S. W. 2009, *Mon. Not. Royal Astron. Soc.*, 399, 1307

Mroczkowski, T. et al. 2009, *Astrophysical Journal*, 694, 1034

Muchovej, S. et al. 2010a, *Astrophysical Journal*

—. 2010b, *Astrophysical Journal*, 716, 521

—. 2007, *Astrophysical Journal*, 663, 708

Nagai, D., Kravtsov, A. V., & Vikhlinin, A. 2007, *Astrophysical Journal*, 668, 1

Navarro, J. F., Frenk, C. S., & White, S. D. M. 1997, *Astrophysical Journal*, 490, 493

Nevalainen, J., Markevitch, M., & Lumb, D. 2005, *Astrophysical Journal*, 629, 172

Nozawa, S., Itoh, N., Suda, Y., & Ohhata, Y. 2006, Nuovo Cimento B Serie, 121, 487

Pen, U. 1997, New Astronomy, 2, 309

Percival, W. J. et al. 2010, *Mon. Not. Royal Astron. Soc.*, 401, 2148

Rasheed, B., Bahcall, N., & Bode, P. 2010, ArXiv e-prints

Reese, E. D., Carlstrom, J. E., Joy, M., Mohr, J. J., Grego, L., & Holzapfel, W. L. 2002, *Astrophysical Journal*, 581, 53

Riess, A. G. et al. 2009, *Astrophysical Journal*, 699, 539

Rudy, D. J. 1987, PhD thesis, California Inst. of Tech., Pasadena.

Sanderson, A. J. R., Ponman, T. J., Finoguenov, A., Lloyd-Davies, E. J., & Markevitch, M. 2003, *Mon. Not. Royal Astron. Soc.*, 340, 989

Sarazin, C. L., & Lieu, R. 1998, ApJ, 494, L177

Sasaki, S. 1996, PASJ, 48, L119

Saunders, R. et al. 2003, *Mon. Not. Royal Astron. Soc.*, 341, 937

Sehgal, N. et al. 2010, ArXiv e-prints

Shaw, L. D., Nagai, D., Bhattacharya, S., & Lau, E. T. 2010, ArXiv e-prints

Snowden, S. L. 1998, ApJS, 117, 233

Snowden, S. L. et al. 1997, *Astrophysical Journal*, 485, 125

Spergel, D. N. et al. 2006, ArXiv Astrophysics e-prints

Sulkanen, M. E. 1999, *Astrophysical Journal*, 522, 59

Sun, M., Voit, G. M., Donahue, M., Jones, C., Forman, W., & Vikhlinin, A. 2009, *Astrophysical Journal*, 693, 1142

Sunyaev, R. A., & Zel'dovich, Y. B. 1972, Comments Astrophys. Space Phys., 4, 173

Suto, Y., Sasaki, S., & Makino, N. 1998, *Astrophysical Journal*, 509, 544

Takei, Y. et al. 2008, *Astrophysical Journal*, 680, 1049

Trac, H., Bode, P., & Ostriker, J. P. 2010, ArXiv e-prints

Vanderlinde, K. et al. 2010, ArXiv e-prints

Vikhlinin, A., Kravtsov, A., Forman, W., Jones, C., Markevitch, M., Murray, S. S., & Van Speybroeck, L. 2006, *Astrophysical Journal*, 640, 691

Vikhlinin, A. et al. 2009, *Astrophysical Journal*, 692, 1060

Voit, G. M. 2005, Reviews of Modern Physics, 77, 207

Watkins, R. 1997, *Mon. Not. Royal Astron. Soc.*, 292, L59

Williamson, R. et al. 2011, *Astrophysical Journal*, submitted

Zhang, Y.-Y., Finoguenov, A., Böhringer, H., Kneib, J.-P., Smith, G. P., Kneissl, R., Okabe, N., & Dahle, H. 2008, A&A, 482, 451